Surface Modified ZnO Nanostructures: Synthesis, Optical Studies and Applications in Photocatalysis

Thesis Submitted to AcSIR for the Award of the Degree of

DOCTOR OF PHILOSOPHY

In Chemical Sciences

By

Leena George

Enrollment Number: 10CC12A26033

Under the guidance of

Dr. R. Nandini Devi

Catalysis and Inorganic Chemistry Division

CSIR- National Chemical Laboratory, Pune - 411008, India

April 2017

सीएसआईआर - राष्ट्रीय रासायनिक प्रयोगशाला
(वैज्ञानिक तथा औद्योगिक अनुसंधान परिषद)
डॉ. होमी भाभा मार्ग, पुणे - 411 008, भारत
CSIR - NATIONAL CHEMICAL LABORATORY
(Council of Scientific & Industrial Research)
Dr. Homi Bhabha Road, Pune - 411 008, India

CERTIFICATE

This is to certify that the work incorporated in this Ph.D. thesis entitled "**Surface Modified ZnO Nanostructures: Synthesis, Optical Studies and Applications in Photocatalysis**" submitted by **Ms. Leena George** to Academy of Scientific and Innovative Research (AcSIR) in fulfillment of the requirements for the award of the Degree of **Doctor of Philosophy in Chemistry,** embodies original research work under my supervision/guidance. I further certify that this work has not been submitted to any other University or Institution in part or full for the award of any degree or diploma. Research material obtained from other sources has been duly acknowledged in the thesis. Any text, illustration, table etc., used in the thesis from other sources, have been duly cited and acknowledged.

Student
Leena George

Research Guide
Dr. R. Nandini Devi
Senior Scientist, CSIR-NCL, Pune, India
Assistant Professor, AcSIR, New Delhi, India

Date: 13th April 2017
Place: CSIR-NCL, Pune

Communication Channels
NCL Level DID : 2590
NCL Board No. : +91-20-25902000
EPABX : +91-20-25893300
: +91-20-25893400
FAX
Director's Office : +91-20-25902601
COA's Office : +91-20-25902660
SPO's Office : +91-20-25902664
WEBSITE
www.ncl-india.org

DECLARATION

I hereby declare that the thesis entitled "**Surface Modified ZnO Nanostructures: Synthesis, Optical Studies and Applications in Photocatalysis**" submitted for the award of the Degree of Doctor of Philosophy in Chemistry to the Academy of Scientific & Innovative Research (AcSIR), New Delhi, has been carried out by me at Catalysis & Inorganic Chemistry Division, CSIR-National Chemical Laboratory, Pune-411008, India, under the guidance of **Dr. R. Nandini Devi**. Research material obtained from other sources has been duly cited and acknowledged in the thesis. The work is original and has not been submitted as a part or full by me for any degree or diploma to this or any other university.

Leena George

Enrollment Number: 10CC12A26033

Date: 13th April 2017

Place: CSIR-NCL, Pune

Acknowledgement

With the help of God Almighty, I am going to achieve the highest degree in my life "Doctor of Philosophy". His helping hands reached me in the form of my teachers, my friends, my colleagues and other forms to fulfill my dream. At this moment, I would like to thank each and everyone who directly or indirectly helped me to achieve this goal.

First and foremost, I would like to express my sincere gratitude to my research supervisor Dr. R. Nandini Devi for her endless support during my Ph.D study and research, for her patience, inspiration, care, encouragement and immense knowledge. Her guidance helped me in all ways of up and down time of my research and writing of this thesis. She was always there for me in throughout my Ph.D life from putting my first synthesis to the entire tough journey of my research. She has given me full freedom in my research and I could not imagine have a better mentor than her….. She is the person who showed me the way of writing a manuscript, reports, research proposal, etc. By assigning research interns under my supervision, she taught me how to guide a student. I learned enormously from her and she made me confident enough to stand on my own foot as an independent researcher in the next phase of my career. Working with her was really a great pleasure and fetched me a lot of learning experience.

Special thanks go to Dr. G.J. Sanjayan (NCL) with whom I started my research career. He is the person who showed me the world of synthetic organic chemistry.

I am thankful to Dr. Chithra Manikandan (Shell Technology Centre, Bangalore) who helped me to improve my research work. I learned a lot of photochemistry lessons from her. Special thanks to Dr.Divya Ottoor (Department of Chemistry, Savitribai Phule Pune University) for her fruitful discussions and suggestions. My heartfelt thanks to Dr. C. S. Gopinath for valuable discussions and advises. I am thankful to Dr. P. K. Sudhadevi Antharjanam (IIT Chennai) for life time measurements. I am also thankful to my Doctoral Advisory Committee (DAC) members Dr. Paresh L. Dephe, Dr. C. S. Gopinath and Dr. S. Mayadevi (valuable advice and care) for continuously monitoring the progress of the research work and for scientific discussions. I sincerely acknowledge the help provided by Dr. Sreenivas Darbha, Dr. C. V. V. Satyanarayana, Dr. P. A. Joy, Dr. Rahul Banerjee, Dr. C.P. Vinod and Dr. T. Raja at various stages of my PhD work. I sincerely acknowledge the help provided by Dr. P. R. Rajamohanan and Dr. T. G. Ajith Kumar (NMR measurements), Dr. K. Sreekumar (Electrochemical measurements), Dr. S. K. Asha (Lifetime measurements) and Dr. Suresh Bhat (DLS measurements). I am also thankful to Dr. A.T. Biju and Dr. Santhosh Babu Sukumaran for their care and support.

I express my deep sense of gratitude to Dr. Kala Raj, who has always been very affectionately concerned, creatively helpful and support at every stage in the progress of my work.

I am forever indebted to all my former teachers (from St. Kuriakose Public School, Devamatha College (B.Sc) and Cochin University of Science and Technology (M.Sc and M.Tech)) as they built the foundation for this achievement.

I would like to thank the former student academic office Chairman Dr. P. A. Joy, Dr. C. G. Suresh and the current Chairman Dr. Sasidhar, AcSIR Coordinator Dr. Chetan Gadgil and other staff in SAO for their timely help in processing the documents related to my coursework and PhD. Special thanks to Kolhe madam for her support.

I am grateful to Ms. Violet Samuel and Ms. Rupali Waichal for their help. I am also thankful to Dr. Naren, Anuj, Pandiraj, Sahithi, Sravini, Pankaj, Harshvardha for HRTEM and Ketan for SEM. I acknowledge Mr. Madhavan Nair, Mr. Chowdhary, Mr. John, Mr. P. K. Mane, Mr. S. S. Deo, Mr. Purushotthaman (Catalysis Division Officer) and all others (glass blowing, civil, mechanical and electrical sections) for technical support during my PhD. Timely help from Shiny chechi and Madhu chettan is gratefully acknowledged.

Special thanks to Dr. Prasenjit Ghosh and his student Subrahmanyam Sappati from IISER Pune, for useful discussions, valuable advises and fruitful collaboration work for computational studies.

My deepest and heartiest thanks go to all my seniors Dr. Kala Raj, Atul, Anupam, Rajesh & Soumya. I am overwhelmed by the friendly atmosphere and support provided by my labmates Jijil, Sumona, Shibin, Anurag, Pavan, Sourik, Priyanka, Shunottara, Emmanuel, Chinnu, Jishna, Anjumol, Amruta, Neethu, Monojit, Satej, Pranav Ghore, Santosh. I am also thankful to the project trainee students Mohit, Sabna, Vineetha, Fessy, Akhil, Ajay, Shivesh, Saranya, Sandhya, Anantha, Rajith, Ali, Remith, Srujan, Dhaval and Surya for creating a happily environment in the lab.

I also acknowledge the homely environment provided by Hilda, Leena chechi, Remya, Bindhu, Nishamol, Nisha, Jayachechi, Roshna,Thushara,Teena, Suyana, Varsha, Jayaprabha, Govind, Suresh chettan, Jishnu, Athira, Anjali, Ruby, Vinisha, Priya, Reji, Rahul, Renny, Hari, Sadiq, Mufsir, Anu, Vijayadas, Beena chechi, Reema, Anshu, Pushpanjali, Soumya, Sreeja chechi, Aany, Yamuna, Jima, Manoj chettan, Hari chettan, Shijo chettan, Venu chettan, Eldho chettan, Alson chettan, Jijo chettan, Gireesh, Renjith, Shoy, Joby, Unni, Jithesh, Bipinlal, Sabareesh, Vishal, Jino, Sanil, Sudheesh, Sanjush, Meera, Maya, Sanjini, Christy, Meghna, Panchami chechi, Gowri chechi, Arup bhayya, Sangeeta chechi, Vineetha, Anjali K, Dhanya, Divya, Neeta, Anumon chettan, Bihag, Biyas, Vishal M, Siddheshwar, Geethu, Vijayannan, Khajaannan, Rekha chechi, Mohanraj, Sijinettan during my stay in NCL.

I am thankful to my colleagues and friends Karthika, Kavya, Nishina, Megha, Shareef, Nadir, Aneesh, Vyshakh, Sunil, Kiran, Sreedevi, Sreedhala, Anju, Mohan, Lenin, Ashok, Aswathi, Manu, Rupa, Periyasami, Manikandan, Prabu K., Prabu M., Srikanth, Richa Bobade, Laxmi, Pranjal, Dheeran, Siva, Vipul, Seema, Kalpana, Nishitha, Narshimha Kanan, Jay, Amlan, Mangesh, Anup, Tanusree, Richa, Neha, Maneesha, Sagar, Sandeep, Nilesh, Prasenjit, Ramakanta Sahu, Betsy, Prithi, Trupthi, Swathi, Vidya, Atul, Prakash Chandra, Devaraj, Pradnya, Swapnil, Chinmay, Nagesh, Shekhar, Momitha, Meena, Subrajyotsna, Sneha, Raji chechi, Richa Edwin, Mangesh, Anantharamaiah, Ram Sunder, Suman Devi, Senthil, Rajambal for their indispensable help and for allowing me to spend wonderful time with them.

I would like to express my sincere thanks to my junior brothers Pranav, Shibin, Sanoop, Tony, Rejith, Vidyanand, Renjeesh, Shebib, Sandeep, Abdul Kayum, Munnavir, Fayis, Vipin, Sarath, Sarath K, for their lovely care and support.

Special thanks to my lovely younger sisters Chinnu and Fessy for their constant support and encouragement. I would like to express my appreciation to my junior friends Bijoy, Bavitha, Vidya, Cyggu, Gayu, Achu, Anusha, Keerthi, Shyma, Anu, Ahalya, Sneha, Geethu, Pathu, Krishnaveni, Thulasi, Athulya, Dona, Tincy, Ananjana, Cris, Sajna, Navya, Shanti, Ashwin, Abi, Arun, Aswathy, Sada, Aswath, Haritha, Madhuja, Amarjith, Ajith,Hasna, Shivaganga, Deepti, Deepa, Remya, Anila, Aswathy, Aswathy C. P., Shilpa, Nikki, Reshma, Mona, Jenny, Kabeer, Robin, Thomas, Manu, Sabareesh, Jeevan, Yadu, Archana, Anu, Anju, Drishya, Ammu, Meera, Nasrin, Reeshma, Rahul, Nikil, Nithin, Junior Joy, Rejath, Fahad, Anju, Chaithanya, Cami, Irin, Reeshma, Roshni, Jaladhara, Lakshmi, Ralph, Abhishek, Arya, Rekha, Shebin, Ramesh,Sumi, Anu, Ashraf, Freddy, Manila, Jeena for spending wonderful time with them.

My special thanks to my roommates-cum-friends Lulu, Priyanka, Neha, Shweta, Smitha, Harshali, Prachi, Raji, Ayeesha, Prachna for creating a cheerful environment.

It is needless to use the word thanks to my sisters Praji, Deepa and Minu for their care, love and support during my stay in NCL. They were with me at every up and down in my life in NCL. I am very thankful to NCL for giving me such best companions. My heartfelt thanks to Manjunath bro for his care and support.

I would like to thank Sreekuttan and Arun chettan for their care, love, support, criticism and fruitful scientific discussions during my stay in NCL. I thank God for providing me such wonderful personalities as my close friends and brothers. Their scientific suggestions and criticisms always polished my knowledge, writing skill, character, presentation skill and personality.

In this occasion I would like thank my friends Anu, Raji, Anju P, Divya, Smitha, Anumol, Minu, Rosemary, Soniya, Preethi, Ligil, Anisha, Sr. Betty, Anisha, Indhu, Kavitha, Teena, Simi, Joshni, Saritha, Sona, Manju for their constant support and help.

Special thanks to my grandpa and grandma for their love, support, prayer and blessings throughout my life.

I would like to express my deep sense of gratitude to my Parents and my Sister (kunjumol) for their enthusiastic encouragement, advice, moral support and selfless love. Without their support, I will not grow into this position. I don't know, what I should write for them. But I know their life is for me. I find no words to express the love of my Pappa and Amma who have always given me the best of everything. The love, support and blessings provided by them have always been my strength. I am very thankful to my sister kunjumol for her valuable suggestions throughout my education and growth. My sister encouraged me at each stage of my education.I am deeply indebted to all my family members for their constant support and help to finish this work.

More importantly, I would like to thank (I know it is nothing, if I mention the word 'thank') my Appayi (father-in-law) and Mummy (mother-in law) for their care, love, support and prayer to finish this work. I thank God for providing me such wonderful parents as my in-laws. Special thanks to Manish (brother-in-law), Anie (sister) and Jhonson (brother) for their constant support, prayer and encouragement. I also thank Mummy and Anie for their delicious food. Even though I didn't stay enough time with my 'Angelitta Vava' (Manish's daughter), her love and affection are memorable. Special thanks to all family members of Appayi and Mummy for their love, care and support.

Words are not enough to express my gratitude to a very special person, my husband, 'Mathews', for his support, endless care, unconditional love, affection and understanding throughout. I thank God for providing me such a wonderful person as my close friend and husband. I am very much thankful to him for his constant support and suggestions to complete my thesis work. He encouraged me a lot at the final stage of my research work. His scientific suggestions and criticisms always refined my knowledge, character and personality. Mathews (my better half), you made my life more cherish and memorable. It gives me great pleasure to thank his grandfather (Kunjachan) and grandmother (ammachi) for their constant support, prayer and encouragement.

Finally, my thanks are due to CSIR, Government of India, for awarding the research fellowship, and to Dr. S. Sivaram, Dr. Sourav Pal, Dr. Vijayamohanan K. Pillai (former Directors) and Dr. Ashwini Kumar Nangia, Director, CSIR-National Chemical Laboratory for allowing me to carry out my research work by providing all possible infrastructural facilities, and for permitting me to submit this work in the form of a thesis for the award of Ph.D. degree.

Though, many have not been mentioned, none is forgotten.

Leena George

Table of Contents

Abstract

Energy and environmental issues like pollution, greenhouse effect at a universal level are central problems in the current scenario. Researchers have been trying to mimic natural photosynthesis, hoping to find a greener fuel generation by clean renewable energy for the future alternative for non-renewable and polluting fossil fuels. Hydrogen generation by photocatalytic water splitting with solar radiation is a renewable process, which can be carried out under ambient conditions for clean energy production. Several semiconductor oxides, sulfides, and selenides have been explored which has led to various exciting and attractive developments in solar hydrogen producing system However, attention is focused on oxide systems due to the availability, ease of synthesis, and limited photocorrosion. In general, photocatalytic reactions on semiconductors proceed through absorption of photons, charge separation of the electrons and holes into conduction and valence bands, respectively, and their migration to the catalyst surface. These charge pairs can be effectively used in a variety of electron transfer or redox reactions provided that they do not recombine (excited e- with the hole in the valence band or with the defect centers), where the recombination sites vary from grain boundaries and bulk crystal defects to surface sites. Most of the semiconductors absorb light in the UV region, thus wasting the abundance of visible light irradiance in sunlight falling on earth's surface. Hence the two most important problems to be addressed here is to identify visible light absorbing semiconductors and minimisation of recombination by appropriate strategies. Among the various semiconductor oxides, zinc oxide nanostructures have been attracting increasing interest due to their favourable aspects which include its broad chemistry: particle size over the largest possible range, narrow size distribution, good crystallinity, high luminescence and desired surface properties. Consequently, even though there is considerable interest in studying ZnO in the form of nanostructures, pure ZnO nanoparticles cannot be utilized effectively for solar excitation or conversion because their poor visible light absorption and fast electron–hole recombination limit potential applications. Hence, surface modifications of nanostructured ZnO with appropriate organic

linker molecules are required to address this problem in a bipronged approach: (i) organic moiety helps in visible light absorption by creating appropriate donor bands to ZnO and (ii) modifications to surface sites can be achieved advantageously in tandem with reducing the recombination sites. The ligands of choice are perylenes, thiophenes and azo based aromatic conjugated systems formed by coupling amino benzoic acids with β-naphthol and 8-hydroxy quinoline.

The thesis will be presented in six chapters, a brief summary of which is given below.

Chapter 1 presents a general introduction to environmental issues, hydrogen as greener fuel for the future, photocatalytic water splitting reaction and a detailed literature survey of metal oxides used as photocatalysts. This chapter further discusses the principle and processes behind the photocatalytic water splitting and the basic requirement of a material to act as a visible based photocatalyst for water splitting. Detailed literature survey of the strategies involved in the utilization of visible light in photocatalytic water splitting systems. The role of sensitizers in DSSC and the importance of ZnO are discussed. Finally the scope and objective of the thesis are stated.

Chapter 2 describes synthesis, characterization and photocatalytic water splitting activity of ZnO-azonaphthol composites**.** ZnO nanoparticles (ZnONPs) are grafted with two azonaphthols, one conjugated and the other non-conjugated. Photophysical properties of modified ZnO indicate an effective electron transfer from the conjugated azonaphthol to ZnO but not in case of nonconjugated molecule. It is also observed from lifetime studies that conjugated molecule stabilises the defect sites on ZnONPs. It is possible that excited electrons from the conjugated molecule are transferred to specific defect sites in ZnO. This apparently does not occur in non-conjugated molecule bringing to focus the importance of photophysical characteristics of organic modifiers in designing visible light active photocatalysts. Enhanced H_2 evolution from water−methanol mixtures was observed in the composite systems compared to pristine ZnO under visible light irradiation without any

cocatalyst. The experimental observations are corroborated with computational studies, which also point to a localization of valence band maximum of the interface on the organic moiety and conduction band minimum on ZnO.

Chapter 3 describes synthesis, characterization and photocatalytic water splitting activity of ZnO-azoquinoline composites**.** Further, the multimodal anchoring of azoquinoline on ZnO nanoparticles (ZnONPs) for enhanced electron transfer, stability and H_2 evolution were investigated. Among various azo-aromatic molecules, azo-8-hydroxy quinoline (8-HQ) is well known as a ligand forming chelating complexes. (E)-3-((8-hydroxyquinolin-5-yl)diazenyl) benzoic acid (3ABBN8HQ) and (E)-4-((8-hydroxyquinolin-5-yl)diazenyl) benzoic acid (4ABBN8HQ) were designed so that carboxylic group as well as quinoline group would be potentially interacting with ZnO surface on grafting. A comprehensive photophysical characterization and correlation to H_2 evolution activity through computational studies is attempted in both the cases and reveals that the alignment of dye orbitals to the band positions of the semiconductor is appropriate resulting in facile electron transfer and enhanced activity.

Chapter 4 presents synthesis, characterization and photocatalytic water splitting activity of ZnO-perylene composites**.** Our next aim was to examine the impact of electronic coupling and charge transfer process in perylene dyes which are bound to the ZnO surface. Surface site modulation by the π system of the perylene chromophore to the ZnO nanoparticles extend in a conjugative manner, which is understood based on absorption and fluorescence spectroscopy. The photostability and photophysical properties of the perylene composites with ZnO is understood based on the electron and charge transfer mechanisms using time resolved photoluminescence and corroborated by electrochemical studies. Enhanced H_2 evolution from water−methanol mixtures was observed in the composite systems for longer durations even after visible light irradiation.

Chapter 5 presents synthesis, characterization and photocatalytic water splitting activity of ZnO-terthiophene composites. ZnO-terthiophene composites have been

prepared and characterized. The photophysical properties of the composites by absorption and fluorescence spectroscopy indicate an effective electron transfer between thiophene linkers and ZnO nanoparticles. Electrochemical studies are performed to see the effect of electron transfer in ZnO-terthiophene composites. Photocatalytic water splitting activities of ZnO-terthiophene composites were studied and found to be visible light active and stable. This is further proved by computational studies.

Chapter 6 summarizes the results and conclusions based on the work reported in the thesis. This thesis reports the detailed structural and photophysical characterizations of ZnO-azonaphthol composites, ZnO-azoquinoline composites, ZnO-perylene composites and ZnO-terthiophene composites. In addition, it also discusses the electrochemical measurements, computational studies and photocatalytic hydrogen evolution capability of ZnO-azonaphthol, ZnO-azoquinoline, ZnO-perylene and ZnO-terthiophene composites.

List of Figures

List of Schemes and Tables

List of Abbreviations

ATR	Attenuated total reflectance
$CDCl_3$	Deuterated chloroform
CV	Cyclic Voltammetry
DMSO-d6	Deuterated dimethyl sulfoxide
DFT	Density functional theory
DLS	Dynamic light scattering
DSSC	Dye sensitized solar cells
EJ	ExaJoule
EIS	Electrochemical Impedance Spectroscopy
FT	Fourier Transform
GC	Gas Chromatography
g	Gram
HER	Hydrogen Evolution Rate
IR	Infra-red
JCPDS	Joint Committee on Powder Diffraction Standards
LSV	Linear Sweep Voltammetry
LED	Light emitting diode
mmol	Millimole
NMR	Nuclear Magnetic Resonance
OER	Oxygen Evolution Reaction
OD	Optical density
PL	Photoluminescence
TEM	Transmission Electron Microscopy
UV-vis	Ultraviolet-visible
XRD	Powder X-ray Diffraction
ZnO NPs	Zinc oxide nanoparticles
XRD	Powder X-ray Diffraction
3ABBN	3-((2-hydroxynaphthalen-1-yl)diazenyl) benzoic acid
4ABBN	4-((2-hydroxynaphthalen-1-yl)diazenyl) benzoic acid

3ABBNHQ	((E)-3 -((8-hydroxyquinolin-5-yl)diazenyl) benzoic acid)
4ABBNHQ	((E)-4 -((8-hydroxyquinolin-5-yl)diazenyl) benzoic acid)
PTCDACOOH2	(N,N'-Bis(p-carboxyl-phenylene)perylene-3,4:9,10perylenebisimide)
TTT	2,2':5',2"-Terthiophene
TTTCOOH	5-carboxy-2,2'5', 2"- terthiophene
BrTTTCOOH	5-Bromo--(-2,2':5',2"-terthiophene) -5-carboxylic acid

Chapter 1

Introduction and Literature Survey

1.1. Introduction

Technological advances and the growing world economy have led to major improvements in the living conditions of the people, which in turn cause excessive use of fossil fuels. These are also considered to be the backbone of industries and the most exploited sources of energy, due to which they are fast depleting. The environmental problem associated with the excessive use of fossil fuel is even worse, which results in serious air pollution due to the emission of CO_2 along with oxides of nitrogen and sulfur. These gases are mainly responsible for the environmental issues like greenhouse effect and global warming due to their heat trapping properties, intensifying the earth's natural greenhouse effect and causing average global temperatures to rise at an increasing rate. Other dangerous consequences like acid rain also originate from such polluting gases. In addition, incomplete combustion of fossil fuel results in the emission of CO, which is more poisonous than CO_2 as it can irreversibly combine with blood haemoglobin reducing the affinity towards O_2 and leading to dangerous effects on the human body. Due to all these adverse environmental effects, fossil fuels are of great concern globally [1-8].

In this disturbing situation of fastly depleting oil and an increasing dependence on international markets for energy supplies, it is time to focus on limitless resources and energy forms which are renewable and sustainable that withstands exploitation and at the same time is virtually without hazardous emissions as a result of their operation. At this point, the role of alternate sources of energy comes into play which can be harnessed in the form of sun, wind, water and biomass. Governments have already taken steps towards addressing these issues through policymaking. Moreover, nearly 174 countries are signatory to COP21 (a global agreement on the reduction of climate change) promising to reduce global warming and green house gas emissions [9].

Of the renewable sources, solar energy seems especially attractive due to various reasons. Sun is the primary source of energy and this energy is virtually inexhaustible and freely available. Solar energy is also the largest renewable carbon-free resource amongst all other renewable energy options. The amount of sunlight (~1.2× 105 TW) which falls on the earth's surface in 1 h is more than that used by all human activities in 1 year globally.

About 174,000 terawatts (TW) of incoming solar radiation on the earth's surface is received by the upper atmosphere. Of the total incoming energy, roughly 70 % of the sun's radiation is only penetrating and reaching the earth. Approximately 30% is reflected back to space and the rest of the radiation is absorbed by clouds, oceans and land masses, that is, ~ 3,850,000 EJ (EJ-exajoule, 10^{18} J) per year. The energy use of mankind on earth is only ~ 500 EJ per year which is about 0.01 % of the sun's total yearly energy coming to the earth. The spectrum of the solar light at the Earth's surface is mostly spread across the visible range (46 %) and the rest near-infrared ranges experienced as heat with a small part in the near-ultraviolet (5 %). Hence, a proper exploitation of the solar spectral distribution specially the visible light spectrum of the solar irradiance will be the ultimate aim of sustainable energy solutions [10].

In general, solar energy can be harvested in different ways, but the energy content of the solar radiation can be captured as excited electron-hole pairs in a semiconductor, a dye, or a chromophore, or as heat in a thermal storage medium. These excited electrons and holes can be used for immediate conversion to electrical power, or converted to biological or chemical molecules for conversion to fuel.

The life sustainability on earth has been developed by nature through a very efficient process utilizing solar energy called photosynthesis. This occurs in two stages of reactions. In the first stage, light-dependent reactions or light reactions capture the energy of light and use it to make the energy-storage molecules ATP and NADPH. During the second stage of photosynthesis, the light-independent reactions use these products to capture and reduce carbon dioxide. Carbon dioxide is converted into sugars in a process called carbon fixation. Carbon fixation is a redox reaction, so photosynthesis needs to supply both a source of energy to drive this redox process, and also the electrons needed to convert carbon dioxide into carbohydrate, which is a reduction reaction. In the overall reaction of photosynthesis, oxygen and carbohydrates are formed when plants transform water and carbon dioxide in the presence of light. Effectively, H_2O is split into O_2 and H_2, here the hydrogen is bound by carbon and not in the gaseous form. In effect, the solar energy fixation in plants is achieved via the photosynthetic growth process. The primary fuels obtained by the combustion of biomass and the conversion to secondary fuels like ethanol

and hydrogen are possible from these plants. However, from natural photosynthesis, the idea of artificial photosynthetic systems has evolved which is very promising for the future carbon-free power fuels. In such a process, C fixation does not occur, instead, water splitting directly yields hydrogen and oxygen. Hydrogen is projected as the best alternative energy fuel of the future that would be a great substitution to the fossil fuels; emission free and environmentally friendly.

Hydrogen has been used for energy since the 1800s and is considered as a green fuel for two reasons: it can be produced from renewable sources and is emission less; H_2 when reacted with O_2 produces water as the product with enormous amount of energy. At normal atmospheric conditions, hydrogen is a colourless and odourless gas. It is stable and coexists harmlessly with oxygen until an input of energy drives the exothermic reaction that forms water. Most of the H_2 produced currently comes from the steam reforming of methane and other fossil fuel sources. Syngas which is generated from the gasification of coal, wood, or municipal wastes consists of ~50% by volume of hydrogen. The ultimate goal would be to produce H_2 with little or no greenhouse gas emissions and the process which may become economically feasible is the electrolysis of water using power generated by renewable energy sources such as wind turbines and solar energy [11]. However, the holygrail of solar energy harvesting is harnessing abundant visible light radiation of sunlight *directly* for the production of greener fuel hydrogen. There are two possible ways of utilizing visible light of solar energy for H_2 production:

(i)Photoelectrolysis

(ii)Photocatalytic water splitting.

Photoelectrolysis of water occurs in a photoelectrochemical cell (PEC) and the source of energy is light for the electrolysis of water thereby producing hydrogen as a fuel. In other words, photoelectrochemical cells or PECs are another type of solar cells that produce electrical energy or hydrogen in a process similar to the electrolysis of water. When a semiconducting material (working electrode) and metal electrode (counter electrode) are immersed in H_2O, upon light irradiation, excitation of the semiconducting material can lead to redox processes in the interfacial region around each particle, thereby

creating a potential gradient at the interface of a semiconducting material and a liquid phase. In other words, photoexcited electrons reduce H_2O to give H_2 and the electron vacancies oxidize H_2O to form O_2 [12]. But the disadvantage in electrochemical cells is that the separation of the products formed during the reaction is a bottle neck and there are chances of reverse reaction also (Figure 1.1).

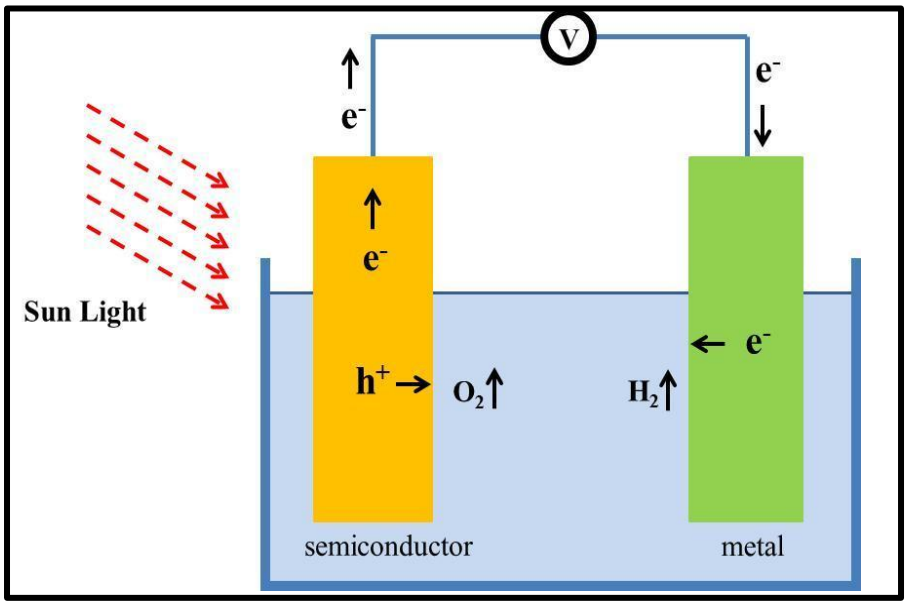

Figure 1.1. Illustration of photo electrolysis (Adapted from reference 13).

Photocatalytic water splitting is an artificial photosynthesis process with powdered or thin-film based semiconductor which acts as photocatalyst for the dissociation of water into its constituent elements, hydrogen and oxygen using either artificial or natural light. Theoretically, only solar energy (photons), water and a catalyst are needed. Powdered catalysts have the potential to be produced at much lower costs through easily scalable processes. It can be thought of as a short-circuited version of the PEC; the reactions are spatially separated on the powdered catalyst, but on a much finer length scale than for the PEC. Handling of the powder photocatalyst system is simple and economical, making it advantageous over photoelectrochemical cells [14-20].

Photocatalytic reactions are divided into two types, one which is considered as a ‘‘down-hill’’ (negative Gibbs free energy) and the other as ‘‘up-hill’’ (positive Gibbs free energy) reactions (Figure 1.2). Down-hill reactions are generally photodegradation

reactions such as photo-oxidation of organic compounds using oxygen molecules and the reaction proceeds through an irreversible mechanism. TiO_2 photocatalyst has been extensively studied in these reactions. Here, the photocatalyst initially works as a trigger to produce O_2^-, HO_2 (perhydroxyl radical), OH^-, and H^+ as active species for oxidation and can also be called as a photoinduced reaction. On the other hand, photocatalytic water splitting into H_2 and O_2, which is an up-hill reaction, is followed by a large positive Gibbs free energy change (ΔG^0 = 273 KJ/mol). Hence attaining overall photocatalytic water splitting is very tough [21-27]. Here the process is similar to natural photosynthesis where solar (photon) energy is converted into chemical energy through certain chemical reactions, so the term "artificial photosynthesis".

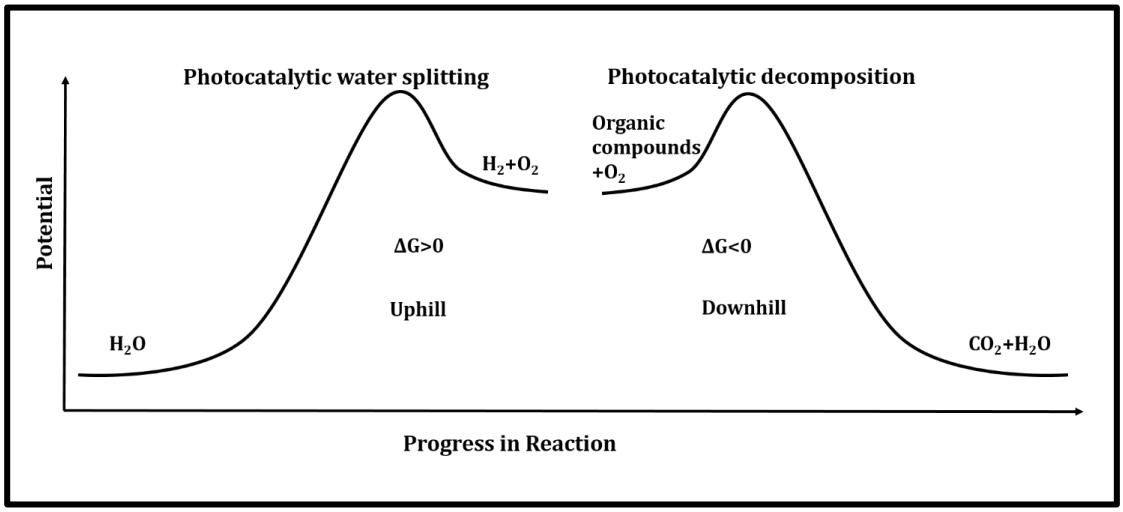

Figure 1.2. Energy profiles of photocatalytic water splitting and photocatalytic decomposition reactions (Adapted from reference 21).

Photocatalytic reaction systems for overall water splitting can be divided into two primary approaches. One approach is to split water into H_2 and O_2 using a single visible-light-responsive photocatalyst with a sufficient potential to achieve overall water splitting (Figure 1.3). In this system, the photocatalyst should have a suitable thermodynamic potential for water splitting, a sufficiently narrow band gap to harvest visible photons, and stability against photocorrosion. Because of these stringent requirements, the number of

reliable and reproducible visible light based photocatalysts suitable for one-step water splitting is limited. The other approach is to apply a two-step excitation mechanism using two different photocatalysts. The combined system involving two photoexcitation processes is called 'Z-scheme system' because of the similarity to the natural photosynthesis scheme in green plants. In photosynthesis, the photosystems I and II harvest 700 and 680 nm photons, oxidizing H_2O into O_2 under sunlight. Similarly, in the Z-scheme system, two different photocatalysts are combined using an appropriate shuttle redox mediator (Figures 1.4). Visible light can be utilized more efficiently than in the conventional one-step photoexcitation water splitting systems because the energy required to drive each photocatalyst is reduced [28]. It is also possible to apply a photocatalyst that has either water reduction or water oxidation potential to one side of the system.

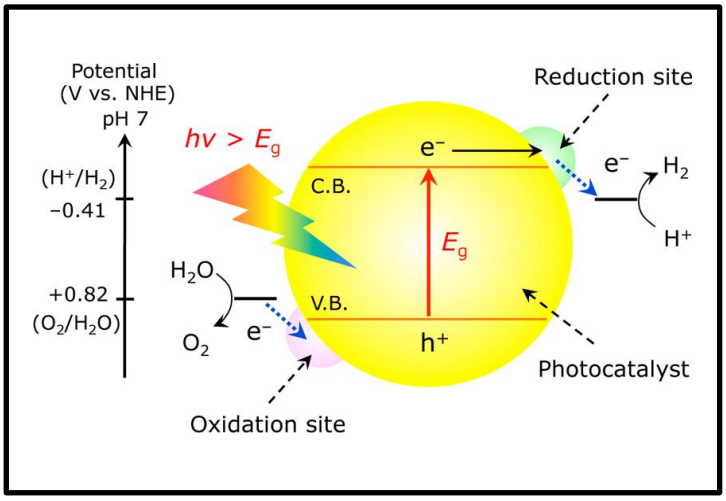

Figure 1.3. One-step photoexcitation process in photocatalytic water splitting (Adapted from reference 28).

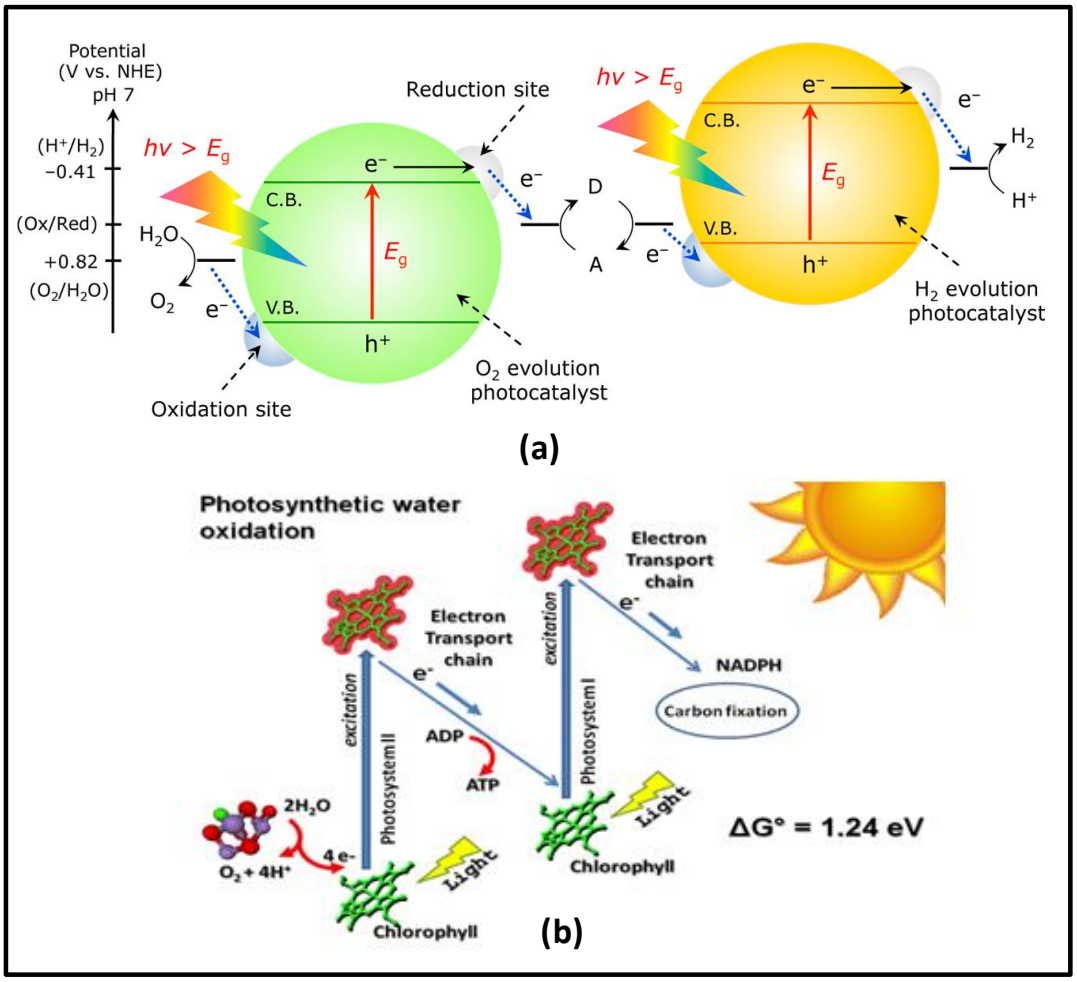

Figure 1.4. (a)Two-step photoexcitation process in Z-scheme photocatalytic water splitting (Adapted from reference 28) and (b) Schematic representation of photosynthesis by green plants (Adapted from reference 29).

1.2. Mechanism and Processes in Photocatalytic water splitting

$$2H_2O \rightleftharpoons H_2 + 2O_2$$

Photon energy › 1.23 ev

Photocatalytic water splitting involves three major steps and the general mechanism of photocatalytic water splitting using powder semiconductor photocatalysts is schematically represented in Figure 1.5.

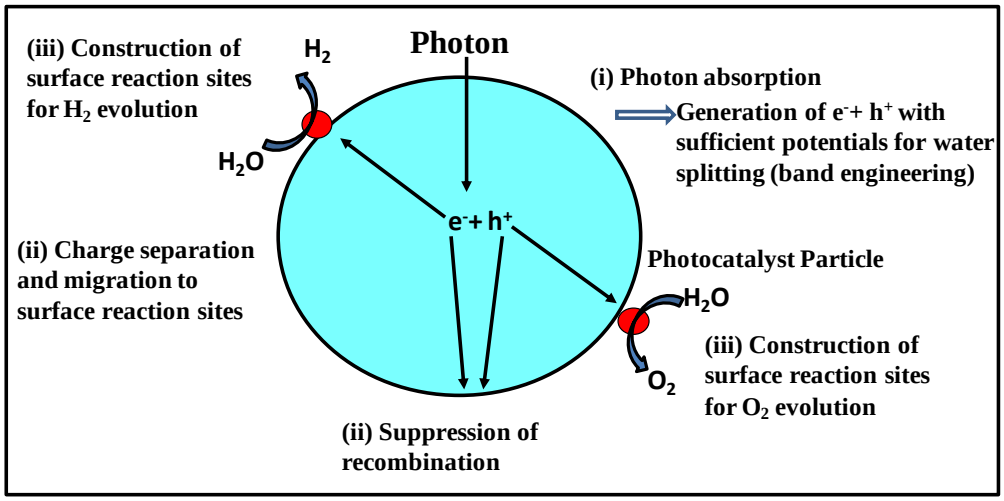

Figure 1.5. Main processes involved in photocatalytic water splitting.

The first step of the photocatalytic reaction is the absorption of photons to form electron-hole pairs called excitons and the process can be termed as band-gap excitation. The main criterion for the semiconductor material used for this reaction is that it should have appropriate energy levels such that the band gap energies are in the range of photon energies of the solar spectrum. The semiconductor electrons can have energies only within certain bands, i.e., between the energy of the ground state (electrons tightly bound to the atomic nuclei of the material) and the free electron energy (the energy required for an electron to escape entirely from the semiconducting material). The ground state energy bands can be called as valence band which correspond to a large number of discrete quantum states of the electrons in which most of the states with low energy (closer to the nucleus) are full. These electrons on excitation are available in the conduction band (the band immediately above the valence band). When the radiation strikes a semiconductor photocatalyst, it may excite an electron from the valence band to the conduction band and leave behind a hole, thereby generating an electron–hole pair. This in turn promotes charge-separation by the utilization of the free energy gradient.

$$\text{Photocatalyst} \longrightarrow e_{CB}^- + h_{VB}^+ \quad (1.1)$$

Photocatalysts used in H_2O splitting have strict band requirements to carry out the reaction. The basic mechanisms of photocatalytic hydrogen production and oxygen

production are the reduction and oxidation reactions (0 V vs NHE). The photoreduction reaction of H_2O to form H_2 occurs at 0 V vs NHE, i.e., the bottom level of the conduction band has to be more negative than the redox potential of H^+/H_2 (conduction band must be at a potential less than 0 V). Secondly, the hole left behind in the valence band will pass to water, which will get oxidized and produce O_2 and for that the top level of the valence band (VBM) has to be more positive than the redox potential of O_2/H_2O (1.23 V),ie., the valence band must be at a potential greater than 1.23 V. In overall water splitting, the reduction reaction to form H_2 occurs at 0 V and pH 0 and the oxidation reaction to form O_2 occurs at 1.23 V. Therefore, the minimum photon energy required thermodynamically to drive the photocatalytic water splitting reaction is 1.23 eV (Figure 1.6) [30,31].

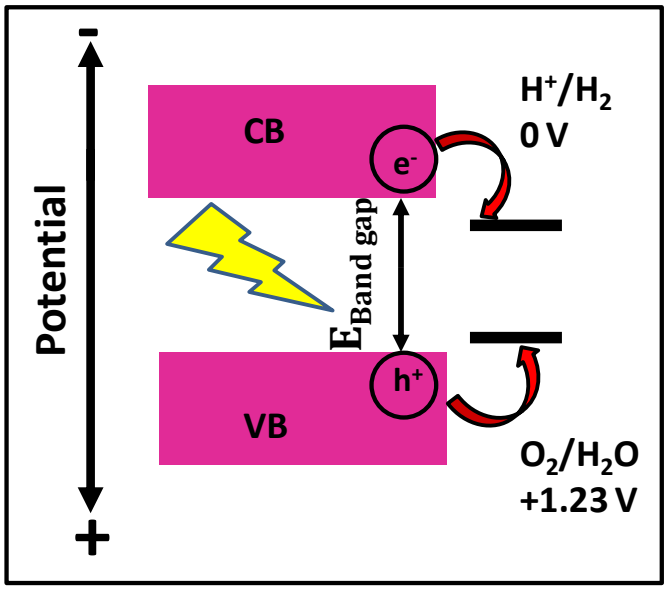

Figure 1.6. Principle of photocatalytic water splitting using semiconductor photocatalysts.

In natural photosynthesis, the water splitting process is based on the four-hole requirement (one molecule of oxygen from two water molecules requires four holes and therefore four photons). Thermodynamically, oxidation of water to produce O_2 is more feasible but kinetically oxygen evolution reaction (OER) is competitive. Photocatalytic OER is sluggish and requires large over potentials. Oxygen evolution reaction from water is a four-electron reaction but the photon capture is a single electron process. Photochemically,

this slow kinetics leads to the recombination of photogenerated charge carriers, which is one of the major bottlenecks for photocatalytic water splitting. There is an electrostatic coulombic interaction between the photogenerated e^--h^+ charge carriers, since the electron is negatively charged and the hole is arbitrarily positively charged. As a result, even though semiconductors possess suitable band structure for photocatalytic water splitting, many of them like TiO_2, ZnO and CdS undergo a phenomenon called photocorrosion [32-34]. For example, ZnO upon band gap excitation undergoes photocorrosion by photogenerated holes accompanied by the formation of Zn^{2+}. The reaction is as follows:

$$\mathbf{ZnO + 2h^+ \longrightarrow Zn^{2+} + \frac{1}{2} O_2} \qquad \mathbf{(1.2)}$$

Here comes the role of sacrificial reagents (electron donors or hole scavengers) which can improve the H_2 evolution. The photocatalytic reactions using sacrificial reagents are not "overall" water splitting reactions but are considered to be test reactions for overall water splitting. When the photocatalytic reaction is carried out in an aqueous solution along with a reducing reagent (methanol), photogenerated holes in the valence band irreversibly oxidize the reducing agent instead of H_2O, thus facilitating water reduction by conduction band electrons if the bottom of the conduction band of the photocatalyst is located at a more negative potential than the water reduction potential. It enriches photogenerated electrons in the conduction band of a photocatalyst by excitation, thereby enhancing H_2 evolution reaction. Organic compounds, such as alcohols (methanol, ethanol, isopropanol, etc.), acids (formic acid, acetic acid, etc.), and aldehydes (formaldehyde, acetaldehyde, etc.), have been used as electron donors for photocatalytic hydrogen generation reaction. S^{2-}, SO_3^{2-} and I^-/IO^{3-} can act as sacrificial inorganic reagents for the photocatalytic H_2 generation because they are also very efficient hole acceptors, enabling the effective separation of the charge carriers. On the other hand, photogenerated electrons in the conduction band are consumed by oxidizing reagents known as electron acceptors or electron scavengers such as Ag^+ and Fe^{3+} resulting in efficient O_2 evolution reaction [35-38].

The basic principle of photocatalytic reactions using sacrificial reagents is depicted schematically in Figure 1.7.

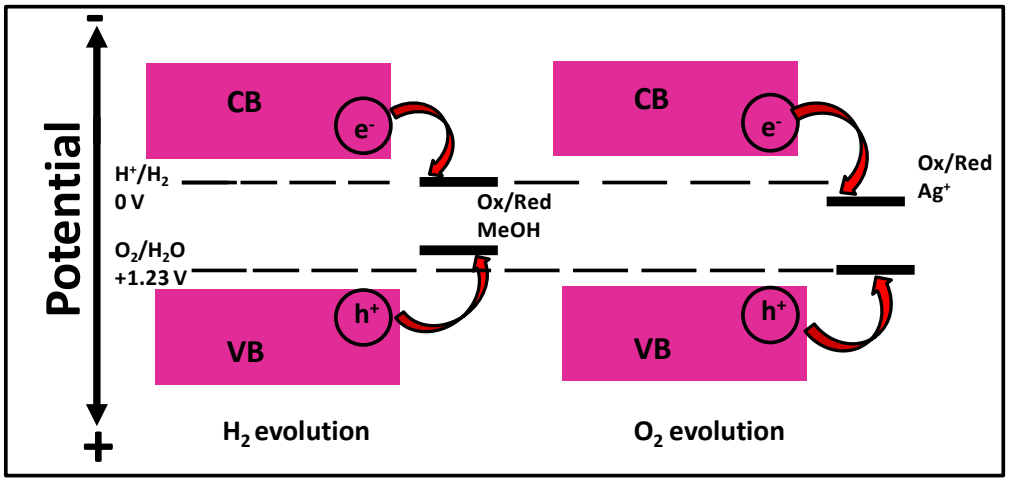

Figure 1.7. Basic principle of photocatalytic reactions in the presence of sacrificial reagents.

Among the above examples, methanol is frequently used as a sacrificial reagent for the hydrogen generation process. Valence band maximum of most of the semiconductor photocatalysts is situated more positive to the reduction potential and highly feasible for the generation of hydroxyl radicals. •OH radicals are products formed by the trapping of VB holes by surface −OH groups or adsorbed water molecules. Photo-oxidation of alcohols can also generate reductive hydroxyl radicals. During methanol oxidation, hydroxyl radicals, are known to react with methanol mainly through the abstraction of a hydrogen atom from the C−H bond for the formation of α-hydroxymethyl radical (E_0 ($^{\cdot}CH_2OH$/ CH_2O) = −0.95 v NHE). The radical formed in turn injects an additional electron into the conduction band of the photocatalyst. This phenomenon is called current doubling effect, thereby two photoelectrons are generated; one by single photon band gap excitation and another from electron injection by hydroxyl radical [39,40]. The suggested mechanistic routes for methanol as sacrificial reagent are as follows.

$$h^+ + H_2O \longrightarrow {}^{\cdot}OH + H^+ \qquad (1.3)$$

$$CH_3OH + {}^{\cdot}OH \longrightarrow {}^{\cdot}CH_2OH + H_2O \qquad (1.4)$$

$$\cdot CH_2OH \longrightarrow HCHO + H^+ + e^- \quad (1.5)$$

$$2H_2O + e^- \longrightarrow H_2 + 2OH^- \quad (1.6)$$

$$\text{Overall reaction} \quad CH_3OH \xrightarrow{\text{Photocatalyst/hv}} HCHO + H_2 \quad (1.7)$$

Further HCHO reacts with water in the presence of the photocatalyst and light to give two more moles of hydrogen.

$$HCHO + H_2O \xrightarrow{\text{Photocatalyst/hv}} HCOOH + H_2 \quad (1.8)$$

$$HCOOH \xrightarrow{\text{Photocatalyst/hv}} CO_2 + H_2 \quad (1.9)$$

The second step consists of charge separation of the photogenerated charge carriers in bulk and their migration to the surface of the semiconductor photocatalyst. The crystal structure and the crystallinity strongly affect these processes, i.e., higher the crystalline quality, smaller is the amount of defects. These defects can operate as trapping and recombination centres between photogenerated electrons and holes, thereby resulting in the decrease in photocatalytic activity [41]. Therefore, a high degree of crystallinity, rather than a high surface area, is required for photocatalysts. If the particle size becomes small, the mean free distance that photogenerated electrons and holes have to migrate to the reaction sites on the surface becomes short and this results in a decrease in the recombination probability [42].

The final step involves the surface chemical reactions and it depends on the surface character (active sites) and quantity (surface area). The photogenerated charge carriers (holes and electrons) which have migrated to the semiconductor photocatalyst surface through interfacial charge transfer can oxidize and reduce surface adsorbed molecules. Photocatalytic reduction and oxidation reactions are the basic mechanistic steps for the

photocatalytic water splitting [43]. The overall catalytic reactions involved in photocatalytic water splitting are:

Photocatalytic reduction : $2H^+ + 2e^- \rightarrow H_2$ **(2.0)**

Photocatalytic oxidation : $H_2O + 2h^+ \rightarrow ½O_2 + 2H^+$ **(2.1)**

Photocatalytic overall water splitting: $H_2O \rightarrow H_2 + ½O_2$ **(E = -1.23 eV)** **(2.3)**

Hence the vital requirement for photocatalytic water splitting reaction is the existence of active sites for oxidation and reduction reactions on the surface of the photocatalyst. The active sites should be readily available to prevent recombination centres, even if the photogenerated holes and electrons possess thermodynamically sufficient potentials for water splitting. This critical situation can be solved by loading the photocatalyst with co-catalysts of noble metals, such as Pt, Pd, Au and Ag and metal oxides such as NiO, CuO_2 and RuO_2, having a low over potential for hydrogen evolution . The role of co-catalysts is that they can create active sites on the surface of the photocatalysts, facilitating the oxidation and reduction reactions. The cocatalyst can also provide trapping sites for the photogenerated charges and promote the charge separation enhancing the quantum efficiency, improve the photostability of the catalysts by timely consumption of the photogenerated charges, particularly the holes and catalyze the reactions by lowering the activation energy. There are some requirements for cocatalyst, viz., smaller barrier for migration of electrons from the semiconductor photocatalyst to the cocatalyst, sufficient catalytic activity for water reduction/oxidation and finally, it should not catalyze the reverse reaction, where the hydrogen and oxygen produced react to form water (Figure 1.8) [44-46].

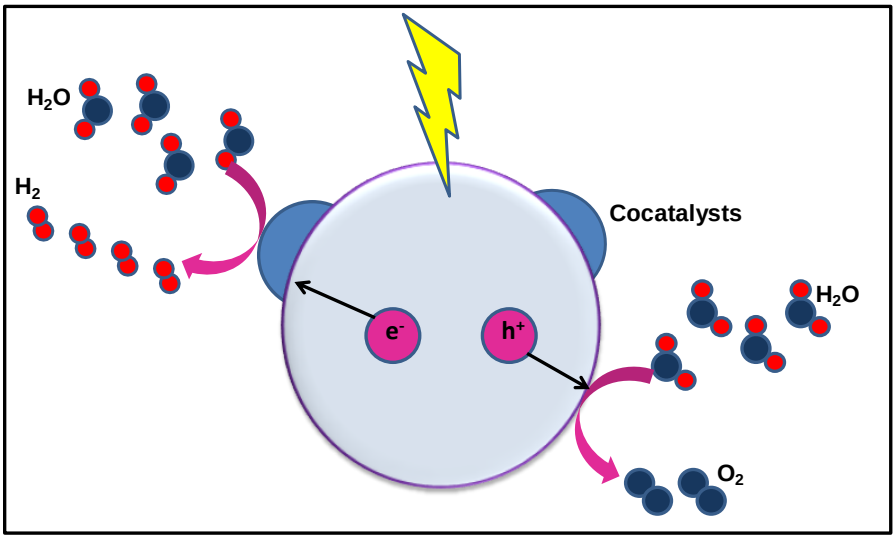

Figure 1.8. Basic principle of photocatalytic water splitting reactions in the presence of cocatalyst for water reduction. Here, photocatalyst surface site acts as water oxidation catalytic sites.

1.3. Strategies to utilize visible light by a photocatalyst

H_2 and O_2 production by water decomposition using sunlight on semiconductor photocatalysts has attracted great research interest since the revolutionary work on a photo-electrochemical cell was carried out by Honda and Fujishima in 1972 using TiO_2 anode and a Pt cathode under ultraviolet irradiation and an external bias. Afterwards extensive efforts have been made to develop semiconductor photocatalysts for photocatalytic water splitting reactions. Many types of semiconductors comprising oxides, nitrides, oxynitrides, sulphides, selenides, carbides, phosphides, perovskite type materials, inorganic complexes, layered compounds etc. have been reported to be appropriate candidates as photocatalysts for hydrogen evolution via water splitting. Among these, simple oxides like, ZnO, TiO_2, ZrO_2, SnO_2 etc. are reported to be active in photocatalytic hydrogen evolution under UV irradiation due to large band gaps. From the above discussions, it is clear that the semiconductor systems with optimized band gap and band alignment vis-à-vis positioning to the reduction/oxidation potentials of H_2O are suitable for photocatalytic water splitting, so as to make maximum utilization of solar radiation and sufficient chemical stability against photocorrosion.

Various methods are recommended to achieve visible light absorption in these semiconductor oxides such as doping, using sensitizers etc. Band gap engineering plays a crucial role in designing a photocatalyst which is visible light active (Figure 1.9).

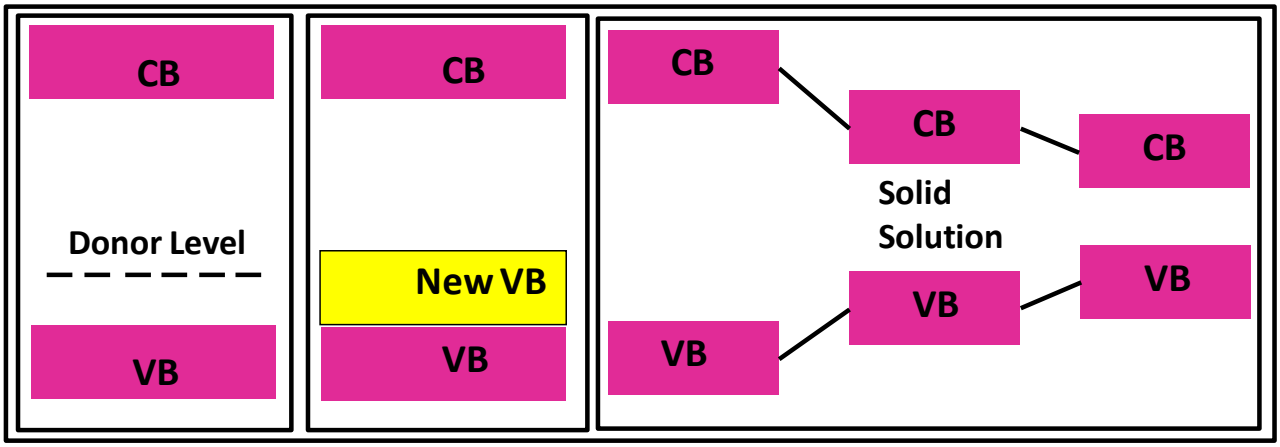

Figure 1.9. Three types of band engineering for the design of visible-light-driven photocatalysts .

The conduction band level of oxide semiconductors are composed of empty orbitals (LUMOs) of their metal cations. The valence band is usually filled O 2p orbitals. Band gap energy can be tuned by introducing a new valence band or an electron donor level near to the valence band by dopants consisting of orbitals other than O 2p orbitals to utilize visible light wavelengths. The newly formed energy bands should be associated with sufficient thermodynamic potential and kinetic ability for photoelectrolysis. The charge imbalance caused by these dopants is maintained by the addition of codopants [47-50].

Anion doping is also a well-accepted way of band gap engineering to introduce visible light absorption in metal oxides. In anion doping, mixing of the p states of doped anion (N, S and C) with the O 2p states shift the valence band edge upwards to narrow the overall band gap energy of the metal oxide. Among these, nitrogen doping is the most efficient anion dopant because of the sufficient overlapping of O 2p and N 2p states which reduces the effective band gap. Making a solid solution catalyst is also a useful band gap engineering stratagem. This will reduce the effective band gap by providing new electronic levels. For example, CdS-ZnS solid solution is active for visible light hydrogen production

[51-54]. Another efficient method to utilize visible light irradiation is Z scheme water splitting which was originally introduced by Prof. A. J. Bard. As already mentioned above, in Z scheme photocatalysis two different kinds of photocatalysts are jointly used as a redox mediator. Here the systems must have two excitation centres. Usually the first system produces hydrogen and an oxidizing agent which is used up by the second system to produce oxygen [28, 55].

Another strategy to make visible light driven photocatalysts is to incorporate sensitizers capable of absorbing visible light. Oxide photocatalysts with visible light response has been extensively studied as dye sensitized solar cells (DSSC). The key to the breakthrough for DSSC was the use of a mesoporous TiO_2 electrode to support the monolayer of an organic sensitizer in 1991 [56]. In DSSC, upon irradiation the dye molecule became photo-excited and ultrafastly injects an electron into the conduction band of the semiconductor electrode, then the original form of the dye is subsequently restored by electron donation from the electrolyte, usually an organic solvent or ionic mediator I^{3-}/I^{-} redox system (Figure 1.10). The photosensitizer should fulfill some essential characteristics [56]:

(i) the absorption spectrum of the sensitizer should cover the whole visible region and some portion of the near-infrared (NIR) for maximum solar energy utilization

(ii)should have binding groups (-COOH, $-H_2PO_3$, $-SO_3H$, etc.) to strongly anchor the dye onto the surface of the semiconductor

(iii) the excited state level of the photosensitizer should be higher in energy than the conduction band edge of the semiconductor (n-type) so that an efficient electron transfer process can occur between the excited dye and conduction band (CB) of the semiconductor

(iv) the oxidized state level of the photosensitizer must be more positive than the redox potential of electrolyte/sacrificial reagent for dye regeneration.

(v) the photosensitizer should be stable photolytically, electrochemically and thermally.

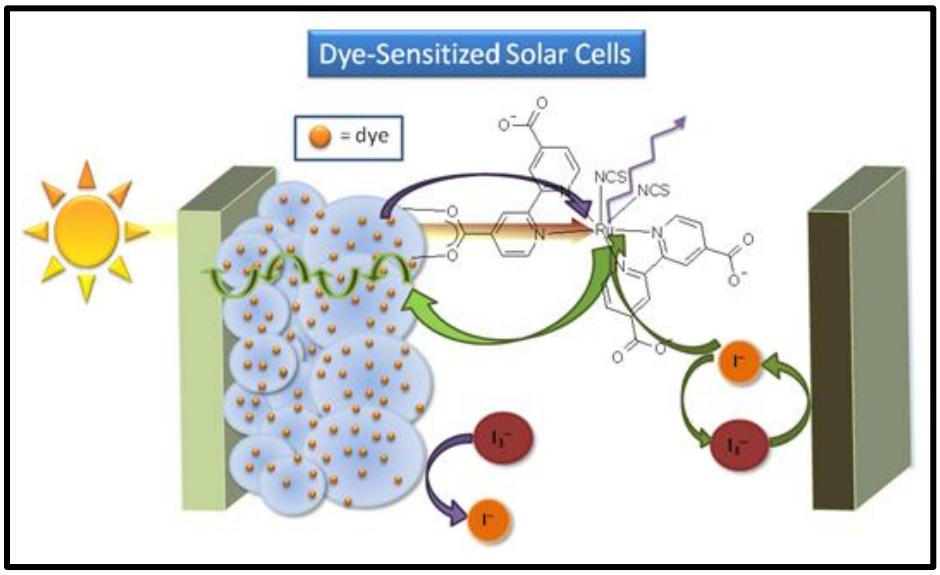

Figure 1.10. Schematic representation of DSSC (Adapted from reference 57).

Different photosensitizers have been designed and applied in photocatalysis in the past few decades which include metal complexes, porphyrins, phthalocyanines and metal-free organic dyes. Metal complexes have been investigated extensively because of their broad absorption spectra. Visible light absorption in metal complexes is due to a metal to ligand charge transfer (MLCT) process. Among the metal complexes, Ru complexes have excellent visible light active properties: a broad absorption spectrum, suitable excited and ground state energy levels, relatively long excited-state lifetime, and good electrochemical stability. Gratzel and co-workers improved visible light absorption in Ru complexes by modifying Ru center using a trinuclear thiocyanato ligands and one terpyridine ligand with three carboxyl groups on mesoporous TiO_2 electrode [58-75]. The main drawback of ruthenium complexes is the limited absorption in the near-infrared region (NIR) of the solar spectrum. Porphyrin and phthalocyanine systems exhibit intense spectral response bands in the near-IR region and possess photo stability as sensitizers in DSSC. Porphyrins have strong absorptions extending from 400-700 nm range. Several studies by Kay *et al*, Durrant *et al* and Otero *et al* have confirmed that porphyrin dyes can show efficient photoinduced electron injection into the conduction band of TiO_2 [76-78]. Phthalocyanine dyes possess intense absorption around 700 nm and used as NIR photosensitizers for DSSCs [79-84] .

Organic dyes exhibit many advantages as photosensitizers compared to metal complexes. They are easily synthesized, low-cost and have high molar-extinction coefficient. To date, organic dyes including coumarin dyes, indoline dyes, tetrahydroquinoline dyes, triarylamine dyes, heteroanthracene dyes, carbazole dyes, *N*,*N*-dialkylaniline dyes, hemicyanine dyes, merocyanine dyes, squaraine dyes, perylene dyes, anthraquinone dyes, boradiazaindacene (BODIPY) dyes, oligothiophene dyes, polymeric dyes, and natural dyes have been used as sensitizers for DSSCs and have obtained impressive efficiencies (Figure 1.11). In coumarin dyes, coumarin unit acts as an electron donor. Triarylamine dyes have been investigated widely due to their electron donating ability and hole-transporting properties. Heteroanthracene dyes include xanthene, phenothiazine and phenoxazine. They show relatively low efficiency due to their narrow light harvesting region and instability. Sun and co-workers developed a series of organic dyes by changing the triphenylamine units, making them strong electron donors. Hemicyanines are considered as D-π-A-type cationic dyes with basic p-dialkyl aniline groups as electron donor and cationic moieties as strong electron acceptor linked by methane π-bridge. Squaraine dyes exhibit sharp and intense absorption bands in the visible and NIR regions. Perylene dyes are well-known for their excellent chemical stability and light fastness. They exhibit a high molar extinction coefficient in visible light ($\sim 10^5$ $M^{-1}cm^{-1}$). Oligothiophene dyes are known as conducting polymers due to their strong inter-molecular π –conjugated interactions. But the bottleneck is its aggregation property on introducing larger thiophene framework [85-140].

The adsorption modes of dyes on semiconductor surfaces are very important for the DSSC efficiency. The adsorption modes can be summarized in six different ways: covalent attachment via linking agents, electrostatic interactions via ion exchange, ion-pairing or donor –acceptor interactions, hydrogen bonding, hydrophobic interactions, physisorption of molecules, van der Waals forces and physical entrapment inside the pores or cavities of hosts. The dye should possess an anchoring group which should react with surface hydroxyl groups of the semiconductor oxide to form chemical bonds. The standard anchoring group for photosensitizer organic dye is carboxylic acid (-COOH) [141-145].

The key problems of DSSC are low-efficiency, low stability and low scalability. In other words, the synthetic procedures, complex nature, stability and the narrow spectral

response of these dyes have led researchers to explore short conjugated organic dyes, which are advantageous because of their easier synthesis, broad spectral response and ultrafast photoexcited electron transfer.

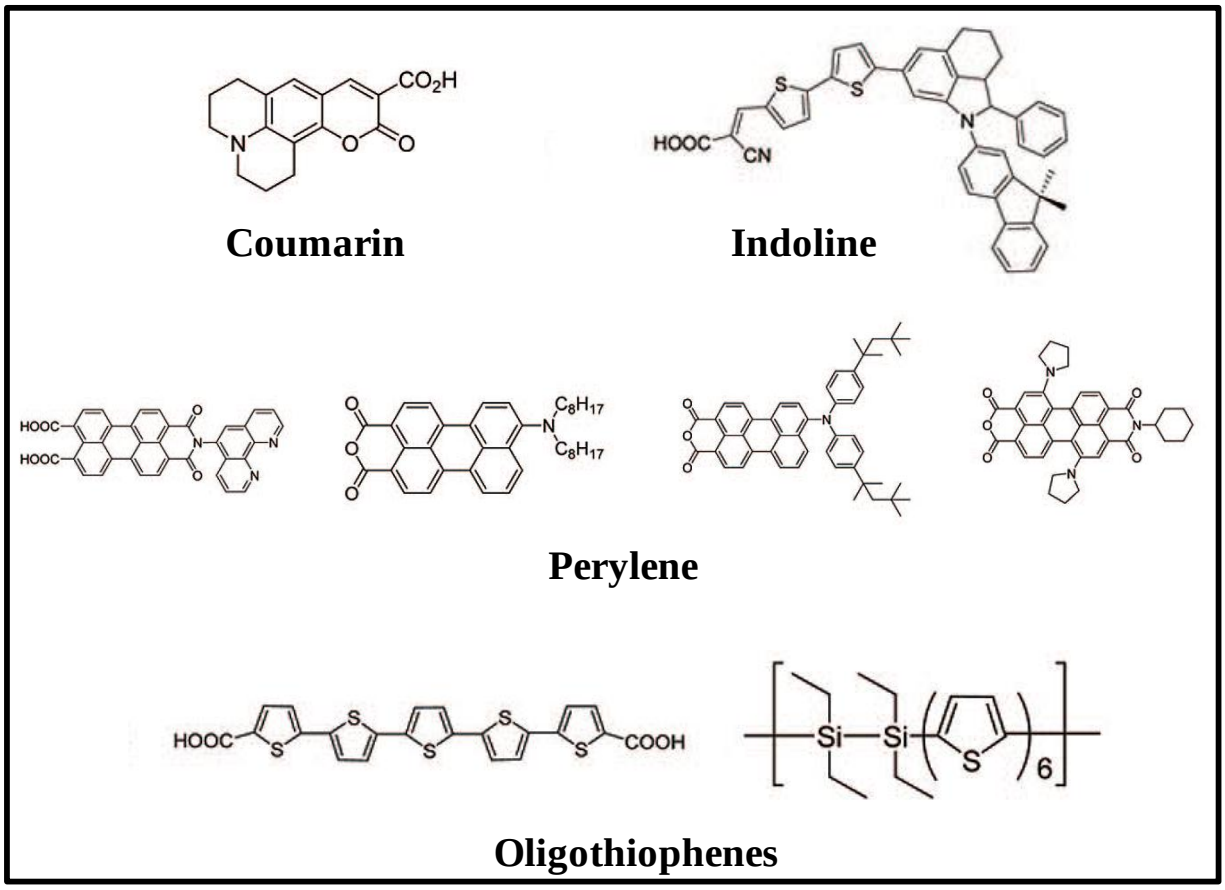

Figure 1.11. Common organic dyes used as sensitizers in DSSC (Adapted from reference 56).

Historically, ZnO was one of the first semiconductors used in DSSCs with the band gap and conduction band edge similar to that of TiO_2 (anatase). ZnO possesses higher electron mobility than TiO_2 favoring electron transport. The use of ZnO in DSSCs has increased dramatically in recent years which can be mainly attributed to the relative ease of synthesizing highly crystalline ZnO with different morphologies, such as nanoparticles, nanowires, nanorods, nanotubes, nanoflowers, nanosheets and branched nanostructures (in the wurtzite structure). Nanostructured ZnO has been synthesized via a wide range of

techniques and is so far the runner up to TiO_2. Also, zinc oxide semiconducting nanostructures have been attracting increasing interest due to their large potential applications in different UV-emitting devices, spintronics, or transparent electronics and may be used as building blocks to construct new synthetic materials with unique properties mainly opto-electronics. ZnO is a chemically stable and environmentally friendly material which makes it all the more attractive to be used in greener options. Other favourable aspects of ZnO include its broad chemistry: particle size over the largest possible range, narrow size distribution, good crystallinity, high luminescence and desired surface properties [146-155]. The size quantization of ZnO NPs can change the spectral position of the visible emission and exciton emission. The fluorescence characteristics of nano particles of ZnO have been studied as a function of the excitation wavelength and particle size. It is found that emission shifts with the change of the excitation wavelength. The ZnO nano particles have various luminescence transitions since different preparation techniques lead to varying structures and surface properties in ZnO [156-202]. Generally, the luminescence spectrum of ZnO exhibits a narrow emission band in the UV region (~3.22 eV) which originates from the radiative recombination of a hole in the valence band and an electron in the conduction band (excitonic emission) and a broad band in the visible (~2.11 eV) due to the recombination of an electron in or near the conduction band with a hole at a defect site (defect emission). But the broad visible emission band can extend from 380 to 650 nm. The most commonly seen defect-related visible emission is green luminescence though other emissions such as yellow or blue have also been observed. But the phenomenon of green luminescence is still controversial and a number of suggestions have been proposed. The proposed suggestions for green luminescence arises due to various types of defects such as oxygen vacancies, zinc ion vacancies as well as donor-acceptor pairs. Vanheusden et al. found that oxygen vacancies are responsible for the defect green luminescence in ZnO. Oxygen vacancies occur in three different charge states: the neutral oxygen vacancy (Vo^0), the singly ionized oxygen vacancy (Vo*) and the doubly ionized oxygen vacancy (Vo**) of which only Vo* can act as the so called luminescent center (Figure 1.12) [203-230].

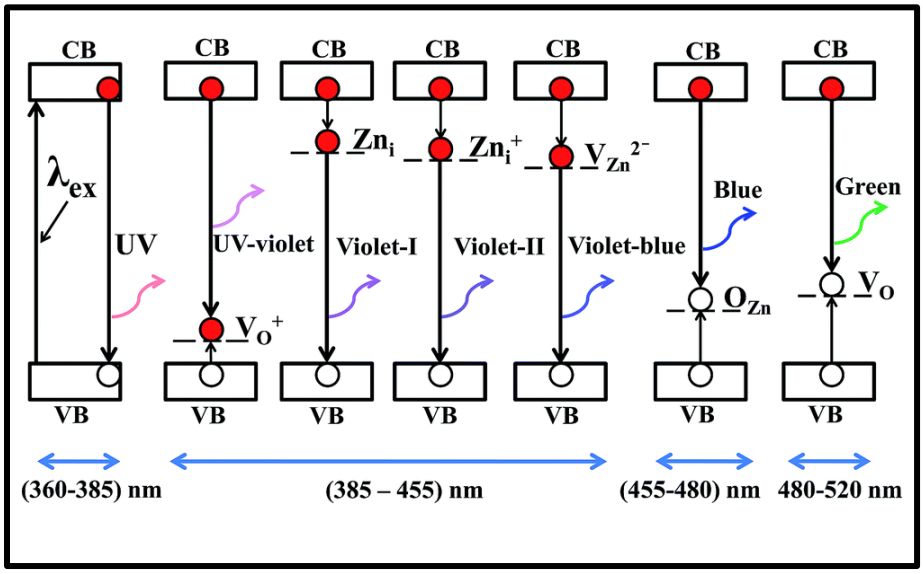

Figure 1.12. Schematic band diagram, demonstrating various Photoluminescence emission components originated due to electronic transitions between different defect levels and the band edges of ZnO films (Adapted from reference 156).

1.4. Scope and objective of the thesis

From the discussions in the previous sections, it is clear that ZnO semiconductor nanostructures with appropriate band structure will have enough work function for the excited electron to split water into H_2 and O_2. Efficiencies achieved so far is not high enough for a viable use of the technology; however, the bottleneck in photocatalytic water splitting is more in materials designing rather than the thermodynamics or kinetics. The main drawback lies in recombination of the exciton pairs before the catalytic process since the transfer is kinetically controlled. Hence, efficient ways of space separation of holes and electrons produced is a prerequisite in utilizing them in catalytic processes. Several mechanisms are suggested to minimise the recombination centers like defect sites in bulk structure, grain boundaries, and surface sites. A simple and yet potent way of countering this would be to reduce the particle size without compromising on the crystallinity, thereby decreasing the possibilities of bulk defect sites. However, this strategy has adverse effects on the semiconductor behaviour, especially in altering the band structure and band gap and also in increasing surface sites-the former decreasing the applicability in the visible light solar spectrum and the latter assisting recombination. Consequently, even though

there is considerable interest in studying ZnO in the form of nanostructures, pure ZnO nanoparticles cannot be utilized effectively for solar excitation or conversion because their poor visible light absorption and fast electron–hole recombination limit potential applications. One way we propose to achieve this is to attach appropriate conducting organic molecules to the semiconductor surfaces so that fast electron transfer happens to the conducting path rather than recombination. Another way is the surface modifications of nanostructured ZnO with appropriate organic linker molecules to address this problem in a bipronged approach: (i) organic moiety helps in visible light absorption by creating appropriate donor bands to ZnO and (ii) modifications to surface sites can be achieved advantageously in tandem with reducing the bulk recombination sites. In addition, enhanced surface areas of nanomaterials will aid in increasing the catalytic activity. Here, the organic moiety acts as a sensitizer facilitating photo- absorption and excitation, leading to possible electron transfer from the HOMO to the LUMO energy levels of the sensitizer to the semiconductor conduction band as in the case of DSSCs. In such a case, the mechanism of water splitting can be expected to differ from that occurring through photoexcitation of semiconductors, where electrons are excited from valence band to the conduction band creating a hole in the former when light falls on it. Photosensitizers usually reported for DSSCs have tedious synthetic procedures, are complex in nature and less stable, with narrow spectral response and low molar extinction coefficient which led researchers to explore short conjugated organic dyes. This aspect is very recently reported by Carlo *et al* who showed that PbS quantum dots by surface modification with short conjugated ligands like p-methylbenzenethiolate linker can be exploited to enhance solar-light absorption of colloidal QDs across the entire UV–vis–NIR spectral range, without affecting the molar absorption coefficient and preserving good long-term colloidal stability [231]. This design concept is based on the evidence that organic ligands and inorganic cores constituting the colloidal semiconductor nanocrystals are inherently electronically coupled by the chemical nature and coordination geometry of the anchoring group and its π conjugation with the pendant moiety of the organic ligand. Short conjugated molecules are advantageous because of their easier synthesis, broad spectral response, high molar absorption coefficient and ultrafast photoexcited electron transfer. Hence photocatalytic systems

consisting of visible light absorbing short conjugated organic molecules end functionalized with carboxyl groups, which can bind to the surface hydroxyl groups on ZnO surface effecting better interfacial interactions, are ideal for this purpose.

Based on these concepts, the following specific works were selected for the present thesis.

1. Synthesis and characterization of ZnONPs.
2. Synthesis and characterization of short conjugated organic ligands like azonaphthols, azoquinolines, perylenes and thiophenes functionalized with carboxylic anchoring group.
3. Synthesis and characterization of ZnO-ligand composites (ZnO-azonaphthols, ZnO-azoquinolines, ZnO-perylenes and ZnO-thiophenes).
4. The study of the photocatalytic hydrogen evolution activity and electron transfer mechanisms in bare ZnO and surface grafted ZnO-ligand composites under various conditions.

   The position of carboxylate functionality (anchoring group) in the phenyl group is changed from meta-analogue to para- to achieve the variation in extended conjugation in the organic moiety. Energy levels near the ZnO conduction band to facilitate electron transfer as well as bond conjugation within the organic linker for enhancing electron conduction are also considered. This work also briefly explains the computational study carried out in collaboration with Dr. Prasenjit Ghosh, IISER Pune and his group for correlating catalytic activity and electronic structure of the composites.

References

1. Dresselhaus, M. S.; Thomas, I. L., *Nature* **2001**, *414*, 332.
2. Lewis, N. S; Nocera, D. G., *Proc. Natl. Acad. Sci. U. S. A*. **2006**, *103*, 15729.
3. Bockris, J. O'M., *Int. J. Hydrogen Energy* **2002**, *27*, 731.
4. Bard, A. J.; Fox, M. A., *Acc. Chem. Res.* **1995**, *28*, 141.
5. Kawai, T.; Sakata, T., *Nature* **1980,** *286*, 474.
6. Nowotny, J.; Sorrell, C. C.; Sheppard, L. R.; Bak, T., *Int. J. Hydrogen Energy* **2005**, *30*, 521.
7. Chu, S.; Majumdar, A., *Nature* **2012,** *488*, 295.
8. Florin, N.; Harris, A., *Environmentalist* **2007**, *27*, 207.
9. Maeda, K.; Domen, K., *J. Phys. Chem. Lett.* **2010**, 1 (18), 2655.
10. http://solarcellcentral.com/solar_page.htmlAa
11. Solar Hydrogen Generation: Toward a Renewable Energy Future, Rajeshwar, K., McConnell, R., Licht, S., Ed.; Springer Science: New York, 2008.
12. Miller, E. L., *Energy Environ Sci.* **2015**, *8*, 2809-2810.
13. http://www.solarnovus.com/simple-and-easy-to-produce-material-for-solar-water-splitting_N3426.html
14. Lee, J. S., *Catal. Surv. Asia* **2005**, *9*, 217.
15. Abe, R., *Bull. Chem. Soc. Japan* **2011**, *84*, 1000.
16. Maeda, K., *J. Photochem. Photobiol*. C **2011**, *12*, 237.
17. Hao, X. H.; Guo, L. J.; Mao, X.; Zhang, X. M.; Chen, X. J., *Int. J. Hydrogen Energy* **2003**, *28*, 55.
18. Ashokkumar, M., *Int. J. Hydrogen Energy* **1998**, *23*, 427.
19. Fujishima, A.; Rao, T. N.; Tryk, D. A., *J. Photoch. Photobio. C* **2000**, 1, 1.
20. Rufino M. N. Y.; Consuelo lvarez Galvn M.; Del Valle F.; Jos A. V.; JosL. G. F., *Chem. Sus. Chem.* **2009**, *2*, 471.
21. Kudo, A., *Catal. Surv. Asia* **2003**, *7*, 1.
22. Tachibana, Y.; Vayssieres, L.; Durrant, J. R., *Nat. Photonics* **2012**, *6*, 511.
23. Fujishima, A.; Honda, K., *Nature* **1972**, *238,* 37.
24. Maeda, K.; Domen, K., *J. Phys. Chem. C* **2007**, *111*, 7851.
25. Kudo, A., *Int. J. of Hydrogen Energy* **2007**, *32*, 2673.

26. Osterloh, F. E., *Chem. Mater.* **2008**, *20*, 35.
27. Chen, X.; Shen, S.; Guo, L.; Mao, S. S., Chem. Rev. **2010**, *110*, 6503.
28. Maeda, K., *ACS Catal*., **2013**, *3*, 1486-1503.
29. http://solarfuel.clas.asu.edu/comparison-photosynthetic-and-photovoltaic-efficiencies
30. Kudo, A.; Miseki, Y., *Chem. Soc. Rev.* **2009**, *38*, 253.
31. Yuzun F.; Dongmei L. I.; Minghui D.; Yanhong L.; Qingbo M., *Front. Chem. China* **2009**, *4*, 343.
32. Tang, J.; Durrant, J. R.; Klug, D. R., *J. Am. Chem. Soc.* **2008**, *130*, 13885.
33. Walter, M. G.; Warren, E. L.; McKone, J. R.; Boettcher, S. W.; Mi, Q.; Santori, E. A.; Lewis, N. S., *Chem. Rev.* **2010**, *110*, 6446.
34. Seabold, J. A.; Kyoung-Shin, C., *Chem. Mater.* **2011**, *23*, 1105.
35. Ni, M.; Leung, M. K. H.; Leung, D. Y. C.; Sumathy, K., *Renew. Sust. Energ. Reviews* **2007**, *11*, 401.
36. Maitra, U.; Lingampalli, S. R.; Rao, C. N. R., *Curr. Scie. India* **2014**, *106*, 25.
37. Zieliñska, B.; Borowiak-Palen, E.; Kalenczuk, R. J., *Int. J. of Hydrogen Energy* **2008**, *33*, 1797.
38. Schneider, J.; Bahnemann, D. W., *J. Phys. Chem. Lett.* **2013**, *4*, 3479.
39. Teoh, W. Y.; Scott, J. A.; Amal, R., *J. Phys. Chem. Lett.* **2012**, *3*, 629.
40. Hykaway, N.; Sears, W. M.; Morisaki, H.; Morrison, S. R., *J. Phys. Chem.* **1986**, *90*, 6663.
41. Kayaci, F.; Vempati, S.; Donmez, I.; Biyikliab, N.; Uyar, T., *Nanoscale* **2014**, *6*, 10224.
42. Sabio, E. M.; Chamousis, R. L.; Browning, N. D.; Osterloh, F. E., *J. Phys. Chem. C* **2012**, *116*, 3161.
43. Maeda, K.; Teramura, K.; Lu, D.; Saito, N.; Inoue, Y.; Domen, K., *Angew. Chemie.* **2006**, *118*, 7970.
44. Dennis Y. C. L.; Xianliang, F.; Cuifang, W.; Meng, N.; Michael, K. H. L.; Xuxu, W.; Xianzhi, F., *Chem. Sus. Chem.* **2010**, *3*, 681.
45. Min, S.; Lu, G., *J. Phys. Chem. C,* **2012**, *116*, 25415.
46. Iwase, A.; Kato, H.; Kudo, A., *Catal. Lett.* **2006**, *108*, 7.
47. Kudo, A., *Int. J. of Hydrogen Energy* **2007**, *32*, 2673.
48. Zhu, J.; Zäch, M., *Curr. Opin. Colloid. In.* **2009**, *14*, 260.

49. Ishii, T.; Kato, H.; Kudo, A., *J. Photochem. Photobiol. A* **2004**, *163*, 181.
50. Kim, H. G.; Hwang, D. W.; Lee, J. S., *J. Am. Chem. Soc*. **2004**, *126*, 8912.
51. Chen, X.; Shen, S.; Guo, L.; Mao, S. S., *Chem. Rev.* **2010**, *110,* 6503.
52. Zhang, J.; Dang, W.; Ao, Z.; Cushing, S. K.; Wu, N. *Phys. Chem. Chem. Phys.* **2015**, *17*, 8994.
53. Asahi, R.; Morikawa, T.; Ohwaki, T.; Aoki, K.; Taga, Y., *Science* **2001,** *293*, 269.
54. Kakuta, N.; Park, K. K.; Finlayson, M. F.; Ueno, A.; Bard, A. J.; Campion, A.; Fox, M. A.; Webber, S. E.; White, J. M., *J. Phys.Chem.* **1985**, *89*, 732.
55. Bard, A. J., *J. Photochem.* **1979**, *10*, 59.
56. Hagfeldt, A.; Boschloo, G.; Sun, L.; Kloo, L.; Pettersson, H., *Chem.Rev.* **2010**, *110*, 6595-6663.
57. https://photochemistry.wordpress.com/2009/08/17/dye-sensitised-solar-cells-dssc/
58. Kuang, D.; Klein, C.; Ito, S.; Moser, J. E.; Humphry-Baker, R.; Evans, N.; Duriaux, F.; Grätzel, C.; Zakeeruddin, S. M.; Grätzel, M., *Adv. Mater*. **2007**, *19*, 1133.
59. Kuang, D.; Ito, S.; Wenger, B.; Klein, C.; Moser, J. E.; Humphry-Baker, R.; Zakeeruddin, S. M.; Grätzel, M., *J. Am. Chem. Soc*. **2006**, *128*, 4146.
60. Haque, S. A.; Palomares, E.; Cho, B. M.; Green, A. N. M.; Hirata, N.; Klug, D. R.; Durrant, J. R., *J. Am. Chem. Soc*. **2005**, *127*, 3456
61. Haque, S. A.; Handa, S.; Peter, K.; Palomares, E.; Thelakkat, M.; Durrant, J. R., *Angew. Chem., Int. Ed*. **2005**, *44*, 5740.
62. Klein, C.; Nazeeruddin, M. K.; Liska, P.; Di Censo, D.; Hirata, N.; Palomares, E.; Durrant, J. R.; Grätzel, M., *Inorg. Chem*. **2005**, *44*, 178.
63. Nazeeruddin, M. K.; De Angelis, F.; Fantacci, S.; Selloni, A.; Viscardi, G.; Liska, P.; Ito, S.; Takeru, B.; Grätzel, M. G., *J. Am. Chem. Soc*. **2005**, *127,* 16835.
64. Nazeeruddin, M. K.; Klein, C.; Liska, P.; Grätzel, M., *Coord. Chem. Rev*. **2005**, *249*, 1460.
65. Schmidt-Mende, L.; Kroeze, J. E.; Durrant, J. R.; Nazeeruddin, M. K.; Grätzel, M., *Nano Lett*. **2005**, *5*, 1315.
66. Wang, P.; Wenger, B.; Humphry-Baker, R.; Moser, J. E.; Teuscher, J.; Kantlehner, W.; Mezger, J.; Stoyanov, E. V.; Zakeeruddin, S. M.; Grätzel, M., *J. Am. Chem. Soc*. **2005**, *127*, 6850.

67. Barolo, C.; Nazeeruddin, M. K.; Fantacci, S.; Di Censo, D.; Comte,P.; Liska, P.; Viscardi, G.; Quagliotto, P.; De Angelis, F.; Ito, S.;Gra¨tzel, M., *Inorg. Chem*. **2006**, *45*, 4642.
68. Chia-Yuan Chen, S. J. W.; Chun-Guey, W.; Jian-Ging, C.; Kuo-Chuan, H., *Angew. Chem., Int. Ed.* **2006**, *45*, 5822.
69. Ghosh, S.; Chaitanya, G. K.; Bhanuprakash, K.; Nazeeruddin, M. K.; Grätzel, M.; Reddy, P. Y., *Inorg. Chem*. **2006**, *45*, 7600.
70. Jang, S. R.; Lee, C.; Choi, H.; Ko, J. J.; Lee, J.; Vittal, R.; Kim, K. J., *Chem. Mater*. **2006,** *18*, 5604.
71. Kuang, D. B.; Klein, C.; Snaith, H. J.; Moser, J. E.; Humphry-Baker, R.; Comte, P.; Zakeeruddin, S. M.; Grätzel, M., *Nano Lett*. **2006**, *6*, 769.
72. Mazille, F.; Fei, Z. F.; Kuang, D. B.; Zhao, D. B.; Zakeeruddin, S. M.; Grätzel, M.; Dyson, P. J., *Inorg. Chem*. **2006**, *45*, 1585.
73. Jiang, K. J.; Masaki, N.; Xia, J. B.; Noda, S.; Yanagida, S., *Chem. Commun*. **2006**, 2460.
74. Fan, S. H.; Wang, K. Z.; Yang, W. C., *Eur. J. Inorg. Chem*. **2009,** 508.
75. Nazeeruddin, M. K.; Pechy, P.; Grätzel, M., *Chem. Commun*. **1997**, 1705.
76. Cherian, S.; Wamser, C. C., *J. Phys. Chem. B* **2000**, *104*, 3624.
77. Fungo, F.; Otero, L. A.; Sereno, L.; Silber, J. J.; Durantini, E. N., *J. Mater. Chem*. **2000**, *10*, 645.
78. Fungo, F.; Otero, L.; Durantini, E. N.; Silber, J. J.; Sereno, L. E., *J. Phys. Chem. B* **2000,** *104*, 7644.
79. Tachibana, Y.; Haque, S. A.; Mercer, I. P.; Durrant, J. R.; Klug, D. R., *J. Phys. Chem. B* **2000**, *104,* 1198.
80. Ma, T.; Inoue, K.; Yao, K.; Noma, H.; Shuji, T.; Abe, E.; Yu, J.; Wang, X.; Zhang, B., *J. Electroanal. Chem*. **2002**, *537*, 31.
81. Kay, A.; Grätzel, M., *J. Phys. Chem*. **1993**, *97*, 6272.
82. Ma, T. L.; Inoue, K.; Noma, H.; Yao, K.; Abe, E., *J. Photochem. Photobiol., A* **2002**, *152*, 207.
83. Gervaldo, M.; Fungo, F.; Durantini, E. N.; Silber, J. J.; Sereno, L.; Otero, L., *J. Phys. Chem. B* **2005**, *109*, 20953.
84. Hara, K.; Sayama, K.; Ohga, Y.; Shinpo, A.; Suga, S.; Arakawa, H., *Chem. Commun*. **2001**, 569.

85. Hara, K.; Kurashige, M.; Dan-oh, Y.; Kasada, C.; Shinpo, A.; Suga, S.; Sayama, K.; Arakawa, H., *New J. Chem*. **2003**, *27*, 783.

86. Hara, K.; Miyamoto, K.; Abe, Y.; Yanagida, M., *J. Phys. Chem. B* **2005,** *109*, 23776.

87. Hara, K.; Dan-oh, Y.; Kasada, C.; Ohga, Y.; Shinpo, A.; Suga, S.; Sayama, K.; Arakawa, H., *Langmuir* **2004**, *20*, 4205.

88. Furube, A.; Katoh, R.; Hara, K.; Sato, T.; Murata, S.; Arakawa, H.; Tachiya, M., *J. Phys. Chem. B* **2005**, *109*, 16406.

89. Horiuchi, T.; Miura, H.; Sumioka, K.; Uchida, S., *J. Am. Chem. Soc*. **2004**, *126*, 12218.

90. Schmidt-Mende, L.; Bach, U.; Humphry-Baker, R.; Horiuchi, T.; Miura, H.; Ito, S.; Uchida, S.; Grätzel, M., *Adv. Mater.* **2005**, *17*, 813.

91. Howie, W. H.; Claeyssens, F.; Miura, H.; Peter, L. M., *J. Am. Chem. Soc*. **2008**, *130*, 1367.

92. Dentani, T.; Kubota, Y.; Funabiki, K.; Jin, J.; Yoshida, T.; Minoura, H.; Miura, H.; Matsui, M., *New J. Chem*. **2009**, *33*, 93.

93. Chen, R.; Yang, X.; Tian, H.; Wang, X.; Hagfeldt, A.; Sun, L.*, Chem. Mater*. **2007**, *19,* 4007.

94. Hao, Y.; Yang, X.; Cong, J.; Tian, H.; Hagfeldt, A.; Sun, L., *Chem. Commun*. **2009**, 4031.

95. Kitamura, T.; Ikeda, M.; Shigaki, K.; Inoue, T.; Anderson, N. A.; Ai, X.; Lian, T. Q.; Yanagida, S., *Chem. Mater.* **2004**, *16*, 1806.

96. Thomas, K. R. J.; Hsu, Y. C.; Lin, J. T.; Lee, K. M.; Ho, K. C.; Lai, C. H.; Cheng, Y. M.; Chou, P. T., *Chem. Mater.* **2008**, *20*, 1830.

97. Hagberg, D. P.; Edvinsson, T.; Marinado, T.; Boschloo, G.; Hagfeldt, A.; Sun, L. C., *Chem. Commun*. **2006**, 2245.

98. Tian, H. N.; Yang, X. C.; Pan, J. X.; Chen, R. K.; Liu, M.; Zhang, Q. Y.; Hagfeldt, A.; Sun, L. C., *Adv. Funct. Mater*. **2008,** *18*, 3461.

99. Zhang, G. L.; Bai, Y.; Li, R. Z.; Shi, D.; Wenger, S.; Zakeeruddin, S. M.; Grätzel, M.; Wang, P., *Energy Environ. Sci*. **2009**, *2*, 92.

100. Zhou, G.; Pschirer, N.; Schoneboom, J. C.; Eickemeyer, F.; Baumgarten, M.; Mullen, K., *Chem. Mater*. **2008**, *20*, 1808.

101. Sayama, K.; Sugino, M.; Sugihara, H.; Abe, Y.; Arakawa, H., *Chem. Lett*. **1998**, 753.

102. Tian, H. N.; Yang, X. C.; Chen, R. K.; Hagfeldt, A.; Sun, L. C., *Energy Environ. Sci*. **2009**, *2*, 674.

103. Koumura, N.; Wang, Z. S.; Mori, S.; Miyashita, M.; Suzuki, E.; Hara, K., *J. Am. Chem. Soc.* **2008**, *130*, 4202.

104. Wang, Z. S.; Koumura, N.; Cui, Y.; Takahashi, M.; Sekiguchi, H.; Mori, A.; Kubo, T.; Furube, A.; Hara, K., *Chem. Mater*. **2008**, *20*, 3993.

105. Ooyama, Y.; Shimada, Y.; Ishii, A.; Ito, G.; Kagawa, Y.; Imae, I.; Komaguchi, K.; Harima, Y. *J. Photochem. Photobiol., A* **2009**, *203*, 177.

106. Hara, K.; Kurashige, M.; Ito, S.; Shinpo, A.; Suga, S.; Sayama, K.; Arakawa, H., *Chem. Commun*. **2003**, 252.

107. Hara, K.; Sato, T.; Katoh, R.; Furube, A.; Yoshihara, T.; Murai, M.; Kurashige, M.; Ito, S.; Shinpo, A.; Suga, S.; Arakawa, H., *Adv. Funct. Mater***. 2005**, *15,* 246.

108. Li, S. L.; Jiang, K. J.; Shao, K. F.; Yang, L. M., *Chem. Commun*. **2006**, 2792.

109. Wang, Z. S.; Huang, Y. Y.; Huang, C. H.; Zheng, J.; Cheng, H. M.; Tian, S*., J. Synth. Met*. **2000**, *114*, 201.

110. Wang, Z. S.; Li, F. Y.; Huang, C. H., *Chem. Commun*. **2000**, 2063.

111. Wang, Z.-S.; Li, F.-Y.; Huang, C.-H.; Wang, L.; Wei, M.; Jin, L.-P.; Li, N. Q., *J. Phys. Chem. B* **2000**, *104*, 9676.

112. Wang, Z. S.; Li, F. Y.; Huang, C. H., *J. Phys. Chem. B* **2001**, *105,* 9210.

113. Yao, Q. H.; Meng, F. S.; Li, F. Y.; Tian, H.; Huang, C. H., *J. Mater. Chem*. **2003,** *13,* 1048.

114. Yao, Q. H.; Shan, L.; Li, F. Y.; Yin, D. D.; Huang, C. H., *New J. Chem*. **2003**, *27*, 1277.

115. Meng, F. S.; Yao, Q. H.; Shen, J. G.; Li, F. L.; Huang, C. H.; Chen, K. C.; Tian, H., *Synth. Met*. **2003**, *137*, 1543.

116. Sayama, K.; Tsukagoshi, S.; Hara, K.; Ohga, Y.; Shinpou, A.; Abe, Y.; Suga, S.; Arakawa, H., *J. Phys. Chem. B* **2002**, *106*, 1363.

117. Zhao, W.; Hou, Y. J.; Wang, X. S.; Zhang, B. W.; Cao, Y.; Yang, R.; Wang, W. B.; Xiao, X. R., *Sol. Energy Mater. Sol. Cells* **1999**, *58*, 173.

118. Alex, S.; Santhosh, U.; Das, S., *J. Photochem. Photobiol., A* **2005**, *172*, 63.

119. Chen, Y.; Zeng, Z.; Li, C.; Wang, W.; Wang, X.; Zhang, B., *New J. Chem*. **2005,** *29,* 773.

120. Li, C.; Wang, W.; Wang, X. S.; Zhang, B. W.; Cao, Y., *Chem. Lett*. **2005**, *34*, 554.

121. Burke, A.; Schmidt-Mende, L.; Ito, S.; Gra¨tzel, M., *Chem. Commun*. **2007**, 234.

122. Ferrere, S.; Gregg, B. A., *J. Phys. Chem. B* **2001**, *105*, 7602.

123. Ferrere, S.; Gregg, B. A., *New J. Chem*. **2002**, *26*, 1155.

124. Edvinsson, T.; Li, C.; Pschirer, N.; Schoneboom, J.; Eickemeyer, F.; Sens, R.; Boschloo, G.; Herrmann, A.; Mullen, K.; Hagfeldt, A., *J. Phys. Chem. C* **2007**, *111,* 15137.

125. Shibano, Y.; Umeyama, T.; Matano, Y.; Imahori, H., *Org. Lett*. **2007**, *9,* 1971.

126. Zafer, C.; Kus, M.; Turkmen, G.; Dincalp, H.; Demic, S.; Kuban, B.; Teoman, Y.; Icli, S., *Sol. Energy Mater. Sol. Cells* **2007**, *91*, 427.

127. Fortage, J.; Severac, M.; Houarner-Rassin, C.; Pellegrin, Y.; Blart, E.; Odobel, F., *J. Photochem. Photobiol., A* 2**008**, *197*, 156.

128. Jin, Y. H.; Hua, J. L.; Wu, W. J.; Ma, X. M.; Meng, F. S., *Synth. Met*. **2008**, *158*, 64.

129. Li, C.; Yum, J. H.; Moon, S. J.; Herrmann, A.; Eickemeyer, F.; Pschirer, N. G.; Erk, P.; Schoeboom, J.; Mullen, K.; Gra¨tzel, M.; Nazeeruddin, M. K., *ChemSusChem* **2008**, *1,* 615.

130. Li, C.; Yang, X.; Chen, R.; Pan, J.; Tian, H.; Zhu, H.; Wang, X.; Hagfeldt, A.; Sun, L., *Sol. Energy Mater. Sol. Cells* **2007**, *91*, 1863.

131. Erten-Ela, S.; Yilmaz, M. D.; Icli, B.; Dede, Y.; Icli, S.; Akkaya, E. U., *Org. Lett*. **2008**, *10*, 3299.

132. Kumaresan, D.; Thummel, R.; Bura, T.; Ulrich, G.; Ziessel, R., *Chem. Eur. J.* **2009,** *15*, 6335.

133. Tan, S. X.; Zhai, J.; Fang, H. J.; Jiu, T. G.; Ge, J.; Li, Y. L.; Jiang, L.; Zhu, D. B. *Chem. Eur. J.* **2005**, *11*, 6272.

134. Tanaka, K.; Takimiya, K.; Otsubo, T.; Kawabuchi, K.; Kajihara, S.; Harima, Y., *Chem. Lett*. **2006**, *35,* 592.

134. Hao, Y.; Yang, M.; Yu, C.; Cai, S.; Liu, M.; Fan, L.; Li, Y., *Sol. Energy Mater. Sol. Cells* **1998,** *56*, 75.

135. Hong, J. S.; Joo, M.; Vittal, R.; Kim, K. J., *J. Electrochem. Soc*. **2002**, *149*, E493.

136. Kim, Y.-G.; Walker, J.; Samuelson, L. A.; Kumar, J., *Nano Lett*. **2003**, *3*, 523.

137. Senadeera, G. K. R.; Kitamura, T.; Wada, Y.; Yanagida, S., *Sol. Energy Mater. Sol. Cells* **2005**, *88,* 315.

138. Mwaura, J. K.; Zhao, X.; Jiang, H.; Schanze, K. S.; Reynolds, J. R., *Chem. Mater*. **2006**, *18,* 6109.

139. Hao, S. C.; Wu, J. H.; Huang, Y. F.; Lin, J. M., *Sol. Energy* **2006**, *80*, 209.

140. Polo, A. S.; Iha, N. Y. M., *Sol. Energy Mater. Sol. Cells* **2006**, *90*, 1936.

141. Kalyanasundaram, K.; Gra¨tzel, M., *Coord. Chem. Rev*. **1998**, *177*, 347.

142. Murakoshi, K.; Kano, G.; Wada, Y.; Yanagida, S.; Miyazaki, H.; Matsumoto, M.; Murasawa, S., *J. Electroanal. Chem*. **1995**, *396*, 27.

143. Pechy, P.; Rotzinger, F. P.; Nazeeruddin, M. K.; Kohle, O.; Zakeeruddin, S. M.; Humphry-Baker, R.; Gra¨tzel, M., *J. Chem. Soc., Chem. Commun* **1995**, *1*, 65.

144. Galoppini, E., *Coord. Chem. Rev*. **2004**, *248,* 1283.

145. Nazeeruddin, M. K.; Humphry-Baker, R.; Liska, P.; Gra¨tzel, M., *J. Phys. Chem. B* **2003,** *107*, 8981.

146. Anderson, J.; Chris, G. V. d. W., *Rep. Prog. Phys*. **2009,** *72*, 126501.

147. Bahnemann, D. W.; Kormann, C.; Hoffmann, M. R., *J. Phys. Chem*. **1987**, *91,* 3789-3798.

148. Djurišić, A. B.; Leung, Y. H., *Small* **2006**, *2*, 944-961.

149. Gong, Y.; Andelman, T.; Neumark, G.; O'Brien, S.; Kuskovsky, I., *Nanoscale Res Lett* **2007**, *2*, 297-302.

150. Irimpan, L.; Nampoori, V. P. N.; Radhakrishnan, P.; Deepthy, A.; Krishnan, B., *J. Appl. Phys.* **2007**, *102*, 063524.

151. Kamat, P. V. *Chem. Rev*. **1993**, *93*, 267.

152. Kamat, P. V.; Patrick, B., *J. Phys. Chem* **1992**, *96*, 6829.

153. Özgür, Ü.; Alivov, Y. I.; Liu, C.; Teke, A.; Reshchikov, M. A.; Doğan, S.; Avrutin, V.; Cho, S.J.; Morkoç, H. *J. Appl. Phys*. **2005**, *98,* 041301.

154. Schoenhalz, A. L.; Arantes, J. T.; Fazzio, A.; Dalpian, G. M., *J. Phys. Chem. C* **2010**, *114,* 18293-18297.

155. Viswanatha, R.; Sapra, S.; Satpati, B.; Satyam, P. V.; Dev, B. N.; Sarma, D. D., *J. Mater. Chem.* **2004**, *14*, 661-668.

156. Triboulet, R.; Perriere, J., *Prog. Cryst. Growth Charact. Mater.* **2003**, *47,* 65.

157. Janisch, R.; Gopal,P.; Spaldin, N. A., *J. Phys. Condens. Matter* **2005**, *17*, R657.

158. Huang, M. H.; Mao, S.; Feick, H.; Yan, H.; Wu, Y.; Kind,H.; Weber, E.; Russo, R.; Yang, P., *Science* **2001**, *292*, 1897.

159. Huang, M. H.; Wu, Y.; Feick, H.; Tran, N.; Weber, E.; Yang, P., *Adv. Mater*. **2001**, *13*, 113.

160. Yao, B. D.; Chan, Y. F.; Wang., *Appl. Phys. Lett*. **2002**, *81*, 757.

161. Greene, L. E.; Law, M.; Tan, D. H.; Montano, M.; Goldberger, J.; Somorjai, G.; Yang, P., *Nano Lett*. **2005**, *5*, 1231.

162. Liu, C.; Zapien, J. A.; Yao, Y.; Meng, X.; Lee, C. S.; Fan, S.; Lifshitz, Y.; Lee, S. T., *Adv. Mater.* **2003**, *15*, 838.

163. Li, S. Y.; Lin, P.; Lee, C. Y.; Tseng, T. Y., *J. Appl. Phys.* **2004**, *95*, 3711.

164. Liu, B.; Zeng, H. C., *J. Am. Chem. Soc.* **2003**, *125*, 4430.

165. Guo, M.; Diao, P.; Cai, S., *J. Solid State Chem.* **2005**, *178*, 1864.

166. Park, W. I.; Jun, Y. H.; Jung, S. W.; Yi, G. C., *Appl. Phys. Lett.* **2003**, *82*, 964.

167. Hartanto, A. B.; Ning, X.; Nakata, Y.; Okada, T., *Appl. Phys. A* **2003**, *78*, 299.

168. Yu, W. D.; Li, X. M.; Gao, X. D., *Appl. Phys. Lett.* **2004**, *84*, 2658.

169. Dai, Y.; Zhang, Y.; Li, Q. K.; Nan, C. W., *Chem. Phys. Lett.* **2002**, *358*, 83.

170. Dai, Y.; Zhang, Y.; Wang, Z. L., *Solid State Commun.* **2003**, *126*, 629.

171. Roy, V. A. L.; Djurisˇic´, A. B.; Chan, W. K.; Gao, J.; Lui, H. F.; Surya, C., *Appl. Phys. Lett.* **2003**, *83*, 141.

172. Yan, H.; He, R.; Pham, J.; Yang, P., *Adv. Mater.* **2003**, *15*, 402.

173. Pan, Z. W.; Dai, Z. R.; Wang, Z. L., *Science* **2001**, *291*, 1947.

174. Yan, H.; Johnson, J.; Law, M.; He, R.; Knutsen, K.; McKinney, J. R.; Pham, J.; Saykally, R.; Yang, P., *Adv. Mater.* **2003**, *15*, 1907.

175. Li, Y. B.; Bando, Y.; Sato, T.; Kurashima, K., *Appl. Phys. Lett.* **2002**, *81*, 144.

176. Lao, J. Y.; Wen, J. G.; Ren, Z. F., *Nano Lett.* **2002**, *2*, 1287.

177. Lao, J. Y.; Huang, J. Y.; Wang, D. Z.; Ren, Z. F., *Nano Lett.* **2003**, *3*,235.

178. Xing, Y. J.; Xi, Z. H.; Zhang, X. D.; Song, J.H.; Wang, R. M.; Xu, J.; Xue, Z. Q.; Yu, D. P., *Solid State Commun.* **2004**, *129*, 671.

179. Park, J. H.; Choi, H. J.; Choi, Y. J.; Sohn, S. H.; Park, J. H., *J. Mater. Chem.* **2004**, *14*, 35.

180. Wang, Z. L.; Kong, X. Y.; Ding, Y.; Gao, P.; Hughes, W. L.; Yang, R.; Zhang, Y .,*Adv. Funct. Mater.* **2004**, *14*, 943.

181. Gao, P. X.; Wang, Z. L., *Appl. Phys. Lett.* **2004**, *84*, 2883.

182. Kong, X. Y.; Wang, Z. L., *Nano Lett.* **2003**, *3*, 1625.

183. Fan, Z. Y.; Lu, L. G., *J. Nanosci. Nanotechnol.* **2005**, *5*, 1561.

184. Yi, G. C.; Wang, C. R.; Park, W. I., *Semicond. Sci. Technol.* **2005**, *20*, S22.

185. Heo, Y. W.; Norton, D. P.;Tien, L. C.; Kwon, Y.; Kang, B. S.; Ren, F.; Pearton, S. J.; LaRoche, J. R., *Mater. Sci. Eng. R* **2004**, *47*, 1.

186. Grabowska, J.; Meaney, A.; Nanda, K. K.; Mosnier, J. P.; Henry, M. O.; DuclQre, J. R.; McGlynn, E., *Phys. Rev. B* **2005**, *71*, 115439.

187. Chen, S Y. Liu, C. Shao, R. Mu, Y. Lu, J. Zhang, D. Shen, X. Fan., *Adv. Mater.* **2005**, *17*, 586.

188. Hsu, H. C.; Hsieh, W. F., *Solid State Commun.* **2004**, *131*, 371.

189. Zhang, B. P.; Binh, N. T.; Segawa, Y.; Wakatsuki, K.; Usami, N., *Appl. Phys. Lett.* **2003**, *83*, 1635.

190. Djurisˇic´, A. B.; Choy, W. C. H.; Roy, V. A. L.; Leung, Y. H.; Kwong, C. Y.; Cheah, K. W.; Gundu Rao, T. K.; Chan, W. K.; Lui, H. F.; Surya, C., *Adv. Funct. Mater.* **2004**, *14*, 856.

191. Park, W. I.; Jun, Y. H.; Jung, S. W.; Yi, G. C., *Appl. Phys. Lett.* **2003**, *82*, 964.

192. Zhang, B. P.; Liu, C. Y.; Segawa, Y.; Kashiwaba, Y.; Haga, K., *Thin Solid Films* **2005**, *474*, 165.

193. Jie, J.; Wang, G.; Chen, Y.; Han, X.; Wang, Q.; Xu, B.; Hou, J. G., *Appl. Phys. Lett.* **2005**, *86*, 031909.

194. Suh, H. W.; Kim, G. Y.; Jung, Y. S.; Choi, W. K.; Byun, D., *J. Appl. Phys.* **2005**, *97*, 044305.

195. Kwok, W. K.; Djurisˇic´, A. B.; Leung, Y. H.; Chan, W. K.; Phillips, D. P.; Chen, H. Y.; Wu, C. L.; Gwo, S.; Xie, M. H., *Chem. Phys. Lett.* **2005**, *412*, 141.

196. Tong, Y. H.; Liu, Y. C.; Lu, S. X.; Dong, L.; Chen, S. J.; Xiao, Z. Y., *J. Sol-Gel Sci. Technol.* **2004**, *30*, 157.

197. Ozaki, S.; Tsuchiya, T.; Inokuchi, Y.; Adachi, S., *Phys. Stat. Sol. A* **2005**, *202*, 1325.

198. Zhang, Z. H.; Liu, Y. C.; Wang, X. H.; Chen, S. J.; Wang, G. R.; Zhang, J. Y.; Lu, Y. M.; Shen, D. Z.; Fan, X. W., *J. Phys. Condens. Matter* **2005**, *17*, 3035.

199. Hsu, H. C.; Hsieh, W. F., *Solid State Commun.* **2004**, *131*, 371.

200. Greene, L. E.; Law, M.; Goldberger, J.; Kim, F.; Johnson, J. C.; Zhang, Y.; Saykally, R. J.; Yang, P., *Angew. Chem.* **2003**, *115*, 3030.

201. Meng, X. Q.; Shen, D. Z.; Zhang, J. Y.; Zhao, D. X.; Lu, Y. M.; Dong, L.; Zhang, Z.; Liu, Y. C.; Fan, X. W.; *Solid State Commun.* **2005**, *135*, 179.

202. Chen, Y. Q.; Jiang, J.; He, Z. Y.; Su, Y.; Cai, D.; Chen, L., *Mater. Lett.* **2005**, *59*, 3280.

203. Das, D.; Mondal, P., *RSC Adv.* **2014,** *4,* 35735-35743.

204. McCluskey, M. D.; Jokela, S. J., *J. Appl. Phys*., **2009**, *106*, 071101.

205. Li, L. P.; Qiu, X. Q.; Li, G. S., *Appl. Phys. Lett*., **2005**, *87*, 124101.

206. Wu, X. L.; Siu, G. G.; Fu, C. L.; Ong, H. C., *Appl. Phys. Lett*. **2001**, *78*, 2285–2287.

207. Djuriˇsi´c, A. B.; Leung, Y. H.; Tam, K. H.; Hsu, Y. H.; Ding, L.; Ge, W. K.; Zhong, Y. C.; Wong, K. S.; Chan, W. K.; Tam, H. L.; Cheah, K. W.; Kwok, W. M.; Phillips, D. L., *Nanotechnology*, **2007**, *18*, 095702.

208. Qiu, J. J.; Li, X. M.; He, W. Z.; Park, S. J.; Kim, H. K.; Hwang, Y. H.; Lee, J. L.; Kim, Y. D., *Nanotechnology*, **2009**, *20*, 155603.

209. Liu, J. P.; Xu, C. X.; Zhu, G. P.; Li, X.; Cui, Y. P.; Yang, Y.; Sun, X. W., *J. Phys. D: Appl. Phys*., **2007**, *40*, 1906–1909.

210. Zhou, H.; Alves, H.; Hoffmann, D. K.; Kriegseis, W.; Meyer, B. K.; Kaczmaczyk, G.; Hoffmann, A., *Appl. Phys. Lett.,* **2002**, *80*, 210–212.

211. Sharma, A.; Singh, B. P.; Dhar, S.; Gondorf, A.; Spasova, M., *Surf. Sci*. **2012**, *606*, L13–L17.

212. Patra, M. K.; Manzoor, K.; Manoth, M.; Vadera, S. R.; Kumar, N., *J. Lumin*. **2008,** *128,* 267–272.

213. Shi, S.; Xu, J.; Zhang, X.; Li, L., *J. Appl. Phys.* **2011**, *109*, 103508.

214. Zeng, H. B.; Duan, G. T.; Li, Y.; Yang, S. K.; Xu, X. X.; Cai, W. P., *Adv. Funct. Mater.* **2010**, *20*, 561–572.

215. Look, D. C.; Hemsky, J. W.; Sizelove, J. R., *Phys. Rev. Lett.* **1999**, *82*, 2552–2554.

216. Travnikov, V. V.; Freiberg, A.; Savikhin, S. F., *J. Lumin.* **1990**, *47*, 107–112.

217. Anpo, M.; Kubokawa, Y., *J. Phys. Chem*. **1984**, *88*, 5556–5560.

218. Schoenmakers, G. H.; Vanmaekelbergh, D.; Kelly, J. J., *J. Phys. Chem*. **1996**, *100*, 3215–3220.

219. Van, A.; Dijken,; Meulenkamp, E. A.; Vanmaekelbergh, D.; Meijerink, A., *J. Phys. Chem. B* **2000**, *104*, 1715–1723.

220. Zhang, L.; Longwei, Y.; Wang, C.; Lun, N.; Qi, Y.; Xiang, D., *J. Phys. Chem. C* **2010**, *114*, 9651–9658.

221. Ahn, C. H.; Kim, Y. Y.; Kim, D. C.; Mohanta, S. K.; Cho, H. K., *J. Appl. Phys.* **2009**, *105*, 013502.

222. Abdullah, M.; Lenggoro, I. W.; Okuyama, K.; Frank, G. S., *J. Phys. Chem. B* **2003**, *107*, 1957–1961.

223. Monticone, S.; Tufeu, R.; Kanaev, A. V., *J. Phys. Chem. B* **1998**, *102*, 2854–2862.

224. Han, L. L.; Cui, L.; Wang, W. H.; Wang, J. L.; Du, X. W., *Semicond. Sci. Technol*. **2012**, *27*, 065020.

225. Qin, W. J.; Sun, J.; Yang, J.; Du, X. W., *Mater. Chem. Phys.* **2011**, *130*, 425–430.

226. Joshi, A. G.; Sahai, S.; Gandhi, N.; Radha Krishna, Y. G.; Haranath, D., *Appl. Phys. Lett.* **2010**, *96*, 123102.

227. Tay, C. B.; Chua, S. J.; Loh, K. P., *J. Cryst. Growth* **2009**, *311*, 1278–1284.

228. Cao, B.; Cai, W.; Zeng, H., *Appl. Phys. Lett*. **2006**, *88,* 161101.

229. Sun, Y. M.; Ph.D. thesis, *University of Science and Technology of China*, **2000**.

230. Willander, M.; Nur, O.; Sadaf, J. R.; Qadir, M. I.; Zaman, S.; Zainelabdin, A.; Bano, N.; Hussain, I., *Materials* **2010**, *3*, 2643–2667.

231. C. Giansante, I. Infante, E. Fabiano, R. Grisorio, G. P. Suranna and G. Gigli, *J. Am. Chem. Soc*., **2015**, *137*, 1875-1886.

Chapter 2

Synthesis, Characterization and Photocatalytic Water Splitting Activity of ZnO-azonaphthol Composites

2.1. Introduction

To effectively utilise the concept of surface modulation of semiconductor nanoparticles with short conjugated organic linkers, it is imperative to understand the electron transfer mechanisms between them. The structure and electronic properties of the organic moiety become pivotal in deciding the efficiency of such phenomena. Here, the broad absorption properties extending from UV to visible spectral range and ease of synthesis of azonaphthols make them highly attractive. Hence in this chapter, we have selected two simple azo compounds with different π delocalization properties for grafting on ZnO nanoparticles of size ~ 3-5 nm in an attempt to throw light on the effect of conjugation on the electron transfer process. Such conducive absorption features of the organic ligands create appropriate donor bands to ZnO, which is otherwise inactive for visible light photocatalytic water splitting [1-7]. The azo compound is designed such that one end contains a carboxylic acid group which can bind to the surface hydroxyl groups on ZnO surface effecting better interfacial interactions and the other end with beta substituted naphthol moiety ensuring dispersion in aqueous solvents [8-13]. The position of carboxylate functionality in the phenyl group is changed from meta- to para- to achieve the variation in extended conjugation in the organic moiety. Azonaphthols can be synthesised by simple reactions like diazotisation followed by coupling with a suitable coupling agent.

The azobenzene chromophore has been studied for over 70 years, yet it continues to present new and unique optical effects. Azobenzenes can be classified into three spectroscopic classes based on the absorption spectrum : azobenzene-type molecules, aminoazobenzene-type molecules and pseudo-stilbenes. Azobenzene is one of the functional groups that exhibit a range of thermal, chemical, photochemical and biological properties and each of these properties form the basis for a distinct class of functional molecules in the vast world of chemistry. The azobenzene class of chromophores is characterized by the azo linkage (–N=N–) that bridges two phenyl rings which may be further functionalised. The presence of a double bond generally has profound consequences on the stereochemistry; it gives the molecule more rigidity and restricts the number of possible forms. The strong electronic absorption band of the azobenzene molecules can be tailored by ring substitution to fall anywhere from the ultraviolet to

visible regions, allowing chemical fine-tuning of color. Among the azobenzene class of chromophores, carboxyl substituted azobenzene plays a very important role in complexation with various metal oxides, particularly ZnO. The conjugation in these structures can be extended by various coupling agents like naphthols (α-naphthol or β-naphthol). This extended aromatic structure gives rise to azobenzenes' tunable optical absorption and emission properties. Due to their clean photochemistry, and efficient photochemical isomerization that can occur in the azo linkage when the chromophore absorbs a photon, they have been investigated as an active component for a variety of applications like non-linear optical devices, optical switches and so on. The two photoisomerization states in azobenzene are *trans* and meta-stable *cis* configurations. The cis form is termed as Z isomer and the trans as E isomer. Azobenzene can be converted from the *trans* to the *cis* state photochemically, and will revert back to the stable *trans* state thermally. The spectra of trans and cis azobenzene are distinct but overlapping. Trans azobenzene shows a weak n-π* band and a strong π-π* transition. Cis azobenzene also has a stronger n-π* band and shorter π-π* bands. The trans conformation is near planar and has a dipole moment near zero. The lifetime of these photoisomerized states depends on the azo group's substitution pattern. For azobenzene molecules, change of electron transport properties could take place due to their specific response to the change of molecular conformation or orientation, chemical reactions and tautomerization [14,15].

The work described in this chapter focuses on understanding the electron transfer mechanisms and the photocatalytic water splitting activities of the grafted ZnO nanoparticles by conjugated (para substituted) and non-conjugated (meta substituted) azo-naphthols. In the present study, the coupling agent used is β-naphthol. Distinct differences in photostability and photophysical properties are observed for the organic molecules when they form composites with ZnO. This variation is understood based on electron transfer mechanisms using absorption, emission and time resolved photoluminescence studies. Electrochemical studies are attempted to see the effective electron transfer between ZnO and the organic moiety under illumination. The experimental observations are also corroborated with the computational studies.

2.2. Experimental Section

2.2.1. Synthesis

2.2.1.1. ZnO nanoparticles (ZnO NPs)

In a typical procedure, KOH (56 mM, 75 mL) in methanol was refluxed at 60 °C for 30 min. In another reaction mixture, $Zn(OAc)_2.2H_2O$ (56 mM, 25 mL) in methanol was prepared by stirring at room temperature. The dissolved solution of zinc acetate was then added drop wise through an addition funnel into the refluxing KOH solution maintained at 60 °C with vigorous stirring. The formation of ZnO NPs started immediately and the solution becomes clear (particle size range 8-10 nm from TEM studies explained later). The same procedure is used for the ZnO NPs synthesis presented in all the chapters.

2.2.1.2. 3-(2-Hydroxy-naphthalen-1-ylazo) benzoic acid (3ABBN) and 4-((2-hydroxynaphthalen-1-yl)diazenyl) benzoic acid (4ABBN)

The azo compounds are synthesised by diazotization and coupling reactions (Scheme 2.1).

Scheme 2.1. Synthesis of azonaphthols by diazotization and coupling reactions

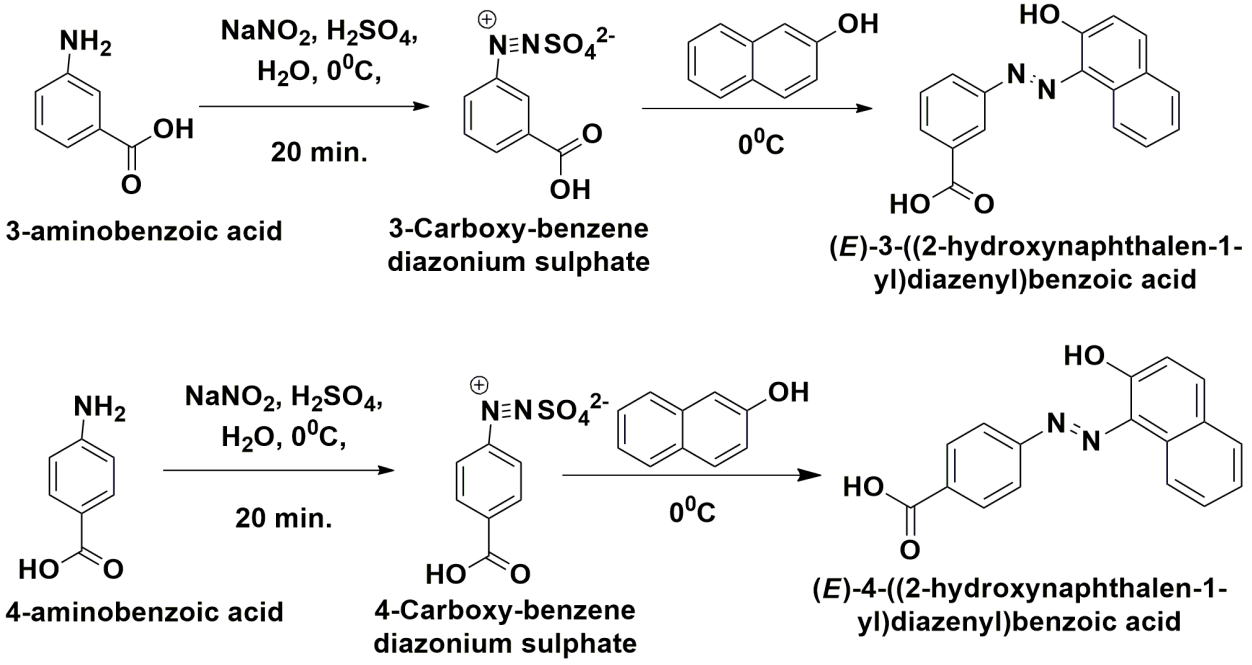

In a typical synthesis, to a solution of amino benzoic acids (3-aminobenzoic acid or 4-aminobenzoic acid;1.35g, 9.843 mmoles), distilled water (8.44 mL) and concentrated H_2SO_4 (2.1 mL) was added drop wise. The mixture was cooled to 0 °C. A solution of sodium nitrite (1.006 g, 14.58 mmoles) in 3 mL of distilled water maintained at 0 °C, was added to the above cold mixture drop wise with good stirring. After 20 min, the diazotization was complete, which was verified by adding a solution of 4-(N,N-dimethylamine) benzaldehyde which would generate colour if undiazotized aromatic amine is still present. To the diazotized product obtained, β-naphthol (2.012 g, 13.95 mmoles) was added very slowly with vigorous stirring over 15 min. The reaction mixture was further stirred for 1 h and left to stand overnight. A reddish orange coloured precipitate of (2-Hydroxy-naphthalen-1-ylazo)-benzoic acid (4ABBN and 3ABBN) was observed which was purified by column chromatography (5% pet ether and ethyl acetate).

2.2.1.3. ZnO-azonaphthol composites

Concentration of the dye was selected based on full surface coverage of a 8 nm spherical particle assuming a bridge type of chelation so that each dye molecule is bonded to two Zn atoms on the surface of the NP. Hence a concentration ratio of surface Zn:dye as 1:0.5 is arrived at corresponding to total concentration ratio of 1.69×10^{-3} ZnO: 9.04×10^{-4} dye (details of the calculation is given in Appendix 2). The same calculation is used for the composites synthesis presented in all the chapters. In a typical synthesis, 4ABBN or 3ABBN (23 μmol) was added in-situ during the synthesis of ZnO to the alkaline zinc acetate solution (0.142 mmol). The solution was stirred in methanol at 25 °C for 1 h. The products (ZnO-3ABBN and ZnO-4ABBN composites) were washed with methanol, centrifuged and collected.

2.2.2. Instruments for Characterization

The principles and instrumentation of all the techniques used throughout the work for structural and photophysical characterizations are briefly discussed in Appendix 1. Specification of the instruments used for these characterizations is described below. Powder X-ray diffraction (PXRD) of all the samples was carried out in a PANalytical X'pert Pro dual goniometer diffractometer working under 40 kV and 30 mA at room temperature.

The radiation used was Cu Kα (1.5418 Å) with a Ni filter and the data collection was carried out using a flat holder in Bragg–Brentano geometry with a 1° slit at the source and receiving sides. A X'celerator solid-state detector with a scan speed of 0.012° min^{-1} was employed.

FEI Tecnai T-20 electron microscope, operating at 200 kV, with an information resolution limit of 0.15 nm respectively were used for transmission electron microscopy (TEM) sample observations. Samples were dispersed in methanol under sonication before drop casting on the grid. Samples for TEM were prepared by evaporating a droplet of solution onto a carbon-coated copper mesh 200 grid.

Zeta potential measurement was performed on a 90 Plus particle size analyzer (Brookhaven Instruments, USA). Infra red spectra were recorded using a Bruker FTIR (ATR mode) in the 4000–400 cm^{-1} range. Raman spectra were recorded on a HORIBA Jobin Yvon LabRAM HR 800 spectrometer excited with 633 nm lasers.

The photophysical characterizations were mainly done using absorption and photoluminescence spectroscopies. UV-vis absorption spectra were recorded using an Agilent Cary 5000 series UV-vis-NIR spectrophotometer and the measurements were carried out using a quartz cell of 10 mm path length (volume 3.5 mL) and methanol is used as solvent. Steady-state fluorescence measurements were performed using a Photon Technology International fluorescence spectrophotometer (PTI) with a quartz cell of 10 mm path length (volume 3.5 mL). The emission as well as excitation band width was maintained at 2 nm throughout the experiments.

Bruker 200- 400- and 500 MHz NMR spectrophotometers were used for recording ^{1}H and ^{13}C NMR spectra of organic linkers in DMSO containing small amounts of tetramethylsilane (TMS) as an internal standard. Samples for ^{1}H NMR measurements have been prepared by dissolving 10-15 mg of sample in a 5mm diameter NMR tube using a suitable deuterated solvent. 50 to 100 mg of sample was used for ^{13}C NMR experiments. The chemical shifts for the solvent peak is found at 2.5 ppm (^{1}H, DMSO-d6) and 39.9 ppm (^{13}C, DMSO-d6). The purity of the compounds was determined by elemental analysis done on Thermofinnigan Flash EA 1112 series CHNS analyzer.

Time resolved fluorescence lifetime measurements were performed using a HORIBA Jobin Yvon Fluorolog 3 fluorescence spectrophotometer. For lifetime measurements, decay curves were obtained by the time-correlated single-photon counting (TCSPC) technique using a HORIBA Jobin Yvon Nano-LED source with wavelengths 260 and 320 nm. Decay measurements were carried out at excitonic emission of 325 nm and defect emission of 520 nm. All experiments were performed under identical conditions. Fluorescence lifetime values were determined by deconvoluting the data with exponential decay using DAS6 decay analysis software. The quality of fit (monoexponential, biexponential or triexponential) was judged by fitting parameters such as $\chi 2$, as well as the visual inspection of the residuals.

Biologic electrochemical workstation (SP-300) was used for all the electrochemical measurements (cyclic voltammetry and linear sweep voltammetry) with a three-electrode set-up (working, reference and counter electrodes). ZnO-dye composite coated on glassy carbon of area 0.0706 cm^2 was used as the working electrode. The catalyst ink was prepared by ultrasonically dispersing 5 mg of the catalyst in 1 ml of methanol. 10 µl of the catalyst slurry was drop casted on the glassy carbon working electrode and dried under an IR lamp for electrochemical analysis. Pt reference electrode and graphite rod as a counter electrode were used for the electrochemical measurements using a scan rate of 50 mV/s. The supporting electrolyte was $LiClO_4$ dissolved in acetonitrile. A three-electrode photoelectrochemical cell inserted inside a black box consisting of 200W tungsten lamp by front-side illumination was designed for performing the CV experiments. During the actual CV measurement, the potential of the electrode is ramped linearly versus time. A schematic representation of photoelectrochemical set up for photocurrent measurement is given below (Figure 2.1). The linear sweep voltammetry (LSV) were carried out at a scan rate of 10 mV/s in an acetonitrile solution containing $LiClO_4$ as supporting electrolyte. Bio-Logic VMP-3 instrument was used for the electrochemical impedance analysis (EIS) of the samples. A frequency range of 200 KHz to 100 mHz was applied against the open circuit potential with sinus amplitude of 10 mV.

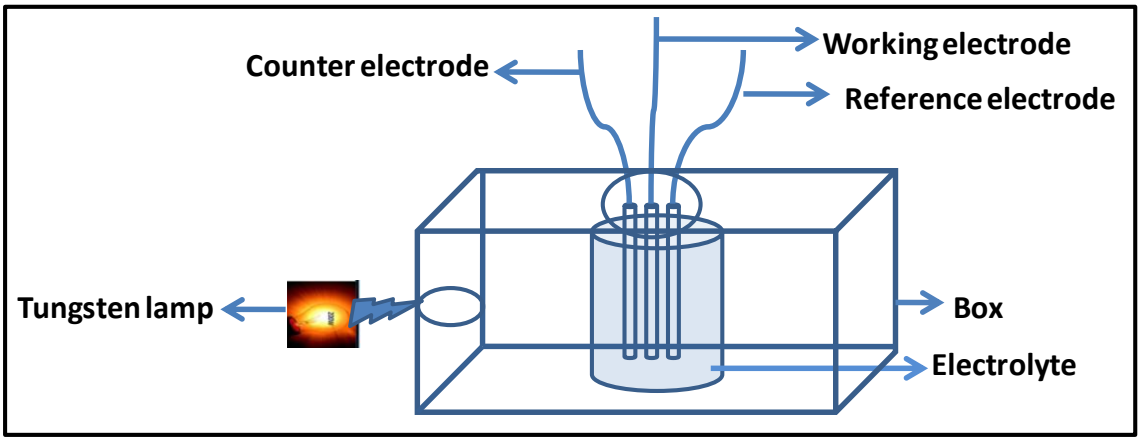

Figure 2.1. Photoelectrochemical set up for the comparison of photocurrent with potential.

The photocatalytic water splitting was performed under static conditions in a gas closed irradiation cell made of quartz of 70 mL capacity. A schematic representation of reactor set up for photocatalytic water splitting is given below (Figure 2.2). Typically, 0.025 g of the catalyst was dispersed in varying volumes of methanol in water by means of a magnetic stirrer. The UV and visible light sources were 400 W low and high pressure mercury lamps covered with water circulating pyrex jackets. The direct sunlight experiments were also performed using the same gas closed irradiation cell placed on the terrace with full exposure throughout the day and the optimized conditions were followed. Here, the quartz reactor was placed inside a beaker containing crushed ice mixed with water as a coolant, which was periodically changed. $NaNO_2$ chemical filter was used in control experiments to rule out presence of UV light while using high pressure Hg lamp. The amount of H_2 evolved was determined using gas chromatography (Agilent 7890 GC with Carbosphere column and N_2 as carrier gas) with thermal conductivity detector (TCD). The program used in GC for all the analysis involved the detector temperature of 200 °C and oven temperature of 80 °C at the time of injection. The makeup flow of N_2 is 5 mL/min. The reaction was carried out for 4 h for optimization of reaction conditions. Time study was carried out by irradiating the photocatalytic quartz reactor in 1 h intervals for 8 h. The evolved gas mixture from the headspace was taken in a syringe and injected into the GC. The reactor set up for photocatalytic water splitting is given in Figure 2.3.

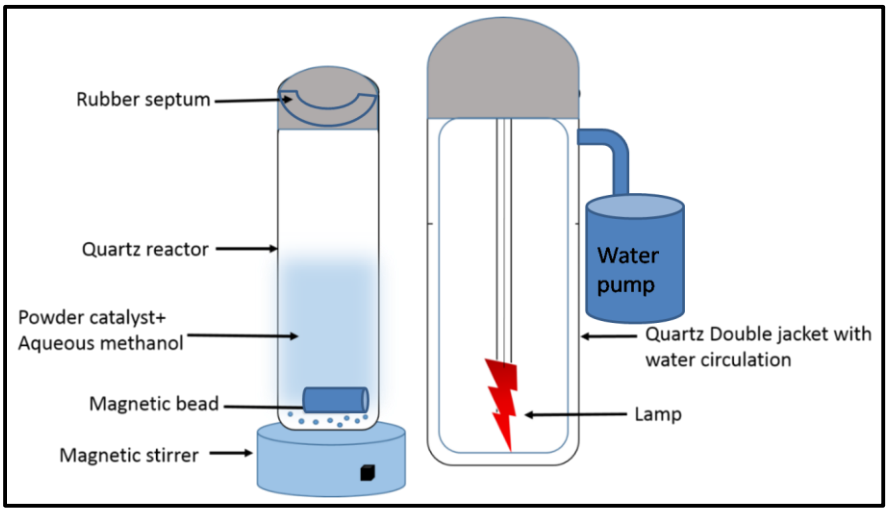

Figure 2.2. Scheme of the photocatalytic water splitting reactor set up.

Figure 2.3. Reactor set up for photocatalytic water splitting which consists of a quartz cell having 70 ml capacity and it is gas closed by means of rubber septum. The light sources are inside the quartz jackets where cold water circulates continuously.

2.2.3. Computational Studies

Theoretical calculations with DFT for the ZnO NPs and the dye molecule (4ABBN) are briefly discussed in Appendix 3.

2.3. Results and Discussion

2.3.1. Characterization of ZnO NPs

The powder X-ray diffraction pattern of the synthesized ZnO NPs shows 2θ values and relative intensities of the peaks that coincide with the JCPDS No. 36:1451. XRD studies ascertained the formation of ZnO in wurtzite phase in the ZnO NPs prepared by controlled precipitation of methanolic KOH at 0 °C (Figure 2.4).

ZnO NPs formed by controlled precipitation are observed to be of spherical morphology with fairly uniform size of 10±2 nm. On the basis of TEM images the size distribution of the nanoparticles are calculated and showed as an inset (Figure 2.4). The zeta potential measurement of ZnO nanoparticles show that the isoelectric point was + 4.83 mV.

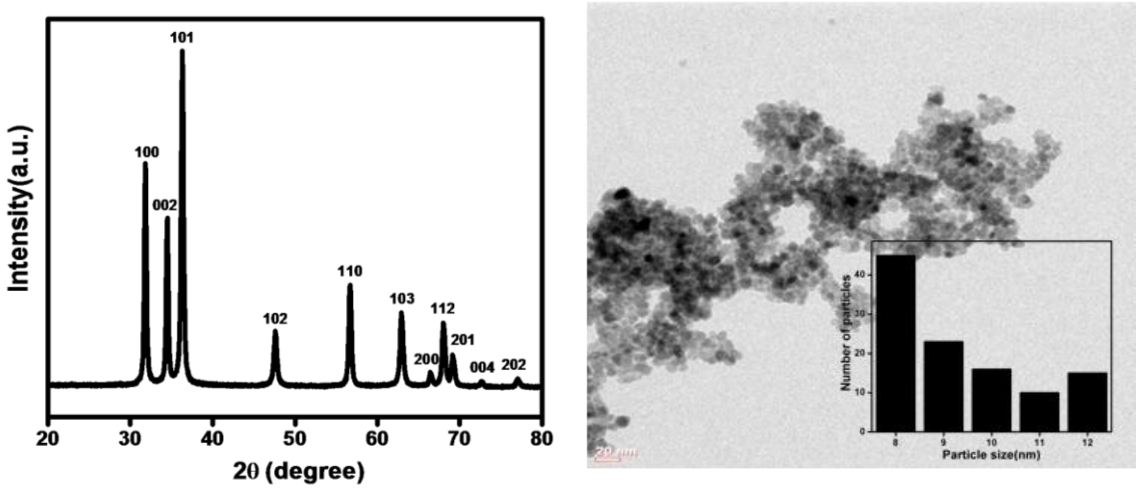

Figure 2.4. XRD pattern of ZnO NPs (left) and TEM images of bare ZnO NPs by precipitation method with histogram (right).

In the IR spectrum of the pure ZnO NPs, a broad peak at 3370 cm^{-1} indicates the presence of –OH which could be surface adsorption of moisture. The analysis of the ZnO nanoparticles show characteristic bands at 1572, 1118 and 977 cm^{-1}, which are attributed to the vibrations of ZnO (Figure 2.5). The Raman spectrum was measured at 630 nm excitation

laser pulse and shows peaks at 434,496,608,708, and 837 cm^{-1}. The peak at 434 cm^{-1} corresponds to the E_2 phonon mode (Figure 2.5).

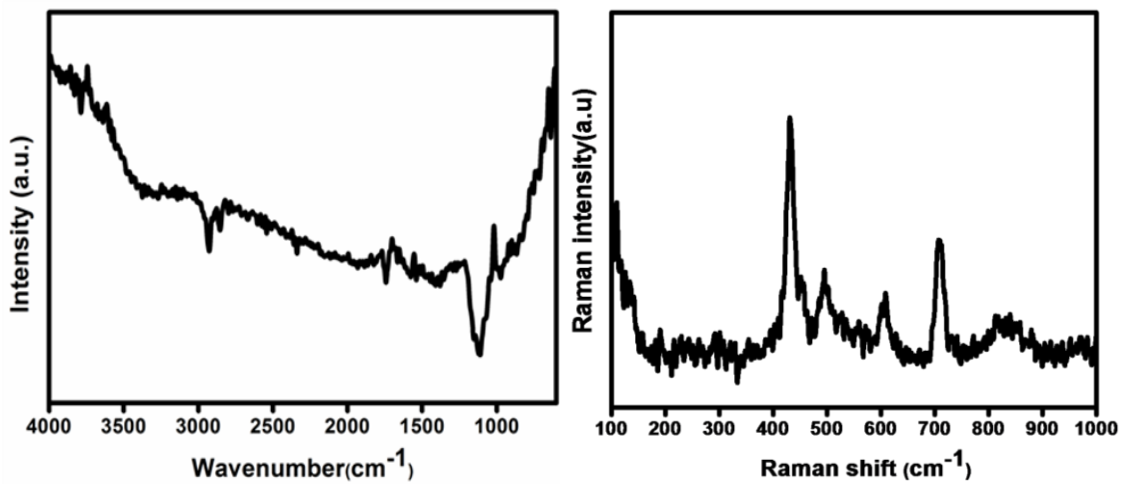

Figure 2.5. IR spectra of ZnO NPs (left) and Raman spectra of ZnO NPs (right).

UV-visible spectra of pristine ZnO NPs by precipitation method display slight variations as expected with decrease in particle size. The absorption onset shifted to 346 nm as calculated from the band gap obtained from the absorption spectra as the particle size is decreased (Figure 2.6). The surface to volume ratio in the ZnO nanoparticles is very high, so a substantial increase in surface defects can be expected in such materials, even though bulk recombination sites are minimised. These surface defects greatly influence the luminescence properties of ZnO nanoparticles and these characteristics of ZnO have been reported as a function of the excitation wavelength and particle size. The ZnO nanoparticles have various luminescence transitions dependent on varying structures and surface properties. Generally, the luminescence spectrum of ZnO nanoparticles exhibits a narrow exciton emission band in the UV region and a broad defect emission band extending from 500 to 650 nm. The size quantization of ZnO NPs can change the spectral positions of the defect and exciton emissions. For the ZnO NPs in this study, a weak emission at 360 nm and a strong wide band emission from 540-550 nm were observed at 325 nm excitation wavelength. The corresponding weak UV band-edge emission at 360 nm is due to the recombination of free excitons and the broad green emission band at ~550 nm is due to trap levels on the surface of pristine ZnO (Figure 2.6).

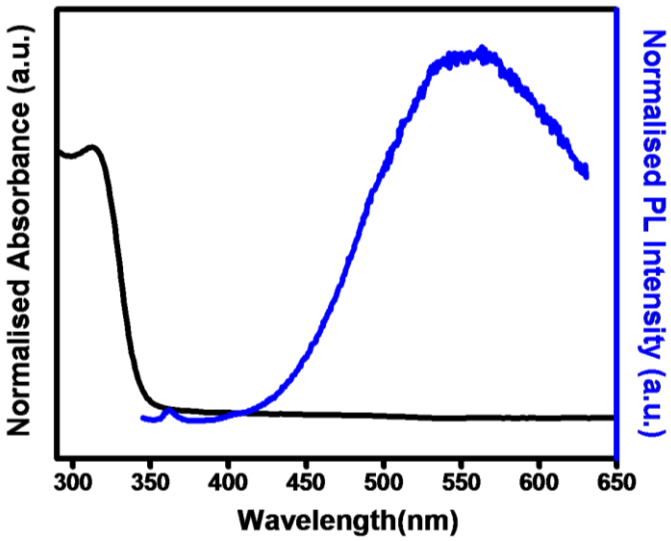

Figure 2.6. UV-Vis spectra of ZnO NPs (black) and Photoluminescence spectrum at λexc= 325 nm of pristine ZnO NPs (blue).

2.3.2. Characterization of Azonaphthols: 3-((2-hydroxynaphthalen-1-yl)diazenyl) benzoic acid (3ABBN) and 4-((2-hydroxynaphthalen-1-yl)diazenyl) benzoic acid (4ABBN)

Elemental analysis was carried out for purity confirmation of 3ABBN and 4ABBN and the experimental CHN values were almost matching with the calculated values.

3ABBN calcd(%): C 69.86, H 4.14, N 9.18; found (%): C 72.21, H 5.48, N 7.96.
4ABBN calcd(%): C 69.86, H 4.14, N 9.18; found (%): C 72.24, H 5.46, N 7.99.

The structure of azonaphthols was confirmed by ^{1}H NMR, ^{13}C and DEPT. ^{1}H NMR spectrum for 3ABBN is as follows: 6.98 ppm (multiplet, -CH aromatic proton near to the hydroxyl group attached carbon of the naphthalene ring), 7.03-7.53 ppm (multiplet, -CH aromatic protons attached to the unsubstituted naphthalene ring), 7.68 ppm (multiplet, -CH aromatic proton meta to the the –N=N linkage connected to the benzene ring), 7.79-7.86 ppm (multiplet, -CH aromatic protons of the substituted naphthalene ring), 7.97-8.02 ppm

(doublet, -CH aromatic protons near to the quarternary carbon in the naphthalene ring), 8.27 ppm (singlet, aromatic proton in the benzene ring (between –C-N=N and –C-COOH linkages)), 8.58-8.62 ppm (doublet, -CH aromatic protons connected near to the –N=N and carboxyl group of the benzene ring) and 15.96 ppm (singlet, carboxyl hydroxyl proton in the azobenzene ring). The spectra are given in appendix 4 (Figure 1).

^{1}H NMR (400 MHz, DMSO-d_6) δ ppm:

6.98 (1H, m), 7.03-7.53 (2H, m), 7.68 (1H, m), 7.79-7.86 (1H, m),7.97-8.02 (2H, d, J=9.47 Hz), 8.27(1H, s), 8.58-8.62(2H, d, J=7.96Hz), 15.91 (1H, s)

^{13}C (100 MHz, DMSO-d_6) δ ppm:

170.25,166.93,145.26,140.70,132.85,130.26,129.40,129.14,128.30,128.10,126.25,126.10,124.28,122.95,121.42,119.16.

NMR spectrum analysis for 4ABBN is as follows: 6.78-6.83 ppm (multiplet, -CH aromatic proton attached ortho to the hydroxyl group of the naphthalene ring), 7.48-7.63 ppm (multiplet, -CH aromatic protons attached to the unsubstituted naphthalene ring), 7.72ppm (multiplet, -CH aromatic proton of the substituted naphthalene ring), 7.83-7.87 (doublet) and 7.92-7.97 ppm (doublet, -CH aromatic protons near to the quaternary carbon in the naphthalene ring), 8.03-8.07 ppm (doublet, aromatic protons attached ortho to the N=N linkage connected to the benzene ring), 8.46-8.50 ppm (doublet, -CH aromatic protons attached ortho to the carboxyl group connected carbon substituted in the azobenzene ring) and 15.91 ppm (singlet, carboxyl hydroxyl proton in the azobenzene ring). The spectra are given in appendix 4 (Figure 2).

^{1}H NMR (400 MHz, DMSO-d_6) δ ppm:

6.78-6.83 (1H, m), 7.48-7.63 (2H, m), 7.72 (1H, m),7.83-7.87(2H, d, J=8.59 Hz), 7.92-7.97(1H, d, J=9.85 Hz), 8.03-8.07(2H, d, J=8.72Hz), 8.46-8.50 (1H,d, J=7.32Hz), 15.91 (1H, s).

^{13}C (100MHz, DMSO-d_6) δ ppm :

170.07,167.14,145.61,140.53,133.19,132.98,130.07,129.24,129.04,128.53,128.28,126.17,124.15, 122.76, 121.59,119.56.

2.3.2.1. Spectroscopic studies

The experimentally observed FTIR band for 3ABBN at 3420 cm^{-1} (strong and sharp) corresponds to the alcohol hydroxyl bond. The FTIR peaks of O-H bond in acids are observed at 3052 and 2921 cm^{-1}, which are medium stretching vibrations. The frequencies of C=O stretching vibration present in carboxylic acids normally appear at 1693 cm^{-1}. The vibrational bands appearing at 1386 and 1328 cm^{-1} of medium intensities correspond to the N=N and C-O stretching vibrations of meta substituted carboxylic acids in azo based compounds. Alcohol C-O stretching vibrational frequencies is observed at 1207and 1111 $cm^{-1.}$ A strong vibrational band at 986 cm^{-1} is attributed to the C-H bending of phenyl ring which shows the presence of an aromatic framework in the molecule (Figure 2.7).

For 4ABBN, the IR spectral bands appeared at 3353, 2973, 2894, 1696, 1389, 1319, 1207, 1044 and 879 cm^{-1}. The infra-red peaks at 2973 and 2894 cm^{-1} are the stretching vibrations of O-H bond in acids. The absorption peak at 1696 cm^{-1} is the C=O stretching vibration present in carboxylic acids. The experimentally observed vibrational bands appearing at 1389 and 1319 cm^{-1} of medium intensities in the FTIR spectra correspond to the N=N and C-O stretching vibrations. 1207 and 1044 cm^{-1} bands are observed with alcohol C-O stretching vibrational frequencies. The vibrational band at 879 cm^{-1} is attributed to the C-H bending of phenyl ring which indicates the presence of an aromatic skeleton in 4ABBN (Figure 2.7) [16,17].

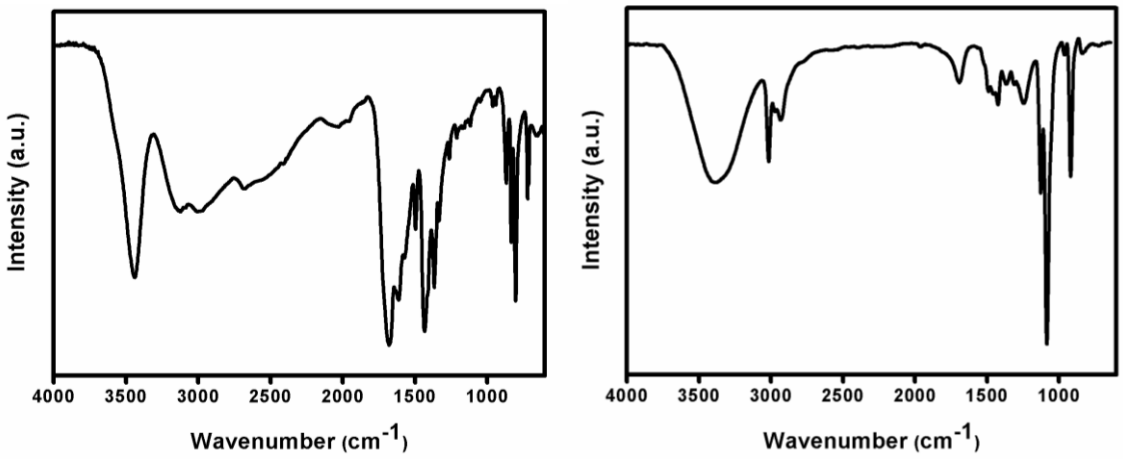

Figure 2.7. IR spectrum of 3ABBN (left) and 4ABBN (right).

From the figures, it is clear that the most intense Raman fundamentals of 3ABBN appear at 432, 711, 1658, 1699, 1768 cm^{-1} and 4ABBN at 432, 710, 1658, 1700, 1769 cm^{-1} followed by a few weak modes at 496, 607, 1266, 1387 cm^{-1} (3ABBN) and 498, 604, 1255, 1382 cm^{-1} (4ABBN) (Figure 2.8).

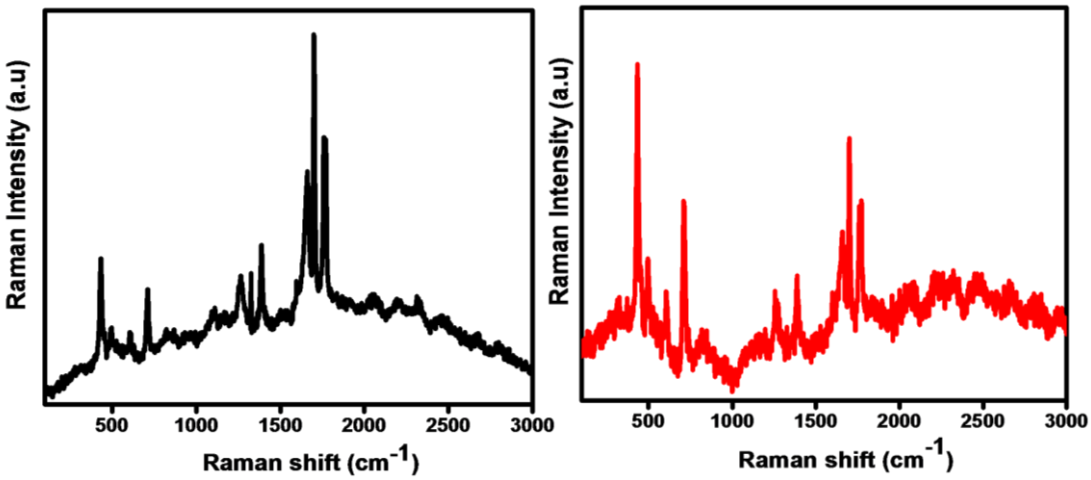

Figure 2.8. Raman spectrum of 3ABBN (left) and (b) 4ABBN (right).

UV-vis spectrum of 3ABBN ($9.04x10^{-4}$ M) shows absorption bands at 310 and 480 nm and small shoulder bands around 415 nm and 510 nm. 4ABBN also shows similar absorption features (305, 410, 480 and 505 nm), typical of coloured azo dyes comprising of several π-π* and n-π* absorption bands (Figure 2.9).

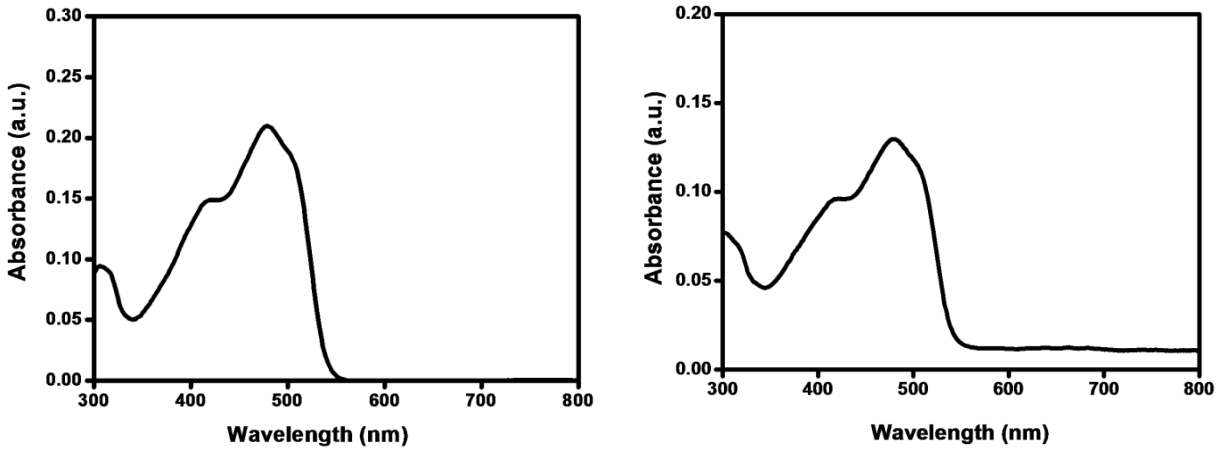

Figure 2.9. UV-Vis spectrum of 3ABBN (left) and 4ABBN (right).

Emission characteristics of azobenzenes are extensively studied and absorption spectra of simple azobenzenes consist of S2 ← S0 (ππ*) and S1 ← S0 (nπ*) transitions in UV and visible regions respectively. For these systems, nπ* transitions are forbidden in the ground *trans* state while it becomes allowed due to photoisomerisation. It is also widely accepted that simple azobenzenes are not fluorescent due to this photoisomerisation. Photoisomerisation can happen in azobenzenes only in excited state efficiently. This causes a change in the direction of the lone pair of one nitrogen atom. However, in more complex azo compounds like azonaphthols, additional phenomena like hydrogen bond, tautomerism and other structural features restricting rotation along N=N or N=N-C bonds come into play and may have different implications on the optical and electronic properties. It is suggested that phenyl azo naphthols exist as azo and hydrazone forms and the equilibrium concentration of each is determined by structure stabilising electronic factors. Only hydrazone tautomer is fluorescent and any factors stabilising hydrazone tautomer brings about fluorescence in this otherwise non-emissive system. The position and the nature of the substituent in the ring is a key factor here and electron withdrawing groups are understood to stabilise the hydrazone form. Extended conjugation and consequent molecular planarity also stabilises the hydrazone form. In 3ABBN, azo tautomeric form is major, hence the system is non-fluorescent as expected. Referring to Figure 2.10, displaying the resonance structures of the two dyes, the stability of an azo molecule is ascertained by the extent of charge on C* adjacent to the –N=N- group. It is clear that hydrazone form in 3ABBN is not stabilised, whereas for 4ABBN, extended conjugation facilitates charge in C* stabilising the hydrazone form. Hence an intense emission peak at ~360 nm can be observed for this compound at 310 nm excitation wavelength unlike in the case of 3ABBN (Figure 2.11). The excited azo form undergoes an excited state intramolecular proton transfer to the excited state hydrazone form manifesting in abnormal Stokes shift (describes the difference in wavelength between the maximum of the excitation spectrum (shorter wavelength, higher energy) and the maximum of the emission spectrum (longer wavelength, lower energy). However, we do not observe such abnormal Stokes shift (observed value is ~50 nm) indicating that probably, most of the 4ABBN exist in hydrazone form (Figure 2.12) [18-26].

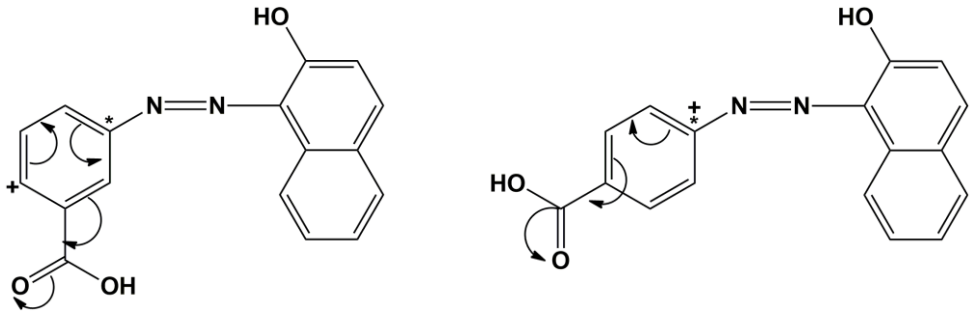

Figure 2.10. Resonance structures of 3ABBN (left) and 4ABBN (right).

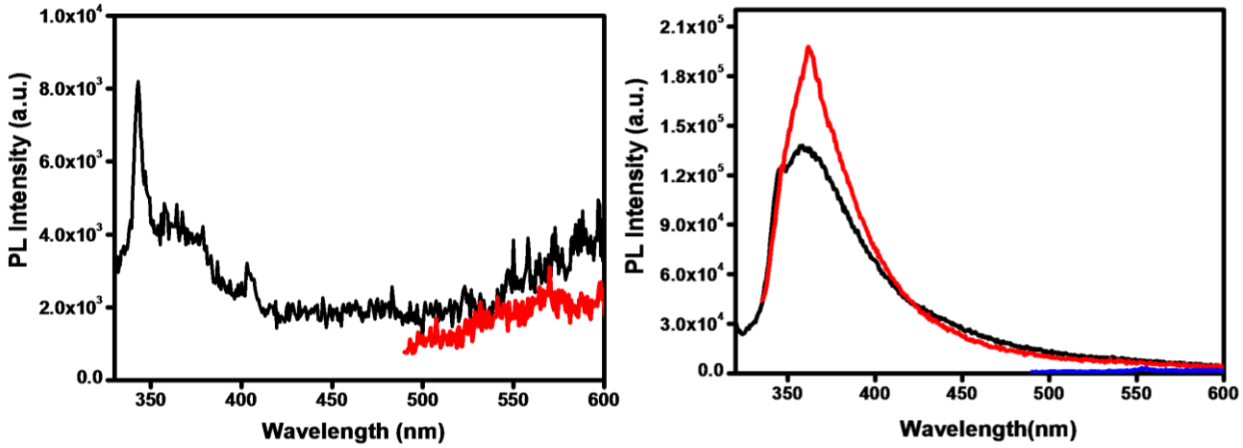

Figure 2.11. Photoluminescence spectrum of (left) 3ABBN at λexc= 310 (black) and 480 nm (red) and (right) 4ABBN at λexc= 310 (black), 325 (red) and 480 nm (blue).

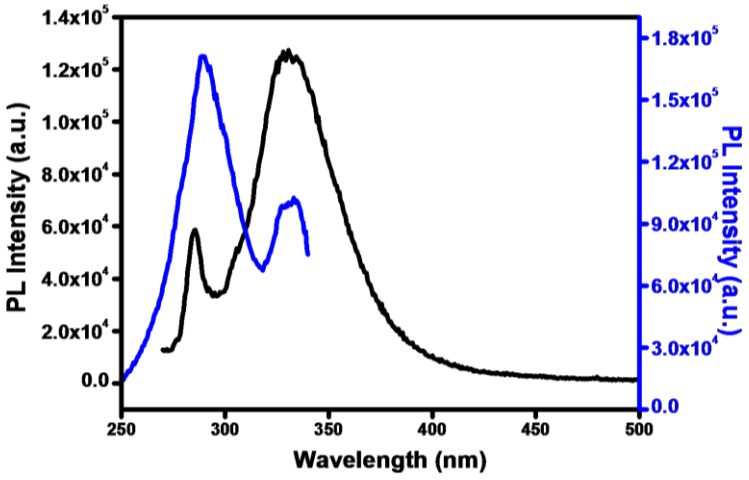

Figure 2.12. Emission spectrum of 4ABBN (9.04 x 10^{-4} M) at λexc=260 nm (black) and excitation spectrum at λem=350 nm (blue).

2.3.3. Structural Characterization of ZnO-azonaphthol composites

Powder X-ray diffraction patterns show that the parent wurtzite phase of ZnO NPs is not altered in the case of ZnO-3ABBN and ZnO-4ABBN composites during the surface modification (Figure 2.13). Surface charges of the grafted ZnO were found from zeta potential measurements to be -27 and -28 mV for 3ABBN and 4ABBN respectively when compared to 4 mV for naked ZnO. From these observations, it is clear that the grafting has stabilised the ZnO NPs against agglomeration. TEM images of naked and grafted NPs also corroborate surface grafting, wherein the particles were found to be well separated from each other with particle size of 3.5±1.5 nm. This may be due to the arrest of solution ripening possible for naked ZnO as a consequence of in-situ addition of the organic ligands. The corresponding histogram is also shown as an inset along with the TEM images (Figure 2.13).

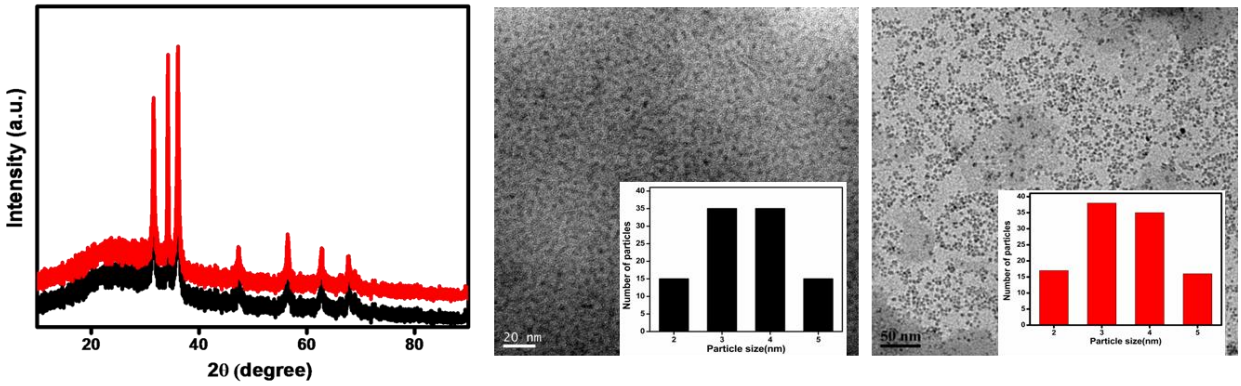

Figure 2.13. XRD patterns of (left) ZnO-3ABBN (black) and ZnO-4ABBN (red) composites and TEM images of ZnO-3ABBN (middle) and ZnO-4ABBN (right) composites with the corresponding histograms as inset.

Surface grafting of the organic moieties on ZnO was ascertained by IR spectroscopy by following the C=O and N=N stretching frequencies. The broad absorption peak observed at 1750-1650 cm^{-1} is the characteristic C=O stretching vibration present in carboxylic acids (Figure 2.7). The vibrations appearing at 1416 and 1401 cm^{-1} correspond to the N=N stretching for the meta and para substituted carboxylic acid aromatic systems. IR spectra of the composites show substantial shifts in the –CO and N=N stretching vibrational

frequencies when compared to the pristine dyes (3ABBN and 4ABBN) indicating successful grafting. The –CO stretch varies from 1696 cm^{-1} (4ABBN) to 1614 cm^{-1} for ZnO-4ABBN and 1693 cm^{-1} (3ABBN) to 1626 cm^{-1} for ZnO-3ABBN; more pronounced for 4ABBN. N=N stretch in the composites were found to shift to 1382 cm^{-1} for 4ABBN and 1394 cm^{-1} for 3ABBN from 1401 and 1416 cm^{-1} respectively (Figure 2.14).

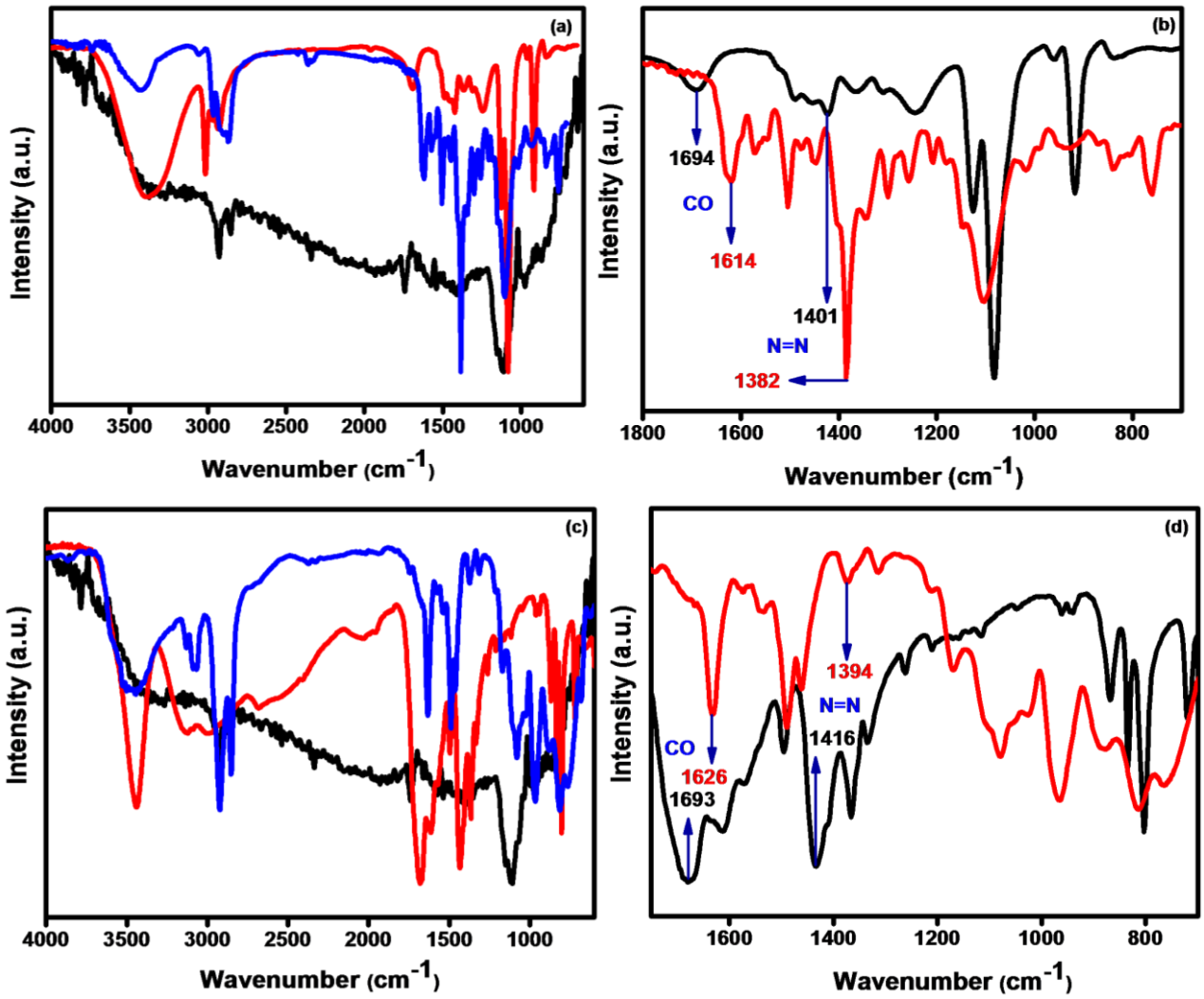

Figure 2.14. IR spectra of (a) ZnO (black), 4ABBN (red) and ZnO-4ABBN composite (blue), (b) indicating changes in C-O and N=N stretching frequencies of 4ABBN (black) and ZnO-4ABBN composite (red), (c) ZnO (black), 3ABBN (red) and ZnO-3ABBN composite (blue) and (d) indicating changes in C-O and N=N stretching frequencies of 3ABBN (black) and ZnO-3ABBN composite (red).

2.3.4. Photophysical Characterization of ZnO-azonaphthol Composites

2.3.4.1. ZnO-3ABBN Composite

A systematic study was set up to understand the mechanism as well as the effect of linker concentration on the absorption as well as emission spectra. First, the case of a simple aliphatic acid, oxalic acid was selected. The emission spectrum of pristine ZnO NPs and oxalic acid functionalised ZnO NPs are given in Figure 2.15.

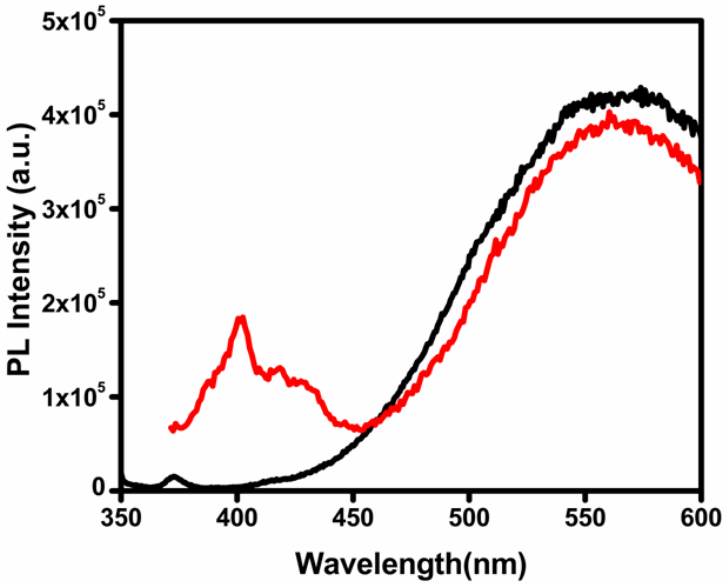

Figure 2.15. Emission spectrum of pristine (black) and oxalic acid grafted ZnO (red) at λexc= 325 nm.

However, ZnO-oxalic acid composite also shows the intense green emission and marginal enhancement of UV excitonic emission showing that the trap level is unaffected in the composite. Lesser suppression of the intense green emission with the aliphatic oxalic acid may be due to the unfavourable band structure for electron transfer. This indicates that trap level formation and its suppression may involve more complicated processes than a simple surface phenomenon.

Further spectroscopic studies were done on ZnO-azonaphthol composites. UV-vis spectrum of ZnO-3ABBN (1.69 x 10^{-3} M -9.04 x10^{-4} M) shows absorption bands at 320, 380 and 495 nm. From the UV-vis spectroscopy studies, it is evident that the ZnO-3ABBN composite

shows combined features of both ZnO nanoparticles and 3ABBN. A slight red shift of the absorption bands is observed in the case of composites compared to pure 3ABBN, whereas ZnO absorption edge is not substantially altered. This can be attributed to a reduction in size observed after grafting (Figure 2.16).

PL studies show that the molecule is not highly fluorescent in 310-510 nm excitations, but the emission spectrum of the ZnO-3ABBN composites clearly shows that the green fluorescence of ZnONP is suppressed on grafting with the 3ABBN organic linker. The absence of intense fluorescence in 3ABBN clearly indicates a lack of efficient electron transfer interaction between the azo linkage and carboxyl group due to the absence of conjugation, even in the presence of conventional fluorophores like azo group in the organic linker. Another possibility is the ring rotations around the double bonds (photoisomerisation) of the azo molecules. The suppression of green defect emission in the ZnO-3ABBN composites indicates that the interaction between 3ABBN and ZnO is sufficiently energetically favoured to alter the trap sites. Also, the aromatic moiety may assist in electron transfer albeit to a smaller extent even in the absence of conjugation when compared to aliphatic oxalic acid (Figure 2.16).

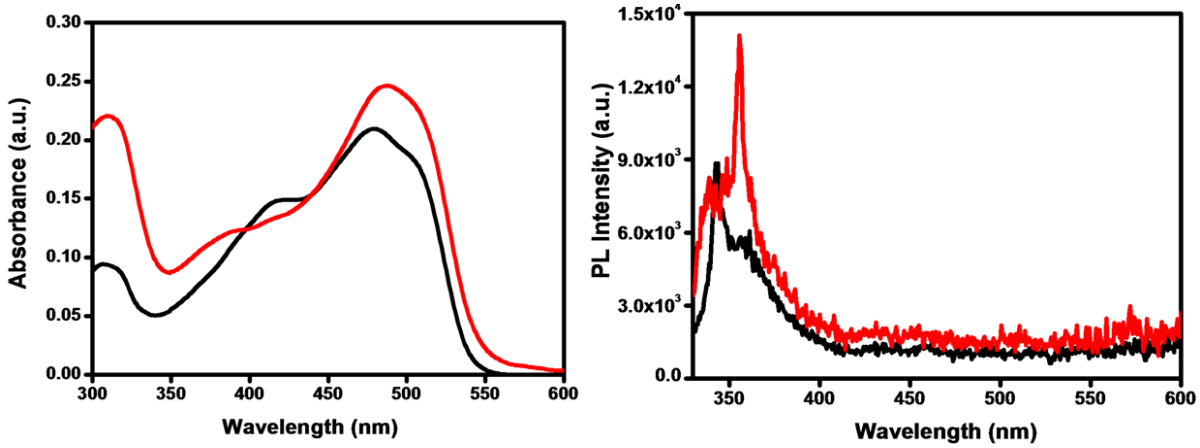

Figure 2.16. Absorption spectra of (left) 3ABBN: 9.04 x 10^{-4} M (black) and ZnO-3ABBN composite: 1.69 x10^{-3} M ZnO + 9.04 x 10^{-4} M 3ABBN (red) and emission spectra of (right) 3ABBN: (λ_{exc}=310 nm, black) and ZnO-3ABBN composite: (λ_{exc}=320 nm, red).

However, a complete degradation is visually observed on continuous irradiation of the composite even under visible light for 1- 8 h (T0-T8). After 1 h, the characteristic peaks of 3ABBN completely disappeared and only the distinct trace of ZnO could be observed. This behaviour can be attributed to the absence of conjugation which prevents fast transfer of charges leading to charge accumulation and photodegradation of the dye (Figure 2.17).

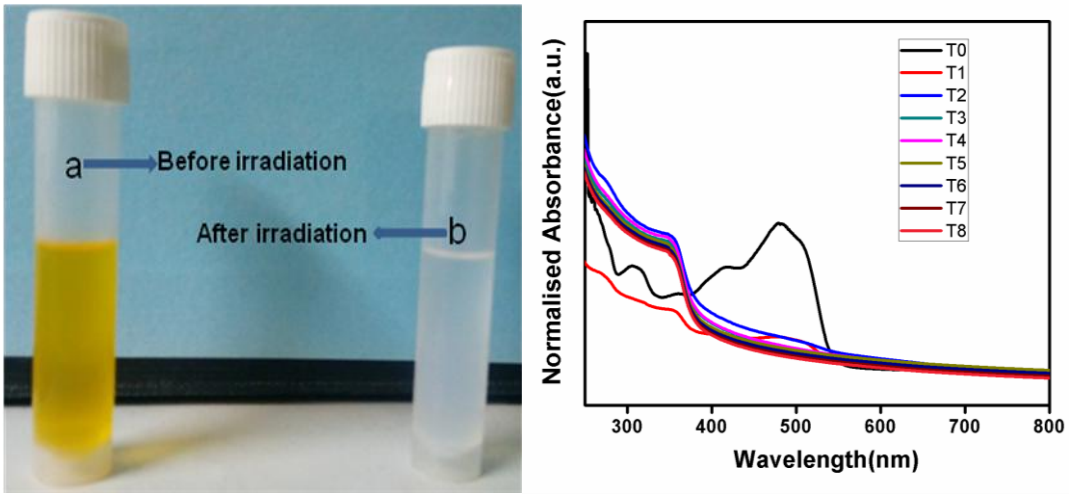

Figure 2.17. Degradation of (left) 3ABBN with visible light irradiation (T0-T8 h) and (right) UV-vis spectrum of the degradation of 3ABBN with visible light irradiation (T0-T8 h).

2.3.4.2. ZnO-4ABBN Composite

However, in the composite with 4ABBN, such a photodegradation was not observed and it was found to be stable under visible light irradiation and displayed high activity for hydrogen evolution reaction in photocatalytic water splitting (explained in 2.2.2. section). The absorption peaks at 295, 301 and 495 nm of the composite display characteristics of both ZnO and 4ABBN (Figure 18). A slight blue shift was observed in the absorption edge of the ZnO-4ABBN composite from 346 to 335 nm which is probably due to reduction in particle size. In addition, the composite showed visible light absorption contributed by the organic linker.

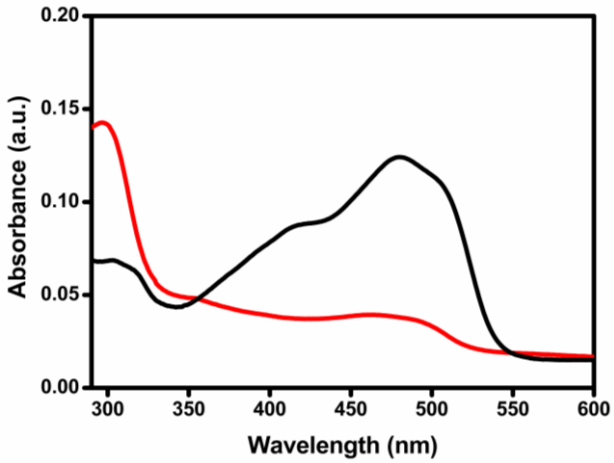

Figure 2.18. Absorption spectra of 4ABBN: 9.04 x 10^{-4} M (black) and ZnO-4ABBN composite: 1.69 x10^{-3} M ZnO + 9.04 x 10^{-4} M 4ABBN (red).

Emission spectra display the characteristic intense and sharp emission at 360 nm as in the case of pure 4ABBN (Figure 2.19). However, a drastic reduction in intensity in UV emission is seen in the composite when compared to the pure 4ABBN (of same concentration). Interestingly, green emission corresponding to defect sites in ZnO is also present albeit with a reduction in intensity compared to pristine ZnO. These characterizations indicate that even though trap sites, which may act as electron sinks, are minimized in the composites, some new energy levels in appropriate positions are created. These allow visible light absorption and an electron transfer probably from the organic linker to ZnO as evident from the reduction in intensity of the UV emission peak of 4ABBN upon surface grafting on ZnO.

The effect of concentration of the dye on the photophysical properties of the composite in terms of surface coverage of the smaller ZnO particles is also studied. Three more concentrations with higher (13.56 x 10^{-4} M) and lower (7.23 x 10^{-4} M, 5.42x 10^{-4} M) ratios of the 4ABBN (corresponding to 1:1.5, 1:0.3 and 1:0.15 surface coverage) other than the 1:0.5 composite are considered. The PL spectra show some interesting features. The UV emission peak intensities of the composites decrease with decrease in dye concentration (Figure 2.19). In case of pristine 4ABBN also, intensity of UV emission peak decreases with decrease in concentration (Figure 2.19). Hence, this can be considered as a characteristic of

the dye and not have any contribution from the exciton emission of ZnO. On the contrary, as 4ABBN concentration decreases, green emission increases. In other words, as more ZnO surface is exposed free from grafting with 4ABBN, green emission intensity increases. We also observe an isosbestic point indicating an increase in UV emission and concomitant decrease in defect emission as 4ABBN concentration increases (Figure 2.19).

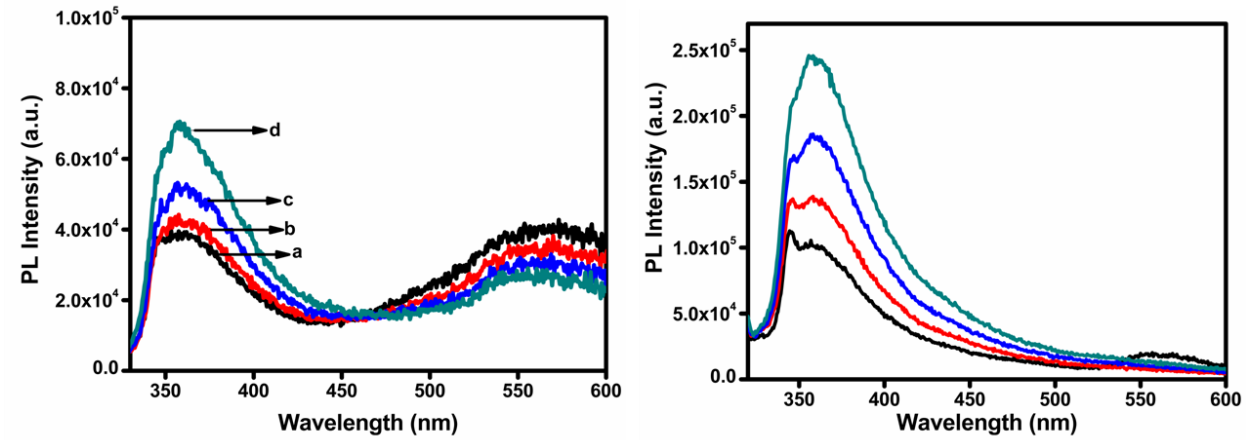

Figure 2.19. Emission spectra (left) of ZnO-4ABBN composite with different concentrations of 4ABBN indicating varying surface coverage of ZnO: (a) 1.69 x 10^{-3} +13.56 x 10^{-4} M; ZnO:dye = 1:1.5-black, (b) 1.69 x 10^{-3}+9.04 x 10^{-4} M; ZnO:dye = 1:0.5- red, (c) 1.69 x 10^{-3}+7.23 x10^{-4} M; ZnO:dye = 1:0.3- blue and (d) 1.69 x 10^{-3}+5.42 x 10^{-4} M; ZnO:dye = 1:0.15 - cyan; λ_{exc}=310 nm) and (right) 4ABBN (13.56 x 10^{-4} M-cyan), (9.04 x 10^{-4} M-blue), (7.23 x10^{-4}M-red) and (5.42 x 10^{-4} M-black), λexc=310 nm.

Because of the choice of donor-acceptor combination in this study (ZnO-NP and 4ABBN), where both have overlapping emissions around 360 nm, the exciton emission of ZnO NPs is rendered useless as a tool to monitor electron/charge transfer between the partners. However, monitoring variations in the predominant defect emission (560 nm) seen in pristine ZnO NPs upon grafting can assist in understanding the trap sites. With this intent, fluorescence lifetime study for the system was undertaken by TCSPC (Time-correlated single photon counting). These experiments were carried out for ZnO NPs, 4ABBN and ZnO-4ABBN composite (1.69 x10^{-3} M, 9.04 x 10^{-4} M and 1.69 x10^{-3} + 9.04 x 10^{-4} M respectively) at room temperature. The emission decay profiles are shown in Figure 2.20 and the observations are tabulated in Table 2.1.

Table 2.1. Lifetime parameters of ZnO, 4ABBN and ZnO-4ABBN composite.

System	Experimental Setup	Lifetime (ns)			
		τ1(a1)	τ2(a2)	τ3(a3)	<τ>
ZnO+4ABBN	λex=260nm λem=360 nm	0.452 (0.54)	2.68 (0.26)	8.61 (0.2)	2.633
4ABBN	λex=260nm λem=360 nm	0.945 (0.58)	3.97 (0.27)	9.44 (0.15)	3.06
ZnO Defect Band	λex=320nm λem=500nm	1.08 (0.92)	9.42 (0.07)	47.7 (0.01)	1.51
ZnO+4ABBN Defect Band	λex=320nm λem=500nm	1.68 (0.71)	10.7 (0.25)	64.13 (0.04)	5.57

The decay curves are deconvoluted by numerical convolution technique with the assumption that the delta pulse response is tri-exponential for ZnO NPs, 4ABBN and ZnO-4ABBN composites. It is observed in literature that ZnO decay profiles usually exhibit a biexponential fit but it is suggested that as particle size decreases, there is a possibility of emergence of other species (multiple defect sites). The defect emission lifetime is reported to have slower components compared to exciton emission and we also observe ~50 ns components. 4ABBN shows triexponential fit with three components at 0.452 (55 %), 2.68 (26 %) and 8.61 (20 %) ns. In the case of the composite, the 360 nm emission seems to be originating from three species with lifetimes of 0.945 (58 %), 3.97 (27 %) and 9.44 (15 %) ns, in which major contribution is from dye molecule and not from ZnO. It is observed that the average lifetime of the UV emission in the ZnO-4ABBN composite (at 2.633 ns) is slightly less when compared to that of the 4ABBN dye molecule (at 3.08 ns). On the other

hand, a fourfold increase in the defect emission lifetime for the composite is clearly seen in comparison to pristine ZnO [27-37].

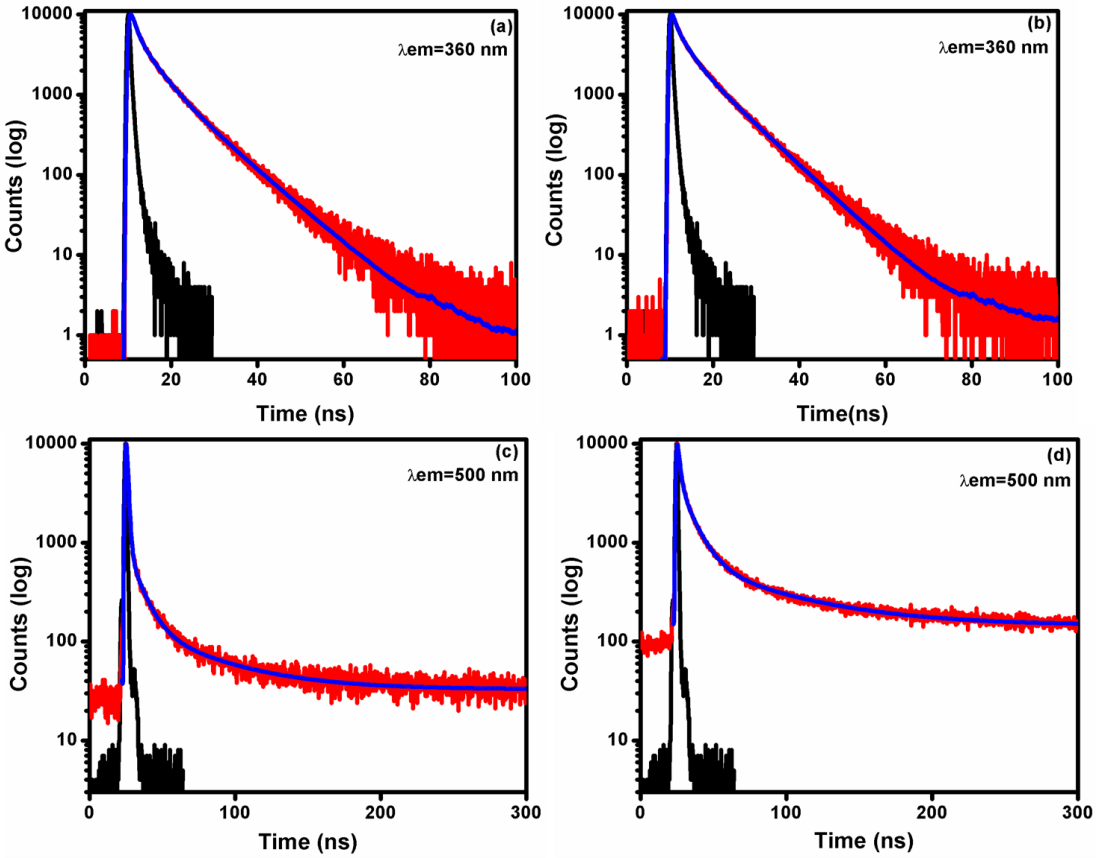

Figure 2.20. The emission decay profiles on excitation at 260 nm of (a) 4ABBN (9.04×10^{-4}M) and (b) ZnO-4ABBN ($1.69\times10^{-3}+9.04\times10^{-4}$M) and on 320 nm excitation of (c) ZnO NPs (1.69×10^{-3} M) and (d) ZnO-4ABBN ($1.69\times10^{-3}+9.04\times10^{-4}$M). Instrument response function in black, decay profile in red and experimental fit in blue.

The redox and the electron transfer properties of the samples were also investigated by cyclic voltammetry (Figure 2.21). The potential and current are found to be considerably enhanced on grafting when compared to ZnO and 4ABBN [ZnO (1V, 0.0075mA), 4ABBN (1.3V, 0.0094mA) and ZO-4ABBN (1.4V, 0.0156mA)]. To demonstrate the difference in the light induced electrical properties of ZnO NPs on grafting, voltammograms are observed under repeated on/off cycles in presence of visible light (200 W Tungsten lamp) (Figure 2.22). No increment in current is seen in pristine ZnO NPs and 4ABBN on illumination

(Figure 2.23). However, substantial enhancement in the photo current is observed in case of the composite under illumination authenticating a light induced electron transfer. To further corroborate this fact, we have performed same study on SiO_2 surface decorated with 4ABBN (Figure 2.21). CV under the same conditions of this control material does not display any change in current-voltage profile indicating absence of electron transfer, as expected due to the absence of any electron accepting orbitals in SiO_2. The significant photocurrent rise evidences an electron transfer pathway in the case of ZnO-4ABBN composite. The photocurrent was observed to be stable even after three consecutive cycles indicating the photostability of the composite. To further substantiate the electron/charge transfer in the ZnO-4ABBN composite, linear sweep voltammetry (LSV) and electrochemical impedance spectroscopy (EIS) were carried out under illumination and dark (Figure 2.24). The LSVs of the composite were investigated by scanning in a potential window of -0.5 to 1.7 V. The Nyquist plots suggest that the ZnO-4ABBN composite has the fastest electron transfer process under light, which could be associated with the conducting nature of the composite. In ZnO-4ABBN composite, the resistance from EIS was also found to be less under illumination (1105 Ω) compared to the dark condition (1135 Ω) in the ZnO-4ABBN composite [38-40] .

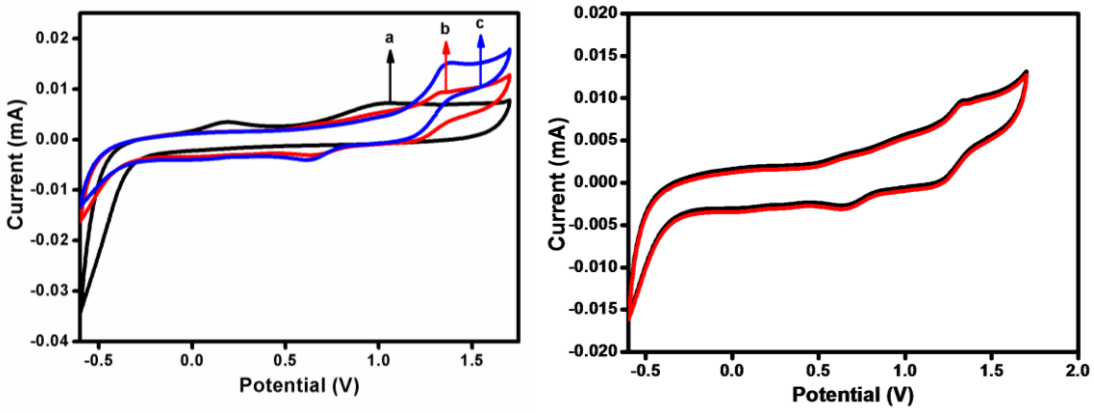

Figure 2.21. (Left) Current–voltage profile for photoelectrochemical cells employing (a) ZnO (black), (b) 4ABBN (red) and (c) ZnO-4ABBN composite (blue) by cyclic voltammetry at a scan rate of 50 mv/s. Supporting electrolyte was $LiClO_4$ in acetonitrile. Current–voltage data for photoelectrochemical cells employing 4ABBN (black) and 4ABBN-SiO_2 (red) by cyclic voltammetry (right).

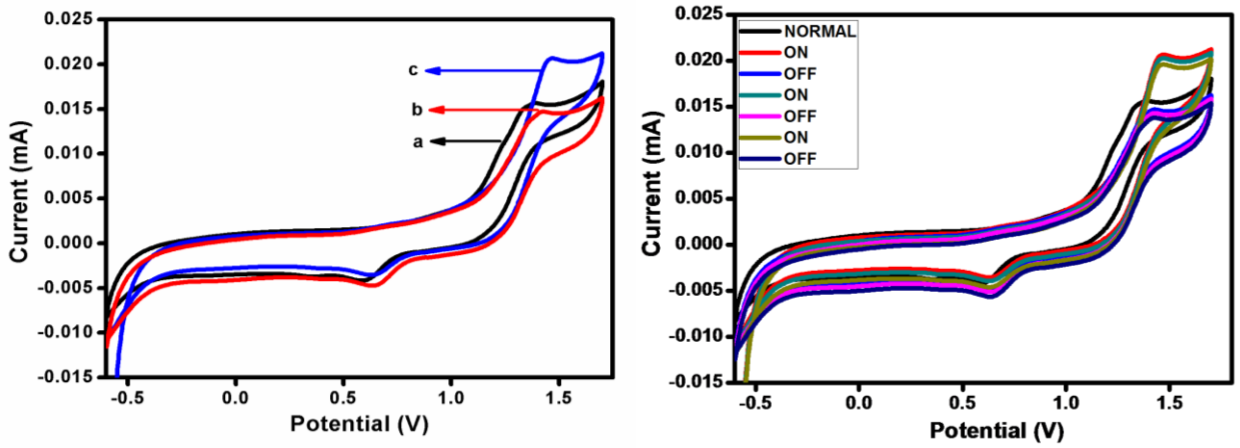

Figure 2.22. Comparison of photocurrent with potential of ZnO-4ABBN composite on repeated on/off cycles under irradiation from 200W tungsten lamp; (a) CV under ambient light (black), (b) under dark (red) and (c) under irradiation (blue) (left) and (right) comparison of photocurrent with potential of ZnO-4ABBN composite upon turning on and off 200W tungsten lamp in by cyclic voltammetry.

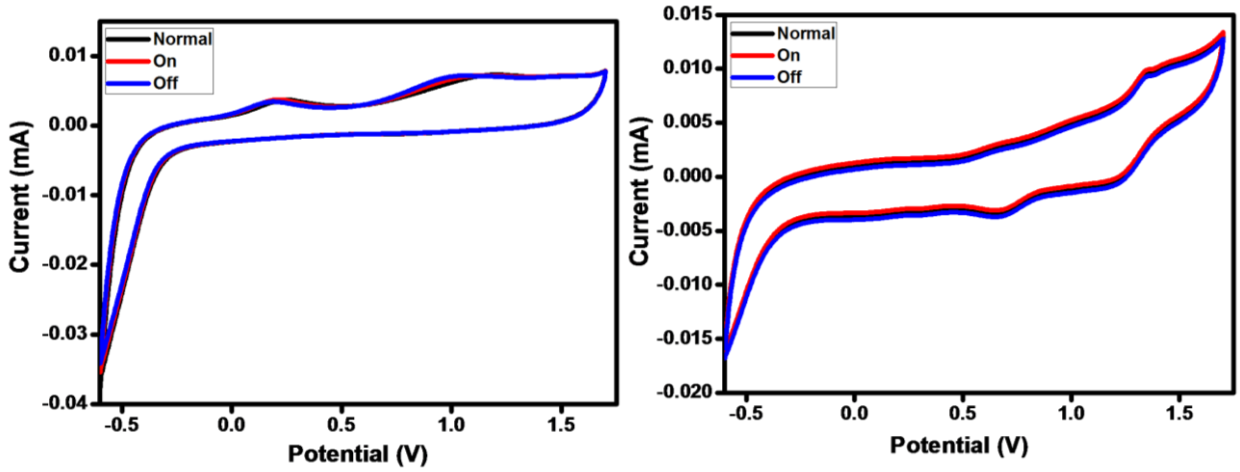

Figure 2.23. Comparison of photocurrent with potential of (left) ZnO and (right) 4ABBN under normal condition (black) and upon turning on (red) and off (blue) 200W tungsten lamp by cyclic voltammetry.

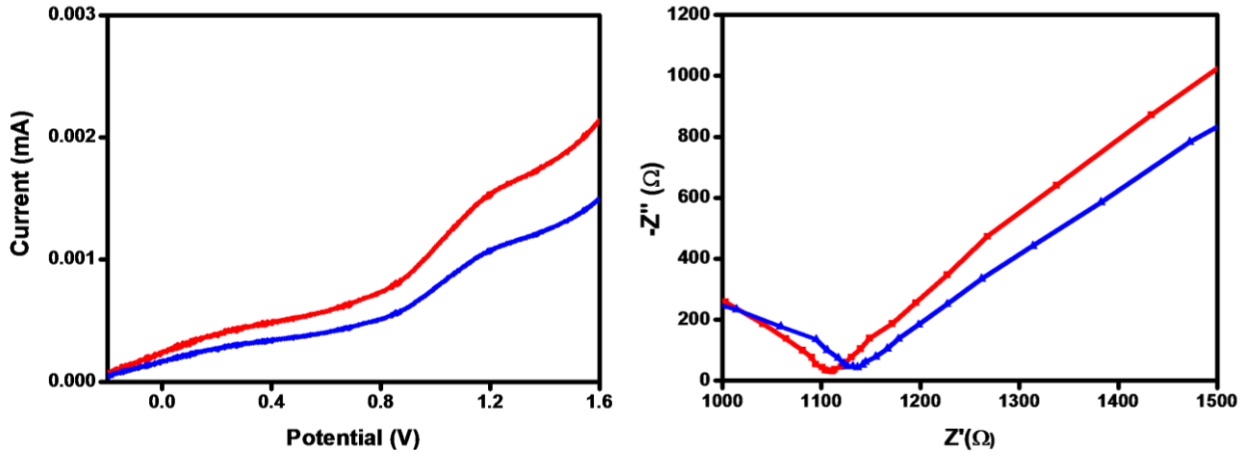

Figure 2.24. LSV profile for photoelectrochemical cells employing (left) ZnO-4ABBN Composites(10 mv/s) upon turning on (red) and off (blue) 200W tungsten lamp by cyclic voltammetry and Electrochemical Impedance employing (right) ZnO- -4ABBN Composites upon turning on (red) and off (blue) 200W tungsten lamp .

2.3.5. Computational studies

The clean ZnO $(10\bar{1}0)$ surface contains ordered rows of buckled Zn-O dimers along the polar [0001] direction with a net electron accumulation on the O atoms. The calculations show that 4ABBN binds vertically to the ZnO surface with a binding energy of 1.83 eV and creating two Zn-O bonds through the –COOH group. During the relaxation process, it spontaneously gets deprotonated, releasing an H^+ ion from the –COOH group, which gets attached to the neighbouring electron rich O of the ZnO surface. The newly formed Zn-O bond lengths are about 1.96 and 1.97 Å. The density of states (DOS) of the ZnO-4ABBN is shown in Figure 2.25(a). The electronic states are aligned with respect to the energy at vacuum. Upon modifying the surface of the ZnO nanoparticles with 4ABBN, the effective band gap of the interface is reduced to 1.47 eV compared to that of 3.77 eV for the clean slab. This is qualitatively consistent with the experimental absorption spectra where the lowest energy peak of the absorption spectra of the ZnO nanoparticles shift from about 346 nm to 495 nm as the surface of the nanoparticles were modified with 4ABBN. The contributions to the total DOS from the ZnO slab and the dye are shown with red circles and blue stars respectively in Figure 2.25(a). The theoretical calculations show that the

valence band maximum (VBM) of the interface is localized on the dye molecule (Figure 2.25(b)) and the conduction band minimum (CBM) is localized on the slab (Figure 2.25(c)). Additionally, there is a weight of the wavefunction on the O atoms of the dye through which it binds to the ZnO slab indicating that there is a possibility of fast electron transfer from the dye to the ZnO. The interface is thus converted to a staggered type II interface, which facilitates absorption in the visible region as observed in the absorption spectra of ZnO-4ABBN.

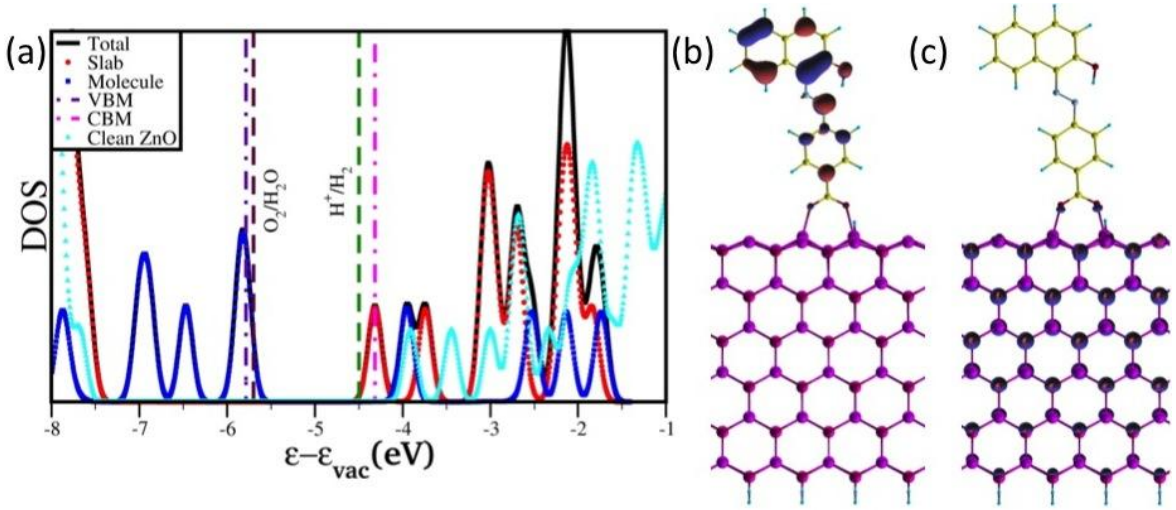

Figure 2.25. (a) DOS of the ZnO-4ABBN. Dot-dashed violet and magenta vertical lines mark the VBM and CBM respectively. The dashed brown and green lines mark the OP and RP. (b) The wavefunction corresponding to the VBM. (c) The wavefunction corresponding to CBM.

The oxidation potential (OP) of oxidizing H_2O to O_2 and the reduction potential (RP) of reducing H^+ to H_2 with respect to the positions of VBM and CBM of the ZnO-4ABBN composite are also looked at. The absolute values of the OP/RP are given by $E_{abs}^{OP/RP}$=-4.5-$E_{NHE}^{OP/RP}$, where $E_{abs}^{OP/RP}$ is the absolute value of the OP/RP and $E_{NHE}^{OP/RP}$ is the OP/RP potential in V vs. the NHE at pH 0. E_{NHE}^{OP} is 1.23 eV and E_{NHE}^{RP} is 0 eV. For the composite to be a good photocatalyst for water splitting, these two potentials should lie in the band gap, i.e., the OP should lie above the VBM and the RP should lie below the CBM. From the calculations, the absolute values of OP and RP are -5.73 eV and -4.5 eV respectively. Thus the OP is about 0.06 eV above the VBM (Figure 2.25(a)) and the RP is 0.18 eV below the

CBM (Figure 2.25(a)). These results suggest that thermodynamically water splitting reaction will be catalysed by the ZnO-4ABBN composite [41-47].

2.3.6. Photocatalytic testing

Due to photodegradation of ZnO-3ABBN, water splitting studies of only ZnO-4ABBN was carried out and methanol was used as the sacrificial agent. Since ZnO-4ABBN was synthesized as a methanolic colloidal solution, it was used as such, which amounted to 0.025 g of catalyst in 35 v/v% methanol in water mixture, and this was taken as optimum. For experiments with lesser volumes of methanol, the initial colloidal solution was dried and redispersed in varying amounts of methanol and added to 20 mL of water. The photocatalytic tests were carried out under steady state conditions by head space analysis for UV, visible and solar irradiations (Figure 2.26). Total H_2 evolution was observed to be 155 mmol/g, 152 mmol/g and 155 mmol/g under UV, visible and solar irradiations at 8 h. Further photocatalytic water splitting studies for the composite were focused only for visible light irradiation. The photocatalytic reaction was stopped after the 8^{th} h, and the reactor set up was purged with N_2 and irradiated again. This experiment was repeated 3 times (Figure 2.27) with the same catalyst. The ZnO-4ABBN catalysts were found to be highly stable during this cycling exposure. The initial H_2 evolution rate was also regained after each purging. Preliminary tests with varying volumes of methanol suggested that after 4 h visible light irradiation, a maximum yield of H_2 at 102 mmol/g was obtained at 35 vol% of methanol in water for ZnO-4ABBN. At low concentrations of methanol, a corresponding decrease in H_2 evolution was observed as expected. However, interestingly, almost saturation was reached at 35 v/v% and further increase in methanol concentration did not affect the yield substantially (Figure 2.28). Moreover, a slight decrease in H_2 yield also was observed indicating that after an optimum level, hydrogen evolution becomes independent of methanol concentration. To rule out the effect of UV light which may be present in the radiation source, control experiment with ZnO-4ABBN under the same conditions but with a $NaNO_2$ (2 M) chemical filter was carried out which showed same H_2 evolution (102 mmol/g).

From computational and emission studies it is clear that the photoexcitation occurs in the azo compound and electron transfer occurs from it to ZnO. Hence it is logical to assume that this electron is responsible for the $H+/H_2$ reduction. This was unambiguously evidenced by studying the methanol assisted water splitting activity of 4ABBN/SiO_2 control material mentioned earlier. Since no electron transfer is observed from 4ABBN to SiO_2 in this composite, we do not expect any catalytic activity under visible light and indeed this was the case and H_2 evolution in this system was found to be negligible at 0.004 mmol/g. This corroborates the observation from computational studies that excited electrons from the LUMO of 4ABBN which are transferred to the conduction band of ZnO reduce H_2O proving the ZnO surface as the catalytic site. Our observation that electrons are excited from HOMO to LUMO of the linker and transferred efficiently to ZnO surface, also brings up the possibility of holes generated in the HOMO of 4ABBN interacting with the sacrificial agent, CH_3OH.

To further test the role of methanol, photocatalytic testing was done in water without adding methanol in case of ZnO-4ABBN. H_2 evolution from pure water splitting was observed albeit to a small extent (1.23 mmol/g) for 4 h irradiation. This shows that methanol plays the role of enhancing the H_2 evolution. Methanol is known to assist in water splitting on semiconductor oxides by acting not only as a hole scavenger but also as electron enricher which enhances the hydrogen evolution. The radical formed after proton abstraction from CH_3OH by the valence band hole injects one electron to the conduction band leading to the formation of formic acid and formaldehyde and eventually CO or CO_2. Interestingly, we do not observe the presence of CO or CO_2 in detectable levels by gas chromatography. Presence of formic acid or formaldehyde, potential products in hole scavenging reactions of methanol, also was ruled out by liquid chromatography analysis of the reaction mixture. This indicates that the utilization of methanol probably proceeds through a photochemical pathway involving HOMO of the azo compound rather than a simple current doubling mechanism involving valence band of ZnO. It is clear that methanol also contributes to the amount of H_2 produced which was further corroborated by employing other inorganic hole scavengers like IO_3^-/I^- and carbonate systems for ZnOPP-4ABBN composites resulting in 7.5 and 9 mmol/g of H_2 respectively. Here inorganic

ions like I^- (electron donors) and IO_3^- (electron acceptors) work as a pair of redox mediators; I^- ions scavenge holes resulting in oxidation product IO_3^- which is an electron acceptor and its reduction to I^- competes with H^+/H_2 reduction. Hence in the current system, these redox mediators are found to be not as effective a sacrificial agent as methanol [48-52]. An evaluation of the stoichiometric relation between H_2 and O_2 generated also was performed by purging the reaction mixture with N_2 for half hour in order to dispel dissolved and atmospheric O_2 before irradiation. The evolved gas mixture analysis indicated a composition of 104 mmol/g of H_2 and 1.17 mmol/g of O_2 with methanol. The negligible amount of O_2 evolution is expected in presence of methanol as sacrificial agent. Moreover, the enhanced quantity of H_2 produced proves that methanol also contributes to the H_2 evolution.

The use of simple organic hole scavengers is widely accepted as a method of enhancing the H_2 production as well as photostability of catalyst systems. The practicality of this method is enhanced when the organic hole scavengers are from renewable sources like ethanol or glycerol. Interestingly, we observed good H_2 evolution in ethanol but poor dispersion of the catalyst consequent to high viscosity of the reaction mixture with glycerol led to lower evolution rates from the latter (Figure 2.28).

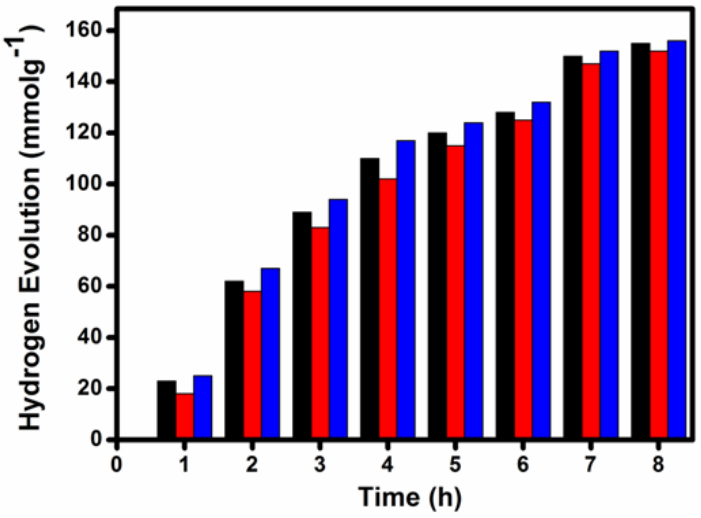

Figure 2.26. Evaluation of photocatalytic activity for H_2 generation under UV (black), visible (red) and solar (blue) at various irradiation time (0,1,2,3,4,5,6,7 and 8 h) .

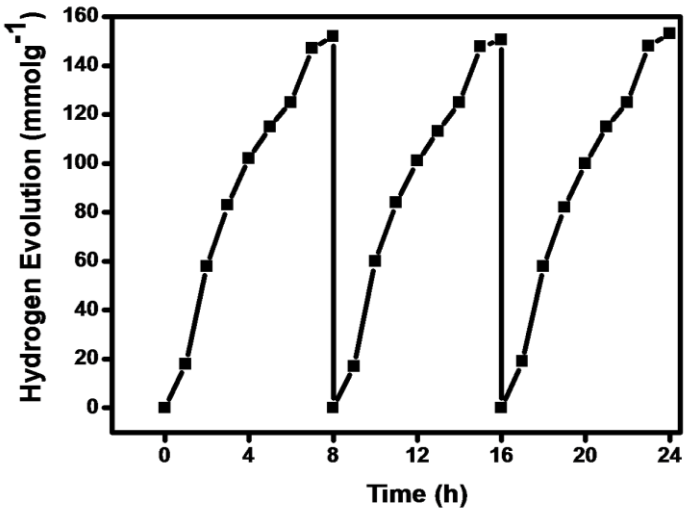

Figure 2.27. H_2 evolution of ZnO-4ABBN composite under visible light irradiation on repeated purging of the headspace.

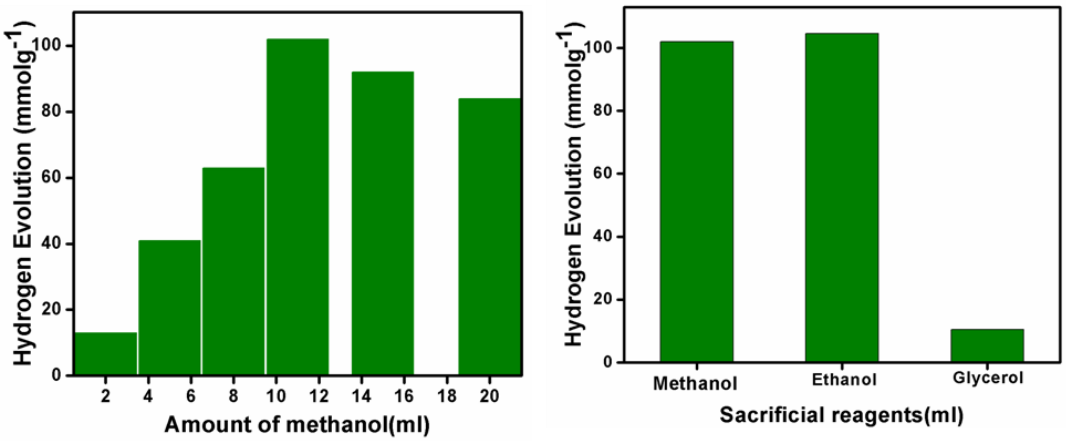

Figure 2.28. Evaluation of photocatalytic activity for H_2 generation in methanol-water mixture at different volumes of methanol (2ml, 5 ml, 8 ml, 11 ml and 20 ml) keeping the amount of water constant (20 ml) in ZnO-4ABBN composites for 4 h under visible light irradiation (left) and (right) comparison of the photocatalytic activity for 4 h visible light irradiation of ZnO-4ABBN composite in methanol, ethanol and glycerol for the hydrogen production.

2.4. Conclusions

In summary, ZnO nanoparticles of size ~3-5 nm are surface modified with azonaphthols of varying conjugation, in a quest to identify potential photocatalysts and understand their efficacy. The azonaphthols are designed to have a carboxylic functionality in the phenyl group and the conjugation property is varied by changing the position of this group from para to meta. The non-conjugated azonaphthol is not fluorescent as expected in case of azo based switches. However, conjugated molecule is fluorescent with an emission in UV region, possibly due to the stabilisation of the hydrazone form consequent to extended conjugation. On grafting to ZnO nanoparticles, a drastic decrease in this UV emission is observed, indicating an electron transfer from the organic molecule to ZnO. Additionally, fluorescence properties of ZnO nanoparticles also are utilised to throw more light upon the mechanism of electron transfer. ZnO nanoparticles are known to exhibit band gap emission in the UV region along with visible emission understood to be due to the presence of various types of defect sites in the bulk as well as on the surface like Zn vacancy, oxide vacancy, surface hydroxyl groups etc. In our case, a broad emission, peaking at 560 nm is observed with a conspicuous absence of UV emission indicating high concentrations of defect sites of multiple types. This defect emission is completely suppressed on grafting with the non-conjugated molecule; however, this is not the case with conjugated molecule. Defect emission lifetime studies in pristine ZnONP and its composites with 4ABBN help in ascertaining the electron transfer mechanism in the composites. A distinct fourfold increase in average lifetime of defect emission along with significant redistribution to longer lifetime species in the composites clearly alludes to the formation of stable and long lived defect sites. In ZnONP, 92% contribution is from a very short lived defect type with overall average lifetime of only 1.51 ns. In the composite, the contribution from this component decreased to 70%, concomitantly increasing the contribution to the component at ~10 ns effectively increasing the average lifetime. This indicates the presence of multiple defect sites contributing to the broad green emission which is widely accepted in literature. On grafting, certain defect sites, possibly surface species, are suppressed and electron transfer to specific defect sites with appropriate energy levels occur. This may lead to an enhancement of population of long living species increasing the average lifetime. Moreover,

lifetime studies indicated a fourfold increase in lifetime of the defect species due to electron transfer from the organic moiety. In addition, the photocurrent enhancement of the composite under illumination corroborates an electron transfer mechanism. The composite with non-conjugated molecule is prone to photodegradation. Hence, it is clear that efficient electron transfer from the organic moiety to the ZnO stabilises the composite and additionally electron transfer to specific defect sites may be occuring during this process.

DFT studies, in agreement with the experimental observations, show that the HOMO of 4ABBN is located in the ZnO band gap, which reduces the effective band gap of the composite facilitating absorption in the visible region of the solar spectrum. The excited electron created due to the absorption of photon energy by the organic moiety is transferred to ZnO. Additionally from the position of the redox potentials with respect to the valence band maxima and conduction band minima of the composite, we predict that this system will act as a good photocatalyst for hydrogen evolution reaction. This claim is further supported by experiments where we show that there is indeed H_2 evolution from pure water splitting. In presence of methanol, which replenishes the electron, there is a much larger yield of hydrogen compared to those in absence of any such hole scavengers.

References

1. Anderson, J.; Chris, G. V. D. W., *Rep. Prog. Phys*. **2009**, *72*, 126501.
2. Özgür, Ü.; Alivov, Y. I.; Liu, C.; Teke, A.; Reshchikov, M. A.; Doğan, S.; Avrutin, V.; Cho, S.-J.; Morkoç, H. J., *Appl. Phys.* **2005**, *98*, 041301.
3. Djurišić, A. B.; Leung, Y. H., *Small* **2006**, *2*, 944.
4. Djurišić, A. B.; Leung, Y. H.; Tam, K. H.; Hsu, Y. F.; Ding, L.; Ge, W. K.; Zhong, Y. C.; Wong, K. S.; Chan, W. K.; Tam, H. L.; Cheah, K. W.; Kwok, W. M.; Phillips, D. L., *Nanotechnology* **2007**, *18*, 095702.
5. Irimpan, L.; Nampoori, V. P. N.; Radhakrishnan, P.; Deepthy, A.; Krishnan, B., *J. Appl. Phys.* **2007**, *102*, 063524.
6. Kamat, P. V., *Chem. Rev.* **1993,** *93*, 267.
7. Litty, I.; Bindu, K.; Deepthy, A.; Nampoori, V. P. N.; Radhakrishnan, P., *J. Phys. D: Appl. Phys*. **2007**, *40*, 5670.
8. Liu, D.; Wu, W.; Qiu, Y.; Yang, S.; Xiao, S.; Wang, Q.-Q.; Ding, L.; Wang, J., *Langmuir* **2008**, *24*, 5052.
9. House, R. L.; Mehl, B. P.; Kirschbrown, J. R.; Barnes, S. C.; Papanikolas, J. M., *J. Phys. Chem. C* **2011**, *115*, 10806.
10. Norberg, N. S.; Gamelin, D. R., *J. Phys. Chem. B* **2005**, *109*, 20810.
11. Hagfeldt, A.; Boschloo, G.; Sun, L.; Kloo, L.; Pettersson, H., *Chem. Rev*. **2010**, *110*, 6595.
12. Giansante, C.; Infante, I.; Fabiano, E.; Grisorio, R.; Suranna, G. P.; Gigli, G., *J. Am. Chem. Soc*. **2015**, *137*, 1875.
13. Hong, R. Y.; Li, J. H.; Chen, L. L.; Liu, D. Q.; Li, H. Z.; Zheng, Y.; Ding, J., *Powder Technol*. **2009**, *189*, 426-432.
14. Bandara, H. M. D.; Burdette, S. C., *Chem. Soc. Rev*. **2012**, *41*, 1809-1825.
15. Merino, E.; Ribagorda, M., *Beilstein J. Org. Chem*. **2012**, *8*, 1071-1090.
16. Biswas, N.; Umapathy, S., *J. Phys. Chem. A* **2000**, *104*, 2734-2745.
17. Nuttall, R. H.; Roberts, E. R.; Sharp, D. W. A., *Spectrochim. Acta*. **1961**, *17*, 947-952.
18. Bandara, H. M. D.; Friss, T. R.; Enriquez, M. M.; Isley, W.; Incarvito, C.; Frank, H. A.; Gascon, J.; Burdette, S. C., *J. Org. Chem*. **2010**, *75*, 4817-4827.
19. Yoshino, J.; Kano, N.; Kawashima, T., *Chem. Commun*. **2007**, 559-561.

20. Nedeltcheva, D.; Antonov, L., *J. Phys. Org. Chem*. **2009**, *22*, 274-281.
21. Biswas, N.; Umapathy, S., *J. Phys. Chem. A* **2000**, *104*, 2734-2745.
22. Nuttall, R. H.; Roberts, E. R.; Sharp, D. W. A.,. Spectrochim. Acta, 1961, 17, 947-952.
23. Joshi, H.; Kamounah, F. S.; Gooijer, C.; van der Zwan, G.; Antonov, L., J. *Photochem. Photobiol., A* **2002**, *152*, 183-191.
24. Gegiou, D.; Fischer, E., *Chem. Phys. Lett.* **1971**, *10*, 99-101.
25. Reeves, R. L.; Kaiser, R. S., *J. Org. Chem.* **1970**, *35*, 3670-3675.
26. Ahmedova, A.; Simeonov, S. P.; Kurteva, V. B.; Antonov, L., *Chem. Cent. J* **2013**, *7*, 29.
27. Berrie, A. H.; Hampson, P.; Longworth, S. W.; Mathias, A., *J. Chem. Soc. B* **1968**, 1308-1310.
28. Burawoy, A.; Salem, A. G.; Thompson, A. R., *J. Chem. Soc*. **1952**, *935*, 4793-4798.
29. Kamat, P. V.; Patrick, B*., J. Phys. Chem* **1992**, *96*, 6829-6834.
30. Kahn, M. L.; Cardinal, T.; Bousquet, B.; Monge, M.; Jubera, V.; Chaudret, B., *Chem. Phys. Chem* **2006**, *7*, 2392-2397.
31. Zhang, Z.-Y.; Xiong, H.-M., *Materials* **2015**, *8*, 3101.
32. Fišerová, E.; Kubala, M., *J. Lumin*. **2012**, *132*, 2059-2064.
33. Marczak, R.; Werner, F.; Gnichwitz, J.-F.; Hirsch, A.; Guldi, D. M.; Peukert, W., *J. Phys. Chem. C* **2009**, *113*, 4669-4678.
34. Bauer, C.; Boschloo, G.; Mukhtar, E.; Hagfeldt, A., *Chem. Phys. Lett*. **2004**, *387*, 176-181.
35. Raymo, F. M.; Tomasulo, M., *Chem. Soc. Rev*. **2005**, *34*, 327-336.
36. Layek, A.; Manna, B.; Chowdhury, A., *Chem. Phys. Lett*. **2012**, *539–540*, 133-138.
37. Yildiz, I.; Tomasulo, M.; Raymo, F. M., *J. Mater. Chem*. **2008**, *18*, 5577.
38. Haynes, K. M.; Kratch, K. C.; Stovall, S. D.; Obondi, C. O.; Thurber, C. R.; Youngblood, W. J., *ACS Appl. Mater. Interfaces* **2015**, 7, 16133-16137.
39. Park, H.; Choi, W., *J. Phys. Chem. B* **2003**, *107*, 3885-3890.
40. Durham, B.; Meyer, T. J., *J. Am. Chem. Soc*. **1978**, *100*, 6286-6287.
41. Paolo, G.; Stefano, B.; Nicola, B.; Matteo, C.; Roberto, C.; Carlo, C.; Davide, C.; Guido, L. C.; Matteo, C.; Ismaila, D.; Andrea Dal, C.; Stefano de, G.; Stefano, F.; Guido, F.; Ralph, G.; Uwe, G.; Christos, G.; Anton, K.; Michele, L.; Layla, M.-S.; Nicola, M.; Francesco, M.;

Riccardo, M.; Stefano, P.; Alfredo, P.; Lorenzo, P.; Carlo, S.; Sandro, S.; Gabriele, S.; Ari, P. S.; Alexander, S.; Paolo, U.; Renata, M. W., J. *Phys.: Condens. Matter* **2009**, *21*, 395502.

42. anderbilt, D., *Phys. Rev. B* **1990**, *41*, 7892-7894.
43. Perdew, J. P.; Burke, K.; Ernzerhof, M., *Phys. Rev. Let*. **1996**, *77*, 3865-3868.
44. Vogel, D.; Krüger, P.; Pollmann, J., *Phys. Rev. B* **1996**, *54*, 5495-5511.
45. Janotti, A.; Segev, D.; Van de Walle, C. G., *Phys. Rev. B* **2006**, 74, 045202-1-9.
46. Calzolari, A.; Ruini, A.; Catellani, A., *J. Am. Chem. Soc*. **2011**, *133*, 5893-5899.
47. Choi, E. A.; Lee, W. J.; Chang, K. J., *J. App. Phy.* **2010**, *108*, 023904-1-6.
48. Nozik, A. J.; Memming, R., *J. Phys. Chem*. **1996**, *100*, 13061-13078.
49. Hykaway, N.; Sears, W. M.; Morisaki, H.; Morrison, S. R., *J. Phys. Chem*. **1996**, 90, 6663-6667.
50. Sabio, E. M.; Chamousis, R. L.; Browning, N. D.; Osterloh, F. E., *J. Phys. Chem.* C **2012**, *116*, 3161−3170.
51. Kudo, A.; Miseki, Y., *Energ Fuel*. **2005**, *19*, 1143-1147.
52. Ni, M.; Leung, M. K. H.; Leung, D. Y. C.; Sumathy, K., *Renew Sust Energ Rev*. **2007**, *11*, 401-425.

Chapter 3

Synthesis, Characterization and Photocatalytic Water Splitting Activity of ZnO-azoquinoline Composites

3.1. Introduction

Influence of the dye structure vis-à-vis conjugation on the photophysical characteristics and water splitting activity of their composites with ZnO was demonstrated in chapter 2. A photo degradation effect was observed in the composite with the non-conjugated azonaphthol, instead of efficient hydrogen generation as displayed by ZnO modified with the conjugated analogue. This has been proved as due to inefficient electron transfer within the composite in the case of the non-conjugated system. These conclusions brought us to examine the possibilities of engineering the electron transfer characteristics of the azo dye. This was achieved by designing it to have multiple chelation sites anticipating incorporation of resonance features. Thus, our aim here is to understand the effect of multiple grafting sites on the activity of the otherwise non-conjugated system. Among various aromatic molecules, hydroxy quinoline is well known as a ligand forming chelation complexes. The 8-hydroxyquinoline (oxine) behaves as a bidentate (N,O-) univalent ligand to form chelates with several metal ions. However, 8HQ chelated systems are poorly soluble in all the common solvents, and to overcome this limitation, substituted 8-HQs have been used. 8HQ is the only one, among seven isomeric monohydroxyquinolines, capable of forming complexes with divalent metal ions through chelation. In the early 1950's, it was observed that 8HQ forms large number of complexes with metals like Zn, Cu, Ni, Pb and Fe to form metalloquinolates. Quinoline moiety is also known to be a chelating agent for catalytic sites like Pt. We selected this moiety to be coupled with 3-aminobenzoic acid to form an azoquinoline. Azoquinolines are also azobenzene class of chromophores with carboxylate ending on one side and the other side functionalized with a coupler, 8-hydroxy quinoline (8HQ). Here, carboxylic group as well as quinoline group would be potentially interacting with ZnO surface on grafting. Indeed, the ability of hydroxyquinoline group to behave like a bidentate ligand along with azo carboxylic moiety makes the conjugate photocatalytically active and stable when compared to its azonaphthol counterpart. For comparison, an analogue with para substitution was also synthesised and anchored onto ZnO, since resonance features and consequent electron transfer characteristics are expected to be enhanced in this molecule [1-8].

3.2. Experimental Section

3.2.1. Synthesis

3.2.1.1. ((E)-3 -((8-hydroxyquinolin-5-yl)diazenyl) benzoic acid) [3ABBNHQ] and ((E)-4 -((8-hydroxyquinolin-5-yl)diazenyl) benzoic acid) [4ABBNHQ]

The azoquinoline compounds are synthesised by diazotization and coupling reactions (Scheme 3.1). In a typical synthesis, to a solution of amino benzoic acids (3-aminobenzoic acid or 4-aminobenzoic acid; 1.35g, 9.843 mmoles), distilled water (8.44 mL) and concentrated H_2SO_4 (2.1 mL) was added drop wise. The mixture was cooled to 0 °C. A solution of sodium nitrite (1.006 g, 14.58 mmoles) in 3 mL of distilled water maintained at 0 °C, was added to the above cold mixture drop wise with good stirring. After 20 min, the diazotization was complete, which was verified by adding a solution of 4-(N,N-dimethylamine) benzaldehyde which would generate colour if undiazotized aromatic amine is still present. To the diazotized product obtained, 8-hydroxyquinoline (2.012 g, 13.95 mmoles) was added very slowly with vigorous stirring over 15 min. The reaction mixture was further stirred for 1 h and left to stand overnight. A reddish orange coloured precipitate of (2-Hydroxy-naphthalen-1-ylazo)-benzoic acid (3ABBNHQ or 4ABBNHQ) was observed which was purified by column chromatography (Scheme 3.1).

Scheme 3.1. Synthesis of azoquinolines by diazotisation and coupling reactions

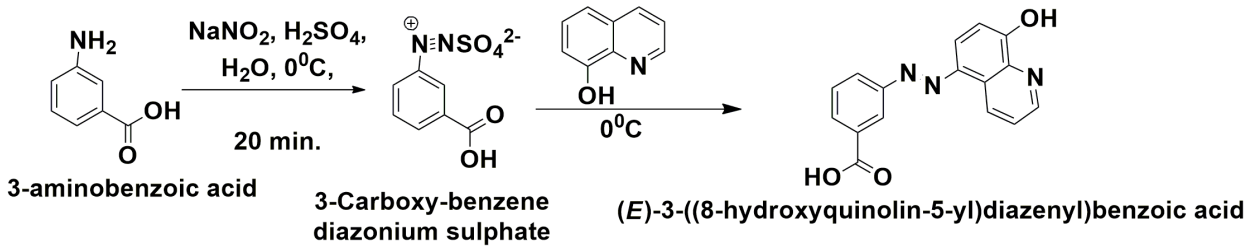

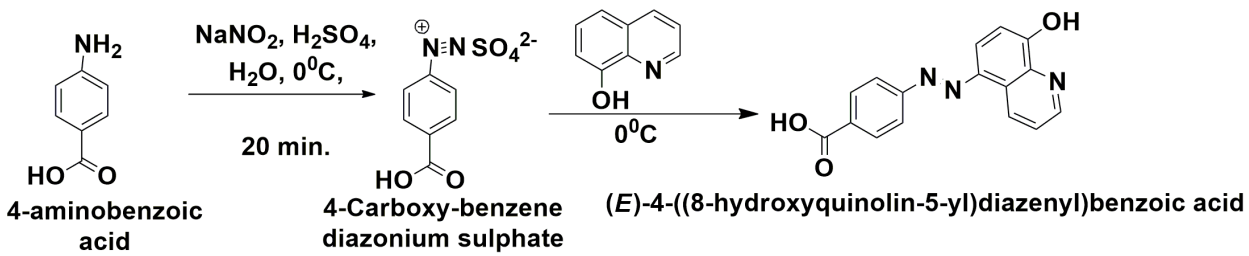

3.2.1.2. ZnO-azoquinoline composites

Typical synthesis procedure for ZnO NPs is described in chapter 2 in section 2.2.1.1. 3ABBNHQ or 4ABBNHQ (23 μmol) was added in-situ during the synthesis of ZnO to the alkaline zinc acetate solution (0.142 mmoles) just after the solution becomes clear indicating formation of ZnO NPs. The solution was stirred in methanol at RT for 1 h. The product (ZnO-3ABBNHQ or ZnO-4ABBNHQ composites) was washed with methanol, centrifuged and collected.

3.2.2. Instruments for Characterization

The principles and instrumentation of all the techniques used throughout the work for structural and photophysical characterizations are briefly discussed in the Appendix 1. The details of the procedures used for PXRD, TEM, IR, Raman, UV-vis, Photoluminescence, Lifetime, NMR, Electrochemical measurements, Elemental analysis and Zeta potential measurement are same as those described in chapter 2 in section 2.2.2.

3.2.2.1. Photocatalytic activity measurements

The set up for photocatalytic activity measurement used was the same as that described in chapter 2 in the section 2.2.2.1.

3.2.2.2. Computational Studies

DFT theoretical calculations for the ZnO NPs and the dye molecules are briefly discussed in Appendix 3.

3.3. Results and Discussion

3.3.2. Structural Characterization of Azoquinolines

Elemental analysis of 3ABBNHQ and 4ABBNHQ was carried out to confirm the purity and the observed CHN values match calculated values.

calcd(%): C 65.30, H 4.08, N 14.28; found (%): C 63.30, H 4.03, N 14.25

calcd(%): C 65.30, H 4.08, N 14.28; found (%): C 63.32, H 4.06, N 14.21

Structure of the dyes was confirmed by ^{1}H NMR, ^{13}C and DEPT (spectra given in Appendix 4-Figures 3 and 4). 3ABBNHQ: 6.86 ppm (multiplet, -CH aromatic proton near to the hydroxyl group attached carbon of the quinoline ring), 7.11-7.29 ppm (multiplet, -CH aromatic protons attached to the imine substituted quinoline ring), 7.40-7.50 ppm (doublet, -CH aromatic proton attached to the hydroxyl substituted quinoline ring), 7.60-7.90 ppm (multiplet, -CH aromatic protons connected to the azobenzene ring), 8.07-8.27 ppm (doublet, -CH aromatic protons connected near to the –N=N and carboxyl group substituted carbon of the benzene ring), 8.48 ppm (singlet, aromatic proton in the benzene ring (between –C-N=N and –C-COOH linkages)), 8.80-8.92 ppm (multiplet, -CH aromatic protons near to the quarternary carbon and imine group of the quinoline ring) and 9.28 ppm (singlet, hydroxyl proton of carboxylic acid azobenzene ring).

3ABBNHQ: ^{1}H NMR (500MHz, $CDCl_3$) δ ppm:

6.86 (1H, m), 7.11-7.29 (1H, m), 7.32-7.34 (1H, m), 7.40-7.50 (1H, d, J =4.2 Hz), 7.60-7.90 (1H, m), 8.07-8.27 (2H, d, J = 7.8 Hz), 8.48 (1H, s), 8.80-8.92 (1H, m), 9.28 (1H, s)

^{13}C (125MHz, $CDCl_3$) δ ppm :

168.28, 152.68, 148.92, 147.65, 145.75, 137.68, 13742, 131.84, 129.13, 128.02, 123.17, 121.89, 119.10, 118.05, 116.26, 111.75

A similar spectrum is obtained for 4ABBNHQ and the peaks are assigned as follows: 6.70 ppm (-CH aromatic proton near to the hydroxyl group in the quinoline ring), 7.35- 7.49 ppm (imine substituted quinoline ring), 7.64-7.69 ppm (hydroxyl substituted quinoline ring), 7.85-7.98 ppm (protons attached near to the –C-N=N linkage of azobenzene ring) 8.00- 8.10 ppm (-CH attached to –C-COOH linkage of azobenzene ring), 8.93 ppm (near to the quaternary carbon of the quinoline ring), 9.00 ppm (near to the imine group in the quinoline ring) and 9.46 ppm (carboxylic hydroxyl proton).

4ABBNHQ: ^{1}H NMR (500MHz, DMSO-d_6) δ ppm:

6.70 (1H, m), 7.35-7.49 (1H, m), 7.64-7.69 (1H, m), 7.85-7.98 (2H, m), 8.00-8.10 (2H, m), 8.93 (1H, m), 9.00 (1H, m), 9.46 (1H, s)

^{13}C (125MHz, DMSO-d_6) δ ppm:

166.14, 147.52, 145.66, 143.88, 142.42, 129.68, 129.09, 128.83, 120.41, 119.11, 116.88, 114.39, 113.58

In IR spectrum of 3ABBNHQ, the aromatic C-H stretching appears at 3079 cm^{-1} and the band for C=C stretching vibration is assigned at 1597 cm^{-1}. A broad band was observed in the region between 3436 and 3430 cm^{-1} due to asymmetric and symmetric O-H stretching modes. The C=N stretching vibrations appear at the region of 1640 cm^{-1}. The weak broad peak at 3743 cm^{-1} is designated to O-H stretching. The band at 1718 cm^{-1} is assigned to the C=O stretching vibration present in carboxylic acids. The peak at 1476 cm^{-1} is attributed to O-H plane bending. The vibrations appearing at 1469, 1322 and 1314 cm^{-1} correspond to the N=N, C-N and C-O stretching vibrations. The sharp bands at 1220 and 1014 cm^{-1} are observed with alcohol C-O stretching. The aromatic C-H plane bending appears at 1126 cm^{-1}. A strong absorption peak at 885 cm^{-1} is ascribed to the C-H bending of phenyl ring and C-H out of plane bending to 766 cm^{-1}.

For 4ABBNHQ also a similar pattern is observed with bands assigned at 1640 cm^{-1} and 1714 cm^{-1} attributed to the C=N and carboxylic C=O stretching vibrations respectively. The absorption band at 1495 cm^{-1} is assigned to O-H plane bending. The vibrational bands at 1410, 1320 and 1300 cm^{-1} correspond to the N=N, C-N and C-O stretching vibrations. Alcoholic C-O stretching is observed as sharp bands at 1223 and 1005 cm^{-1}. The aromatic C-H plane and C-H plane of phenyl ring bending vibrations appear at 1119 cm^{-1} and 881 cm^{-1}. The C-H out of plane bending vibrational band occurs at 765 cm^{-1} (Figure 3.1).

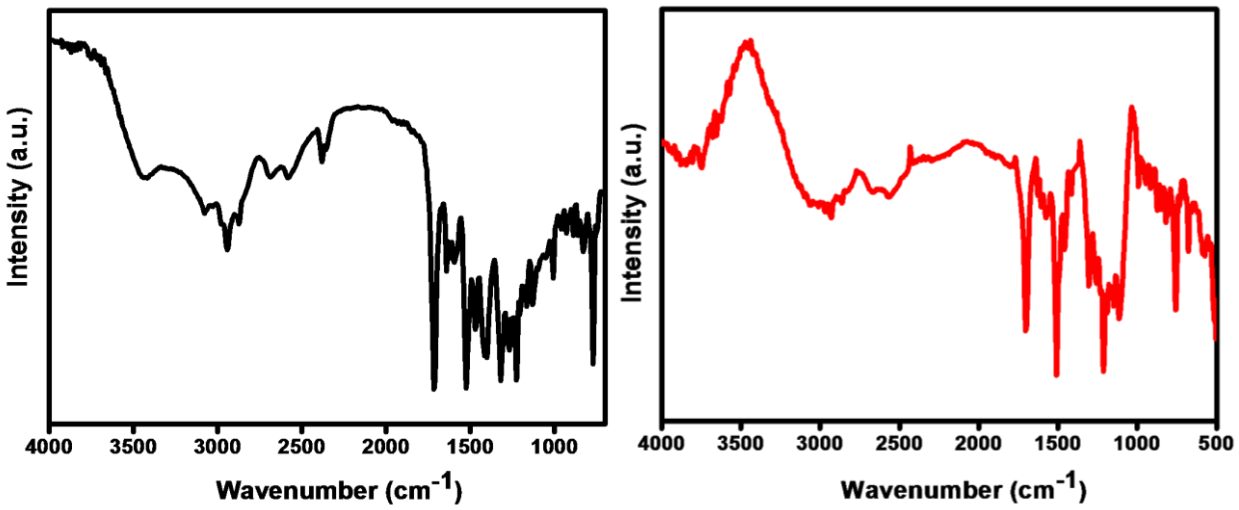

Figure 3.1. IR spectrum of 3ABBNHQ (left) and 4ABBNHQ (right).

The most intense Raman fundamentals of 3ABBNHQ appear at 430, 705, 1652, 1695, 1763 cm^{-1} followed by a few weak modes at 489,603, 1256, 1382 cm^{-1}. In 4ABBNHQ, 427, 595, 710, 1257, 1384, 1653, 1702 and 1774 cm^{-1} are intense Raman bands and 489 and 1114 cm^{-1} are weak Raman modes (Figure 3.2).

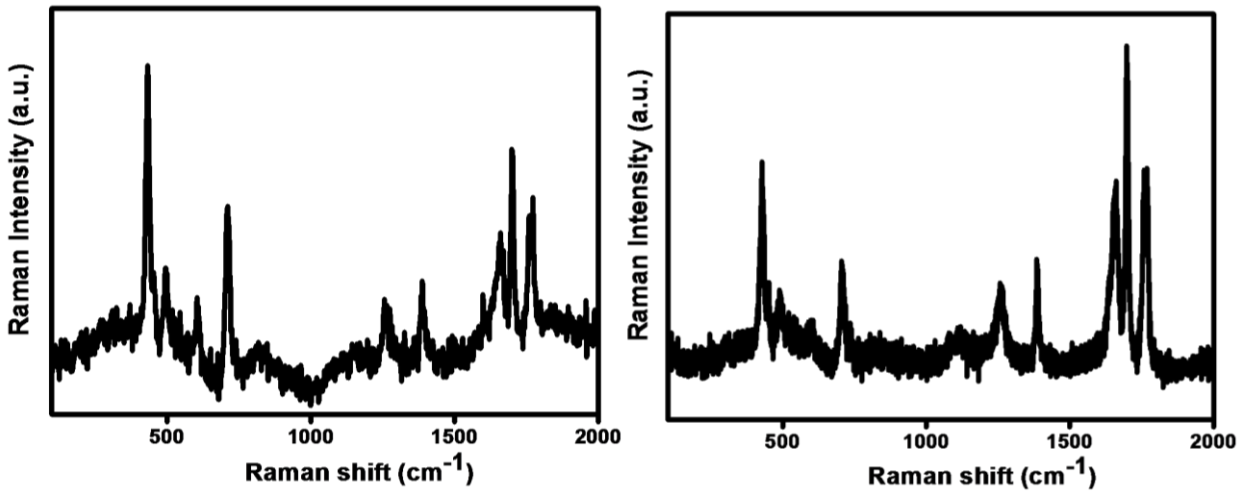

Figure 3.2. Raman spectrum of 3ABBNHQ (left) and 4ABBN8HQ (right).

3.3.3. Photophysical Characterization of Azoquinolines

The absorption spectra of 3ABBNHQ and 4ABBNHQ show typical features of azoquinolines with two prominent peaks, one in UV region and the other in the visible region. The characteristic absorption bands of 3ABBNHQ are observed at 320 and 405 nm with a broad peak at ~475 nm and for 4ABBNHQ, the spectral bands are at 320, 420 and 500 nm (Figure 3.3).

It is to be noted that the absorption peak in the visible region is less intense in para-analogue compared to meta analogue which may be due to difference in tautomer concentrations as explained in Scheme 3,2. Both azo and hydrazone tautomeric forms are possible in azoquinoline benzoic acid (Figure 3.4). Consequence of this is the existence of facile electron transfer pathways between the chromophoric N=N group and the chelating hydroxyimino group in the azoquinoline dye. Normally in substituted azo compounds, the azo form is more predominant than the hydrazone form as we move from polar to non-polar solvents. These two tautomers are manifested in the absorption spectra as the UV

and visible bands respectively. In 3ABBNHQ, it is noticed that the absorption band intensity of the hydrazone form (~ 400 nm) is visible only in polar solvents. This suggests that the dye exists in azo and hydrazone forms in polar solvents. However, in 4ABBNHQ the spectral profile is constant with the change in solvent polarity and the intensity of visible region peak is less, indicating its existence as azo form rather than the hydrazone form (Figure 3.4) [9-11].

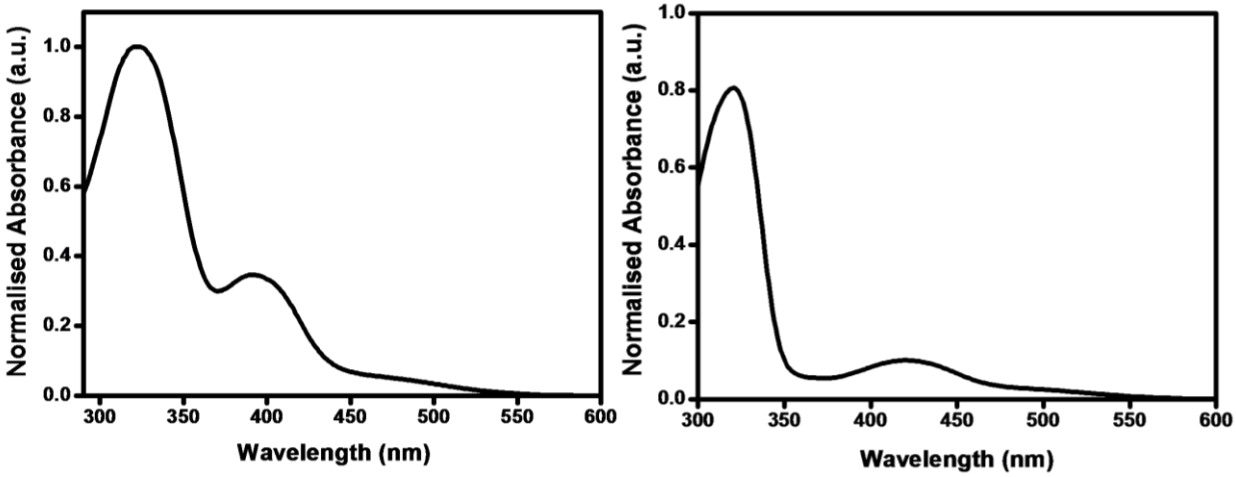

Figure 3.3. UV-vis spectrum of 3ABBNHQ (left) and 4ABBNHQ (right).

Scheme 3.2. Resonance structures of azoquinolines (3ABBNHQ and 4ABBNHQ)

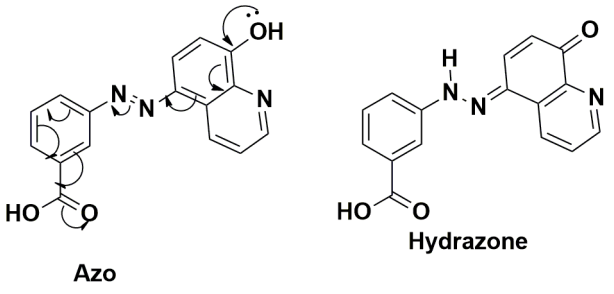

(*E*)-3-(2-(8-oxoquinolin-5(8*H*)-ylidene)hydrazinyl)benzoic acid

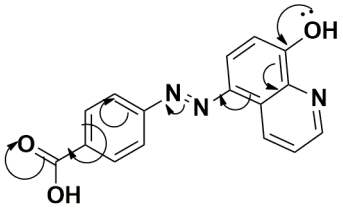

(*E*)-4-((8-hydroxyquinolin-5-yl)diazenyl)benzoic acid

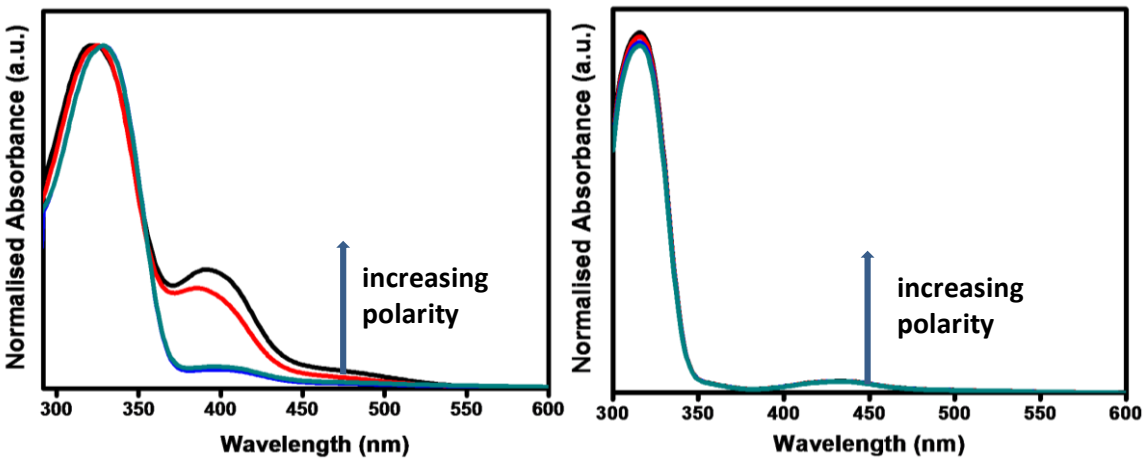

Figure 3.4. UV-vis spectrum of 3ABBNHQ (left) and 4ABBNHQ (right) in ethanol(black) and acetonitrile (red) : polar and DCM (blue) and toluene (cyan) :non-polar solvents.

Both compounds are found to have highly intense emission peaks in the far UV or blue region. The excitation spectra also indicate that the characteristic absorption peak is the one at UV region (S0 ⟵ S1 at 350-400 nm) (Figure 3.5). The emission peak of meta-substituted dye is broader than that of 4ABBNHQ along with a substantial enhancement in Stoke's shift (100 nm for 3ABBNHQ and 50 nm for 4ABBNHQ). Abnormal Stokes shift normally occurs when the molecule upon excitation loses some amount of absorbed energy as molecular collisions, excited state proton transfer, intramolecular charge transfer between the azo and hydrazone tautomeric forms (part of the molecule acts as a donor which absorbs light and the other part of the molecule acts as an acceptor which emits light), change in dipole moment in polar environments and thermal energy. An intramolecular charge transfer to the excited state hydrazone form is possible in case of 3ABBNHQ since hydrazone tautomer also is observed. The excited azo state right after the excitation can undergo relaxation in the presence of the solvent cage around it and this leads to a red shift in the emission. Usually this will show up as a Stokes shift that increases with the solvent polarity which is highly reflected in the absorption spectra of 3ABBNHQ compared to 4ABBNHQ. Hence, it can be envisaged that more efficient electron transfer occurs in para-substituted dye without much loss due to alternative pathways.

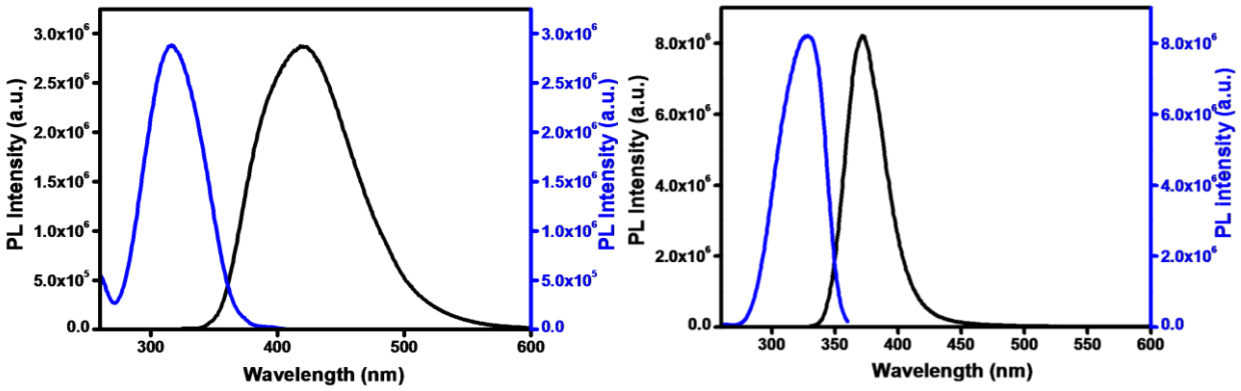

Figure 3.5. Emission (black) and excitation (blue) spectra of (left) 3ABBNHQ (λexc=320 nm and λems=420 nm) and (right) 4ABBNHQ (λexc=320 nm and λems=370 nm).

3.3.4. Structural Characterization of ZnO-azoquinoline composites

Powder X-ray diffraction patterns show that the parent wurtzite phase of ZnO NPs is not distorted in the case of ZnO-3ABBNHQ and ZnO-4ABBNHQ composites during the surface grafting (Figure 3.6).

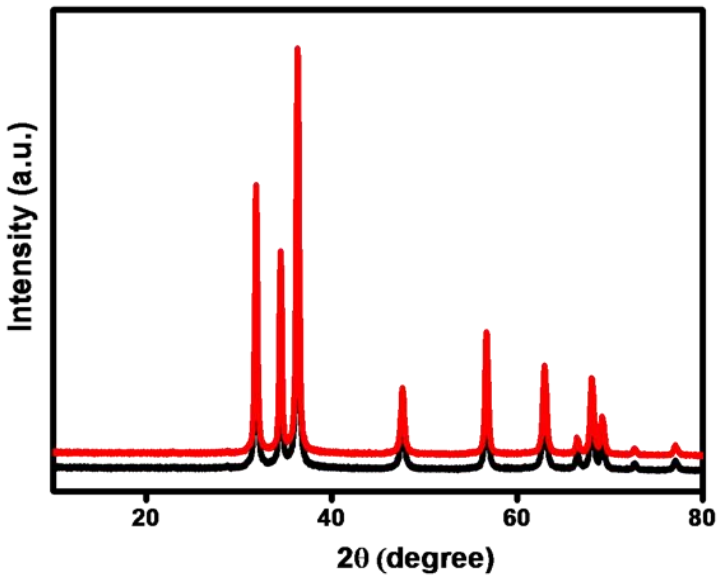

Figure 3.6. XRD patterns of ZnO-3ABBNHQ (black) and ZnO-4ABBNHQ (red) composites.

From zeta potential measurements, surface charges of the composites were found to be -26 and -30 mV for 3ABBNHQ and 4ABBNHQ respectively when compared to 4 mV for naked

ZnO. TEM images of the surface modified ZnO NPs were found to be well separated from each other with particle size of 3.5±1.5 nm and the corresponding histogram is also shown as an inset along with the TEM images (Figure 3.7). From these observations, it is clear that the grafting has stabilised the ZnO NPs against agglomeration and solution ripening.

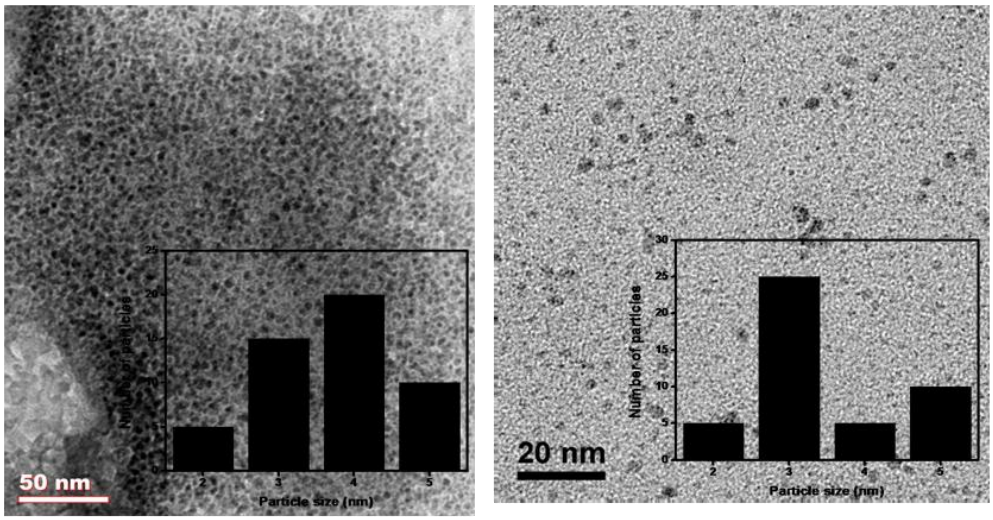

Figure 3.7. TEM images of ZnO-3ABBNHQ (left) and ZnO-4ABBNHQ (right) composites with the corresponding histograms as inset.

FTIR spectroscopic studies unambiguously support anchoring of the dyes (3ABBNHQ and 4ABBNHQ) to ZnO through both carboxylic group as well as imine and hydroxyl group (Figure 3.8). IR spectra of the grafted ZnONP with the 3ABBNHQ ligand shift the intense –C=O stretching vibrational frequency of the carboxylic moiety from 1718 to 1605 cm^{-1}. The band near 1640 cm^{-1} for C=N group in the case of dye is shifted to lower frequency 1550 cm^{-1} in the spectra of composites. Also, the same behavior is observed for ν_{C-N} band; 1322 cm^{-1} for dye is red shifted to 1305 cm^{-1} in the composite. Both N=N(azo) stretch (1469 to 1399 cm^{-1}) and C-O(carboxylic) stretch (1314 to 1304 cm^{-1}) also undergo change in frequencies. The analysis also shows characteristic bands at 1572, 1118 and 977 cm^{-1} which are attributed to the vibrations of ZnO with slight shift in values as 1547, 1167, and 904 cm^{-1} for the composite. The absence of a broad characteristic peak in the region between 3436 and 3430 cm^{-1} corresponding to the O-H stretching vibration confirmed the ZnO-O bond was formed. Similar variations were observed with 4ABBNHQ also, when it

gets grafted with ZnO. The intense –C=O stretching vibrational frequency of the carboxylic moiety shifts from 1714 cm^{-1} in 4ABBNHQ to 1611cm^{-1} on grafting. The bands near 1640 cm^{-1} and 1320 cm^{-1} corresponding to C=N and C-N group attached to the quinoline ring in the dye molecule are also shifted to lower frequency 1533 cm^{-1} and 1309 cm^{-1} in the spectra of ZnO-dye composites. Equally, N=N (azo) stretch (1495 to 1363 cm^{-1}) and C-O (carboxylic) stretch (1300 to 1230 cm^{-1}) also undergo a change in frequencies on grafting. The broad characteristic peak of hydroxyl group between 2956 and 2033 cm^{-1} vanishes due to the formation of ZnO-O bond in the case of composites. So, we can conclude from the IR spectrum that the ZnO has been coordinated to both the carboxylic as well as the quinoline entities in both the ligands (Figure 3.8).

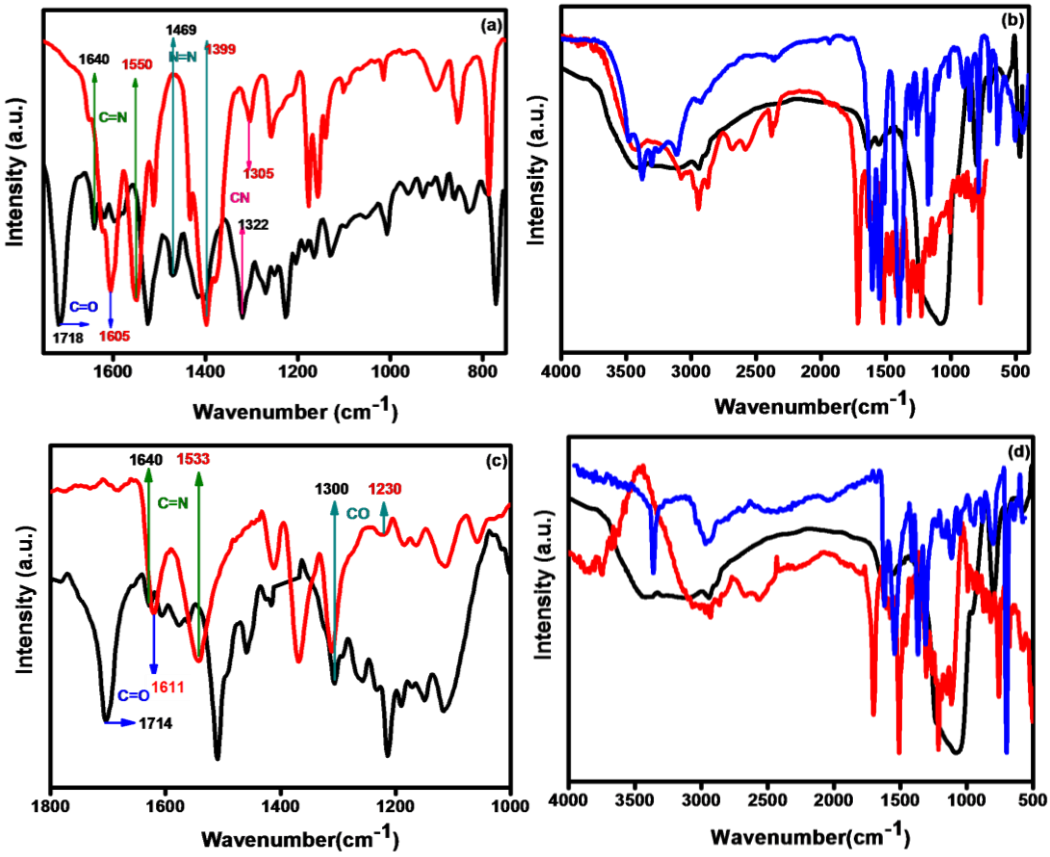

Figure 3.8. FT-IR spectrum of (a) 3ABBNHQ (black) and ZnO-3ABBNHQ composite (red), (b) full-scale spectra of ZnO (black), 3ABBNHQ (red) and ZnO-3ABBNHQ composite (blue),(c) 4ABBNHQ (black) and ZnO-4ABBNHQ composite (red) and (d) full-scale spectra of ZnO (black), 4ABBNHQ (red) and ZnO-4ABBNHQ composite (blue).

3.3.5. Photophysical characterizations of ZnO-3ABBNHQ and ZnO-4ABBNHQ composites

On anchoring the dyes (3ABBNHQ or 4ABBNHQ) to ZnONP, substantial changes are observed in the absorption spectra and emission spectra in terms of peak intensities, even though basic characteristics of the composite spectra resemble the dyes rather than ZnO and no absorption feature (absorption edge at ~ 350 nm) of ZnO is seen in the composite (Figure 3.9). The photophysical experiments were carried out for molecules and composites (9.04 x 10^{-4} M and 1.69 x10^{-3} + 9.04 x 10^{-4} M respectively) at room temperature.

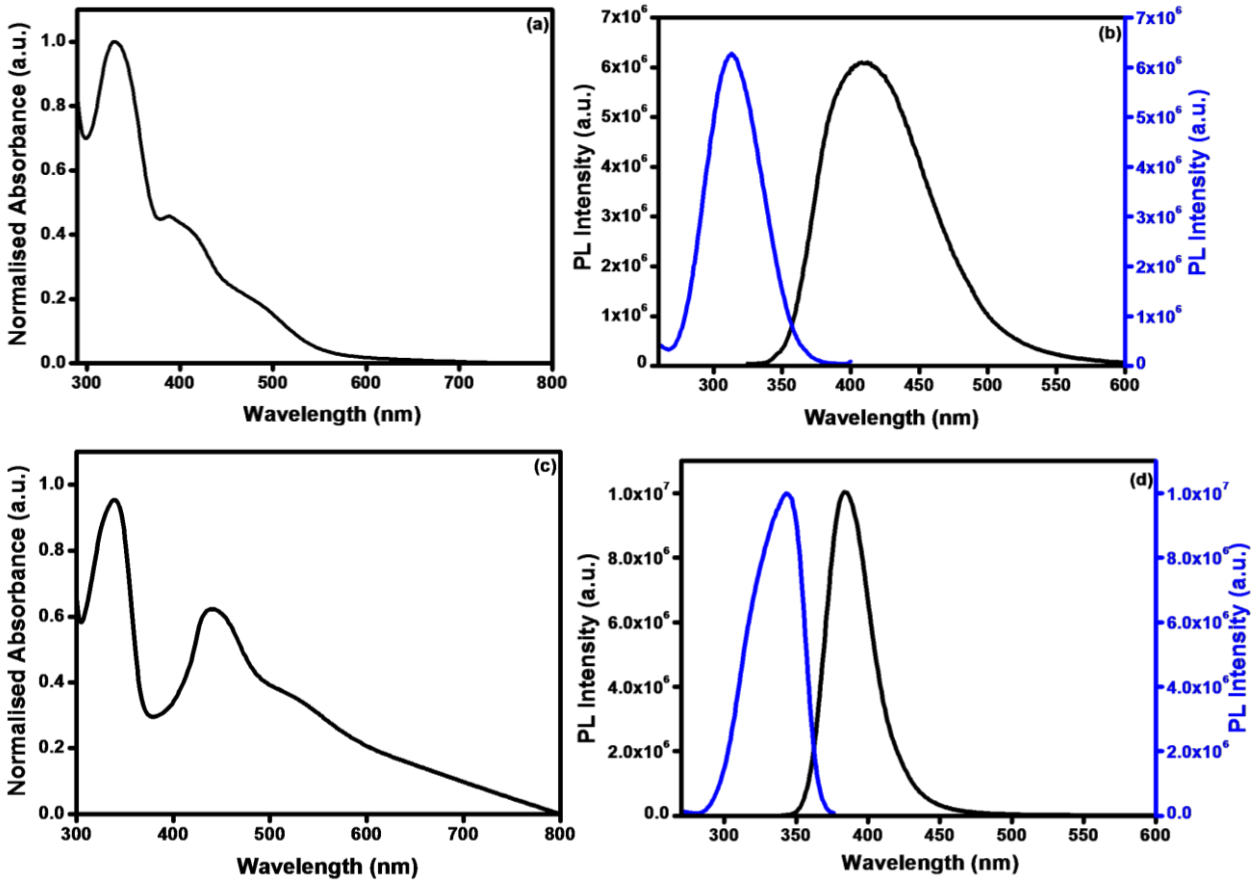

Figure 3.9. UV-vis spectrum of (a) ZnO3ABBNHQ, (b) emission (black) and excitation (blue) spectra of ZnO3ABBNHQ (λexc=330 nm and λems=410 nm), UV-vis spectrum of (c) ZnO4ABBNHQ and (d) emission (black) and excitation (blue) spectra of ZnO4ABBNHQ (λexc=340 nm and λems=380 nm).

The 320 and 405 nm absorption bands of the 3ABBNHQ have been shifted to 330 and 420 nm whereas in 4ABBNHQ, 320 and 420 nm spectral bands shifted to 340 and 442 nm. Substantial enhancement of the visible absorption is observed for both the composites when compared to the corresponding pristine dyes. It is already observed that 4ABBNHQ has less intense visible absorption peak (UV peak intensity:visible peak intensity =1:0.1) when compared to 3ABBNHQ (UV peak intensity:visible peak intensity =1:0.4). However, on anchoring to ZnO, absorption in visible region increases 5 fold in case of 4ABBNHQ while that of 3ABBNHQ only doubled. It can also be observed that anchoring of 4ABBNHQ on ZnO has rendered a composite with very broad absorptions ranging from UV (300 nm) to visible region (700 nm). The composites are anticipated to have electron transfer characteristics which can be discerned from the emission spectra. Interestingly, defect green emission of ZnO is completely suppressed unlike in case of azonaphthols. The intensity of the characteristic dye emission peak seen in the composite increases drastically which indicates an electron transfer from ZnO to dye under UV light in both the cases. The absence of any observable enhancement in band gap emission of ZnO, which is expected at ~ 360 nm, also corroborates this observation. The excitation spectra of the composites are shown in Figure 3.9. No change in Stokes shift was observed in the composites when compared to pristine dyes, indicating that the dye characteristics remain the same in the composites.

For lifetime measurements, decay curves were obtained by the time-correlated single-photon counting (TCSPC) technique using a HORIBA Jobin Yvon Nano-LED source with wavelength 320 nm. Decay measurements were carried out at emission wavelengths of 420 (3ABBNHQ), 410 (ZnO-3ABBNHQ), 370 (4ABBNHQ) and 380 nm (ZnO-4ABBNHQ). These experiments were carried out for ZnO NPs (1.69 $x10^{-3}$ M), 3ABBNHQ (9.04 x 10^{-4} M), ZnO-3ABBNHQ composite (1.69 $x10^{-3}$ + 9.04 x 10^{-4} M), 4ABBNHQ (9.04 x 10^{-4} M) and ZnO-4ABBNHQ composite (1.69 $x10^{-3}$ M, 9.04 x 10^{-4} M and 1.69 $x10^{-3}$ + 9.04 x 10^{-4} M) at room temperature. In both the systems, analysis of the lifetimes of the dye and the composite reveals a marginal increase in lifetime of the dye emission on anchoring (Tables 3.1). ZnO exciton and defect emission decay profiles exhibit a triexponential fit suggesting that as particle size decreases, there is a possibility of emergence of multiple donor and acceptor

sites. However, the decay profiles of characteristic emission peak of ~ 400 nm seen in both dye molecules and the composites could be deconvoluted on a bi-exponential fit, which evidences that the composite has more of dye features than that of the ZnO. This behaviour is very different from the azonaphthol-ZnO composite in which electron transfer is observed from the dye to the ZnO defect sites inducing a stabilising effect also observed in defect emission lifetime. On the contrary, in the present dye systems, defect sites are completely suppressed and it can be assumed that electron transfer occurs between the dye and the conduction band of ZnO. Since the defect emission is fully suppressed, we did not proceed further with analysis in the visible region. From the steady state studies, it was observed that the emission intensity increased in case of the composites when compared to that of the dyes which is clearly reflected in the increment in average lifetime of the composite (Figure 3.10).

Table 3.1. Lifetime parameters of 3ABBNHQ dye, ZnO-3ABBNHQ Composite, 4ABBNHQ dye and ZnO-4ABBNHQ composite.

System	Experimental Setup	Lifetime (ns)		
		$\tau1(a1)$	$\tau2(a2)$	$<\tau>$
3ABBNHQ	λex=320 nm λem=420 nm	0.21 (0.55)	11.1 (0.45)	5.08
ZnO-3ABBNHQ	λex=320nm λem=410 nm	1.98 (0.38)	11.7 (0.62)	8
4ABBNHQ	λex=320nm λem=370nm	0.17 (0.94)	0.75 (0.06)	0.21
ZnO-4ABBNHQ	λex=320nm λem=380nm	0.32 (0.99)	4.9 (0.01)	0.36

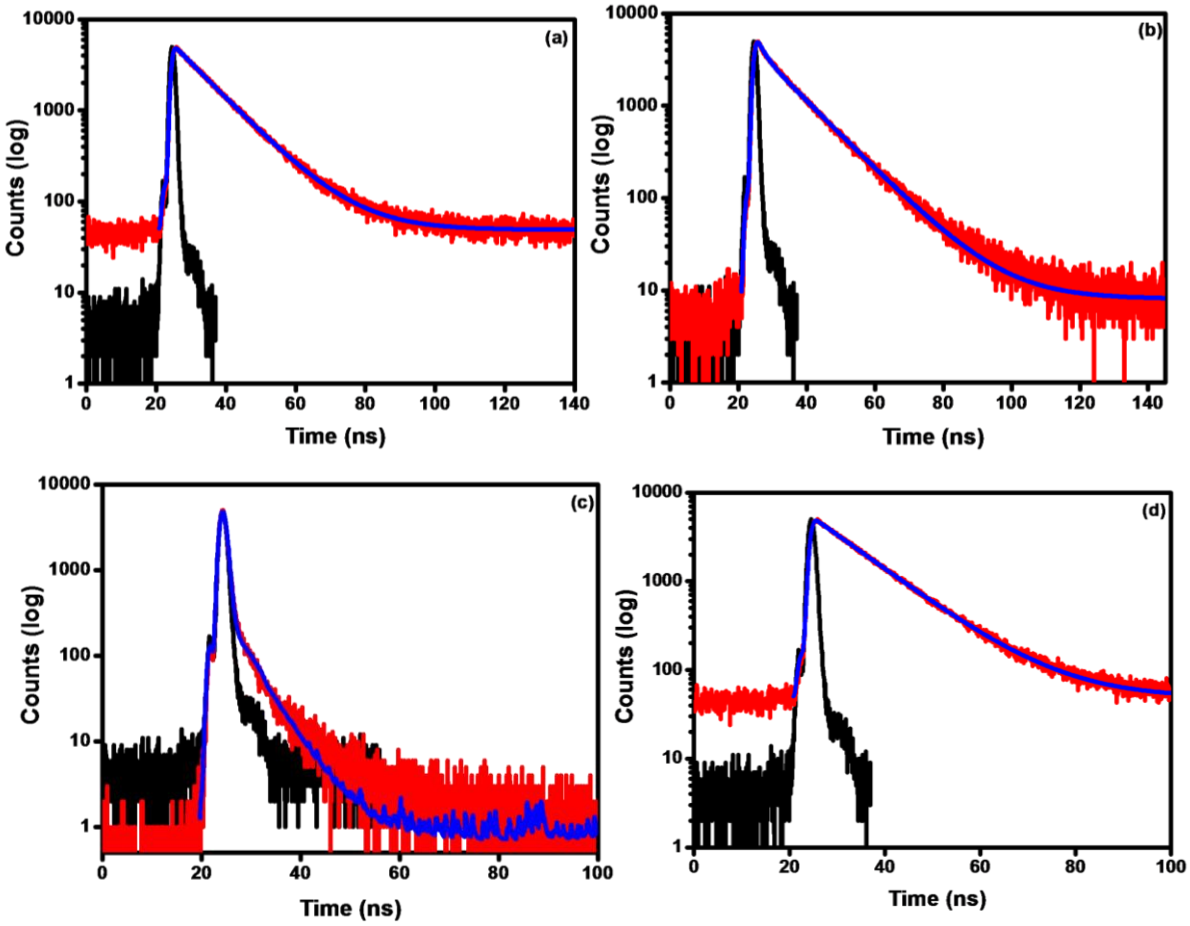

Figure 3.10 . The emission decay profiles on excitation at 320 nm of (a) 3ABBNHQ and (b) ZnO-3ABBNHQ Composites, (c) 4ABBNHQ and (d) ZnO-4ABBNHQ Composite. Instrument response function in black, decay profile in red and experimental fit in blue.

The oxidation–reduction and the electron transfer properties of the samples were also investigated by cyclic voltammetry (Figure 3.11). An electron transfer mechanism at play is very well observed by electrochemical studies of the composite in comparison with pristine dye and ZnO. The onset potential and current are found to be considerably enhanced on grafting when compared to ZnO and dyes [ZnO (0.0075 mA at the onset potential of 1 V), 3ABBNHQ (0.0069 mA at onset potential of 0.75 V) and ZnO-3ABBNHQ Composite (0.014 mA at onset potential of 1.31 V)], 4ABBNHQ (0.0079 mA at onset potential of 0.94 V) and ZnO-4ABBNHQ Composite (0.0103 mA at onset potential of 1.34 V). LSV measurements were conducted at a scan rate of 10 mV/s and . The photocurrent response was found to be enhanced in the case of composite under illumination compared

to dark. This clearly shows that electron transfer is happening in the composite due to the presence of acceptor levels necessary for the crucial electron transport. This enhancement in the photocurrent under illumination (200W tungsten lamp) shows a light induced electron transfer. The effect of the electron transport at the interfaces on the ZnO-dye composites under 200W tungsten lamp can be investigated by electrochemical impedance spectroscopy (EIS). The Nyquist plots suggest that the composite under light has the fastest electron transfer because of low resistance. The resistance was also found to be less under illumination (1470 Ω for ZnO-3ABBN and 1440 Ω for ZnO-4ABBN) compared to the dark condition (1495 Ω for ZnO-3ABBN and 1460 Ω for ZnO-4ABBN). This clearly explains that the composite is highly conducting and faster electron transporter under illumination. Photocurrent response of the composite measured by linear sweep voltammetry (LSV) (by scanning in a potential window of -0.5 to 1.7 V) and Impedance analysis under irradiation and in dark is given in Figures 3.12 and 3.13). From both the techniques, we observe a marked enhancement in conductivity under irradiation indicating charge transfer phenomenon between ZnO and dyes. Current increment is not observed in pristine ZnO NPs and dye on illumination [12-14].

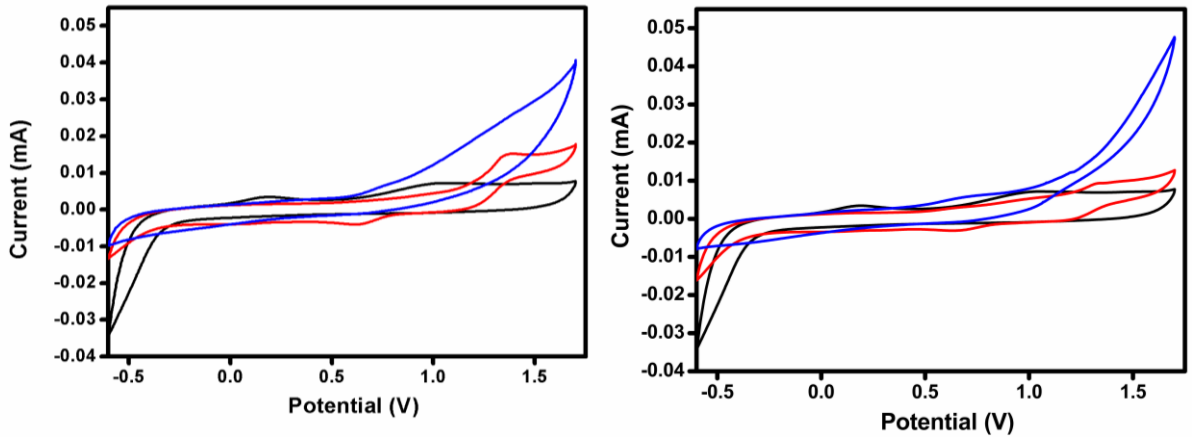

Figure 3.11. Current–voltage profile for photoelectrochemical cells employing (left) ZnO (black), 3ABBNHQ (blue) and ZnO-3ABBNHQ composite (red) and (right) ZnO (black), 4ABBNHQ (blue) and ZnO-4ABBNHQ composite (red) by cyclic voltammetry at a scan rate of 50 mv/s. Supporting electrolyte was LiClO4 in acetonitrile.

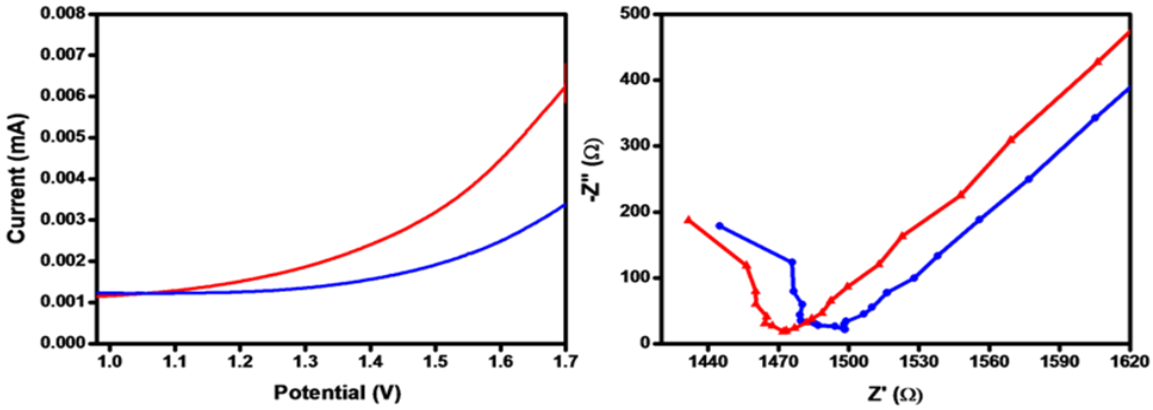

Figures 3.12. LSV profile for photoelectrochemical cells employing (left) ZnO-3ABBNHQ composites(10 mv/s) upon turning on (red) and off (blue) 200W tungsten lamp by cyclic voltammetry and Electrochemical Impedance employing (right) ZnO-3ABBNHQ composites upon turning on (red) and off (blue) 200W tungsten lamp .

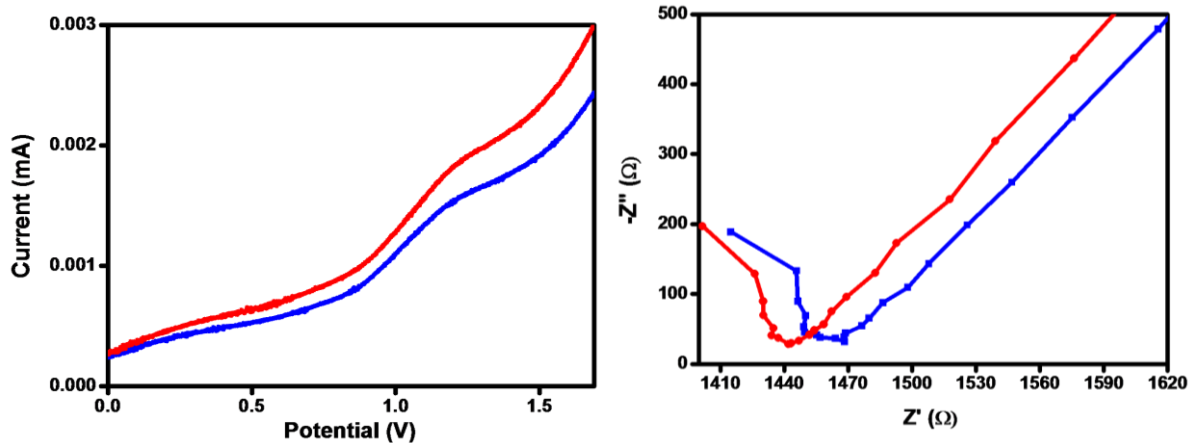

Figures 3.13. LSV profile for photoelectrochemical cells employing (left) ZnO-4ABBNHQ composites(10 mv/s) upon turning on (red) and off (blue) 200W tungsten lamp by cyclic voltammetry and Electrochemical Impedance employing (right) ZnO-4ABBNHQ composites upon turning on (red) and off (blue) 200W tungsten lamp .

3.3.6. Computational Studies

The electron transfer possibilities in the composite was studied by the interactions of the dye molecules with ZnO($10\bar{1}0$). In case of 3ABBNHQ, two configurations were considered where the dye binds to the ZnO surface through the –COOH group and through the

hydroxyl-imine group separately, since structurally connecting a single molecule to two ZnO surfaces was not feasible, However, for 4ABBNHQ this could be achieved and the computational details are more or less same for both composites (Appendix 4) .

Figures 3.14 and 3.16 show the density of states (DOS) and the wavefunctions of the frontier orbitals of the model composite with 3ABBNHQ and 4ABBNHQ. The electronic states plotted in the DOS are aligned with respect to the energy of vacuum that has been set to zero. Upon modifying the surface of the ZnO nanoparticles with dyes, the effective band gap of the interface is reduced to 1.30 eV from 3.25 eV for the clean slab making the composite visible light absorbing.

The contributions to the total DOS from the ZnO slab and the 3ABBNHQ dye are shown with red circles and blue squares respectively. The calculations show that the valence band maximum (VBM) of the interface is localized on the 3ABBNHQ dye molecule (Figures 3.14(b) and (c)) and the conduction band minimum (CBM) is localized on the slab (Figure 3.14(d)). Additionally, the wavefunction of the CBM has a weight on the O atoms of the 3ABBNHQ dye through which it binds to the ZnO slab indicating that there is a possibility of fast electron transfer from the 3ABBNHQ to the ZnO. Alignment of ZnO and 3ABBNHQ bands with each other is an important factor for facile charge transfer. From the DOS of –COOH anchoring mode of the composite, it is clear that the wavefunction corresponding to the CBM+5 (marked by (e) in Figure 3.14(a)) of the composite has considerable weight on ZnO as well as on the 3ABBNHQ dye denoting that there is strong coupling between the electronic states of the 3ABBNHQ and ZnO. Moreover this state is about 1.29 eV above the CBM of ZnO suggesting a strong driving force for electron injection. Hence we envisage that this novel electronic state might enable direct electron transfer from the 3ABBNHQ to ZnO upon visible light absorption. We rule out an indirect electron transfer mechanism (excitation within the 3ABBNHQ dye molecule followed by electron injection to ZnO) because for this an electron from VBM or VBM-1 (corresponding to the occupied frontier orbitals of the 3ABBNHQ dye) of the composite is first excited to CBM+1 (corresponding to the frontier unoccupied dye orbitals). This excited electron will then be injected to ZnO. However, the latter step depends on the driving force of electron injection and the coupling between the ZnO and the dye states. In this composite, though there is a driving force of

about 0.41 eV, the electron transfer density will be negligible due to absence of coupling between the dye and ZnO.

On quinoline anchoring, both LUMO and LUMO+1 have ZnO contributions and the possible scenario of transitions could be an excitation from LUMO of dye (C) to HOMO of dye (F) and transfer to ZnO surface (CBM+1) whose band position is aligned well (Figure 3.15). Here also, this band position is aligned to the H_2O reduction and H_2 generation. However, band position of CB of ZnO at energy lower than the water reduction potential may preclude H_2 generation under UV light in this mode of anchoring. It is interesting to note that in both modes of anchoring, the ZnO bands acting as acceptor of the excited electron from the dye lie on the surface indicating the existence of catalytic sites on the ZnO-dye interface [15-30].

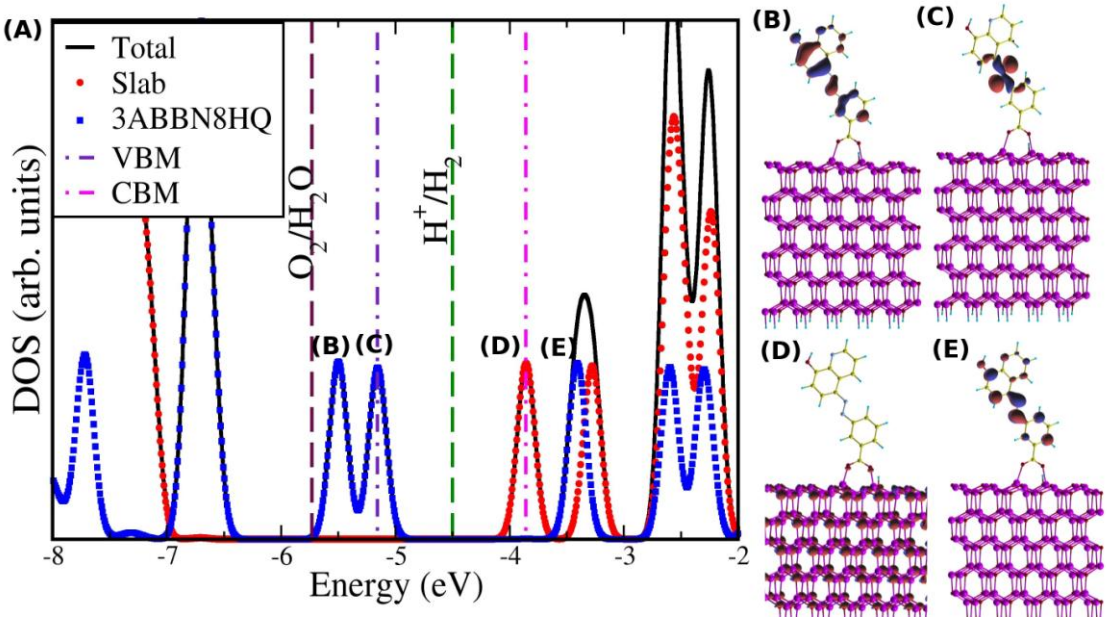

Figure 3.14. (A) DOS of the (-COOH anchoring) ZnO-3ABBNHQ dye. Dot-dashed violet and magenta vertical dashed lines mark the VBM and CBM respectively. The dashed brown and green lines mark the OP and RP. The wave functions corresponding to (B) VBM-1 (C) VBM, (D) CBM and (E) CBM+1 respectively.

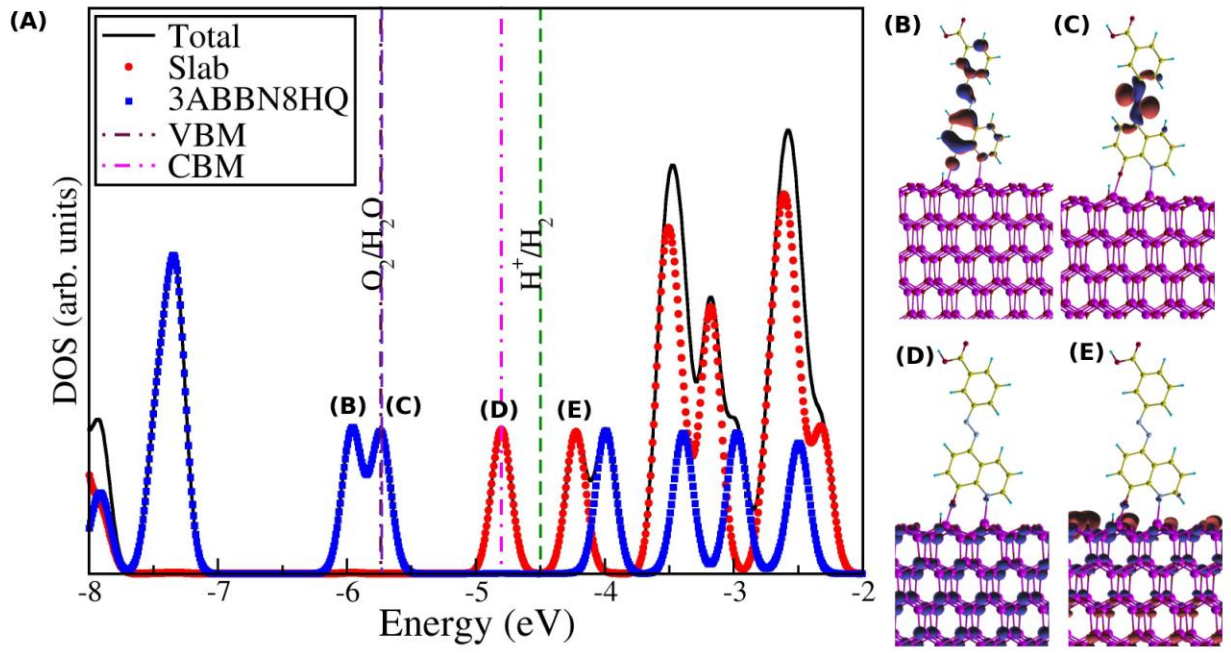

Figure 3.15. DOS of the (quinol anchoring) ZnO-3ABBNHQ dye. Dot-dashed violet and magenta vertical dashed lines mark the VBM and CBM respectively. The dashed brown and green lines mark the OP and RP.The wave functions corresponding to (B) VBM-1 (C) VBM, (D) CBM and (E) CBM+1 respectively.

Similar computational pattern is observed in the case of ZnO-4ABBNHQ composite except a dual anchoring configuration (Figure 3.16). The calculations shows that -COOH of dye binds on two Zn atoms and quinolinic N and -OH moieties with opposite side of Zn atoms as shown in (Figure 3.16). The newly formed Zn-O bond lengths are about 1.92 Å and 1.96 Å for -COOH chelating group and the newly formed Zn-O and Zn-N bond lengths are 1.92 and 2.23 Å with hydroxylamine functional group. The calculations show that the valence band maximum (VBM) of the interface is localized on the 4ABBNHQ molecule (HOMO) and the conduction band minimum (CBM) is localized on the slab (LUMO). Additionally, there is a weight of the wavefunction on the O and N atoms of 4ABBNHQ through which it binds to the ZnO slab, indicating that there is a possibility of fast electron transfer from the dye to the ZnO due to the dual anchoring model. Our hypothesis, though based on ground state band alignment, is supported by the photophysical experimental results where we have

observed well-defined peaks with enhanced intensities in the visible region of the spectrum of both the composites. The two different electron injection mechanisms are shown in Figure 3.17.

For the composite to be a good photocatalyst for water splitting, the reduction and oxidation potentials of water should align appropriately with the bands of the composite. The absolute values of the oxidation and reduction potentials are -5.73 eV and -4.5 eV, respectively. Thus, band position of ZnO surface is conducive for H_2 generation. Therefore, in addition to excitation of the dye in the visible region, ZnO excitation in UV light with electron pumping to CB can also favour H_2 generation.

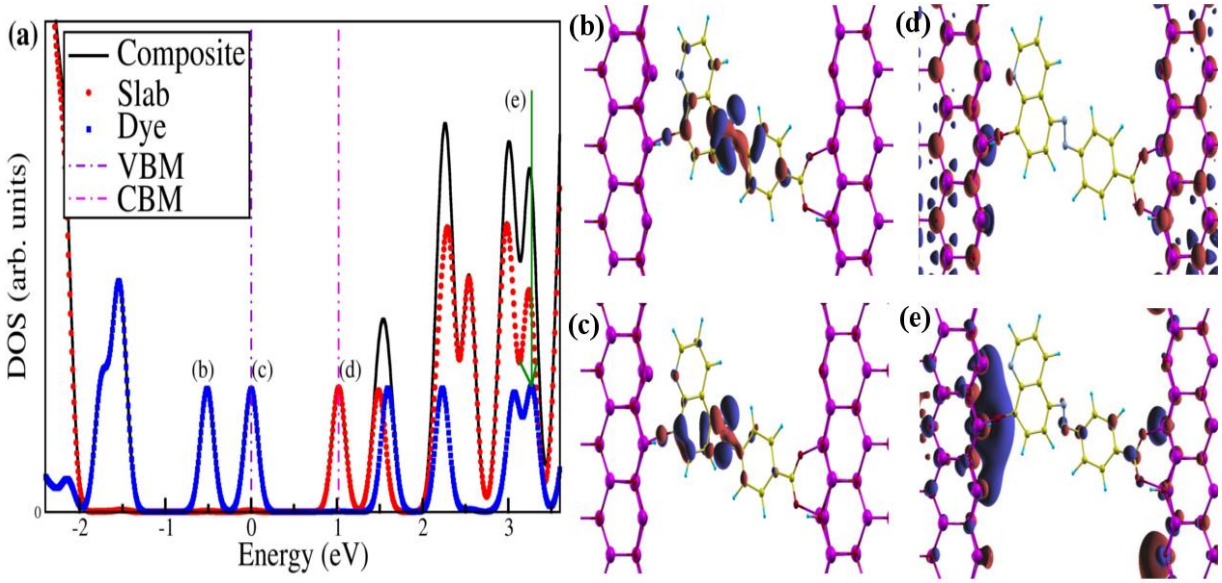

Figure 3.16. (a) Total and projected DOS for the dual anchoring configuration of the 4ABBNHQ dye on ZnO. Dot-dashed violet and magenta vertical dashed lines denote the valence band maxima (VBM) and the conduction band minima (CBM) respectively of the composite. The isosurfaces corresponding to (b) VBM-1, (c) VBM, (d) CBM, and (e) CBM+2.The green arrow highlights the coupling of the 4ABBNHQ dye empty state with ZnO.

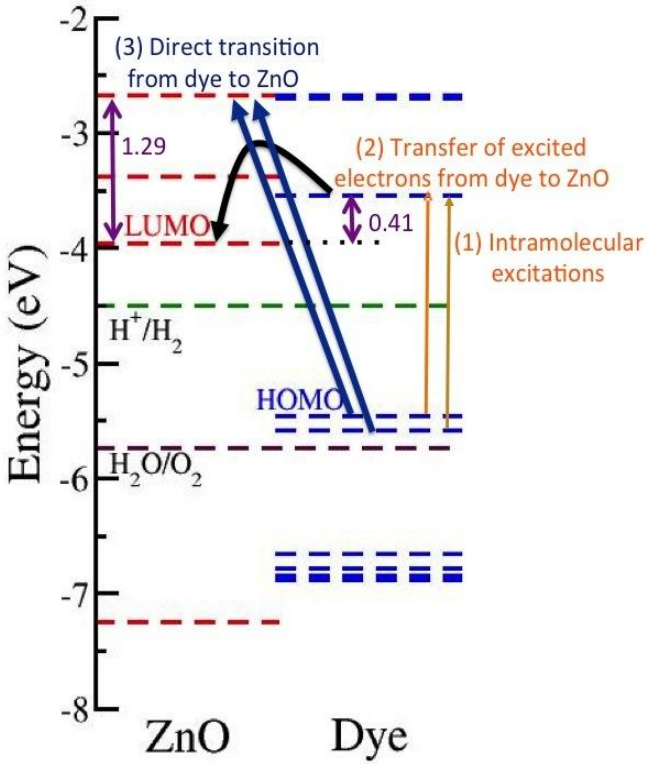

Figure 3.17. Alignment of the electronic states of ZnO and the dye molecule in the composite and schematic representation of the different possible electron transfer mechanisms due to absorption in the visible region (indirect, 1+2 and direct, 3). The energies (in eV) corresponding to the driving forces for electron injection are given in violet.

3.3.7. Photocatalytic testing of ZnO-3ABBNHQ and ZnO-4ABBNHQ Composites

A simple stability test by irradiating with visible light for long durations (8 h) indicated that ZnO-3ABBNHQ composite is stable and does not degrade as observed in case of ZnO-azonaphthol composites (Figure 3.18). This may be attributed to the multimodal anchoring and multiple electron flow pathways consequent to desirable resonance structures.

The photocatalytic water splitting activity for both the composites are tested under different irradiation sources (UV,visible and direct sunlight) for 8 h (Figure 3.19) in steady state conditions by head space analysis [31]. H_2 evolution increases steadily initially and reaches saturation at 6-8 h, which is expected in a gas closed vessel as employed here. The activity of ZnO-4ABBNHQ is ~60% more than that of ZnO-3ABBNHQ. As observed earlier,

alternative electron/energy transfer pathways like excited state charge transfer or collision etc. evidenced by broad emission peaks exists in 3ABBNHQ when compared to 4ABBNHQ. This may lead to a decrease in available electrons for reduction on ZnO/dye interface thereby reducing the activity. After 8 h, the light source was shut down, reactor purged with N_2 and irradiated again. This experiment was repeated 3 times (Figure 3.19) and the catalysts were found to be highly stable during this cycling exposure as well as regained the initial H_2 evolution rate after each purging. The higher photocatalytic water splitting activity under UV irradiation source may be due to the electron transfer from ZnO to the dye, a possibility which is also supported by the increase in intensity of the emission peak in the composites when compared to dyes. The catalytic sites could be ZnO-dye interface since pristine ZnO does not show comparative water splitting activity. But a counter increase in the visible light water splitting activity can be explained only by the enhanced visible light absorption in the composite and consequent electron transfer from the dye to the ZnO, which is very well clear from the computational studies. Solar radiation (direct sunlight), which is a combination of UV, visible and IR imparts an elevation in the water splitting activity to the composite. So these ZnO-dye composites seem to incorporate desirable features spanning UV to visible region.

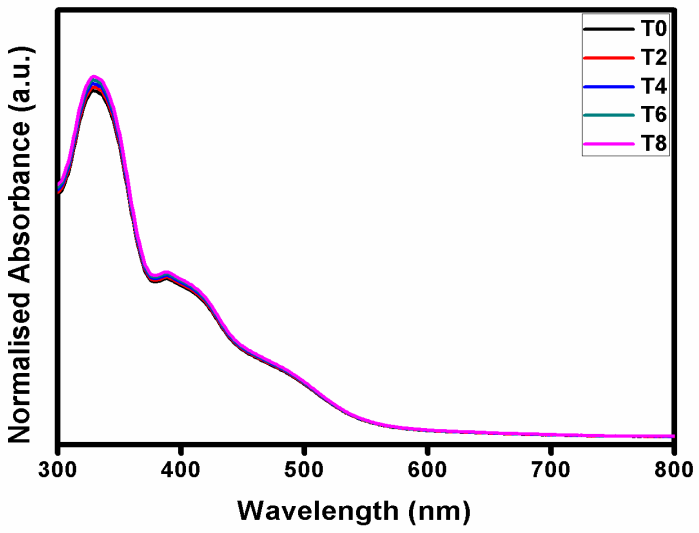

Figure 3.18. UV-vis absorption spectra of ZnO-3ABBNHQ after irradiating with visible light.

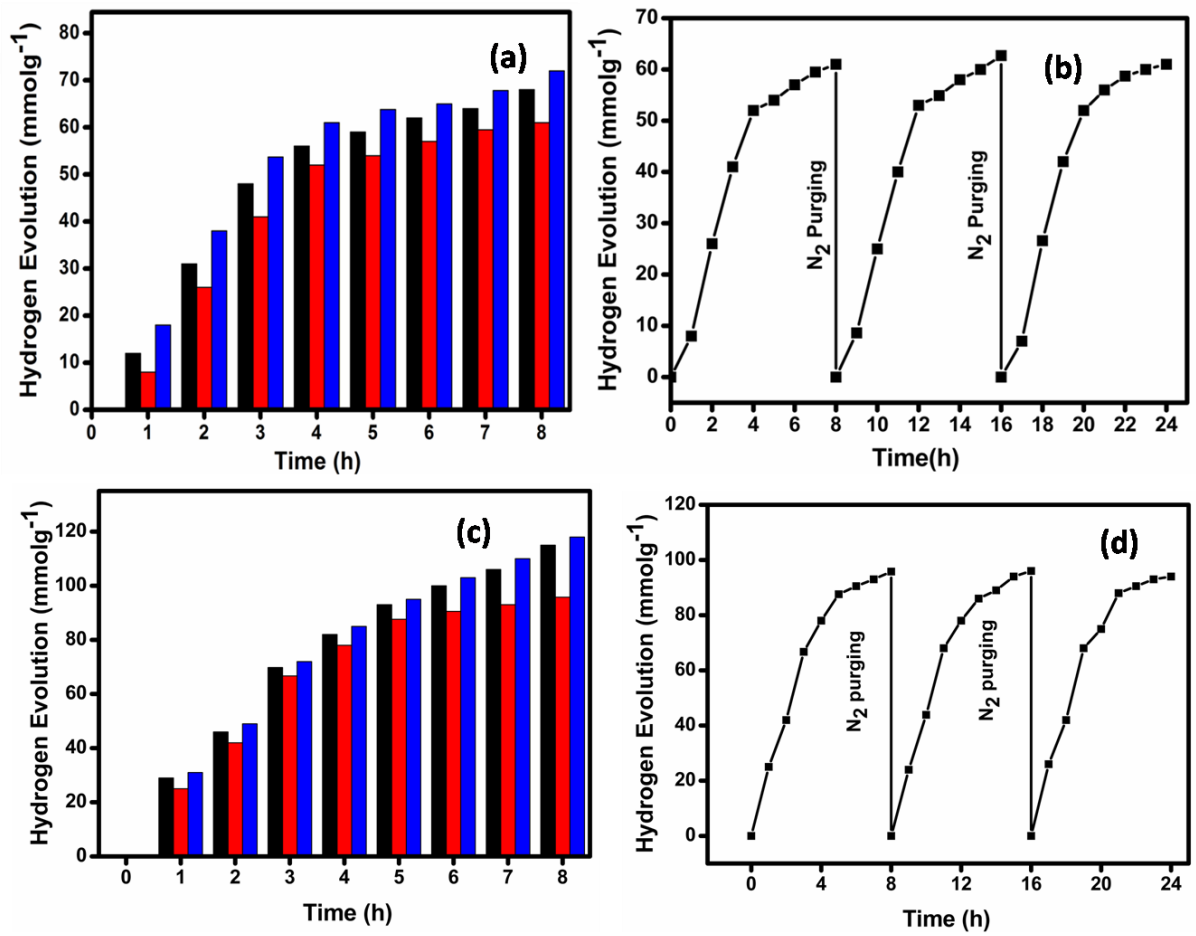

Figure 3.19. Evaluation of photocatalytic activity for H_2 generation under UV (black), visible (red) and solar (blue) at various irradiation time (0 - 8 h) (a) ZnO-3ABBNHQ Composite and (c) ZnO-4ABBNHQ Composite and H_2 evolution under visible light irradiation on repeated purging of the headspace (b) ZnO-3ABBNHQ Composite and (d) ZnO-4ABBNHQ Composite.

To see the effect of sacrificial reagent, water splitting experiments were carried out in different concentrations of methanol for both the composites and a corresponding increase in the H_2 evolution was observed as expected. However, a saturation yield for H_2 evolution was reached after 35 v/v% and further increase in methanol concentration did not affect the yield substantially (Figure 3.19).

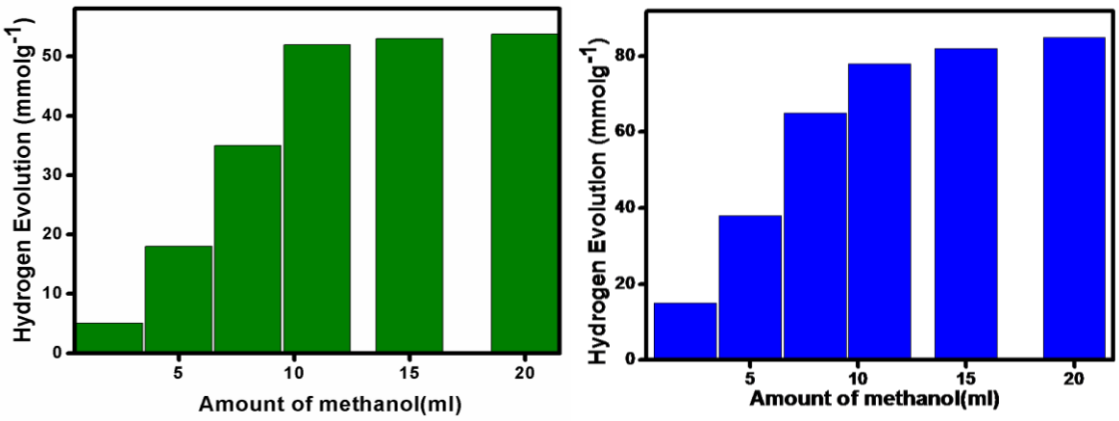

Figure 3.20. Evaluation of photocatalytic activity for H_2 generation under visible irradiation for 4 h from water-methanol mixtures with varying amounts of methanol in (left) ZnO-3ABBNHQ Composite and (right) ZnO-4ABBNHQ Composite (2,5,8, 11, 15 and 20 ml).

3.4. CONCLUSIONS

Semiconductor catalysed photocatalytic water splitting can reach its potential with appropriate design of visible light sensitisers. In this study, we have used two dye molecules capable of multimodal anchoring. Meta substituted azonaphthol benzoic acid which is a nonconjugate system grafted on to ZnO through carboxylate group, is found to degrade under visible light irradiation due to charge accumulation. However on replacing naphthol with hydroxyquinoline presents a dye structure which can anchor to ZnO through dual site grafting via carboxylate and hydroxyl imine groups. This also alters the resonance structure of the dye making electron transfer between ZnO and dye possible. The photophysical characteristics of the dyes manifest in the composite with ZnO absorption and emission features conspicuously absent. An enhancement in visible light absorption in the composite, affected by the dye grafting is translated as visible light photocatalytic activity due to charge transfer from dye to ZnO. It is also found that on excitation in UV light, the emission of the composite increases which indicates an electron transfer from ZnO to dyes. Comparable water splitting activity in UV light may point to catalytically active sites in ZnO-dye interface. Computational studies on the electronic structure of the dye and the composite also support such a charge transfer. Visible light excitation of the dye and

subsequent electron transfer to ZnO surface, as depicted by the calculations, makes the composite visible light active for H_2 generation in carboxylic acid anchoring. An UV light excitation of ZnO, however, is energetically feasible for H_2 generation only in case of quinoline anchoring in the case oof ZnO-3ABBNHQ Composite. Presence of desired catalytic sites on the ZnO-dye interface can thus be envisaged which makes such composites potential candidates as water splitting catalysts amenable for designing and further improvement.

We propose a model in which two types of electron transfer occurs depending on the excitation energy.

1. Under UV irradiation, electrons of both ZnO (VB to CB) and dye (pi-pi*) are excited, but the catalytically active sites exist on the ZnO surface. Pristine ZnO is not catalytically active even under UV irradiation. This is because of faster recombination compared to surface reaction (water reduction). We also observe green defect emission in pristine ZnO which is completely suppressed in ZnO-dye composite thereby blocking the recombination pathway. Hence even though an electron transfer occurs from ZnO to dye, as proven from the increase in intensity of the UV emission in the composite, there is enough electrons on ZnO surface to catalyse water reduction.
2. Under visible light irradiation, it is more straightforward; only dye is excited (n/pi-pi*) and electron transfer occurs from the dye to ZnO. ZnO surface catalyses water reduction.

3. The highly efficient photocatalytic activity of ZnO-dye composite is due to the following reasons: (i) efficient photon absorption, (ii) resourceful generation of excited charge carriers instead of heat, (iii) effective separation of charge carriers and fast reduction of protons to H_2 by ZnO-dye composite system and (iv) efficient adsorption of reactants involved for charge carrier utilization and desorption of products.

References

1. Norberg, N. S.; Gamelin, D. R., *J. Phys.Chem. B* **2005**, *109,* 20810-20816.
2. Guo, L.; Yang, S.; Yang, C.; Yu, P.; Wang, J.; Ge, W.; Wong, G. K. L., *Chem. Mater.* **2000**, *12*, 2268-2274.
3. Hua, Z.; Xu, Q.; Huang, X.; Zhang, C.; Wang, X.; Xiao, M., *ACS Nano* **2014**, *8*, 7060-7066.
4. Kamat, P. V.; Patrick, B *J. Phys. Chem*. **1992**, *96*, 6834-6839.
5. Badger, G. M.; Buttery, R. G. *J. Chem. Soc.* **1955**, 2816.
6. Shavaleev, N. M.; Adams, H.; Best, J.; Edge, R.; Navaratnam, S.; Weinstein, J. A., *Inorg. Chem.* **2006**, *45*, 9410-9415.
7. Hirohata, M.; Kai, F.; Kurosawa, K.; Huang, H.; Ishii, K.; Matsuoka, Y.; Komori, K.; Nakamura, M., *J. Coord. Chem*. **1993**, *30*, 379-391.
8. Zborowski, K. K.; Solá, M.; Poater, J.; Proniewicz, L. M., *Cent. Eur. J. Chem*. **2013**, *11*, 655-663.
9. Ghanadzadeh Gilani, A.; Moradi, E.; Binay, S.; Moghadam, M., *Spectrochim. Acta Mol. Biomol. Spectrosc*. **2012**, *87*, 112-118.
10. Bardez, E.; Devol, I.; Larrey, B.; Valeur, B. *J. Phys. Chem. B* **1997**, *101*, 7786.
11. Cheng, Y.-F.; Zhao, D.-T.; Zhang, M.; Liu, Z.-Q.; Zhou, Y.-F.; Shu, T.-M.; Li, F.-Y.; Yi, T.; Huang, C.-H., *Tetrahedron Lett*. **2006**, *47*, 6413.
12. Durham, B.; Meyer, T. J., *J. Am. Chem. Soc*. **1978**, *100*, 6286-6287.
13. Haynes, K. M.; Kratch, K. C.; Stovall, S. D.; Obondi, C. O.; Thurber, C. R.; Youngblood, W. J., *ACS Appl. Mater. Interfaces.* **2015**, *7*, 16133-16137.
14. Nandi, S.; Singh, S. K.; Mullangi, D.; Illathvalappil, R.; George, L.; Vinod, C. P.; Kurungot, S.; Vaidhyanathan, R., *Adv. Energy Mater*., **2016**, *6*, 1601189.
15. Yanai, T.; Tew, D. P.; Handy, N. C. *Chem. Phys. Lett*. **2004**, *393*, 51−57.
16. Scalmani, G.; Frisch, M. J., *J. Chem. Phys*. **2010**, *132*, 114110.

Chapter 4

Synthesis, Characterization and Photocatalytic Water Splitting Activity of ZnO- Perylene bisimide Composites

4.1. Introduction

Realistic design of semiconducting π -electronic molecules for functionalisation of ZnO nanoparticles capable of charge and electron transport is vital for the accomplishment of outstanding photocatalytic water splitting activity. Perylene compounds are among the most important class of organic n-type semiconducting materials because of their terrific photochemical and opto-electronic properties. As metal-free dyes, perylene derivatives have been widely applied in various optical devices owing to their excellent chemical, thermal and photochemical stability. In addition, they are widely used as dyes, pigments, fluorescent solar collectors, luminescent materials, and molecular switches due to their low band gap, high photoluminescence quantum yield and excellent electron transportation property.

Perylenes are polycyclic aromatic hydrocarbons with a formula $C_{20}H_{12}$. The perylene core has twelve functionalizable positions–the 3,4,9,10 positions, which are known as the *peri*-; the 1,6,7,12, known as the *bay*-; and the 2,5,8,11 known as the *ortho*-positions. Perylene based systems with different chemical and physical properties have been obtained by incorporating substituents, most often in the *bay* positions. Such substituted systems can tune the HOMO and LUMO energies and thereby the absorption properties of the molecule. Perylene-3,4,9,10-tetracarboxylic acid dianhydride (PTCDA) is used as the mother compound for various perylene substituted systems, particularly perylene-3,4,9,10-tetracarboxylic acid diimides (PDIs). PDI modified with carboxylic acids are versatile and very reactive compounds that can accept a wide number of functionalities. Another important substituted class is perylene bisimide (PBI) dyes with excellent optical and electronic properties. The PBI chromophores can create supramolecular assemblies by metal ion–ligand coordination, hydrogen bonding and ionic interactions and can be successfully incorporated in conventional covalent polymers and block copolymers. Perylene and its derivatives are known for their self-aggregation properties due to π-π stacking, but aggregation and solubility can be in general controlled by suitable modifications/functionalisation outside the core. Solubility can be specifically tuned by synthesizing PDIs with different substituents in the imide position. By introducing polar groups in the imide position, water-soluble perylene derivatives can be obtained.

Aggregation can also be minimised by grafting it with semiconductor metal oxide nanostructures, disturbing the π-π stacking and enhancing electron injection and transfer. The nature of the anchoring groups (acid anhydride and carboxylic acid) and the electronic coupling between the perylene core and the semiconductor surface would affect the electron transfer properties greatly [1-30].

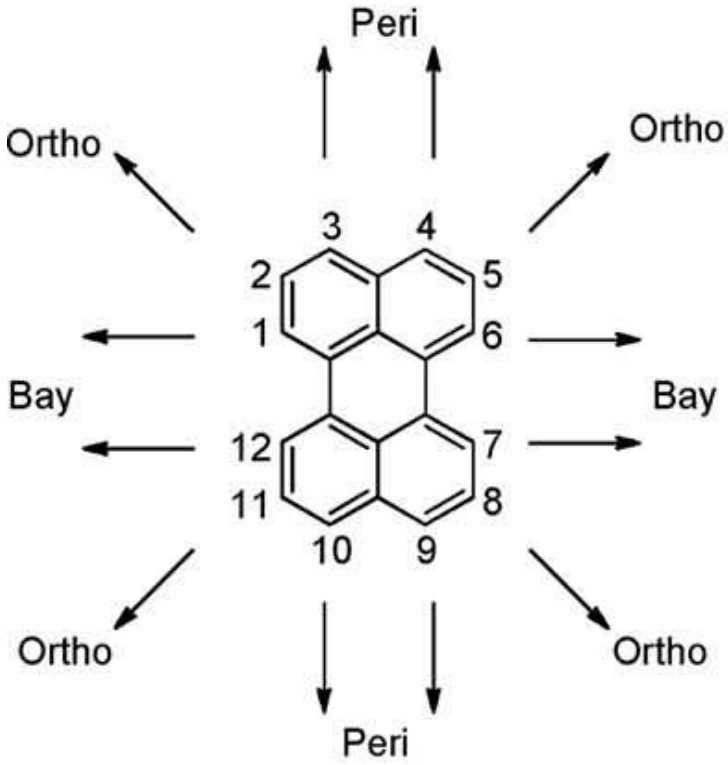

Figure 4.1. Twelve functionalizable positions of perylene

This chapter describes the synthesis of perylene derivative with carboxylate functionality which is suitable for the surface grafting of ZnO nanoparticles that will successfully increase the visible light activity of ZnO based photocatalysts. The bay functionalized perylene core, that is perylene-3,4,9,10-tetracarboxylic acid dianhydride (PTCDA) was coupled to 4-amino benzoic acid, which serves as an anchor group for the covalent anchoring to ZnO nanoparticles, thereby enhancing the photostability and H_2 generation of the composite. The resulting perylene-ZnO system was stable against aggregation and sedimentation and showed electronic communication between the chromophore and the semiconductor.

4.2. Experimental Section

4.2.1. Synthesis

4.2.1.1. (N,N'-Bis(p-carboxyl-phenylene)perylene-3,4:9,10perylenebisimide) [PTCDACOOH2]

A mixture of 302 mg (0.77 mmol) 3,4 : 9, 10-perylene tetracarboxylic dianhydride, 30 g imidazole and 2 mL chloroform were stirred at 90°C. Then 257 mg (1.87 mmol) p-aminobenzoic acid was added. The mixture was refluxed at 130°C with stirring for 24 h, followed by acidizing and filtering using G4 funnel filter. The precipitate was washed by excess water and extracted in anhydrous ethanol. The product was purifiied by column chromatography and desiccated in vacuo to yield pure N,N'- bis(p-carboxyl-phenylene) perylene-3,4 : 9,10-perylene bisimide (PTCDACOOH2) (Scheme 4.1).

Scheme 4.1. Synthesis of PTCDACOOH2

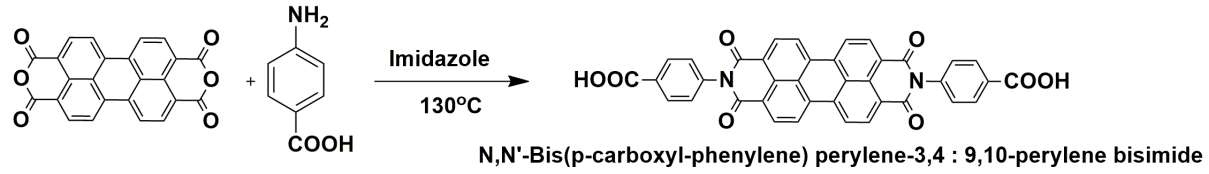

4.2.1.2. ZnO-Perylene composites

Typically, KOH (56 mM, 75 mL) in methanol was refluxed at 60 °C for 30 min. In another reaction mixture, $Zn(OAc)_2.2H_2O$ (56 mM, 25 mL) in methanol was prepared by stirring at room temperature. The dissolved solution of zinc acetate was then added drop wise through an addition funnel into the refluxing KOH solution maintained at 60 °C with vigorous stirring. The formation of ZnONPs started immediately and the solution becomes clear. N,N'- bis(p-carboxyl-phenylene) perylene-3,4 : 9,10-perylene bisimide (23 µmol) was added in-situ during the synthesis of ZnO to the alkaline zinc acetate solution (0.142 mmoles. The solution was stirred in methanol at 25°C for 1 h. The product (ZnO-PTCDACOOH2) was washed with methanol, centrifuged and collected.

4.2.2. Instruments for Characterization

The principles and instrumentation of all the techniques used throughout the work for structural and photophysical characterizations are briefly discussed in the Appendix 1. The details of the procedures used for PXRD, TEM, IR, Raman, UV-vis, Photoluminescence, Lifetime, NMR, Electrochemical measurements, Elemental analysis and Zeta potential are same as those described in chapter 3 in section 3.2.2. The set up for photocatalytic activity measurement used was the same as that described in chapter 3 in the section 3.2.2.1.

4.3. Results and Discussion

4.3.1. Characterisation of N,N'- bis(p-carboxyl-phenylene) perylene-3,4 : 9,10-perylene bisimide [PTCDACOOH2]

Elemental analysis of PTCDACOOH2 was carried out to confirm the purity and the observed CHN values match the calculated values.

calcd(%): C 72.38, H 2.88, N 4.44; found (%): C 72.21, H 2.62, N 4.32.

The structure of PTCDACOOH2 was confirmed by ^{1}H NMR, ^{13}C and DEPT (the spectra given in appendix 4-Figure-5). The broad singlet appearing at 9.93 ppm is the hydroxyl proton attached to the carboxylic moiety of the perylene ring. The doublet at 8.03 and 7.92 ppm corresponds to the –CH aromatic protons of the perylene ring. The multiplets at 7.74-7.57 ppm and 7.49-7.29 ppm correspond to the –CH aromatic protons attached to the azobenezene ring.

^{1}H NMR (500MHz, DMSO-d_6) δ ppm:

9.93 (s., 1 H), 8.03-7.92 (m, 8H, perylene core), 7.74-7.57 (m, 4 H, aromatic ring), 7.49-7.29 (m, 4 H, aromatic ring)

^{13}C (125MHz, DMSO-d_6) δ ppm :

172.15, 169.68, 161.33, 135.90, 133.95, 131.38, 130.48, 119.42, 117.31, 113.07

A broad sharp band was observed in the region at 3411 cm^{-1} due to the symmetric O-H stretching modes. In the IR spectrum, the C-H bonds in the aromatic ring with maxima at

3236, 3040 and 2931 cm^{-1} respectively are registered. The band of valence vibrations of the C=O bond in the carboxyl group is observed at 1740 and 1675 cm^{-1}. The absorption bands with maxima at 1594 and 1498 cm^{-1} belong to the valence vibrations of the C=C bonds in the aromatic ring framework (Figure 4.2) [7].

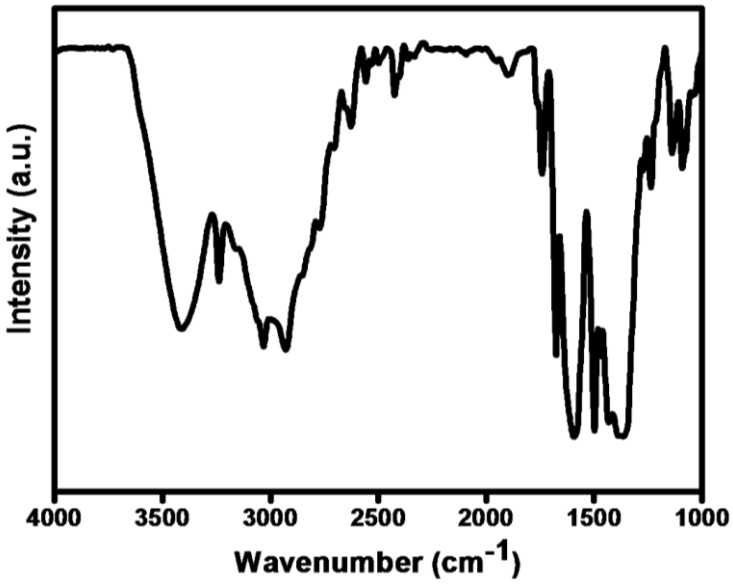

Figure 4.2. FT-IR spectrum of pure PTCDACOOH2

The absorption spectra of the PTCDACOOH2 dye ($9.04x10^{-4}$ M) show typical features of perylenes with two prominent peaks in the visible region. The bay substituents at 1,6,7 and 12 positions in the perylene core (explained briefly in the chapter 4 introduction) tune the HOMO and LUMO energies and thereby the absorption and emission properties of the molecule. The UV-vis absorption spectra of PTCDA(COOH)2 have bands at 410,440, 470 and a small shoulder around 520 nm (Figure 4.3). This shoulder peak is characteristic of perylene bisimide core fragments. Typical emissions at 490 and 525 nm was observed for PTCDA(COOH)2 at 410 and 440 nm excitation wavelengths (Figure 4.4). The excitation spectrum of the PTCDACOOH2 molecule is also given (Figure 4.4).

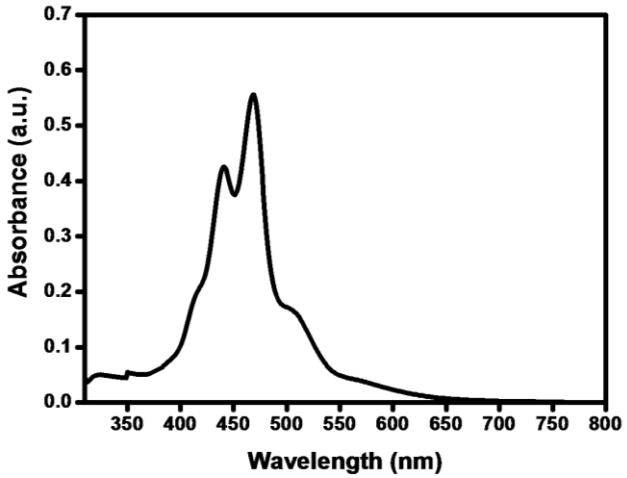

Figure 4.3. UV-vis spectrum of PTCDACOOH2

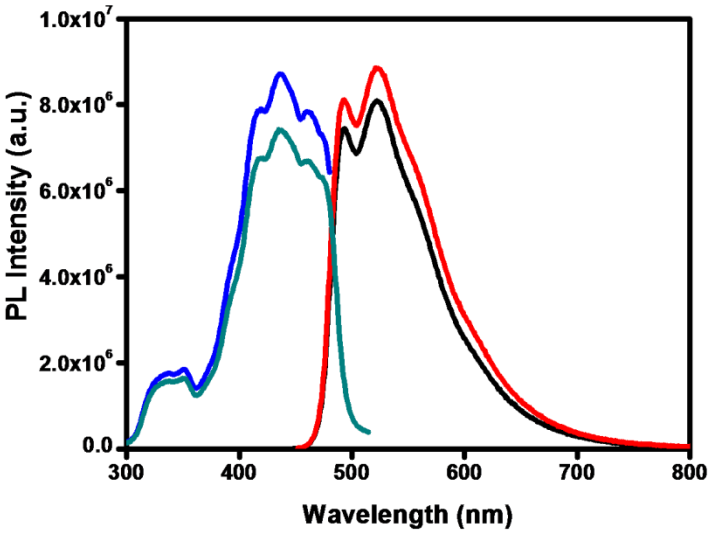

Figure 4.4. Emission spectra of PTCDACOOH2 ,λexc=410(black) and 440 nm(red) and excitation spectra of PTCDACOOH2 ,λems=490(blue) and 525 nm (green).

4.3.2. ZnO-PTCDACOOH2 Composites

Powder X-ray diffraction patterns show that the parent wurtzite phase of ZnO NPs is not altered in the case of ZnO-3ABBN and ZnO-4ABBN composites during the surface modification (Figure 4.5). For the surface functionalized ZnO NPs with PTCDACOOH2, a

zeta potential of -26.1 mV was measured. Zeta potential values near to or above 30 mV are regarded as an indication for a stable dispersion. TEM images of grafted NPs also corroborate surface grafting, wherein the ZnO nanoparticles were found to be separated from each other with particle size of 4±2 nm. The corresponding histogram is also shown as an inset along with the TEM images (Figure 4.5).

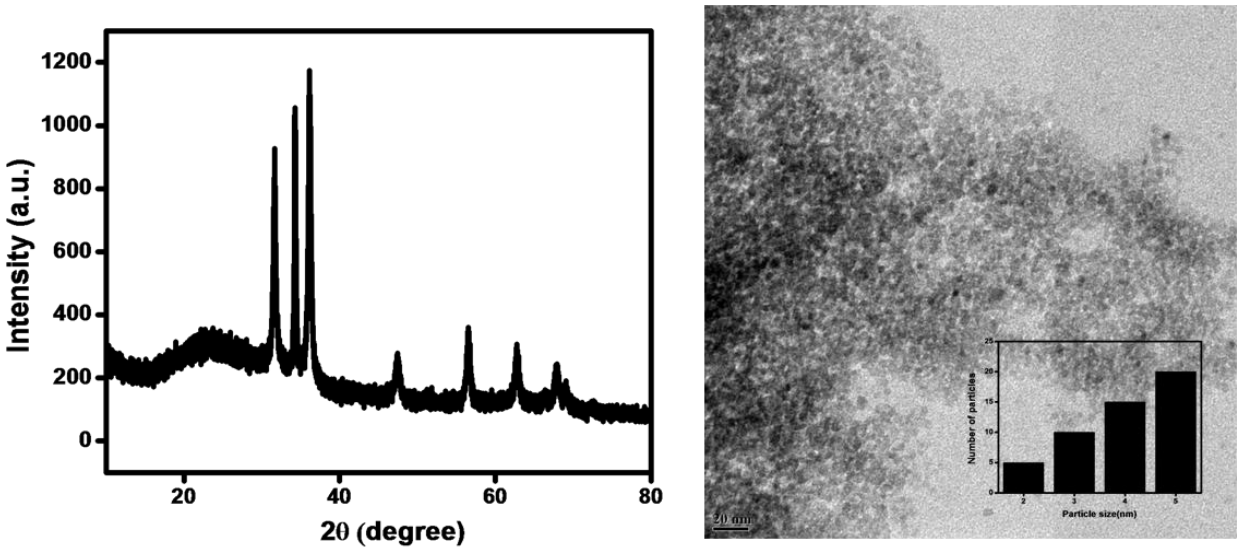

Figure 4.5. XRD patterns of (left) ZnO-PTCDACOOH2 composite and TEM images ZnO-PTCDACOOH2 (right) composite with the corresponding histograms as inset.

Surface grafting of the organic moiety on ZnO was ascertained by IR spectroscopy by following the C=O, C=Cand aromatic -CH stretching frequencies (Figure 4.6). IR spectra of the ZnO-PTCDACOOH2 composites show substantial shifts in the aromatic –CH, C=C and –CO stretching vibrational frequencies when compared to the pristine dye indicating successful grafting. The intense –CO stretching vibrational frequency of the carboxylic moiety is shifted from 1740 to 1550 cm^{-1} in the composite. The band near 3042 cm^{-1} for aromatic -CH group is also shifted to lower frequency of 2905 cm^{-1} in the spectra of composites.

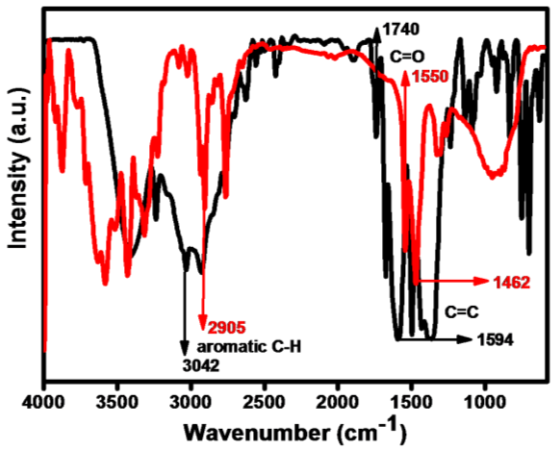

Figure 4.6. FT-IR spectrum of PTCDACOOH2 (black) and ZnO-PTCDACOOH2 composite (red)

ZnO- PTCDACOOH2 (1.69 x10^{-3} M ZnO + 9.04 x 10^{-4} M PTCDACOOH2) have absorptions at 360, 440 , 470 and 510 nm indicating visible light absorption capability (Figure 4.7). From the absorption studies, it is clear that the ZnO-PTCDACOOH2 composite shows combined features of both ZnO nanoparticles and PTCDACOOH2 reminiscent of the behaviour of azonaphthol composites (chapter 2). A slight red shift of the absorption bands is observed in the case of composite compared to pure dye (Δ=30 nm), probably due to grafting. Usually, in substituted perylenes, perylene core can act as the donor and the peri-substituent group as acceptor; bathochromic shifts are observed on variations to this structure. Hence, it is possible that such a functionalisation along with anchoring on ZnO affect the red shift observed in the present case. Most interestingly, the absorption edge of ZnO observed in the composite shows a substantial shift from 3.2 eV to 3.02 eV (Figure 4.7), implicating major surface structure reorganisation creating new band levels associated with ZnO. Emission characteristics of the composite show interesting deviations from pure dye and pure ZnO, mainly in terms of appearance of a new peak at 400 nm which is not observed in either dye or ZnO. This peak may correspond to the red shift in absorption edge seen in the composite. Figure 4.8 shows the emission spectra at different excitation wavelengths. On excitation at higher energy (for ZnO excitation), the newly appearing 400 nm emission is predominant whereas at lower energy (dye excitation), visible emission is more predominant. However, a drastic reduction in emission intensity

is seen in the composite when compared to the pure dye which indicates a charge transfer from dye to ZnO, again similar to azonaphthol composites. This reduction in visible emission of the composite is observed at all excitation wavelengths (325, 410, 440 and 470 nm based on the absorption bands of the composite) when compared to pure dye. This indicates that there is a charge/energy transfer from dye to ZnO in a broad irradiation range. We cannot unambiguously comment on the defect emission since dye emission peaks overlap with the defect emission peak region. An attempt at deconvoluting the peaks of dye molecule and composite was done on the emission spectrum collected at excitation wavelength of 410 nm, where the new emission at 400 nm is not expected (Figure 4.9). The deconvoluted fit of the dye molecule shows three peaks at 490, 518 and 566 nm. A perfect fit was obtained by deconvoluting the composite spectrum to four peaks at 485, 515, 546 and 586 nm, indicating that there are traces of green emission in the composite which is substantially suppressed. The appearance of 400 nm emission may be the formation of a new complex. Along with this, reduction in the π- π stacking of the dye molecule may facilitate the electron transfer between the dye and the composite [2, 7].

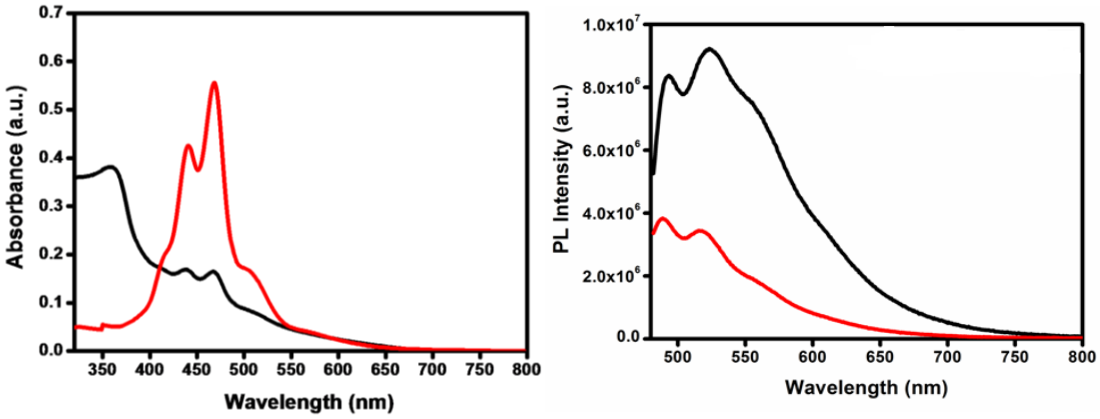

Figure 4.7. UV-vis spectrum (left) of ZnO-PTCDACOOH2(black) and PTCDACOOH2(red) and emission spectra (right) of ZnO-PTCDACOOH2(red) and PTCDACOOH2(black) PTCDACOOH2 , λexc=470 nm (right).

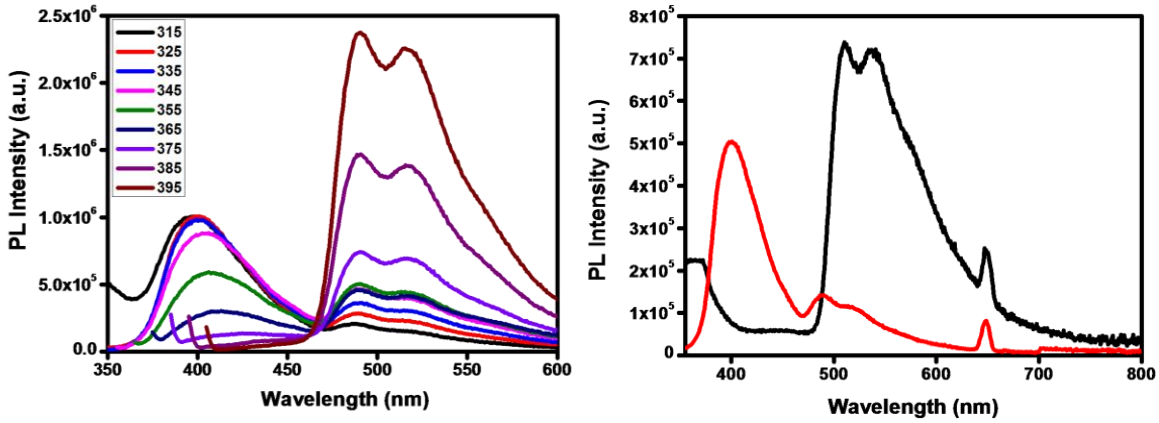

Figure 4.8. Emission spectra of ZnO-PTCDACOOH2 at all excitation wavelengths (left) and PTCDACOOH2 (black) and ZnO-PTCDACOOH2 (red) , λexc=325 nm (right).

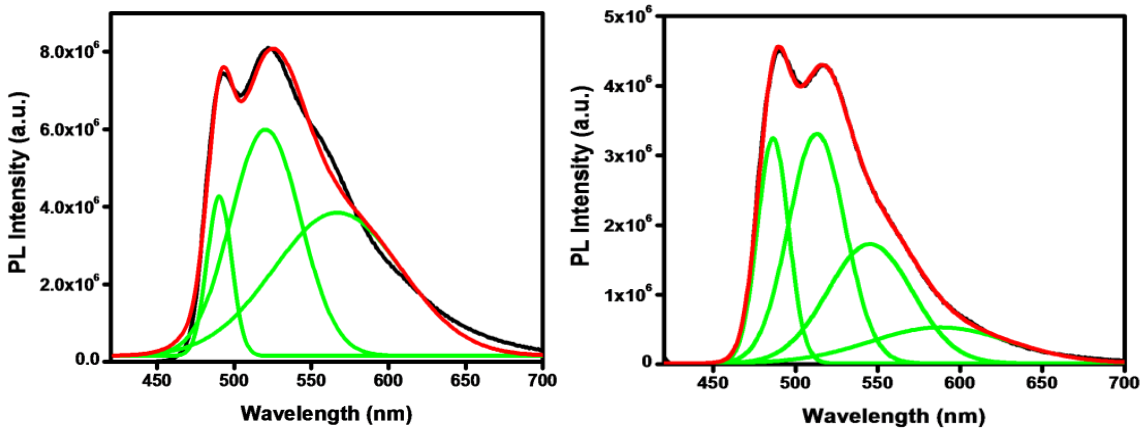

Figure 4.9. Deconvoluted emission spectra of PTCDACOOH2 (left) and ZnO-PTCDACOOH2 (right) , λexc=410 nm.

The fluorescence lifetime study for the system was undertaken by TCSPC (Time-correlated single photon counting) using a HORIBA Jobin Yvon Nano-LED source with wavelength 320 and 390 nm. Decay measurements were carried out at emission wavelengths of 490, 515 and 560 nm (PTCDACOOH2), 400, 490, 515, 560 and 580 nm (ZnO-PTCDACOOH2) and 500 nm (ZnO NPs). These experiments were carried out for ZnO NPs (1.69 $x10^{-3}$ M), PTCDACOOH2 (9.04 x 10^{-4} M) and ZnO-PTCDACOOH2 composite (1.69 $x10^{-3}$ + 9.04 x 10^{-4} M) at room temperature. The emission decay profiles are shown in Figures 4.10, 4.11, 4.12 and the observations are tabulated in Table 4.1.

The decay curves are deconvoluted by numerical convolution technique and the delta pulse response is fitted to mono-exponential for PTCDACOOH2 dye and tri-exponential for ZnO. Decay curves of the composite attained better fit in bi-exponential indicating a dominance of dye features in the composite. Average lifetime of the composite is decreased when compared to that of the dye. From the steady state studies also, it was observed that the emission intensity is decreased in case of the composite when compared to that of the dye which is clearly reflected in the lifetime of the composite, proving a successful electron and charge transfer.

Lifetime studies of pure ZnO NPs as presented in chapter 2 shows three components 1.08 (92 %), 9.42 (7 %) and 47.7 (1 %) ns (as explained in chapter 2, this suggests that as particle size of ZnO decreases, there is a possibility of emergence of multiple donor and acceptor sites). Dye shows monoexponential fit with a single component at 4.7 ns. In case of composite, the 400 nm emission seems to be originating from a new species with lifetime of ~0.2 ns (98%) which is absent in ZnO as well as dye. 490 nm emission, however, originates from dye (~4.7 ns/48%) as well as the new species (~0.2 ns/52%). Rest of the emissions (515, 560 and 580 nm) of the composite shows a shorter lived new species at 0.01-0.04 ns along with dye contribution. This unambiguously shows that the fluorescence phenomenon in the ZnO-perylene composites originates from a new species with substantial contribution in the visible region.

Tentatively, the mechanism of charge transfer can be hypothesised as follows: On dye grafting, a new acceptor level is formed within the band gap as shown by the red shifted emission at 400 nm. Its lower lifetime when compared to dye also corroborates this observation. This composite also shows broad UV-visible region absorption from 400 nm to 600 nm. We expect π-π* transitions occurring in the dye in visible light which maybe transferring charge to newly formed species, probably defect acceptor levels.

Table 4.1 Lifetime parameters of ZnO NPs, PTCDACOOH2 and ZnO-PTCDACOOH2 composites.

System	Experimental Setup	Lifetime (ns)		
		τ1(a1)	τ2(a2)	<τ>
PTCDACOOH2 λex= 390 nm	λem=490 nm	4.69 (1.00)		4.69
	λem=515 nm	4.77 (1.00)		4.77
	λem=560 nm	4.97 (1.00)		4.97
ZnO-PTCDACOOH2 λex=390 nm	λem=490 nm	0.22 (0.52)	4.78 (0.48)	2.41
	λem=515 nm	0.01 (0.52)	4.6 (0.48)	2.22
	λem=560nm	0.04 (0.51)	5.36 (0.49)	2.81
	λem=580 nm	0.04 (0.59)	4.80 (0.41)	2.52
ZnO-PTCDACOOH2 λex=320 nm	λem=400 nm	0.27 (0.98)	1.77 (0.02)	0.30
ZnO Defect Band λex=320nm	λem=500nm	1.08 (0.92)	9.42 (0.07)	47.7 (0.01)

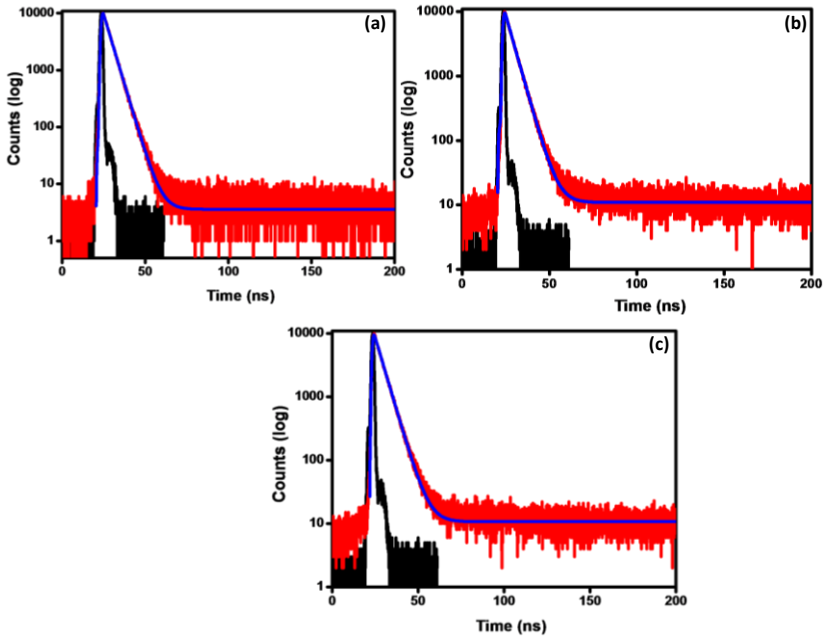

Figure 4.10 . The emission decay profiles on excitation at 390 nm of PTCDACOOH2 (a) 490 (b) 515 and (c) 560 nm. Instrument response function in black, decay profile in red and experimental fit in blue.

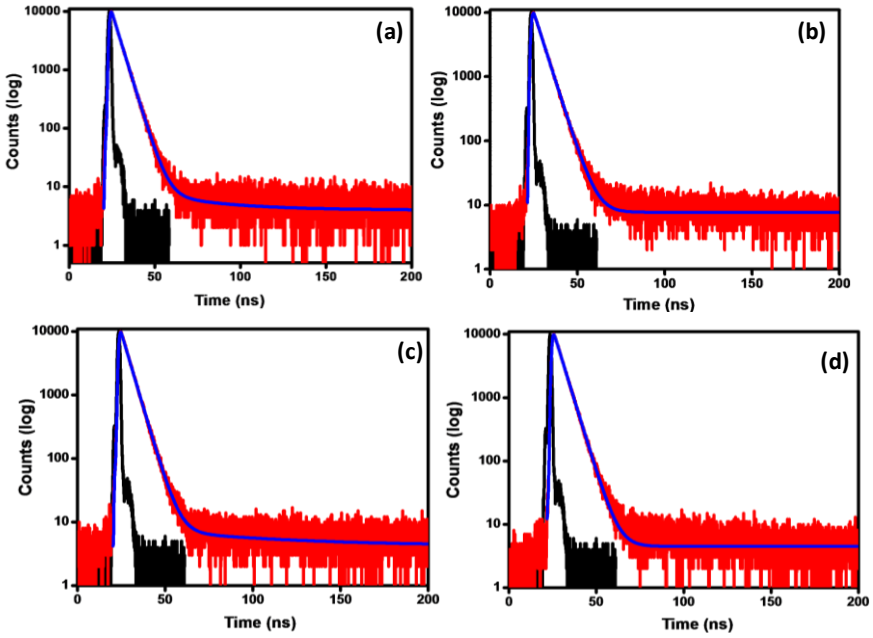

Figure 4.11 . The emission decay profiles on excitation at 390 nm of ZnOPTCDACOOH2 Composite (a) 490 (b) 515 (c) 560 and 580 nm emission wavelengths. Instrument response function in black, decay profile in red and experimental fit in blue.

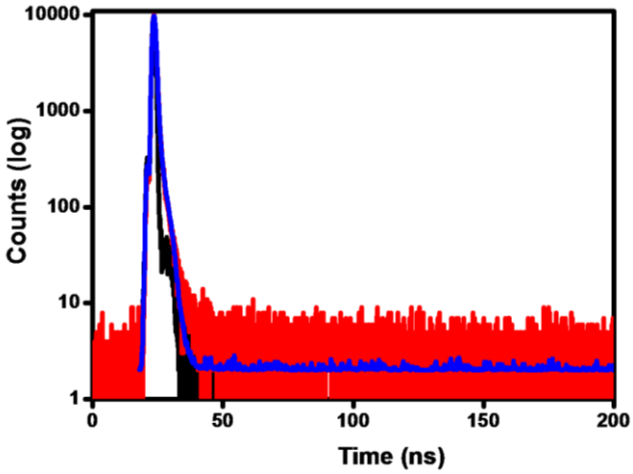

Figure 4.12. The emission decay profiles on excitation at 320 nm of ZnOPTCDACOOH2 composite at 400 nm emission wavelength. Instrument response function in black, decay profile in red and experimental fit in blue.

The redox and the electron transfer properties of the dye and the composite were also investigated by cyclic voltammetry (Figure 4.13).

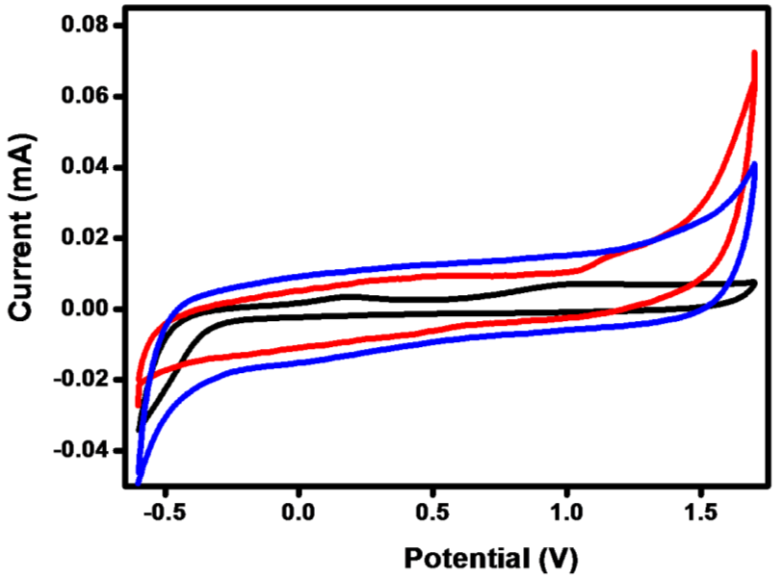

Figure 4.13. Current–voltage profile for photoelectrochemical cells employing ZnO (black), dye (blue) and ZnO-dye composite (red) by cyclic voltammetry at a scan rate of 50 mv/s. Supporting electrolyte was LiClO4 in acetonitrile.

The potential and current are found to be enhanced on grafting when compared to ZnO and PTCDACOOH2[ZnO (1V, 0.0075mA), PTCDACOOH2 (1.136V, 0.0143mA) and ZO-PTCDACOOH2 (1.214V, 0.0178mA)]. To reveal the difference in the light induced electron transfer properties of ZnO NPs on grafting, cyclic voltammograms are observed in the presence and absence of visible light (200 W Tungsten lamp). A significant photocurrent rise is seen which introduces an electron transfer pathway in the case of ZnO-PTCDACOOH2 composite under irradiation. Substantial enhancement in the photo current is also observed by linear sweep voltammetry (scanning in a potential window of -0.5 to 1.7 V) suggesting a light induced electron transfer (Figure 4.14). The resistance was also found to be less under illumination (615 Ω) compared to the dark condition (670 Ω) for ZnO-PTCDACOOH2 composite (Figure 4.14).

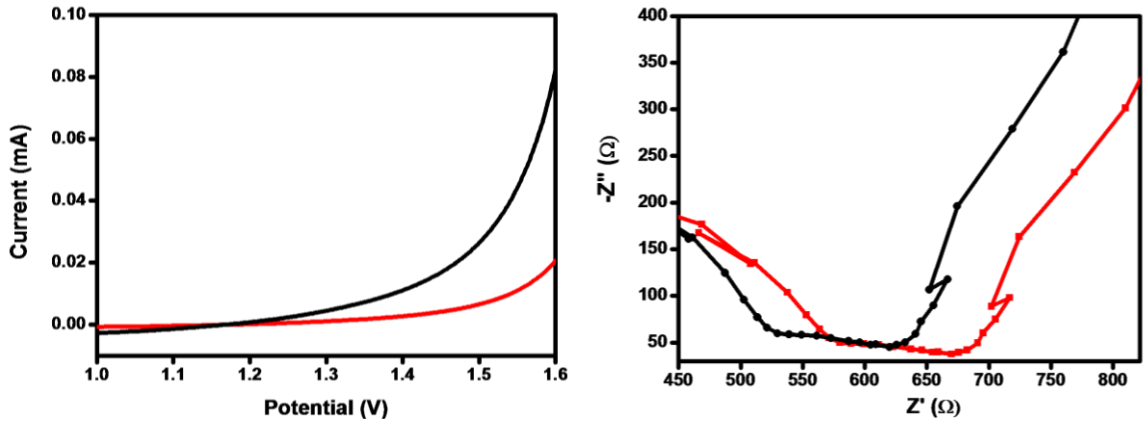

Figure 4.13. LSV profile for photoelectrochemical cells employing (left) ZnO-PTCDACOOH2 composites (10 mv/s) upon turning on (black) and off (red) 200W tungsten lamp by cyclic voltammetry and Electrochemical Impedance employing (right) ZnO-PTCDACOOH2 Composites upon turning on (black) and off (red) 200W tungsten lamp .

4.3.3. Photocatalytic testing ZnO-PTCDACOOH2

The photocatalytic water splitting activity for the composite is tested under different irradiation sources (UV,visible and direct sunlight) for 8 h (Figure 4.14). The catalyst was found to be highly stable during this exposure. The catalyst is found to be highly active with stable hydrogen production rate of 88, 83 and 92 mmol/g of catalyst under UV, visible and solar irradiation for 8 h This experiment was repeated 3 times after the 8^{th} h with N_2

purging under visible light to check the stability of the catalysts (Figure 4.14). The catalysts were found to be highly stable and the initial H_2 evolution rate was regained after each purging. The higher photocatalytic water spitting activity under different irradiation sources may be due to the electron and energy transfer between ZnO and dye. This possibility is also supported by the decrease in intensity of the emission peak in the composite when compared to dye. The ZnO is getting excited under higher energy radiation. From the emission studies, the formation of a new complex is evident by the appearance of a new peak at 400 nm, may facilitate the possibility of electron transfer between ZnO and dye molecule.

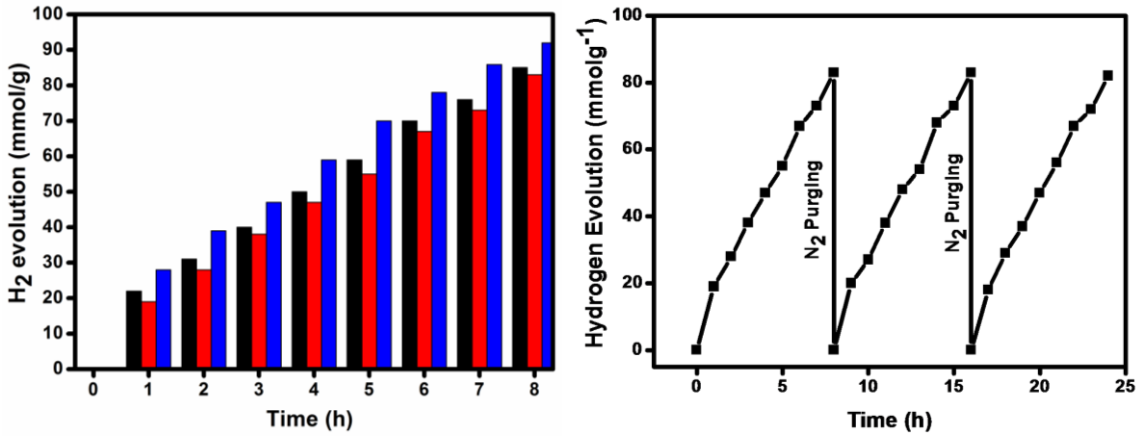

Figure 4.14. Evaluation of photocatalytic activity for H_2 generation under UV (black), visible (red) and solar (blue) at various irradiation time (0,1,2,3,4,5,6,7and 8 h) (left) and H_2 evolution under visible light irradiation on repeated purging of the headspace (right) of ZnO-PTCDACOOH2 composite.

To see the effect of methanol sacrificial reagent, water splitting experiments were carried out in different concentrations of methanol from water-methanol mixture for the ZnO-PTCDACOOH2 composites at 4 h irradiation and the H_2 evolution was found to be slightly increased, but a saturation yield for H_2 evolution was reached after 35 v/v% and further increase in methanol concentration did not affect the yield substantially (Figure 4.15).

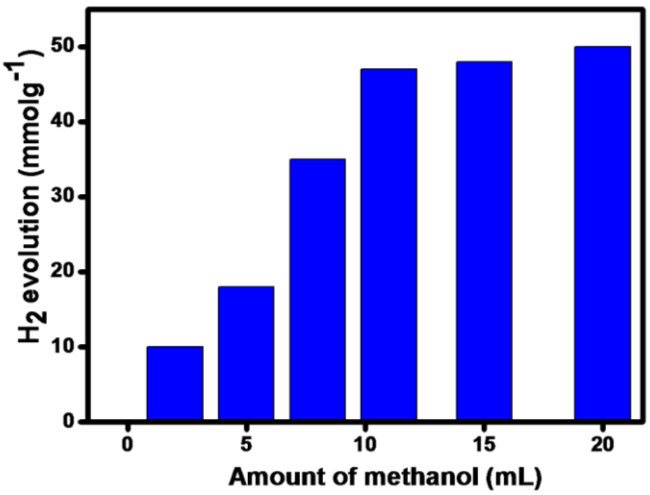

Figure 3.20. Evaluation of photocatalytic activity for H_2 generation under visible irradiation for 4 h from water-methanol mixtures with varying amounts of methanol in ZnO-PTCDACOOH2 composite.

4.4. CONCLUSIONS

The perylene molecules are designed to have a carboxylic functionality in the phenyl group. In ZnO-PTCDA(COOH)2 composite, the conjugated π system of the perylene after functionalization with ZnO, links the surface atoms of the particle to the perylene core in a conjugative manner. In our case, a broad emission and absorption peak is observed in the case of composite indicating a high visible absorption capability. The absorption of the composite also shows combined features of ZnO and dye with a slight shift in ZnO absorption edge properties. On grafting PTCDACOOH2 to ZnO nanoparticles, a drastic decrease in the visible emission is observed, indicating an electron transfer from the organic molecule to ZnO. Surface modification of ZnO induces suppression of certain defect sites. Fluorescence lifetime studies also show an efficient electron transfer between ZnO and dye. The electron transfer properties is further corroborated by the photocurrent increment observed from the electrochemical studies. A novel photocatalytic system, ZnO-PTCDACOOH2 Composite, active for visible light water splitting is developed.

References

1. Guo, L.; Yang, S.; Yang, C.; Yu, P.; Wang, J.; Ge, W.; Wong, G. K. L., *Chem. Mater.* **2000**, *12*, 2268-2274.
2. Schönamsgruber, J.; Zeininger, L.; Hirsch, A., Chem*. Eur. J.* **2014**, *20*, 2529.
3. Zang, L.; Liu, R.; Holman, M. W.; Nguyen, K. T.; Adams, D. M., *J. Am. Chem. Soc*. **2002,** *124*, 10640.
4. Gnichwitz, J.-F.; Marczak, R.; Werner, F.; Lang, N.; Jux, N.; Guldi, D. M.; Peukert, W.; Hirsch, A., *J. Am. Chem. Soc*. **2010**, *132*, 17910.
5. Wan, P.; Muralidharan, S.; McAuley, I.; Babbage, C. A., *Can. J. Chem*. **1987**, *65*, 1775.
6. Vaccaro, A.; Hierrezuelo, J.; Skarba, M.; Galletto, P.; Kleimann, J. R.; Borkovec, M., *Langmuir* **2009**, *25*, 4864.
7. Xu, X.-H.; Liu, X.-Y.; Zhuang, Q.-X.; Han, Z.-W., *J. Appl. Polym. Sci*. **2010,** *116*, 455.
8. Osaheni, J. A.; Jenekhe, S. A.; Perlstein., *J. Phys. Chem.* **1994**, *98*,12727.
9. Jenekhe, S. A.; Osaheni, J. A., *Science* **1994**, *265*, 765.
10. . Osaheni, J. A.; Jenekhe, S. A., *J. Am. Chem. Soc.* **1995**, *117*, 7389.
11. Osaheni J. A.; Jenekhe, S. A., *Macromolecules* **1993**, *26*, 4126.
12. Babel, A.; Jenekhe, S. A., *J. Phys. Chem. B* **2002**, *106*, 6129.
13. Liu, Z.; Wang, S.; Zhuang, Q.; Li, X.; Li, F.; Wu, P.; Han, Z., *Chem. Mater.* **2007**, *19*, 1164.
14. Wang, S.; Wu, P.; Han, Z, . *J. Mater. Sci*. **2004,** *39,* 2717.
15. Wang, S.; Guo, P.; Wu, P.; Han, Z., *Macromolecules* **2004**, *37*, 3815.
16. Chen, Y.; Wang, S.; Zhuang, Q.; Li, X.; Wu, P.; Han, Z., *Macromolecule*s **2005**, *38*, 9873.
17. Jenekhe, S. A.; Johnson, P. O, *Macromolecules* **1990**, *23*, 4419.

18. So, Y. H.; Heeschen, J. P.; Bell, B.; Bonk, P.; Briggs, M.; Decaire,R., *Macromolecules* **1998**, *31*, 5229.

19. Chin, J.; Forster, A.; Clerici, C.; Sung, L.; Oudina, M.; Rice, K., *Polym. Degrad. Stabil.* **2007**, *92*, 1234.

20. Roitman, D. B.; Wessling, R. A.; McAlister, J K., *Macromolecules* **1993**, *26*, 5174.

21. Feng, D.; Wang, S.; Zhuang, Q.; Guo, P.; Wu, P.; Han, Z., *J. Mol. Struct*. **2004**, *707*, 169.

22. Huang, C.; Barlow, S.; Marder, S. R., *J. Org. Chem.* **2011**, *76*, 2386.

23. Anthony, J. E., *Chem. Mater.* **2011**, *23*, 583.

24. Ahrens, M. J.; Fuller, M. J.; Wasielewski, M. R., Chem*. Mater.* **2003**, *15*, 2684.

25. Giacobbe, E. M.; Mi, Q.; Colvin, M. T.; Cohen, B.; Ramanan, C.; Scott, A. M.; Marks, T. J.; Ratner, M. A.; Wasielewski, M. R., *J. Am. Chem. Soc.* **2009**, *131*, 3700.

26. Hill, Z. B.; Rodovsky, D. B.; Leger, J. M.; Bartholomew, G. P., *Chem. Commun.* **2008**, *45*, 6594.

27. Iverson, I. K.; Tam-Chang, S. W., *J. Am. Chem. Soc*. **1999**, *121*, 5801.

28. Lindner, S. M.; Huttner, S.; Chiche, A.; Thelakkat, M.; G. Krausch, A., *Angew. Chem., Int. Ed*. **2006**, *45*, 3364.

29. You, C. C.; Würthner, F., *J. Am. Chem. Soc*. **2003**, *125*, 9716.

30. Yu, W. L.; Pei, J.; Huang, W.; Heeger, A., *J. Adv. Mater*. **2000**, *12,* 828.

Chapter 5

Synthesis, Characterization and Photocatalytic Water Splitting Activity of ZnO-terthiophene Composites

5.1. Introduction

The present chapter describes the synthesis and photophysical and chemical properties of ZnO nanocomposites with conjugated conducting oligomers separated by a heterocyclic π conjugated system. From the work presented in previous chapters, it is clear that efficient electron transfer can occur only through an extended conjugated moiety. Thiophene is an aromatic heterocyclic compound with 6π-e^- cyclic system and two lone pairs of electrons on sulphur. One of the lone pair electrons on sulphur in the thiophene moiety is involved in the aromatic sextet and the other is located in an sp^2 hybrid orbital in the plane of the ring. Polythiophenes are well known for their application as semiconductors in organic devices due to their low cost and excellent charge transfer properties. Thiophene oligomers with the same repeat unit but with shorter chain lengths are also emerging as important molecules because of the same properties with added advantage of defect free structure (which is a bottleneck in polymer devices) and short hopping distances. Short conjugated oligomers like terthiophene exhibit conducting as well as semiconducting behaviour. The electrical conductivity in these oligomers is suggested to arise from delocalized electrons and functionalisation in the thiophene backbone can modify these properties uniquely. Oligothiophenes with pi-conjugation is recently being reported as sensitisers for DSSC. Simple thiophene is not visible light absorbing, but as pi-conjugation increases (number of thiophene rings) or through appropriate fucntionalisation, visible light absorption can be enhanced. So, we carried out a parametric investigation to study the effect of short conjugated functionalized terthiophene moieties as organic linkers on ZnONPs for photocatalytic hydrogen production from water under visible light irradiation. As explained in the previous chapters, for an effective covalent anchoring of the thiophene backbone on ZnO, group like carboxylic acid is essential; hence fucntionalisation with –COOH group is attempted. In addition, to understand the effect of electron density and electron availability in the backbone, a terthiophene carboxylic acid functionalized with Br in one end also is used for forming the composite. We expect this system to behave differently since this can be considered as a composite of two semiconductors and the conducting property of the thiophenes should be exploited rather than absorption property [1-13].

5.2. Experimental Section

5.2.1. Synthesis

5.2.1.1. 2,2':5',2"-Terthiophene (TTT)

Mg (0.56 g, 23.3 mmol) was placed in 10 mL of dry THF and then cooled to 0 °C. 2-bromothiophene (2.9 ml, 30.3 mmol) was added drop wise over half an hour and the reaction mixture was stirred for another 0.5 h. This solution was then transferred slowly via a cannula to a mixture of 2, 5-dibromothiophene (1.3 mL, 11.6 mmol) and Ni(dppp)Cl_2 (305 mg, 0.466 mmol) in dry THF (50 mL) while cooling on ice. The reaction mixture was stirred for 16 h at room temperature and subsequently poured into ice/water (150 mL) containing concentrated HCl (10 mL). The product was extracted with ether and the combined organic layers were washed with plenty of water and brine, successively. The organic extracts were dried over anhydrous $MgSO_4$, evaporated and purified with column chromatography on silica gel with petroleum ether as the eluent to give slight yellowish solid 2.1g (8.3 mmol, yield 71%).

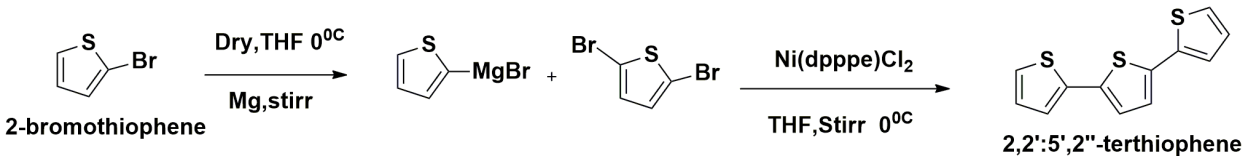

5.2.1.2. 5-carboxy-2,2'5', 2"- terthiophene (TTTCOOH)

5"-formyl-2,2':5',2"-terthiophene (0.27 g) was dissolved in 50 mL of acetone and the temperature thereof was maintained at 15 °C. $CrO_3/H_2O/H_2SO_4$ solution (0.7g/9.3ml/0.15mL) was dropped in slowly and stirred for 4 h at 40 °C. Then 50 mL of water was slowly added in a dropwise manner, and the solution was filtered and washed with chloroform to yield 152 mg of the product. (Yield 53.86%).

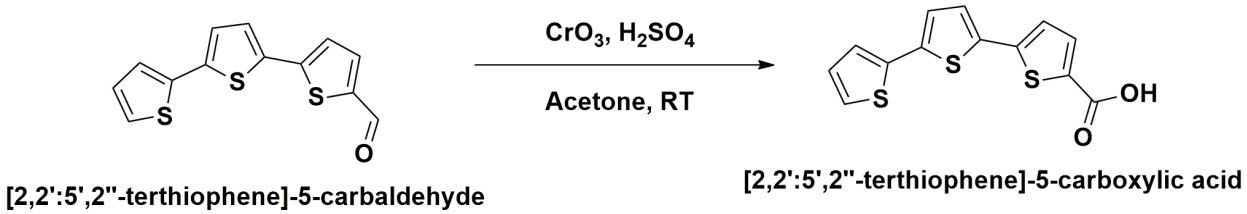

5.2.1.3. 5-Bromo--(-2,2':5',2"-terthiophene) -5-carboxylic acid (BrTTTCOOH)

To a stirred solution of 5"-formyl-2,2':5',2"-terthiophene (2.5 g, 9.1 mmol) in 250 mL of CH_2Cl_2/glacial AcOH (1:1), was added N-bromosuccinimide (1.60 g, 9.1 mmol) at 25 °C. After 24 h the resultant yellow precipitate was filtered, washed with water (pH=7), and dried, yielding 5-bromo-5"-formyl-2,2':5',2"-terthiophene (2.49 g, yield 77%) in the form of an yellow powder. The filtrate was washed with water and the organic layer, after drying over anhydrous Na_2SO_4, and evaporation, gave another fraction of 5-bromo-5"-formyl-2,2':5',2"-terthiophene (0.63 g, 20%), in the form of tan-brown powder. The two fractions were combined and recrystallized from hexane:CH_2Cl_2 mixture affording analytically pure 5-bromo-5"-formyl-2,2':5',2"-terthiophene in the form of brown yellow needles. To the purified brown compound, CrO_3 and H_2SO_4 was added in the presence of acetone at room temperature to obtain 5-bromo-(-2,2':5',2"-terthiophene) -5-carboxylic acid, purified by column chromatography.

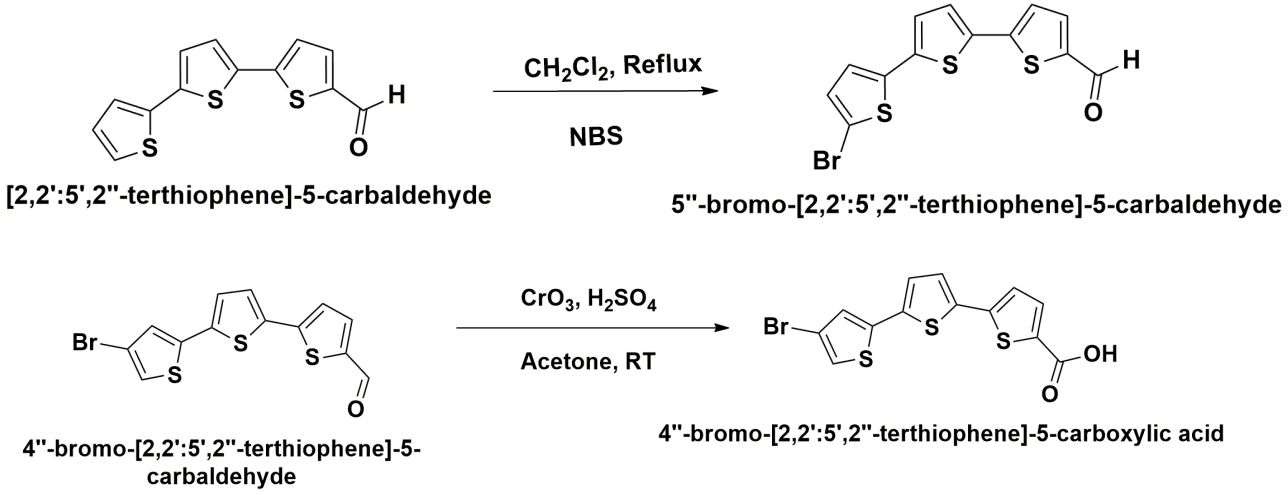

5.2.1.4. ZnO-terthiophene composites

TTTCOOH or BrTTTCOOH (23 µmol) was added in-situ during the synthesis of ZnO to the alkaline zinc acetate solution (0.142 mmoles). The solution was stirred in methanol at 25°C for 1 h. The product (ZnO-TTTCOOH or ZnO-BrTTTCOOH composites) was washed with methanol, centrifuged and collected.

5.2.2. Instruments for Characterization

The principles and instrumentation of all the techniques used throughout the work for structural and photophysical characterizations are briefly discussed in the Appendix 1. Other experimental, photocatalytic testing and instrument details are same as in chapter 2.

5.3. Results and Discussion

5.3.1. Structural Characterization of Terthiophenes

Elemental analysis of TTTCOOH and BrTTTCOOH was carried out to confirm the purity and the observed CHN values match with the calculated values.

TTTCOOH; calcd(%): C 53.6, H 2.76,; found (%): C 52.2, H 2.55.
BrTTTCOOH; calcd(%): C 42.05, H 1.89; found (%): C 41.8, H 1.72.

The structures of both the compounds were confirmed by ^{1}H NMR, ^{13}C and DEPT. The spectra of both the compounds are given in Appendix 4 (Figures 6 and 7). TTTCOOH has the simplest proton NMR spectra with a set of multiplets corresponding to the protons of the aromatic –CH protons of the thiophene ring. The broad singlet appearing at 9.86 ppm is the hydroxyl proton attached to the carboxylic moiety of the terthiophene ring.

^{1}H NMR (500MHz, DMSO-d_6) δ ppm:

9.86 (1H,COOH), 7.63-7.97 (m,6H)

^{13}C (125MHz, DMSO-d_6) δ ppm :

184.76, 162.98, 144.52, 143.02, 139.60, 136.00, 134.76, 127.80, 127.38.

In BrTTTCOOH, the single proton attached to the carboxyl group, was the most downfield with a broad singlet at 9.83 ppm. Also, the two –CH aromatic protons next to the bromine group, were also downfield with the doublet at 7.93 and 7.66 ppm respectively.The multiplet appearing at 7.51-7.18 ppm is the CH aromatic protons attached to the thiophene ring.

^{1}H NMR (500MHz, DMSO-d_6) δ ppm:

9.83 (s,1H), 7.93-7.66 (d, 2H), 7.51-7.18 (m, 4H).

^{13}C (125MHz, DMSO-d_6) δ ppm :

184.36, 145.21, 141.86, 139.70, 134.70, 132.29, 128.45, 111.82, 126.06.

In TTTCOOH, the strong broad IR absorption peak at 3743 cm^{-1} is designated to O-H stretching. The band assigned at 1632 cm^{-1} is attributed to the C=O stretching vibration present in carboxylic acids. The peak at 1377 cm^{-1} is assigned to C-O stretching vibrations. For BrTTTCOOH, the IR absorption bands assigned at 1634 cm^{-1} and 1518 cm^{-1} is attributed to the carboxylic C=O and C-O stretching vibrations. The absorption band at 3515 cm^{-1} is assigned to O-H stretching vibrational band (Figure 5.1).

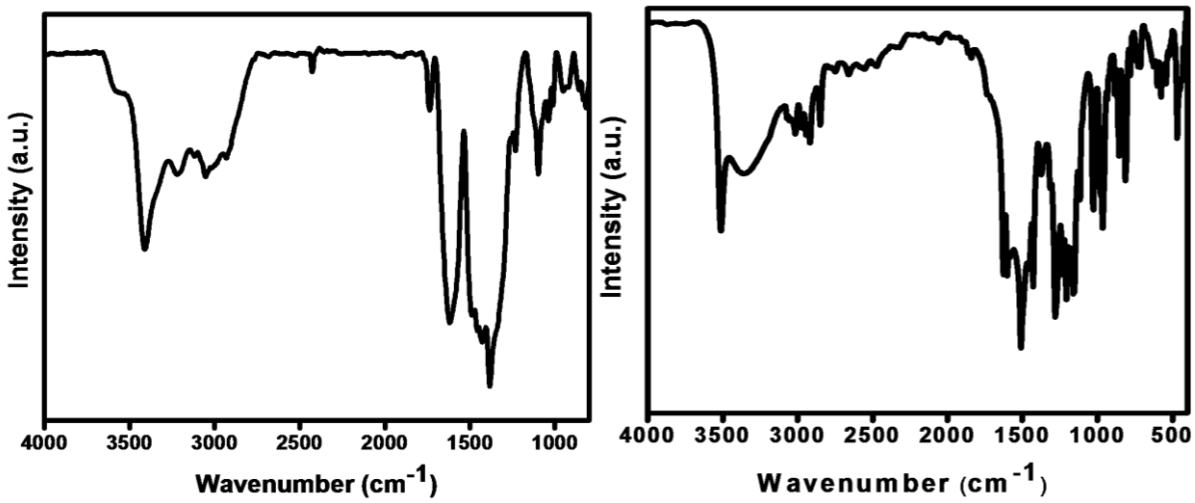

Figure 5.1. IR spectrum of TTTCOOH (left) and BrTTTCOOH (right).

5.3.2. Photophysical Characterization of Terthiophenes

The UV-vis absorption spectrum of TTTCOOH (9.04×10^{-4} M) has absorption at 360 nm and a broad shoulder peak at 420 nm and that of BrTTTCOOH shows a broad absorption range extending from 320-480 nm with λmax at 390 nm (Figure 5.2). The absorption features of terthiophenes originate from the conjugated structure with alternating single and double bonds in the thiophene backbone. Typical single emission peak at 450 nm was observed for TTTCOOH at 360 nm excitation wavelength. PL spectrum of BrTTTCOOH shows emissions at 450 nm (shoulder peak) and 540 nm on excitation at 390 nm (Figure 5.3). The excitation spectra of both the compounds are also given (Figure 5.3).

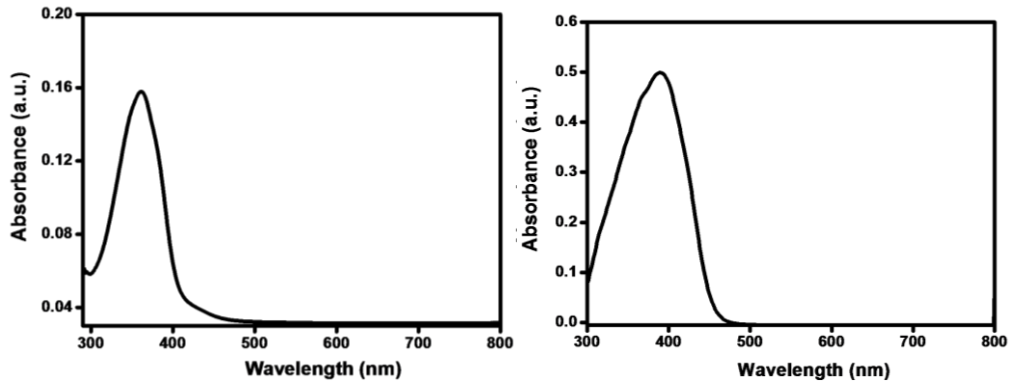

Figure 5.2. UV-vis spectrum of TTTCOOH (left) and BrTTTCOOH (right).

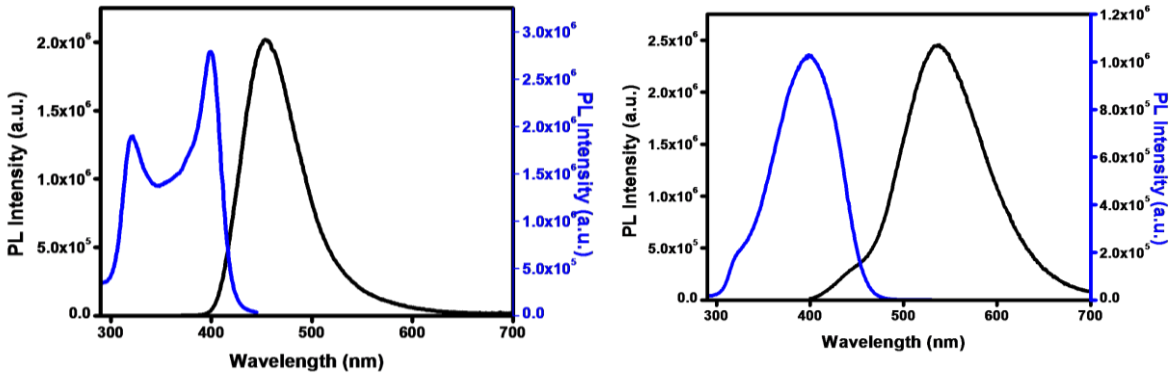

Figure 5.3. Emission and excitation spectra of TTTCOOH (λexc=360 nm, λems=450 nm (left)) and BrTTTCOOH, (λexc=390 nm, λems=540 nm (right)).

The excitation spectra of both the compounds differ from the absorption spectra, more so in TTTCOOH with a very distinct double horn shape. Such a feature is possible in multiple scenarios like (i) presence of fluorescing impurities (ii) same molecule present in different states like aggregates, dimers, trimers etc (iii) excited state reactions like proton dissociation, (iv) conformational change etc. In the present case, thorough structural characterization rules out presence of discernible concentrations of any impurity. Hence, we attribute the multiple peaks in excitation spectra to the presence of other equilibrated states of terthiophene. Another interesting observation is that the Br analogue exhibits abnormal Stoke's shift of ~ 150 nm indicating some form of excited state reactions which could involve solvent relaxation, intramolecular charge transfers or exciplex formation (excited state complexes). This can be considered as a drawback in thiophene systems

since such alternative pathways may lead to reduction in interfacial electron transfer efficiency on grafting to ZnO.

5.3.3. ZnO-terthiophene composites

Powder X-ray diffraction patterns show that the parent wurtzite phase of ZnO NPs is not distorted in the case of ZnO-TTTCOOH and ZnO-BrTTTCOOH composites during the surface grafting (Figure 5.4).

Surface charges of the grafted ZnO were found from zeta potential measurements to be -25 and -26 mV for TTTCOOH and BrTTTCOOH respectively when compared to 4 mV for naked ZnO. TEM images of grafted ZnO NPs also corroborate surface grafting, wherein the particles were found to be well separated from each other with particle size of 4±2 nm (Figure 5.5). From these observations, it is clear that the grafting has stabilised the ZnO NPs against agglomeration. This may be because of the arrest of solution ripening (a kinetically favoured factor) possible for naked ZnO as a consequence of in-situ addition of the organic molecules (TTTCOOH and BrTTTCOOH). The corresponding histograms of both the composites are also shown as an inset along with the TEM images.

FTIR spectroscopic studies clearly support anchoring of the dyes (TTTCOOH and BrTTTCOOH) to ZnO through carboxylic group. IR spectra of the grafted ZnONP with the thiophene ligands show substantial shifts indicating covalent anchoring (Figure 5.6). The intense –CO stretching vibrational frequency of the carboxylic moiety shifts from 1632 to 1553 cm^{-1}, and 1634 cm^{-1} to 1589 cm^{-1} for TTTCOOH and Br analogue respectively. Also, the same behavior is observed for ν_{C-O} band (1377cm^{-1} to 1297 cm^{-1}). Similar shifts were observed with BrTTTCOOH also; the bands near 3515 cm^{-1} and 1518 cm^{-1} corresponding to -OH and C-O group attached to the thiophene ring in the molecule is also shifted to lower frequency 3395 cm^{-1} and 1494 cm^{-1} in the spectra of ZnO-thiophene composites (Figure 5.6).

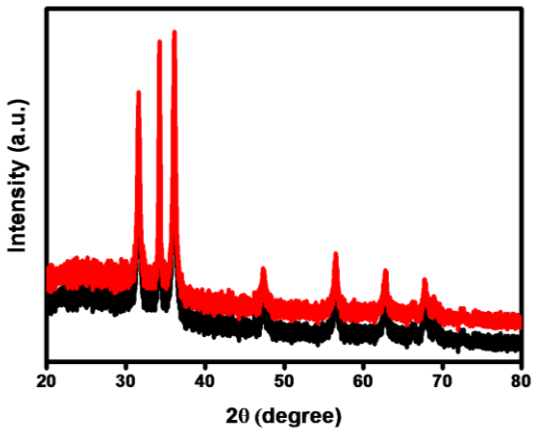

Figure 5.4. XRD patterns of ZnO-TTTCOOH (black) and ZnO-BrTTTCOOH (red)

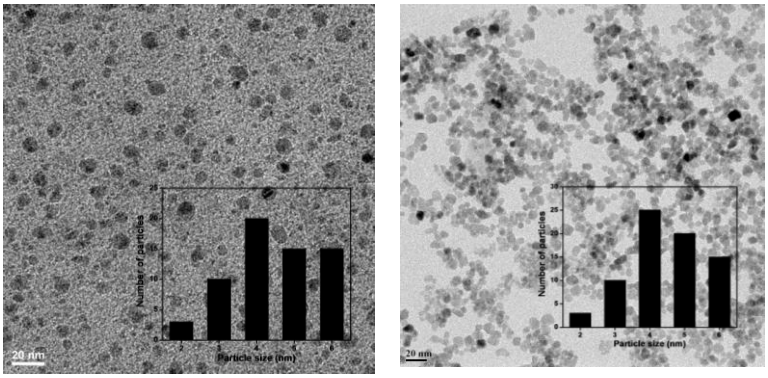

Figure 5.5. TEM images of ZnO-TTTCOOH (left) and ZnO-BrTTTCOOH (right) composites with the corresponding histograms as inset.

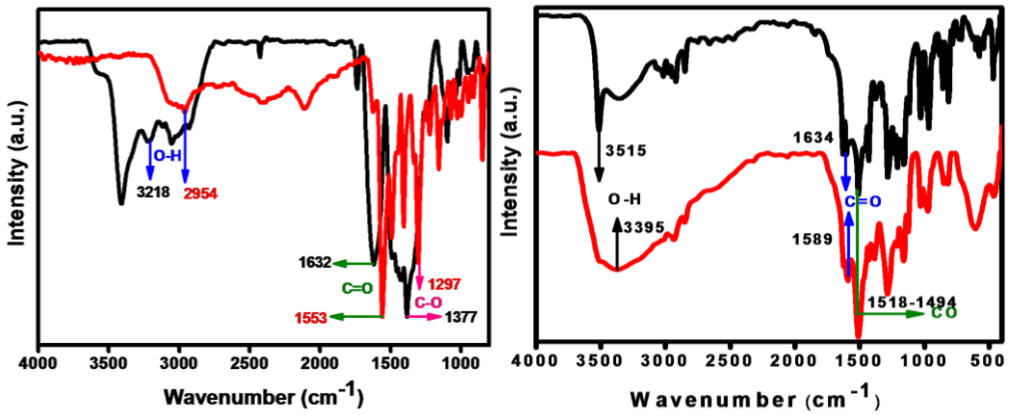

Figure 5.6. FT-IR spectrum of (a) TTTCOOH (black) and ZnO-TTTCOOH composite (red) and BrTTTCOOH (black) and ZnO-BrTTTCOOH composite (red).

5.3.4. Photophysical characterizations of ZnO-TTTCOOH composites

5.3.4.1. ZnO-TTTCOOH composites

On grafting the molecule TTTCOOH to ZnONP, substantial changes are observed in the absorption spectra and emission spectra in terms of peak intensities. It is clear from the UV-vis spectrum that the optical density of the composite has increased from the molecule's optical density after grafting. Visible light absorption is also enhanced in the composite in comparison to pristine molecule indicating potential as visible light sensitizers. UV-vis absorption spectrum of the ZnO-TTTCOOH composite displays predominantly thiophene absorption features (360 nm) along with a new peak at 315 nm and a slight red shifted peak at 430 nm in the visible region (Figure 5.7). In ZnO-TTTCOOH, no absorption feature (absorption edge at ~ 360 nm) of ZnO is seen. Similarly, emission features of the ZnO-TTTCOOH composite resemble that of the organic component than ZnO. Typical emission at 450 nm was observed for ZnO-TTTCOOH at 360 nm excitation wavelength which is also the characteristic emission for the molecule (Figure 5.7). The increase in the emission intensity observed in the case of composite can be correlated to the increase in absorbance. In case of azoquinolines, such an increase in emission intensity in the composite was observed and this was understood to be due to electron transfer from ZnO to dye on UV irradiation. However, in the present case, we cannot conclude any electron transfer or electron conduction from ZnO to the molecule, since ZnO bandgap excitation is not possible in this energy (on excitation at 360 nm). But such an increase may indicate radiative emissive pathways dominating over non-radiative paths on grafting. The excitation spectrum of the composite also shows substantial minimization of the double horn shape, which also indicates that some alternate charge/energy transfer mechanisms at play in the pristine thiophene is reduced after grafting (Figure 5.8). In addition, defect green emission of ZnO is completely suppressed in the case of ZnO-TTTCOOH composite.

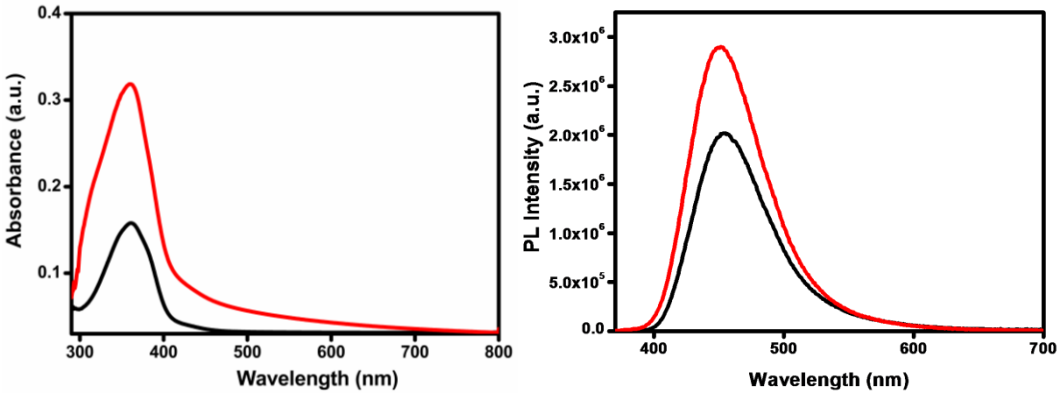

Figure 5.7. UV-vis spectrum (left) of TTTCOOH (black) and ZnO-TTTCOOH (red) and emission spectrum (right) of TTTCOOH (black) and ZnO-TTTCOOH (red), λexc=360 nm.

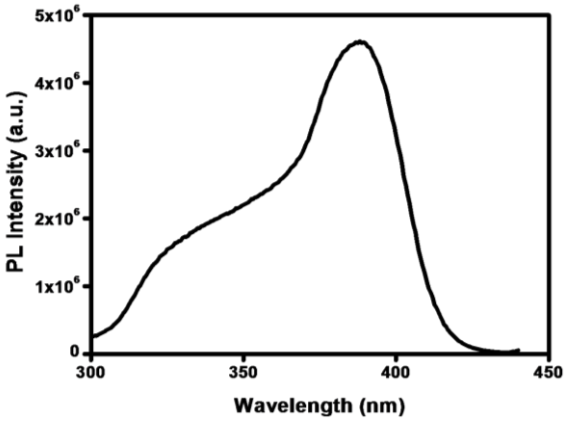

Figure 5.8. Excitation spectrum of ZnO-TTTCOOH composite (λems=450 nm).

For lifetime measurements, decay curves were obtained by the time-correlated single-photon counting (TCSPC) technique using a HORIBA Jobin Yvon Nano-LED source with wavelength 360 nm. Decay measurements were carried out at emission wavelength of 450 nm for TTTCOOH and ZnO-TTTCOOH composites. These experiments were carried out for ZnO NPs (1.69 x10^{-3} M), TTTCOOH (9.04 x 10^{-4} M), ZnO-TTTCOOH composite (1.69 x10^{-3} + 9.04 x 10^{-4} M) at room temperature. Analysis of the lifetime measurements of the molecule and the composite shows interesting features. The observations are tabulated in Table 5.1 and the emission decay profiles are shown in Figure 5.9. The decay curves are deconvoluted by numerical convolution technique and the delta pulse response is fitted to bi-exponential for dye and the composite. ZnO shows a tri-exponential fit (as explained in

chapter 2, this suggests that as particle size of ZnO decreases, there is a possibility of formation of multiple components). Dye shows biexponential fit with two components at 0.75 (major) and 2.06 (minor) ns. On grafting, the lifetime of these individual components doubled leading to an enhancement in average lifetime. This observation is reflected in the fluorescence intensity increment compared to that of the TTTCOOH and also in the absence of defect emission. This clearly shows that the fluorescence phenomenon in the ZnO-TTTCOOH composites originates more from the dye species compared to ZnO with substantial contribution in the visible region.

Table 5.1. Lifetime parameters of TTTCOOH and ZnO-TTTCOOH composites

System	Experimental Setup	Lifetime (ns)		
		τ1(a1)	τ2(a2)	<τ>
TTTCOOH	λex=360nm λem=450 nm	0.75 (0.92)	2.06 (0.08)	0.86
ZnO-TTTCOOH	λex=360nm λem=450nm	1.36 (0.98)	4.46 (0.02)	1.41

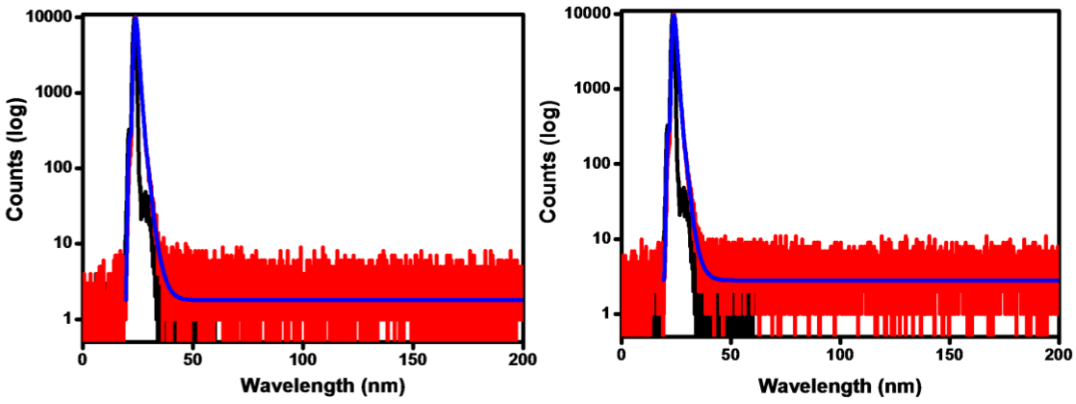

Figure 5.9. The emission decay profiles on excitation at 360 nm of (a) TTTCOOH and (b) ZnO-TTTCOOH Composites. Instrument response function in black, decay profile in red and experimental fit in blue.

5.3.4.2. ZnO-BrTTTCOOH composites

ZnONP grafted with BrTTTCOOH also shows substantial changes in the absorption spectra and emission spectra in terms of peak intensities. Visible light absorption range is highly enhanced from 400-500 nm in the composite in comparison to BrTTTCOOH molecule. This proves the composite as a potential candidate for visible light absorption and also as a sensitiser. The absorption spectrum of ZnO-BrTTTCOOH shows drastic blue shift of the main peak from BrTTTCOOH molecule, with bands at 320, 360 and 430 nm (Figure 5.10). It is ambiguous whether the peak at 360 nm of the composite can be attributed to any other new features in ZnO-BrTTTCOOH composites developed during grafting. To confirm this, an attempt at deconvoluting the absorption peaks of the composite was done. An ideal deconvoluted fit was obtained for the composite absorption spectrum showing four peaks at 320, 360, 400 and 440 nm (Figure 5.10). It is clear that the peak at 320 nm is from ZnO and the one at 400 nm is the contribution from thiophene (390 nm absorption peak of BrTTTCOOH molecule is red shifted). It is possible that the peaks at 360 nm and 440 nm (which enhance the visible light absorption) are newly formed and originates from ZnO-thiophene complex at the interface. From the UV-vis spectroscopy studies, it is clear that the ZnO-BrTTTCOOH composite shows combined features of both ZnO nanoparticles and BrTTTCOOH molecule as well as of the new species. In ZnO-BrTTTCOOH composite emission shows interesting features (Figure 5.11). As observed earlier, BrTTTCOOH shows an intense emission at 540 nm with a shoulder at 450 nm. The emission spectrum of ZnO-BrTTTCOOH also shows similar peaks at all excitation wavelengths (320, 360, 400 and 440 nm). The excitation spectrum is also given in Figure 5.12 and observed to be very broad indicating all possible transitions in the composite. In the composite, interestingly, intensity of the main emission peak (540 nm) decreases in contrast to the observation in ZnO-TTTCOOH. This clearly indicates an electron transfer or electron conduction to ZnO from the bromothiophene molecule. Since the molecule and ZnONPs visible band emissions overlap, we cannot conclude any suppression of defect emission in the case of composite.

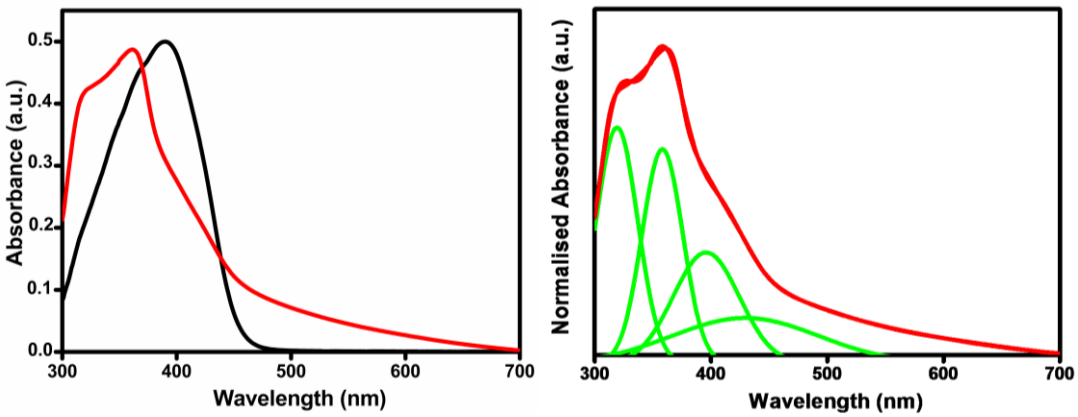

Figure 5.10. UV-vis spectrum (left) of BrTTTCOOH (black) and ZnO-BrTTTCOOH (red) and deconvoluted UV-vis spectrum (right)of ZnO- BrTTTCOOH .

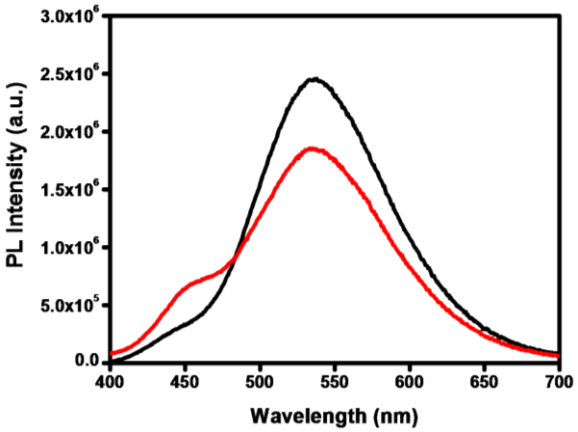

Figure 5.11. Emission spectrum of BrTTTCOOH (black) and ZnO-BrTTTCOOH (red), (λexc=390 nm).

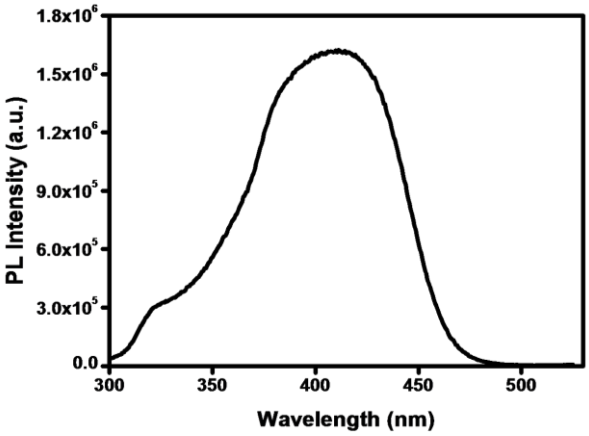

Figure 5.12. Excitation spectrum of ZnO-BrTTTCOOH, (λems=540 nm).

The fluorescence lifetime study for the system was studied by TCSPC (Time-correlated single photon counting). For lifetime measurements, decay curves were obtained using a HORIBA Jobin Yvon Nano-LED source with wavelengths 320, 360 and 390 nm. Decay measurements were carried out at emission wavelengths of 500 nm for ZnO NPs, 540 nm for BrTTTCOOH, 450 and 540 nm for ZnO-BrTTTCOOH composites. These experiments were carried out for ZnO NPs (1.69 $x10^{-3}$ M), BrTTTCOOH (9.04 x 10^{-4} M), ZnO-BrTTTCOOH composite (1.69 $x10^{-3}$ + 9.04 x 10^{-4} M) at room temperature. The emission decay profiles are shown in Figures 5.13 and 5.14 and the observations are tabulated in Table 5.2. The decay curves are deconvoluted by numerical convolution technique and the delta pulse response is fitted to bi-exponential for the molecule and composite, tri-exponential for ZnO with three components (as explained in chapter 2, this suggests that as particle size of ZnO decreases, there is a possibility of emergence of other species). Molecule shows two components at 0.38 (59 %) and 4.8 (41 %) ns at 540 nm λem. Decay curves of the composite attained better fit and chi-square values in bi-exponential indicating a dominance of thiophene features in the composite. In the case of composite, the 450 nm emission shows two components at 0.89 (major-95 %) and 2.65 (minor-5 %) ns. At 540 nm λem, the composite shows two species at 0.77 (92 %) and 2.29 (8 %) ns. The major species at 0.77 ns in the case of composite seems to be originating predominantly from the molecule (0.38 ns) along with a minor contribution from ZnO (1.08 ns). Average lifetime of the composite is decreased when compared to that of the molecule as corroborated from the steady state studies. In steady state, it was observed that the emission intensity is decreased in case of the composite when compared to that of the molecule, which is clearly reflected in the lifetime of the composite, proving a successful electron and charge transfer. This evidently shows that the fluorescence phenomenon and the electron transfer or conduction both in the UV and visible region in the ZnO-BrTTTCOOH composites originates from the molecule with substantial contribution from ZnO.

Table 5.2 Lifetime parameters of ZnO, BrTTTCOOH and ZnO-BrTTTCOOH composites

System	Experimental Setup	Lifetime (ns)			
		τ1(a1)	τ2(a2)	τ3(a3)	<τ>
ZnO Defect Band	λex=320nm λem=500nm	1.08 (0.92)	9.42 (0.07)	47.7 (0.01)	1.51
BrTTTCOOH	λex=390nm λem=540 nm	0.38 (0.59)	4.8 (0.41)		2.2
ZnO-BrTTTCOOH	λex=360nm λem=450 nm	0.89 (0.95)	2.65 (0.05)		0.97
ZnO-BrTTTCOOH	λex=360nm λem=540 nm	0.77 (0.92)	2.29 (0.08)		0.89

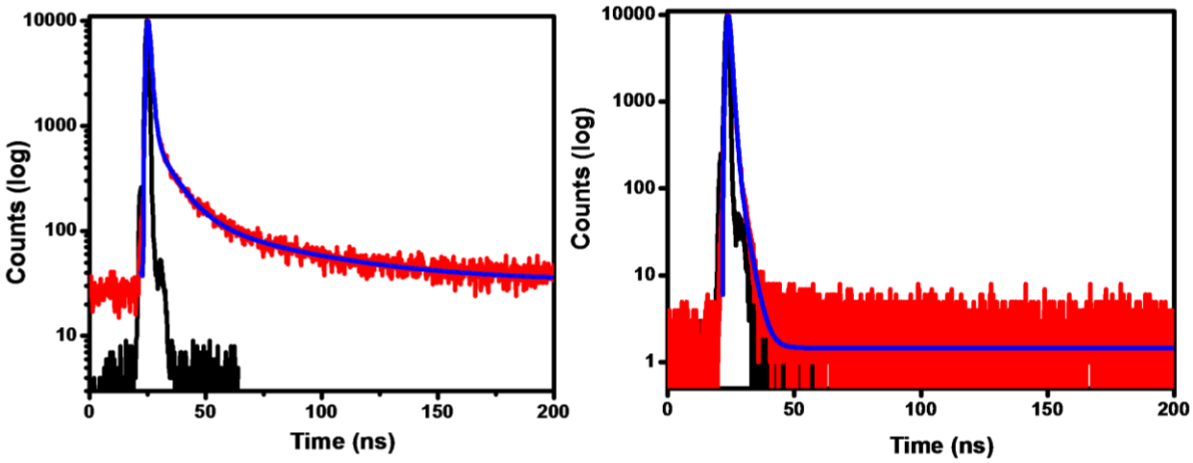

Figure 5.13. The emission decay profiles on excitation at 320 nm of (a) ZnONP and excitation at 390 nm (b) BrTTTCOOH Composites. Instrument response function in black, decay profile in red and experimental fit in blue.

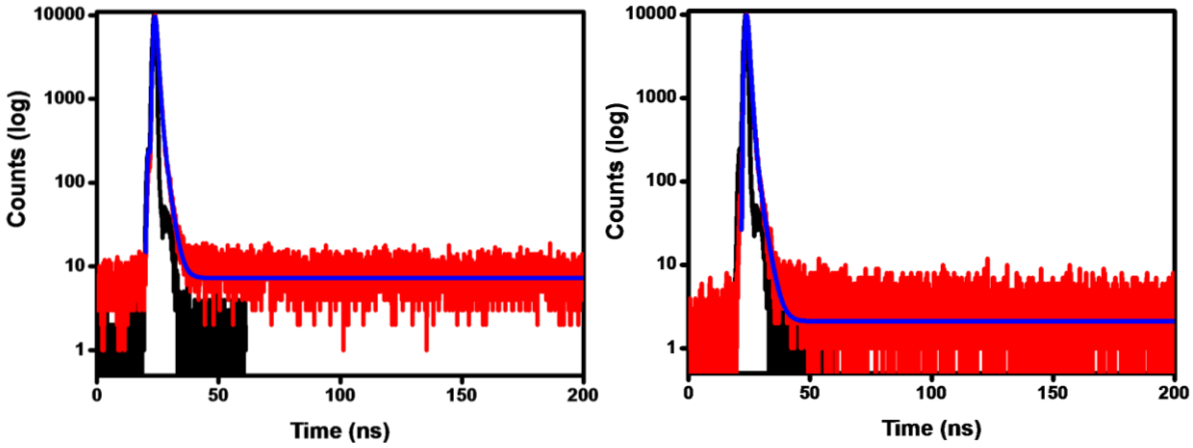

Figure 5.14. The emission decay profiles on excitation at 360 nm of ZnO-BrTTTCOOH Composites (a) 450 nm and (b) 540 nm emissions. Instrument response function in black, decay profile in red and experimental fit in blue.

The redox and the electron transfer properties of the samples were also studied by cyclic voltammetry (Figure 5.15). Both the composites show an electron transfer mechanism different from the pristine ZnO and dye molecules which is very well observed by the electrochemical studies. The onset potential and current are found to be considerably enhanced on grafting when compared to ZnO and dyes [ZnO (0.0075mA at the onset potential of 1 V), TTTCOOH (0.0013 mA at onset potential of 1.181V), BrTTTCOOH (0.0054 mA at onset potential of 0.808V) , ZnO-TTTCOOH Composite (0.018 mA at onset potential of 1.197 V)] and ZnO-BrTTTCOOH Composite (0.081 mA at onset potential of 0.821 V)]. Photocurrent responses of the composites are also measured by linear sweep voltammetry) (by scanning in a potential window of 1 to 1.7 V) and Impedance analysis under irradiation and in dark (Figures 5.16 a-d). The resistance was also found to be less under illumination (1506 Ω for ZnO-TTTCOOH and 570 Ω for ZnO-BrTTTCOOH) compared to the dark condition (1546 Ω for ZnO-TTTCOOH and 630 Ω for ZnO-BrTTTCOOH). This clearly shows that both the composites are highly conducting and faster electron transporters under illumination. We observe a marked enhancement in conductivity under irradiation indicating an electron transfer phenomenon between ZnO and organic molecules. Current increment is not observed in pristine ZnONPs and dyes on illumination [14,15] .

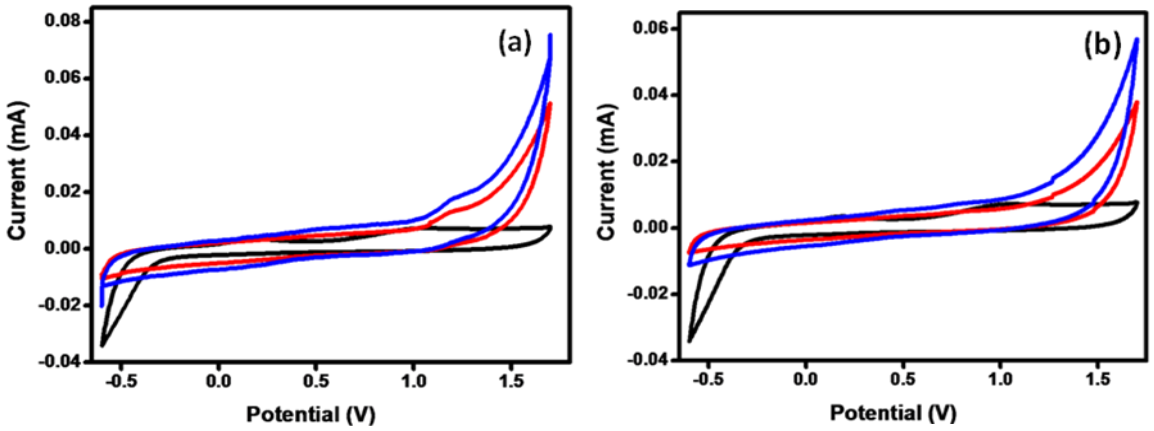

Figure 5.15. Current–voltage profile for photoelectrochemical cells employing (a) ZnO (black), TTTCOOH (blue) and ZnO-TTTCOOH composite (red) and (b) ZnO (black), BrTTTCOOH (blue) and ZnO-BrTTTCOOH composite (red) by cyclic voltammetry at a scan rate of 50 mv/s. Supporting electrolyte was $LiClO_4$ in acetonitrile.

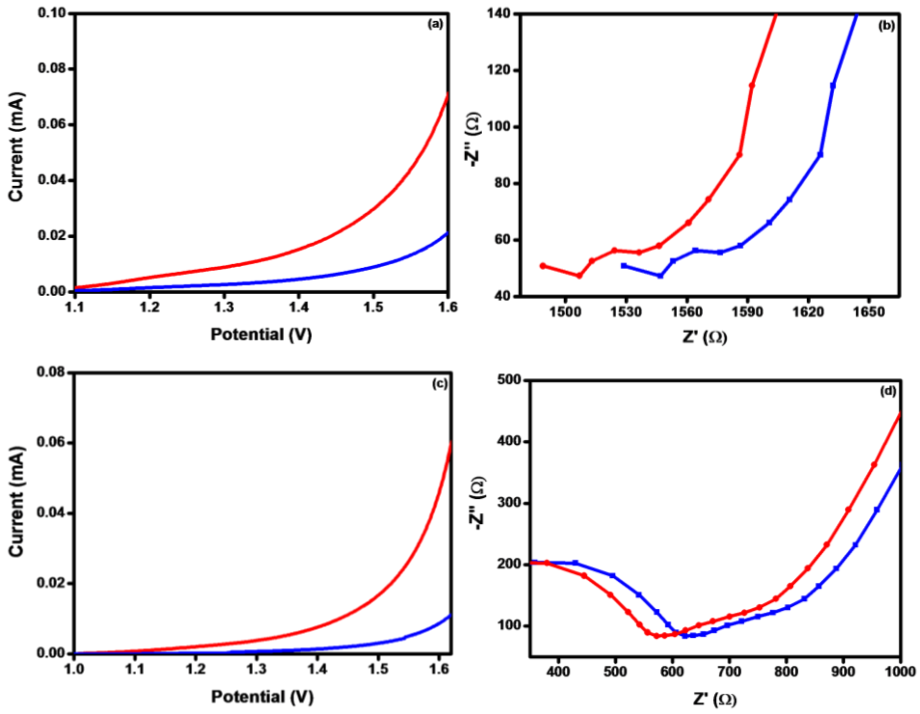

Figures 5.16. LSV profile for photoelectrochemical cells employing (a) ZnO-TTTCOOH and (c) ZnO-BrTTTCOOH Composites(10 mv/s) upon turning on (red) and off (blue) 200W tungsten lamp by cyclic voltammetry and Electrochemical Impedance employing (b) ZnO-TTTCOOH and (d) ZnO-BrTTTCOOH Composites upon turning on (red) and off (blue) 200W tungsten lamp .

5.3.5. Computational Studies

The clean ZnO ($10\bar{1}0$) surface contains ordered rows of buckled Zn-O dimers along the polar [0001] direction with a net electron accumulation on the O atoms. The calculations show that TTTCOOH and BrTTTCOOH molecules bind vertically to the ZnO surface (Figure 5.17) and creating two Zn-O bonds through the –COOH group [16-32].

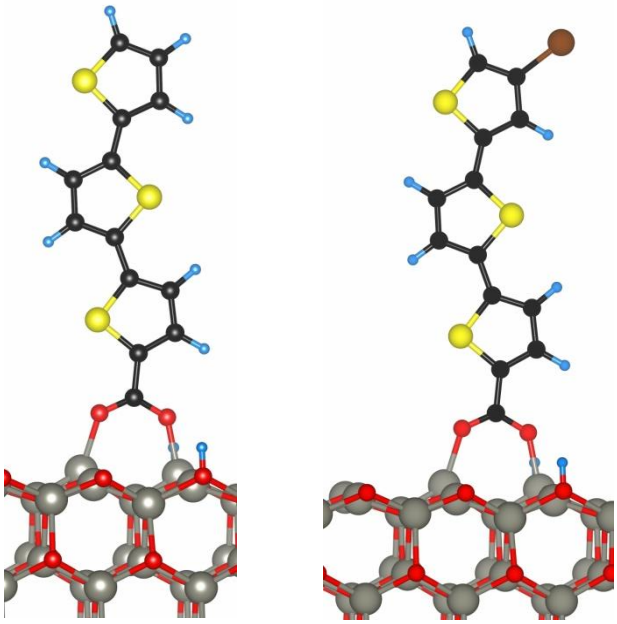

Figure 5.17. Optimized structure of TTTCOOH and BrTTTCOOH on ZnO($10\bar{1}0$). The grey, red, black, blue and yellow spheres represent Zn, O, C, H and S atoms respectively.

From the computational studies, it is observed that the resonance energy stabilization is more in bromine analogue than TTTCOOH. During the relaxation process of the composite, it spontaneously gets deprotonated, releasing an H^+ ion from the –COOH group of both the molecules , which gets attached to the neighbouring electron rich O of the ZnO surface. Any distortion of the surface is not observed except at the adsorption site where the buckling of the Zn-O dimers are reduced compared to the the clean surface of ZnO. The density of states (DOS) of the ZnO-TTTCOOH is shown in Figure 5.18. The electronic states are aligned with respect to the energy at vacuum. Upon modifying the surface of the ZnO nanoparticles

with TTTCOOH, the effective band gap of the interface is reduced to 1.3 eV compared to that of 3.77 eV for the clean slab.. The calculations show that the valence band maximum (VBM) of the interface is localized on the molecule and the conduction band minimum (CBM) is localized on the slab. On substitution of halogen the overlap (Figure 5.19) increases, which is the sign of proper electron transfer. LUMO+1 and LUMO+2 of the composites overlap to different extents in TTTCOOH and its Br analogue; the overlap is higher in case of the latter. We hypothesise that, due to this, a direct electron transfer from HOMO (molecule) to LUMO+1 (ZnO) is more facile in Br analogue. Similarly, an exceptional overlap of molecule and ZnO bands is also observed in LUMO+4 state. This is also reflected in highly altered absorption spectrum of the composite when compared to pristine molecule, in case of BrTTTCOOH.

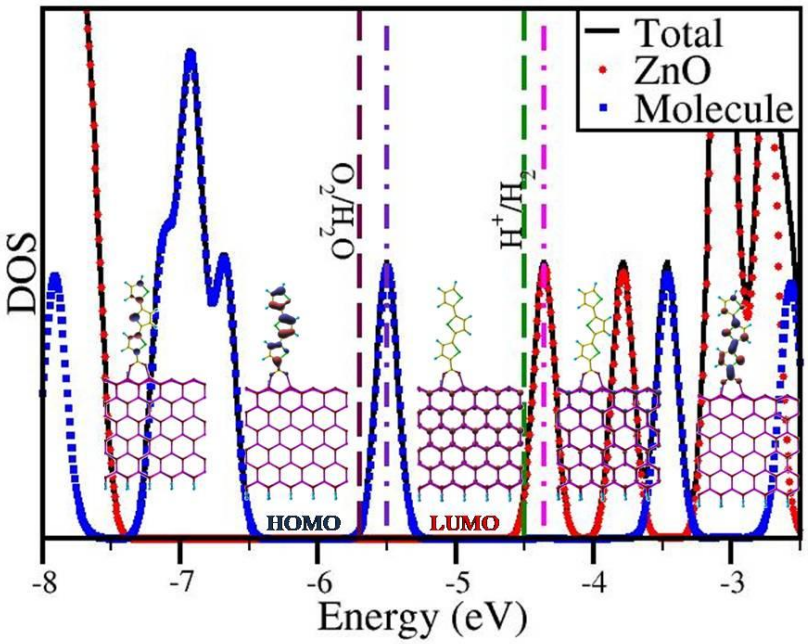

Figure 5.18. DOS of the ZnO-TTTCOOH composite. Dot-dashed violet and magenta vertical lines mark the VBM and CBM respectively. The dashed brown and green lines mark the OP and RP.

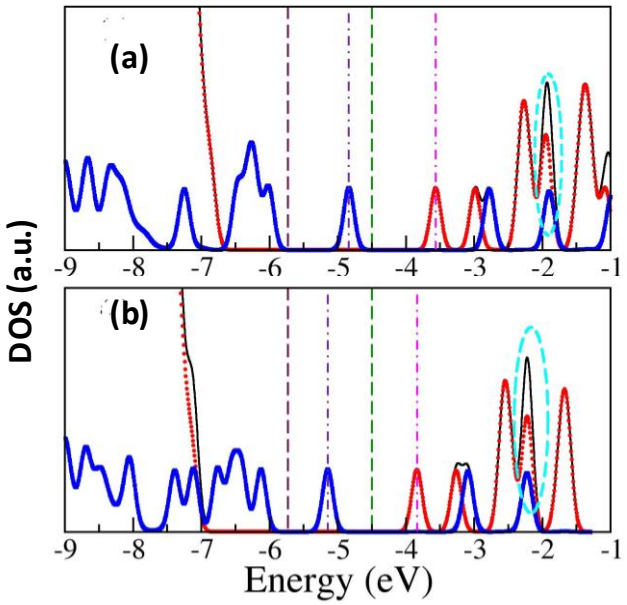

Figure 5.19 : (a) TCA and (b) TCA - Br. Total and projected DOS for the -COOH anchoring configuration of the molecule on ZnO slab. Dot-dashed violet and magenta vertical dashed lines denote the valence band maxima (VBM) and the conduction band minima (CBM) respectively of the composite. The dashed brown and green lines mark the water oxidation and reduction potentials respectively. Dashed eclipse highlights the coupling of the molecules empty states with ZnO.

To explore the possibility of using the composites as photocatalysts for water splitting, the positions of the oxidation potential (OP) of oxidizing H_2O to O_2 and the reduction potential (RP) of reducing H^+ to H_2 with respect to the positions of VBM and CBM of the ZnO-TTTCOOH and ZnO-BrTTTCOOH composites are considered . As mentioned earlier, the electronic states, in the DOS shown in Figure. 5.18 are aligned with respect to the energy at vacuum. Hence ,the absolute values of the VBM and CBM are known. The absolute values of the OP/RP are given by $E_{abs}^{OP/RP}$=-4.5-$E_{NHE}^{OP/RP}$, where $E_{abs}^{OP/RP}$ is the absolute value of the OP/RP and $E_{NHE}^{OP/RP}$ is the OP/RP potential in V vs. the NHE at pH 0.[42] E_{NHE}^{OP} is 1.23 eV and E_{NHE}^{RP} is 0.00 eV (as discussed in chapter 2). For the composites to be a good photocatalyst for water splitting these two potentials should lie in the band gap, i.e., the OP should lie above the VBM and the RP should lie below the CBM. In ZnO-TTTCOOH composite, the CBM is at -3.5 eV which is above the reduction potential of hydrogen. The CBM for ZnO-

BrTTTCOOH composite is found to be at a lower energy (-3.8 eV). From the calculations, the CBM for the ZnO-BrTTTCOOH composite is more facile for electron transfer than ZnO-TTTCOOH. In other words, the CBM of ZnO-BrTTTCOOH is more closer to the RP than ZnO-TTTCOOH (Figure 5.20).

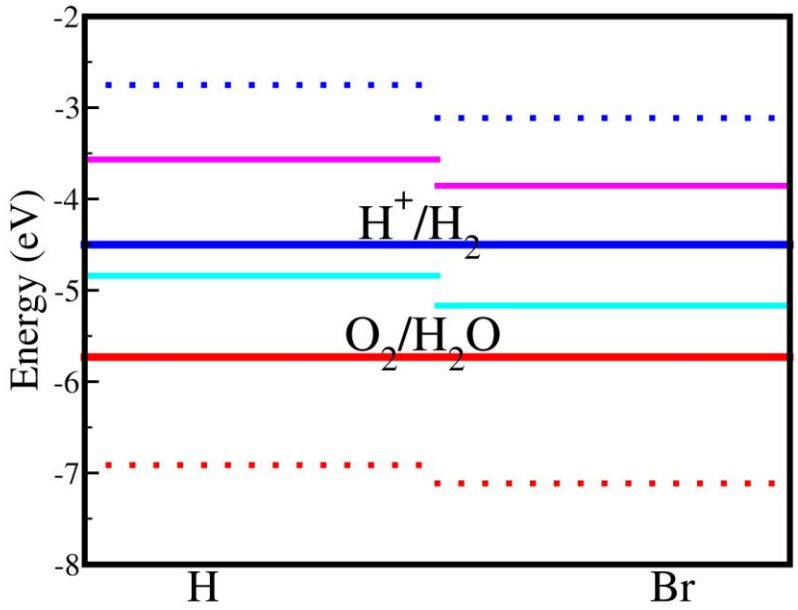

Figure 5.20. The magenta, blue, green and red lines denote the conduction band minima (CBM) , water reduction potential, valence band maxima (VBM) and water oxidation potential respectively of the composites.

5.3.6. Photocatalytic testing of ZnO-TTTCOOH and ZnO-BrTTTCOOH Composites

The photophysical studies of both the systems (ZnO-BrTTTCOOH and ZnO-TTTCOOH) indicate inherent differences imposed on the thiophene backbone by Br substitution. Bromine is considered as an electron withdrawing group, showing –I effect. But bromine can show mesomeric effect (+M effect) also due to its lone pair of electrons. From the computational studies, it is clear that resonance stabilization is more in the case of bromo analogue than TTTCOOH molecule, which is possible only if the lone pair of electrons on bromine also contribute to the resonance structures. So, in the present case, the +M effect

of bromo analogue is dominating, thereby increasing the electron density on the thiophene backbone compared to TTTCOOH molecule. This increase in the electron enrichment on the ZnO-BrTTTCOOH composite facilitates better photocatalytic water splitting activity compared to ZnO-TTTCOOH composites as explained below.

The photocatalytic water splitting activities for both the composites are tested under different irradiation sources (UV, visible and direct sunlight) for 8 h (Figure 5.21) by head space analysis. As evident from the computational studies, there is an overlap with LUMO of the molecule and the conduction band of ZnO in the lower band gap energy (Figure 5.15), which is more in the case of ZnO-BrTTTCOOH composite compared to ZnO-TTTCOOH composites. This may be the reason for the slight enhancement of H_2 evolution in the composite with Br analogue, due to more prominent overlap in this molecule.

To see the effect of sacrificial reagent, water splitting experiments were carried out in different concentrations of methanol for both the composites and a corresponding increase in the H_2 evolution was observed as expected. However, a saturation yield for H_2 evolution was reached after 35 v/v% and further increase in methanol concentration did not affect the yield substantially (Figure 5.22)

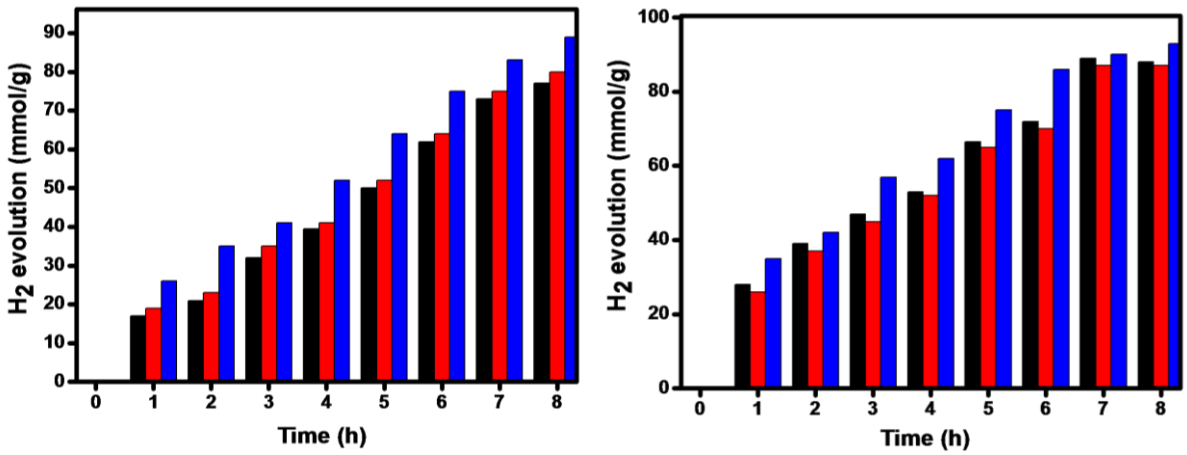

Figure 5.21. Evaluation of photocatalytic activity for H_2 generation under UV (black), visible (red) and solar (blue) at various irradiation time (0 - 8 h) (left) ZnO-TTTCOOH Composite and (right) ZnO-BrTTTCOOH Composite.

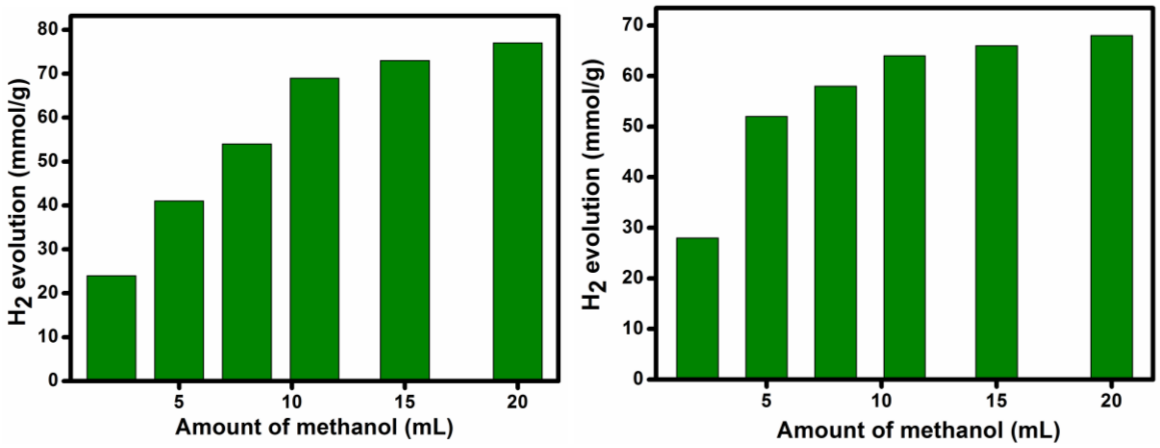

Figure 5.22. Evaluation of photocatalytic activity for H_2 generation under visible irradiation for 4 h from water-methanol mixtures with varying amounts of methanol in (left) ZnO-TTTCOOH Composite and (right) ZnO-BrTTTCOOH Composite (2,5,8, 11, 15 and 20 ml).

5.4. CONCLUSIONS

This chapter describes the design strategy that was adopted to develop appropriately conducting visible light sensitizers. Here, the conjugation length is kept constant and the substituents were varied in the organic molecules. The photophysical characteristics of both the composites show interesting features with slight variations in the fluorescence intensities showing the possibilities of electron transfer between the ZnO-organic molecule interface. The computational studies also proved a better electron transfer in the case of bromo composite. Also, the conduction band minima is more feasible in the bromo analogue for the water reduction reaction. From the photophysical studies, the Br-TTTCOOH molecule showed an enhancement in visible light absorption in the composite compared to the TTTCOOH molecule which is very well projected in the photocatalytic water splitting activity also.

References

1. Norberg, N. S.; Gamelin, D. R., *J. Phys.Chem. B* **2005**, *109,* 20810-20816.
2. Guo, L.; Yang, S.; Yang, C.; Yu, P.; Wang, J.; Ge, W.; Wong, G. K. L., *Chem. Mater.* **2000**, *12*, 2268-2274.
3. Hua, Z.; Xu, Q.; Huang, X.; Zhang, C.; Wang, X.; Xiao, M., *ACS Nano* **2014**, *8*, 7060-7066.
4. Kamat, P. V.; Patrick, B., *J. Phys. Chem*. **1992**, *96*, 6834-6839.
5. Geobaldo, F.; Turnes Palomino, G.; Bordiga, S.; Zecchina, A.; Otero Arean, C., *Phys. Chem. Chem. Phys.* **1999**, *1*, 561.
6. Vatassery, R.; Hinke, J. A.; Sanchez-Diaz, A.; Hue, R.; Mann, K. R.; Blank, D. A.; Gladfelter, W. L., *J. Phys. Chem. C* **2013**, *117*, 10708.
7. Goto, Y.; Taniguchi, K.; Omata, T.; Otsuka-Yao-Matsuo, S.;Ohashi, N.; Ueda, S.; Yoshikawa, H.; Yamashita, Y.; Oohashi, H.;Kobayashi, K., *Chem. Mater*. **2008**, *20*, 4156.
8. Cleveland, C. L.; Landman, U., *J. Chem. Phys*. **1991**, *94*, 7376.
9. Zakharian, T. Y.; Coon, S. R., *Comput. Chem*. **2001**, *25*, 135.
10. Upton, T. H.; Goddard, W. A., *Phys. Rev. Lett*. **1979**, *42*, 472.
11. Ohshita, J., *Macromol. Chem. Phys*. **2009**, *210*, 1360.
12. Jirsak, T.; Dvorak, J.; Rodriguez, J. A., *J. Phys. Chem. B* **1999**, *103*, 5550.
13. Huntley, D. R.; Mullins, D. R.; Wingeier, M. P., *J. Phys. Chem*. **1996**, *100*, 19620.
14. Haynes, K. M.; Kratch, K. C.; Stovall, S. D.; Obondi, C. O.; Thurber, C. R.; Youngblood, W. J., *ACS Appl. Mater. Interfaces.* **2015**, *7*, 16133-16137.
15. Nandi, S.; Singh, S. K.; Mullangi, D.; Illathvalappil, R.; George, L.; Vinod, C. P.; Kurungot, S.; Vaidhyanathan, R., *Adv. Energy Mater*., **2016**, *6*, 1601189.
16. Yanai, T.; Tew, D. P.; Handy, N. C. *Chem. Phys. Lett*. **2004**, *393*, 51–57.

17. Scalmani, G.; Frisch, M. J., *J. Chem. Phys*. **2010**, *132*, 114110.

18. Furche, F.; Ahlrichs, R., *J. Chem. Phys*. **2002**, *117*, 7433–7447.

19. Vanderbilt, D., *Phys. Rev. B* **1990**, *41*, 7892-7894.

20. Vogel, D.; Krüger, P.; Pollmann, J., *Phys. Rev. B* **1996**, *54*, 5495-5511.

21. Perdew, J. P.; Burke, K.; Ernzerhof, M., *Phys. Rev. Lett*. **1996**, *77*, 3865-3868.

22. Janotti, A.; Segev, D.; Van de Walle, C. G., *Phys. Rev. B* **2006**, *74*, 045202-1-9.

23. Calzolari, A.; Ruini, A.; Catellani, A., *J. Am. Chem. Soc*. **2011**, *133*, 5893-5899.

24. Choi, E. A.; Lee, W. J.; Chang, K. J., *J. App. Phy.* **2010**, *108*, 023904-1-6.

25. Dubecký, M.; Derian, R.; Mitas, L.; Štich, I., *J. Chem. Phys*. **2010**, *133*, 244301.

26. Giannozzi, P.; Baroni, S.; Bonini, N.; Calandra, M.; Car, R.; Cavazzoni, C.; Ceresoli, D.; Chiarotti, G. L.; Cococcioni, M.; Dabo, I.; Dal Corso, A.; de Gironcoli, S.; Fabris, S.; Fratesi, G.; Gebauer, R.; Gerstmann, U.; Gougoussis, C.; Kokalj, A.; Lazzeri, M.; Martin-Samos, L.; Marzari, N.; Mauri, F.; Mazzarello, R.; Paolini, S.; Pasquarello, A.; Paulatto, L.; Sbraccia, C.; Scandolo, S.; Sclauzero, G.; Seitsonen, A. P.; Smogunov, A.; Umari, P.; Wentzcovitch, R. M., *J. Phys.: Condens. Matter* **2009**, *21*, 395502.

27. Gong, X. Q.; Selloni, A.; Vittadini, A., *J. Phys. Chem. B* **2006**, *110*, 2804.

28. Meyer, B.; Marx, D.; Dulub, O.; Diebold, U.; Kunat, M.; Langenberg, D.; Woll, C., *Angew. Chem., Int. Ed*. **2004**, *43*, 6641.

29. Quintana, M.; Edvinsson, T.; Hagfeldt, A.; Boschloo, G., *J. Phys. Chem. C* **2007**, *111*, 1035.

30. Savio, L.; Celasco, E.; Vattuone, L.; Rocca, M., *J. Phys. Chem. B* **2004**, *108,* 7771.

31. Schleife, A.; Fuchs, F.; Furthmüller, J.; Bechstedt, F., *Phys. Rev. B* **2006**, *73*, 245212.

32. Tang, J.; Durrant, J. R.; Klug, D. R., *J. Am. Chem. Soc*. **2008**, *130*, 13885.

Chapter 6

Summary and Conclusions

6.1. Summary

Chapter 1 presents a general introduction to environmental issues, hydrogen as greener fuel for the future and photocatalytic water splitting reactions over numerous semiconductor metal oxide photocatalysts. This chapter also explains the idea for the evolution of artificial photosynthetic systems from natural photosynthesis, which is very promising for the future carbon-free power fuels. The principle, processess and the mechanistic steps involved in photocatalytic water splitting reactions vis-à-vis single photon excitation and two-photon excitation (Z-scheme) are discussed in detail. Various strategies are to be adapted to utilize visible light by photocatalysts. Dye sensitized solar cells (DSSCs) have garnered special interest and the dye here plays the role of sensitizer in utilizing visible light and also facilitates efficient electron transfer process between the excited dye and conduction band (CB) of the semiconductor. Such a sensitizing principle can be adapted for photocatalytic water splitting also. The chapter further presents a comprehensive review of literature on various photosensitisers used as photocatalysts including metal complexes and metal-free organic dyes. Several semiconductor oxides systems due to the availability, ease of synthesis and limited photocorrosion can be utilized for photocatalytic water splitting reactions. Among these, zinc oxide has been attracting interest due to its high electron mobility, high thermal conductivity, wide and direct band gap, large exciton binding energy, different synthesizable morphologies, particle size tunability, high luminescence and desired surface properties. The size quantization of ZnONPs can lead to various luminescence transitions, mainly an excitonic emission in the UV region and a defect emission in the visible region. In addition, this chapter describes the most commonly seen defect-related visible emissions, particularly green luminescence and the various types of defects responsible for this emission. The chapter briefly describes the role of short conjugated organic sensitizers in photocatalytic water splitting reaction. Finally the scope and objective of the thesis are stated.

Chapter 2 describes the synthesis of ZnO-azonaphthol composites and their structural evaluation and photophysical studies by various characterization methods. ZnO nanoparticles of size ~3 nm are surface modified with azonaphthols which are designed to have a carboxylic functionality in the phenyl group and the conjugation property is varied

by changing the position of this group from para to meta. Generally azo based systems are non-fluorescent which is observed in the meta analogue (3ABBN) but the conjugated para molecule (4ABBN) is fluorescent with an emission in UV region, possibly due to the stabilisation of the hydrazone form consequent to extended conjugation which is absent in meta azonaphthols. ZnO nanoparticles are known to have an UV excitonic emission and also a defect visible band emission which is observed to be very high in the present study due to the possibility of multiple defect sites like Zn vacancy, oxide vacancy, surface hydroxyl groups etc and the UV emission is minimum. This defect emission is completely suppressed on grafting with the non-conjugated molecule, but the conjugated molecule shows some interesting features. A drastic reduction in intensity in the dye UV emission is seen in the ZnO-4ABBN composite and also the green emission corresponding to defect sites in ZnO is present albeit with a reduction in intensity compared to pristine ZnO, indicating an electron transfer from the dye molecule to ZnO. Moreover, the lifetime studies also show the stabilization of defect species in ZnO due to electron transfer from the organic moiety. In addition, the photocurrent enhancement of the composite under illumination also corroborates an electron transfer mechanism from the dye molecule to ZnO. The composite with non-conjugated molecule is prone to photodegradation whereas that with conjugated molecule is highly stable for photocatalytic water splitting reactions. The electron transfer mechanism in the ZnO-4ABBN composite for photocatalytic water splitting reactions is corroborated by computational studies. DFT studies show that the HOMO of 4ABBN is located in the ZnO band gap, which reduces the effective band gap of the composite and facilitating absorption in the visible region of the solar spectrum. The position of the redox potentials of water reduction and oxidation is aligned with respect to the valence band maxima and conduction band minima of the composite. This claim is further supported by photocatalytic water splitting experiments and there is a much larger yield of hydrogen in presence of methanol, which replenishes the electron. Thus, the ZnO-4ABBN composite photocatalysts, without the use of expensive dyes or cocatalysts pave the way to a more efficient and cost effective method of H_2 generation.

Chapter 3 reported synthesis, characterization and photocatalytic water splitting activity of ZnO-azoquinoline composites (ZnO-3ABBNHQ and ZnO-4ABBNHQ). In this study, two dye molecules, meta and para substituted azoquinoline benzoic acid (3ABBNHQ and 4ABBNHQ) capable of multimodal anchoring are used. On replacing the coupling moiety naphthol with hydroxyquinoline presents a dye structure which can anchor to ZnO through dual site grafting via carboxylate and hydroxyl imine groups, altering the resonance structure of the dye, making electron transfer between ZnO and dye possible. The photophysical characteristics of the dyes show both absorption and emission features. An enhancement in the visible light absorption (5 fold in ZnO-4ABBNHQ and double in ZnO-3ABBNHQ) is observed in both the composites after dye grafting which is responsible for the visible light photocatalytic activity, due to charge transfer from dyes to ZnO. Also, the emission of both the composites increases on excitation in UV light, which indicates an electron transfer from ZnO to dyes, pointing to catalytically active sites on ZnO-dye interface. Electrochemical studies also show an electron transfer in the composite under illumination. Computational studies on the electronic structure of both the dyes and the composites also support such a charge transfer. From the computational calculations, visible light excitation of the dyes and subsequent electron transfer to ZnO surface makes the composites visible light active for H_2 generation when the dye is anchored through carboxylic group. In the case of ZnO-3ABBNHQ composite, an UV light excitation of ZnO is energetically feasible for H_2 generation only in case of quinoline anchoring. Presence of desired catalytic sites on the ZnO-dye interface made the composites (ZnO-3ABBNHQ and ZnO-4ABBNHQ) potential candidates as water splitting catalysts.

Chapter 4 reports synthesis, characterization and photocatalytic water splitting activity of ZnO-Perylene composites (ZnO-PTCDACOOH2). In the present case, perylene tetracarboxylic dianhydride is coupled with para aminobenzoic acid and a symmetrically substituted perylene derivative with carboxylate functionality is designed. Perylene dyes are known for their self-aggregation properties due to π-π stacking, which can be minimized by anchoring it to ZnO nanoparticles. The absorption and emission properties of the ZnO-Perylene composites show interesting features. From the UV-visible

spectroscopic studies of the composite, it is clear that the absorption edge of the ZnO has been slightly red-shifted and also combined features of ZnO and dye molecule is observed. The appearance of a new emission peak at 400 nm is noticed in the case of composite at excitation wavelengths ranging from 315-385 nm. This emission shows the emergence of a new species which is responsible for the enhanced visible light absorption in the composite. The contribution from the new species for the photocatalytic activity is further corroborated from the life time studies. Efficient electron transfer between the dye and ZnO is also proved by the linear sweep voltammetric electrochemical measurements under illumination. Thus, the covalent anchoring of the dye molecule to ZnO nanoparticles increased the electronic communication between the dye chromophore and the semiconductor, thereby enhancing the photostability and H_2 generation of the composite both under UV and visible irradiation. Computational studies were not possible with the ZnO-perylene composites due to the complexity of the composite.

Chapter 5 describes the synthesis, photophysical and photocatalytic water splitting activity of ZnO–terthiophene composites (ZnO-TTTCOOH and ZnO-BrTTTCOOH). Terthiophene molecules are known to be conducting oligomers separated by a heterocyclic π conjugated system. In this chapter, two semiconducting terthiophene molecules are used, one functionalized with –COOH group (TTTCOOH) and the other is terthiophene carboxylic acid functionalized with Br in one end (BrTTTCOOH), inorder to understand the effect of electron density and electron availability in the backbone. In ZnO-TTTCOOH composites, the absorption and emission studies show more of organic molecule features than ZnO with an enhancement in the visible light absorption. Fluorescence intensity has been increased in this case which is further corroborated by the lifetime studies. Electrochemical studies show an efficient electron transfer between ZnO and dye under visible light illumination. The broad absorption range of the composite made it possible as a potential candidate for H_2 generation in photocataytic water splitting. In ZnO-BrTTTCOOH composite, the absorption studies show combined features of both ZnO and the molecule. The fluorescence intensity also decreased in the composite which is reflected in the lifetime studies also. Linear sweep voltammetric and electrochemical impedance measurements

also show a facile electron transfer in the composite under illumination. Computational studies on the electronic structure of both the molecules and the composites also support an efficient charge transfer. From the computational calculations, the valence band maxima (VBM) are on the organic molecules and the conduction band minima (CBM) on the ZnO surface. Also, a direct electron transfer from HOMO (molecule) to LUMO+1 (ZnO) is more facile in Br analogue than TTTCOOH. The overlap of the molecular orbitals of the molecules and ZnO is more prominent in ZnO-BrTTTCOOH than ZnO-TTTCOOH which is evident from the DFT studies. Presence of desired catalytic sites on the composites (ZnO-TTTCOOH and ZnO-BrTTTCOOH) is responsible for the photocatalytic water splitting reactions.

6.2. Conclusions

- Conjugation, resonance properties and effective electron transfer due to appropriate band alignment are the factors found important for photocatalytic water splitting by ZnO composites with organic dyes and semiconductors.
- Photophysical properties of ZnO-azonaphthol composites (ZnO-3ABBN and ZnO-4ABBN) indicate an effective electron transfer from the conjugated azonaphthol to ZnO but not in case of non-conjugated molecule.
- From lifetime studies, it is observed that conjugated molecule stabilises the defect sites on ZnO nanoparticles and the excited electrons from the conjugated molecule (LUMO) are transferred to specific defect sites in ZnO in case of azonaphthols.
- Electron transfer properties under illumination are further proved by the photocurrent enhancement shown by the electrochemical studies.
- The experimental observations are corroborated with computational studies, which also point to a localisation of valence band maximum of the interface on the organic moiety and conduction band minimum on ZnO.
- ZnO-3ABBN composites are prone to photodegradation due to the absence of extended conjugation.
- Presence of multiple chelating sites facilitates dual mode of anchoring on ZnO nanoparticles in case of azoquinoline system, which leads to enhanced photostability and electron transfer properties.

- Electron transfer properties in these composites have been increased by the incorporation of resonance features in the dye molecules through multimodal anchoring.
- Electron transfer from ZnO to dye molecules under UV light and reverse in visible light could be identified from the photophysical studies.
- Computational studies on the electronic structure of the dye molecules and the composite also support such a charge transfer.
- Perylene derivatives are known for their self-aggregation properties, can be minimised by grafting it with ZnO nanoparticles thereby making it efficient for better electron injection and transfer.
- The ZnO-perylene composite shows a broad absorption range with a slight red shift in the ZnO absorption edge and also a new characteristic emission peak at 400 nm, indicating formation of a new species.
- The contribution from new species for the photocatalytic activity is also evident from the lifetime studies.
- The photophysical studies show combined features of both the ZnO and the perylene molecule which shows an efficient electron transfer between ZnO and the dye molecule.
- In ZnO-terthiophene composite, photophysical studies show a major contribution from the molecule than the ZnO nanoparticle, facilitating electron transfer between ZnO-molecule interfaces.
- In the composite with Br analogue, a broad absorption range is noticed extending from 320-440 nm with an enhanced visible light absorption.
- The electron transfer properties are further corroborated by the computational studies. From the DFT studies, the ZnO-BrTTTCOOH composite conduction band minima (CBM) are more aligned with the water reduction potential than the ZnO-TTTCOOH composite.
- Br seems to enhance the electron density of the thiophene backbone through mesomeric effect which may have led to increased visible light absorption and photocatalytic activity.

List of Publications and Patents

1. Understanding the electron transfer process in ZnO–naphthol azobenzoic acid composites from photophysical characterization, **L. George**, A.K. Kunhikannan, R. Illathvalappil, D.Ottoor, S. Kurungot, R.N.Devi., *PCCP*, **2016**, 18, 22179-22187.
2. Surface Site Modulations by Conjugated Organic Molecules to Enhance Visible Light Activity of ZnO Nanostructures in Photo catalytic Water Splitting, L.George**,** S.Sappati, P.Ghosh, R.N. Devi., *JPCC*, **2015**, 119, 3060-3067.
3. Valorization of coffee bean waste: a coffee bean waste derived multifunctional catalyst or photocatalytic hydrogen production and electrocatalytic oxygen reduction reactions, S. M. Unni, **L. George**, S. N. Bhange, R. N. Devi and S. Kurungot, *RSC Adv*., **2016**, 6, 82103-82111.
4. Characterization, non-isothermal decomposition kinetics and photocatalytic water splitting of green chemically synthesized polyoxoanions of molybdenum containing phosphorus as hetero atom, Bessy D'Cruz, J. Samuel and **L. George***, Thermochimica Acta*., **2014**, 596, 29–36.
5. Green chemical incorporation of silicon into polyoxoanions of molybdenum: characterization, thermal kinetics study and their photocatalytic water splitting activity, Bessy D'Cruz, J. Samuel and **L. George**, *RSC Adv*., **2014**, 4, 63328–63337.
6. Photocatalytic H2 evolution from water–methanol mixtures on InGaO3(ZnO)m with an anisotropic layered structure modified with CuO and NiO cocatalysts, S. B. Narendranath, S. V. Thekkeparambil, **L. George**, Shibin Thundiyil, R. N. Devi., *Journal of Molecular Catalysis A: Chemical*, **2016**, 415, 82–88.
7. Nitrogen-doped graphene interpenetrated 3D Ni-nanocages: efficient and stable water- to dioxygen electrocatalysts, Vishal M. Dhavale, Sachin S.Gaikwad, **L.George**, R.N.Devi and Sreekumar Kurungot, *Nanoscale*., **2014**, 6, 13179–13187.
8. Green synthesis of novel polyoxoanions of tungsten containing phosphorus as a heteroatom:characterization, non-isothermal decomposition kinetics and photocatalytic activity, Bessy D'Cruz, J. Samuel, M. K. Sreedhar and **L. George**., *New J. Chem.,* **2014***,* 38, 5436—5444.
9. Low Band Gap Benzimidazole COF Supported Ni3N as Highly Active OER Catalyst, Shyamapada Nandi, S. K. Singh, Dinesh Mullangi, Rajith Illathvalappil, **L. George**,

Chathakudath P. Vinod, Sreekumar Kurungot and Ramanathan Vaidhyanathan., *Adv. Energy Mater.* **2016**, 1601189.

10. Functionalized zinc oxide nanoparticles for photocatalytic water splitting, R Nandini Devi ; **L. George**; Patent Application number: WO2015092816 A8, 2015.
11. Multimodal anchoring of simple organic molecules on ZnO nanoparticles for enhanced electron transfer characteristics, **L.George**, S.Sappati, P.Ghosh, R.N Devi (communicated).
12. Design of azo based dyes for enhanced visible light absorption and photocatalytic water splitting in ZnO, **L.George**, S.Sappati, P.Ghosh, R.N. Devi (to be communicated).

Contributions to Symposia/Conference

1. **International Conference on Materials for the New Millenium**, held at Cochin University of Science and Technology (CUSAT), Kerala on January 2010.

2. **20th National Symposium on Catalysis for Energy Conversion and Conservation of Environment (CATSYMP – 20)**, held at National Centre for Catalysis Research, Indian Institute of Technology Madras, Chennai on December 2010.

3. **National Science Day and IYC-2011 Conference**, held at CSIR-National Chemical Laboratory, Pune on February 2011.

4. **21st National Symposium on Catalysis for Sustainable Development (CATSYMP – 21)**, held at CSIR- Indian Institute of Chemical Technology, Hyderabad on February 2013.

5. **2nd TAPSUN Conference on Advances in Futuristic Solar Energy Materials and Technologies**, held at CSIR-Central Leather Research Institute, Chennai on September 2013.
6. **National Science Day 2014 Conference**, held at CSIR-National Chemical Laboratory, Pune on February 2014.
7. **Workshop on Particle Size Analysis and Colloidal Stability using Dynamic Light Scattering: Nano to Micro**, held at CSIR-National Chemical Laboratory Venture Centre, Pune on February 2012.

Papers/Posters Presented at Conferences

1. *"Surface modified nano ZnO"* poster presented at the 20th National Symposium on Catalysis (CATSYMP – 20), held at National Centre for Catalysis Research, Indian Institute of Technology Madras, Chennai on December 2010.

2. *"Surface modified nano ZnO"* poster presented at the National Science Day and IYC- 2011, held at CSIR-National Chemical Laboratory, Pune on February 2011.
3. *"Surface modified ZnO Nanostructures: Synthesis, Optical Studies and Applications in Photocatalysis"* poster presented at the 21st National Symposium on Catalysis (CATSYMP – 21), held at CSIR- Indian Institute of Technology, Hyderabad on February 2013.
4. *"Surface modified ZnO Nanoparticles for Water Splitting Activity",* poster presented at the 2nd TAPSUN Conference on Advances in Futuristic Solar Energy Materials and Technologies, held at CSIR-Central Leather Research Institute, Chennai on September 2013.
5. *"Surface modified ZnO Nanoparticles for Water Splitting Activity",* poster presented at the National Science Day 2014, held at CSIR-National Chemical Laboratory, Pune on February 2014.
6. *"Surface modified ZnO Nanoparticles for Water Splitting Activity",* poster presented at the International Conference on Advanced Catalytic Science and Technology (TOCAT 7), Kyoto, Japan on June 2014.
7. *"Surface modified ZnO Nanoparticles for Water Splitting Activity",* poster presented at the National Science Day 2014, held at CSIR-National Chemical Laboratory, Pune on February 2015.

Appendix 1

Physicochemical Characterizations

Various physicochemical techniques can be used for the characterization of the ZnO NPs, organic linkers (azonaphthols, azoquinolines, perylenes and terthiophenes) and composites (ZnO-azonaphthols, ZnO-azoquinolines, ZnO-perylenes and ZnO-terthiophenes). The principles of techniques, used in the present study like powder diffraction using laboratory X-rays, TEM, NMR, IR Spectroscopy, Zeta-potential measurements, Raman Spectroscopy, UV-visible spectroscopy, Photoluminescence Spectroscopy, Life time measurements, electrochemical measurements and gas chromatography.

1. Powder Diffraction

Understanding and predicting the properties of scientific and technologically important materials require the exact knowledge of its structure. The structure of an idealized crystal lattice consists of periodic arrangement atoms and single crystal analysis is the most suitable technique to understand it. However, because of the unavailability of suitable single crystals in many cases and to extract information on the bulk material, alternative technique, powder diffraction is routinely used. Moreover it can be used for the determination of microstructural properties, disorder in materials, studies of macroscopic stresses in components, and texture of polycrystalline samples.

X-rays are electromagnetic waves having wavelengths of the order of 1Å, which is comparable with the spacing between lattice planes in crystals. X-ray diffraction, based on wide-angle elastic scattering of X-rays, is the most important and common tool to determine the structure of the materials characterized by the long range ordering. X-ray diffraction involves the measurement of the intensity of X-rays scattered from electrons or neutrons bound to atoms. Waves scattered at atoms at different positions arrive at the detector with a relative phase shift. Therefore, the measured intensities yield information about the relative atomic positions. The diffraction patterns gives information about structure formation, phase purity, degree of crystallinity, and unit cell parameters of the materials. The formation of a structural phase can be confirmed by comparing the powder

diffraction patterns with that of pure reference phases distributed by International Center for Diffraction Data (ICDD).

The use of Bragg's equation is the easiest way to get to the structural information in powder diffraction, the derivation of which considers X-ray diffraction as a reflection of X-rays by sets of lattice planes. As the X-rays penetrate deeply, additional reflections occur at thousands of consecutive parallel planes. The overlap of the scattered X-rays occurs since all are reflected in the same direction.

The Braggs equation is $n\lambda = 2d\sin\theta$, where d is the interplanar spacing of parallel lattice planes and 2θ is the diffraction angle, the angle between the incoming and outgoing X-ray beams.

Sharp intensities emerge from the sample only at the special angles where Bragg's equation holds. For crystalline materials, the destructive interference results in a completely destruction of intensity in all the other directions. In the modern flat-plate powder X-ray diffractometer, used most commonly in industrial and academic laboratories, the divergent incident beam is allowed to reflect from the sample and converges at a fixed radius from the sample position. This configuration is commonly referred to as "Bragg–Brentano" geometry (shown in Figure 6). The spinning of sample about an axis normal to the flat plate results in a good powder average.

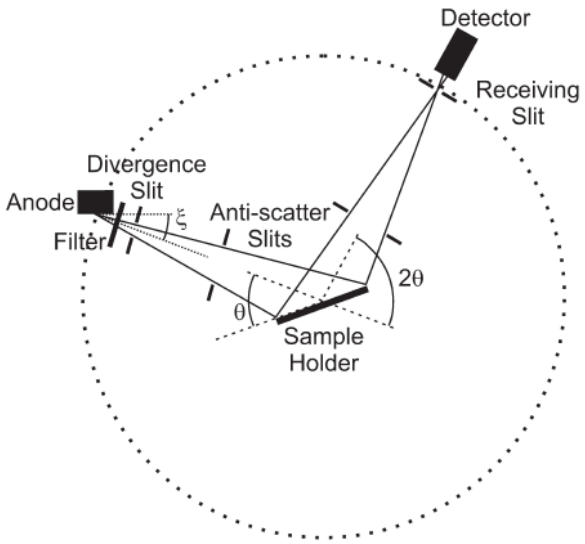

Figure 1. Schematic representation of Bragg–Brentano geometry.

Powder diffraction experiments, exploits X-rays from a laboratory generator or from a high energy storage ring (synchrotron radiation), or neutrons produced in a reactor or spallation source. A typical wavelength used lies in the range 0.1-5 Å, comparable with the spacings between lattice planes in crystals. Data can be collected in transmission or reflection modes, depending on the absorption of radiation by the sample. A brief description of the different sources used for the powder diffraction experiments are given here.

1.1. Laboratory X-ray Sources

In a standard laboratory instrument, the X-rays are produced in a sealed-tube source where electrons, accelerated by a potential difference of up to 60 kV, bombard a metal anode inside a vacuum tube. This results in the formation of a characteristic radiation spectrum composed of discrete peaks arising from the filling of vacant level in the inner shell (created from the ejection of electron by the incoming electron) by a higher atomic level electron. The emission of an X-ray photon is characterised by the difference in energy between the two levels. A higher resolution copper X-ray spectrum consists of components labeled as $K_{\alpha 1}$ (1.54056Å) and $K_{\alpha 2}$(1.54439Å). The most commonly used target element is Cu but Mo, Cr, Fe, Co, Ag and W are also used for specialist applications . Cu tube is the most common choice for routine analysis, which gives X-rays of shortest wavelength above 1A°. Also relatively high power can be applied to the target because of the good thermal conductivity of copper.

Table 1. Approximate principle emission lines for various anode targets.

Anode	Cu	Mo	Cr	Fe	Co	Ag	W
$\lambda(K_{\alpha})$ Å	1.54	0.71	2.29	1.94	1.79	0.56	0.21

2. Transmission Electron Microscopy (TEM)

A TEM works much like a slide projector .A projector shines a beam of light through (transmits) the slide , as light passes through it is affected by structures and objects on the slide. These effects result in only certain parts of light beam being transmitted through certain parts of the slide. This transmitted beam is then projected onto the viewing screen forming an image of the slide. TEM works same way except that they shine beam of

electrons (like light) through the specimen (slide). Whatever part is transmitted is projected into a phosphor screen.

A "light source" at the top of the microscope emits electrons that travel through vacuum in the column of the microscope. The TEM uses electromagnetic lenses to focus electrons into a very thin beam. The electron beam then travel through the specimen .Depending on the density of the material, some of the electrons are scattered and disappear from the beam. At the bottom of the microscope the unscattered electrons hit a fluorescent screen ,which gives rise to a shadow image of the specimen with its different parts displayed in varied darkness according to their density. The image can be studied directly by operator or photographed with a camera. The darker area of the image represent those area of the sample that fewer electrons were transmitted through (they are thicker or denser).The lighter of image represent those area of the sample that more electrons were transmitted through (they are thinner or less dense).

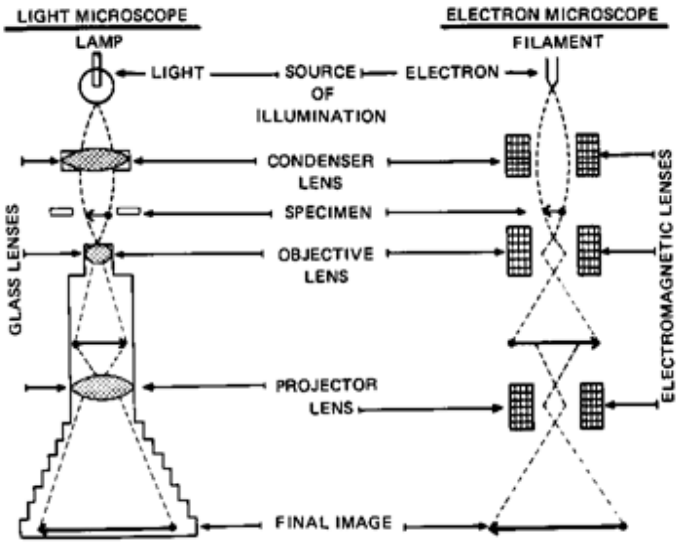

Figure 2. Principle of TEM

3. NMR Spectroscopy

All the NMR measurements were carried out on a Bruker AV400 MHz NMR spectrometer equipped with a 9.4 Tesla superconducting magnet. The resonance frequency for ^{1}H at this magnetic field is 400 MHz and for ^{13}C, it is 100 MHz. The proton NMR spectra were taken with a standard one pulse experiment using a 30 degree flip angle and 1 sec relaxation delay. 32 to 64 scans and 32K data points were used for data collection. The raw data obtained are Fourier Transformed to get the frequency domain spectrum without the application of any window function. ^{13}C spectra were obtained with a standard pulse sequence with continuous proton decoupling. A flip angle of ~ 30 degree, relaxation delay of 2 sec and 32K data points were used for data collection. The proton decoupling was achieved by a standard ZGPG30 pulse technique. A standard DEPT pulse sequence with a sorting pulse of 135 degree (DEPT135) was employed for the ^{13}C spectral editing so that the CH_2 peaks appear as negative and CH and CH_3 as positive. The number of scans for the ^{13}C spectral data collection varied from a few hundred to a couple of thousand depending on the concentration. Prior to Fourier Transformation, the raw ^{13}C data (FID's) were multiplied by an exponential window function with a line broadening (LB) of 2Hz for sensitivity enhancement. The chemical shifts for the solvent peak is found at 2.5ppm (^{1}H, DMSO-d6) and 39.9 ppm (^{13}C, DMSO-d6).

4. IR SPECTROSCOPY (Infra-red Spectroscopy)

In IR Spectroscopy, IR radiation is passed through a sample. Some of the infra radiation is absorbed by the sample and the other is transmitted. The resulting spectrum represents the molecular absorption and transmission, creating a molecular fingerprint of the sample. It represents the fingerprint of the absorption peaks which corresponds to frequencies of the vibrations between the bonds of atoms making up the material .Because each different material is a unique combination of atoms, no two compounds produce the exact same infrared spectrum. Therefore, infrared spectroscopy can result in a positive identification (qualitative) of every different kind of material. In addition the size of peaks in the spectrum is a direct indication of the amount of material present.

FT-IR spectrometers are often called as FT-IRs. FT-IR is a method of obtaining infrared spectra by collecting an Interferogram of a sample signal using an interferometer and then

performing a Fourier transform on the Interferogram to obtain the spectrum. An FT-IR spectrometer collects and digitalizes the Interferogram, performs FT function and displays the spectrum.

The technique works on the fact that bonds and groups of the bonds vibrate at characteristic frequencies. A molecule that is exposed to infrared rays absorbs infrared energy at frequencies which are characteristic to that molecule. During FT-IR analysis, a spot on the specimen is subjected to a modulated IR beam. The specimen's transmittance and reflectance of infrared rays at different frequencies is translated into an IR absorption plot consisting of reverse peaks. The resulting FT-IR spectral pattern is then analyzed and matched with known signatures of identified materials in the FT-IR library. FT-IR spectroscopy bases its functionality on the principle that almost all molecules absorb infrared light. Molecules only absorb at those frequencies where its infrared light affects the dipolar moment of the molecule. Molecule with dipolar moment allows infrared photons to interact with the molecule causing excitation to higher vibrational states. As mentioned earlier almost all molecules absorb infrared light and each molecule absorbs IR light at certain frequencies. This property provides unique characteristic for each molecule. It provides a way to identify the molecular type (qualitative analysis) and the amount or quantity of the molecule in the sample (quantitative analysis). Since each type of molecules only absorbs at certain frequencies it provides the unique absorption spectral pattern or finger print through the entire IR spectrum. As a conventional infrared spectroscopy, FT-IR is used to detect the vibrational transitions of a molecule. The advantage of FT-IR compared to conventional infrared spectroscopy is that all wave numbers are measured at once with the help of Michelson interferometer.

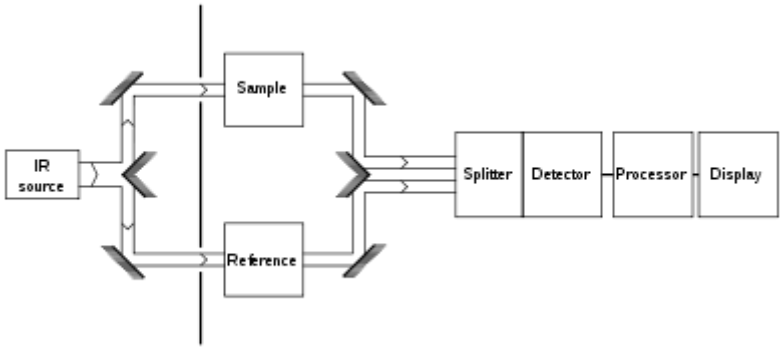

Figure 3. Schematic diagram of Infrared Spectroscopy

5. Dynamic Light Scattering and Zeta Potential

Particle size can be determined by measuring the random changes in the intensity of light scattered from a suspension or solution. This technique is commonly known as dynamic light scattering (DLS), but is also called photon correlation spectroscopy (PCS) and quasi-elastic light scattering (QELS). Dynamic light scattering explains the technique beginning the actual phenomena under study (particle motion, not particle size). The nature of the measurement and data interpretation is then discussed. Finally, there are some concluding comments.

The zeta potential of a sample is most often used as an indicator of dispersion stability. Large zeta potentials predict a more stable dispersion. Fast and accurate measurement of the zeta potential with the SZ-100 can enhance understanding of aggregation and flocculation in samples and speed up the process of developing stable formulations, be they dispersions, emulsions or suspensions. Measurement of the zeta potential, or electrostatic attraction / repulsion, is important to many industries from pharmaceuticals to mineral processing and from water treatment to additives for electronics. The SZ-100 enables fast, reliable and accurate measurement of the zeta potential.

6. Raman Spectroscopy

Raman spectroscopy is a spectroscopic technique based on inelastic scattering of monochromatic light, usually from a laser source. Inelastic scattering means that the frequency of photons in monochromatic light changes upon interaction with a sample. Photons of the laser light are absorbed by the sample and then reemitted. Frequency of the reemitted photons is shifted up or down in comparison with original monochromatic frequency, which is called the Raman Effect. This shift provides information about vibrational, rotational and other low frequency transitions in molecules. Raman spectroscopy can be used to study solid, liquid and gaseous samples.

The Raman effect is based on molecular deformations in electric field E determined by molecular polarizability α. The laser beam can be considered as an oscillating electromagnetic wave with electrical vector E. Upon interaction with the sample it induces

electric dipole moment P = αE which deforms molecules. Because of periodical deformation, molecules start vibrating with characteristic frequency υ_m. Amplitude of vibration is called a nuclear displacement. In other words, monochromatic laser light with frequency υ_0 excites molecules and transforms them into oscillating dipoles. Such oscillating dipoles emit light of three different frequencies when:

1. A molecule with no Raman-active modes absorbs a photon with the frequency υ_0. The excited molecule returns back to the same basic vibrational state and emits light with the same frequency υ_0 as an excitation source. This type if interaction is called an elastic Rayleigh scattering.

2. A photon with frequencyυ_0 is absorbed by Raman-active molecule which at the time of interaction is in the basic vibrational state. Part of the photon's energy is transferred to the Raman-active mode with frequency υm and the resulting frequency of scattered light is reduced to υ_0-υ_m. This Raman frequency is called Stokes frequency, or just "Stokes".

3. A photon with frequency υ_0 is absorbed by a Raman-active molecule, which, at the time of interaction, is already in the excited vibrational state. Excessive energy of excited Raman active mode is released, molecule returns to the basic vibrational state and the resulting frequency of scattered light goes up to υ_0+ υ_m. This Raman frequency is called Anti-Stokes frequency, or just "Anti-Stokes".

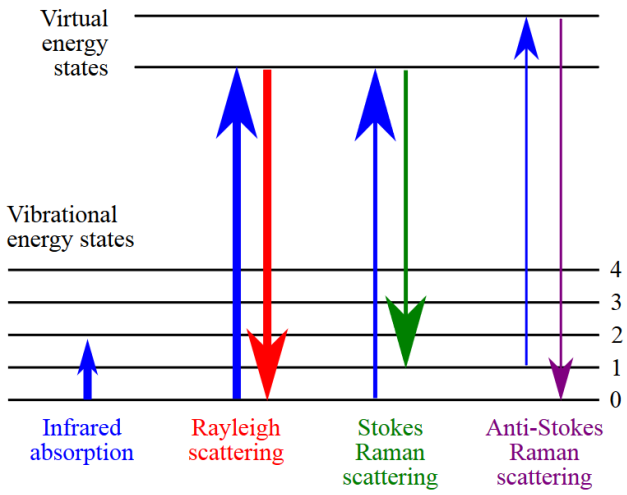

Figure 4. Raman frequencies

A Raman system typically consists of four major components:

1. Excitation source (Laser).
2. Sample illumination system and light collection optics.
3. Wavelength selector (Filter or Spectrophotometer).
4. Detector (Photodiode array, CCD or PMT).

A sample is normally illuminated with a laser beam in the ultraviolet (UV), visible (Vis) or near infrared (NIR) range. Scattered light is collected with a lens and is sent through interference filter or spectrophotometer to obtain Raman spectrum of a sample. Since spontaneous Raman scattering is very weak the main difficulty of Raman spectroscopy is separating it from the intense Rayleigh scattering. More precisely, the major problem here is not the Rayleigh scattering itself, but the fact that the intensity of stray light from the Rayleigh scattering may greatly exceed the intensity of the useful Raman signal in the close proximity to the laser wavelength. In many cases the problem is resolved by simply cutting off the spectral range close to the laser line where the stray light has the most prominent effect. People use commercially available interference (notch) filters which cut-off spectral range of ± 80-120 cm-1 from the laser line. This method is efficient in stray light elimination but it does not allow detection of low-frequency Raman modes in the range below 100 cm^{-1}.

Stray light is generated in the spectrometer mainly upon light dispersion on gratings and strongly depends on grating quality. Raman spectrometers typically use holographic gratings which normally have much less manufacturing defects in their structure then the ruled once. Stray light produced by holographic gratings is about an order of magnitude less intense then from ruled gratings of the same groove density. Using multiple dispersion stages is another way of stray light reduction. Double and triple spectrometers allow taking Raman spectra without use of notch filters. In such systems Raman-active modes with frequencies as low as 3-5 cm^{-1} can be efficiently detected. In earlier times people primarily used single-point detectors such as photon-counting Photomultiplier Tubes (PMT). However, a single Raman spectrum obtained with a PMT detector in wavenumber scanning mode was taking substantial period of time, slowing down any research or industrial activity based on Raman analytical technique. Nowadays, more and more often researchers

use multi-channel detectors like Photodiode Arrays (PDA) or, more commonly, a Charge-Coupled Devices (CCD) to detect the Raman scattered light. Sensitivity and performance of modern CCD detectors are rapidly improving. In many cases CCD is becoming the detector of choice for Raman spectroscopy.

Raman spectra were recorded on a Horiba JY Lab RAM HR 800 spectrometer excited with 633 nm lasers.

7. UV-visible Spectroscopy

UV-Vis spectroscopy involves the spectroscopy of photons in the UV-visible region. This means it uses the light in the visible and adjacent (near UV and near IR ranges). The absorption in the visible ranges directly affects the color of chemicals involved. In the region of electromagnetic spectrum molecules undergo electronic transitions. UV spectroscopy is useful as an analytical technique for two reasons. First it can be used to identify some functional groups in molecules and secondly it can be used for assaying. This second role -determining content and strength of a substance is extremely useful. When light –either ultraviolet or visible is absorbed by valence (outer) electrons, these electrons are promoted from their normal (ground) states to higher energy (excited) states .The energies of the orbitals involved in electronic transition have fixed values. Because energy is quantized, it seems to assume that absorption peak in UV Spectrum will be sharp peaks. However this is rarely if ever observed. Instead the spectrum has broad peaks. This is because there are also vibrational and rotational energy levels available to absorbing materials.

The Beer-Lambert's law states the absorbance of a solution is directly proportional to the concentration of the absorbing species in the solution and the path length.

$A = \log (Io/I) = \varepsilon l c$

Io= Intensity of incident radiation

I= Intensity of transmitted radiation

L=Path length through the sample

C= Concentration of absorbing species

E=Molar absorption coefficient

The instrument used in UV Spectroscopy is called UV spectrophotometer. It measures the intensity of the light passing through the sample (I) and compares it to the intensity of light before it passes through the sample(Io).The ratio(I/Io) is called Transmittance and is usually expressed as a percentage (%T).The absorbance(A) is based on the Transmittance.

A= -log (%T/100%)

The basic parts of a spectrophotometer are a light source, a holder for the sample, a diffraction grating or a monochromator to separate the different wavelengths of light and a detector. The radiation source is often a Tungsten filament, a deuterium arc lamp which is continuous over the UV region and more recently light emitting diode s and xenon arc lamps for visible wavelengths. The detector is typically a photodiode or CCD. A spectrophotometer may be either single beam or double beam. In single beam instrument, all of the light passes through the sample cell. In a double beam instrument, the light is split into two beams before it reaches the sample. One beam is used as reference and the other beam is passes through the sample. Some detectors have two detectors (photodiodes) and the sample and reference beams are measured at the same time. In other instruments the two beams pass through a beam chopper, which blocks one beam at a time. The detector alternate between measuring the sample beam and the reference beam. An UV Spectrum is essentially a graph of absorbance versus wavelength in a range of ultraviolet or visible range.

8. Photoluminescence Spectroscopy

Photoluminescence is a term used to designate a number of effects, including fluorescence, phosphorescence, and Raman scattering. Photoluminescence spectroscopy is a contactless, nondestructive method of probing the electronic structure of materials. Light is directed onto a sample, where it is absorbed and imparts excess energy into the material in a process called photo-excitation. One way this excess energy can be dissipated by the sample is through the emission of light, or luminescence. In the case of photo-excitation, this luminescence is called photoluminescence. Photo-excitation causes electrons within a material to move into permissible excited states. When these electrons return to their equilibrium states, the excess energy is released and may include the emission of light (a radiative process) or may not (a nonradiative process). The energy of the emitted light

(photoluminescence) relates to the difference in energy levels between the two electron states involved in the transition between the excited state and the equilibrium state. The quantity of the emitted light is related to the relative contribution of the radiative process.

Fluorescence is the result of a three-stage process that occurs in certain molecules called fluorophores or fluorescent dyes. A fluorescent probe is a fluorophore designed to localize within a specific region of a biological specimen or to respond to a specific stimulus. The process responsible for the fluorescence of fluorescent probes and other fluorophores is illustrated by a Jablonski diagram. Stage 1: Excitation. A photon is supplied by an external source such as an incandescent lamp or a laser and absorbed by the fluorophore, creating an excited electronic singlet state (S1'). This process distinguishes fluorescence from chemiluminescence, in which the excited state is populated by a chemical reaction. Stage 2: Excited-State Lifetime. The excited state exists for a finite time (typically 1–10 nanoseconds). During this time, the fluorophore undergoes conformational changes and is also subject to a multitude of possible interactions with its molecular environment. These processes have two important consequences. First, the energy of S1' is partially dissipated, yielding a relaxed singlet excited state (S1) from which fluorescence emission originates. Second, not all the molecules initially excited by absorption (Stage 1) return to the ground state (S0) by fluorescence emission. Other processes such as collisional quenching, fluorescence resonance energy transfer (FRET) and intersystem crossing (see below) may also depopulate S1. The fluorescence quantum yield is the ratio of the number of fluorescence photons emitted (Stage 3) to the number of photons absorbed (Stage 1).

Stage 3: Fluorescence Emission. A photon of energy is emitted, returning the fluorophore to its ground state S0. Due to energy dissipation during the excited-state lifetime, the energy of this photon is lower, and therefore of longer wavelength, than the excitation photon. The difference in energy or wavelength represented by the absorbed and emitted photon is called the Stokes shift. The Stokes shift is fundamental to the sensitivity of fluorescence techniques because it allows emission photons to be detected against a low background, isolated from excitation photons. In contrast, absorption spectrophotometry requires measurement of transmitted light relative to high incident light levels at the same wavelength.

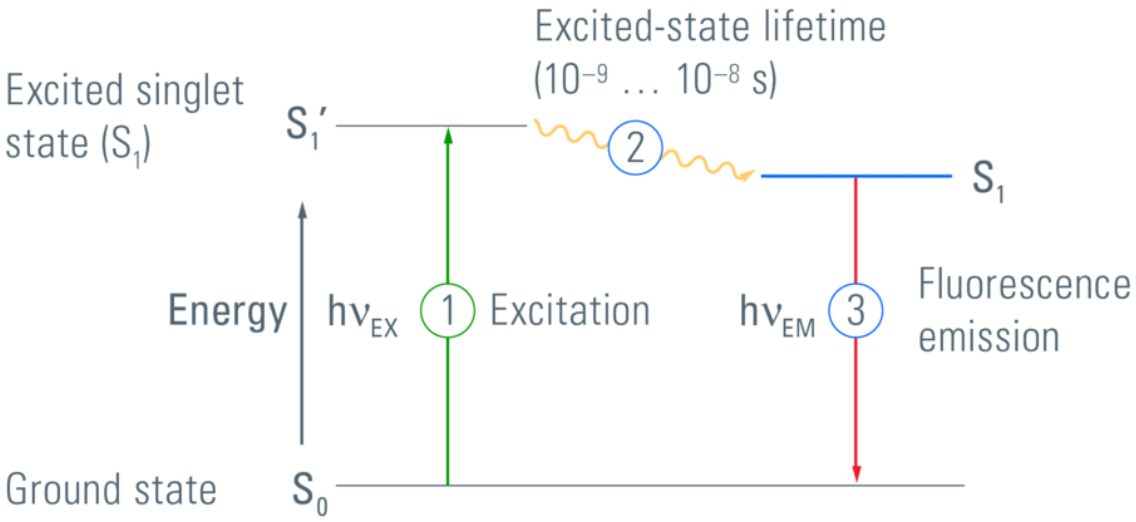

Figure 5. Jablonski Diagram

9. Electrochemical measurements

9.1. Cyclic Voltammetric Analysis

Cyclic Voltammetry **(**CV) is the most commonly used potential controlled electrochemical technique which is routinely used to investigate the electrochemical properties of materials. This technique offers a fast location of the redox potentials of electroactive species. In CV, generally three-electrode systems are used even though two-electrode systems can also be used. In three-electrode systems, the potential is applied between WE and reference electrode (RE) while the current is measured in between the WE and the counter electrode (CE). To tackle with large currents, normally counter electrode will be with very high surface area. In CV, the potential of the WE is cycled linearly with time between two potential ends at which the oxidation and reduction of the sample occurs. Here, the potential is scanned at a particular scan rate and the current-time curve is plotted. As the scan rate is constant and the initial and switching potential are known, time can be converted into potential. The resulting current-potential plot is known as cyclic voltammogram.

9.2. Electrochemical Impedance Spectroscopy

Electrochemical impedance spectroscopy (EIS) is a very versatile electrochemical tool to characterize intrinsic electrical properties of any material and its interface. This is a steady state method measuring the current response to the application of an AC voltage as a function of the frequency. The basis of impedance spectroscopy is the analysis of the impedance (resistance of alternating current) of the observed system with respect to the applied frequency and applied signal. An important advantage of EIS over other techniques is the possibility of using tiny ac voltage amplitudes exerting a very small perturbation on the system. EIS provides quantitative information about the conductance, dielectric coefficient and some interfacial properties. EIS data for electrochemical cells are most often represented in Nyquist and Bode plots. Bode plots refer to representation of the impedance magnitude (or the real or imaginary components of the impedance) and phase angle as a function of frequency. Because both the impedance and the frequency often span orders of magnitude, they are frequently plotted on a logarithmic scale. Bode plots explicitly show the frequency-dependence of the impedance of the device under test. A complex plane or Nyquist plot depicts the imaginary impedance, which is indicative of the capacitive and inductive character of the cell, versus the real impedance of the cell. Nyquist plots have the advantage that activation-controlled processes with distinct time-constants show up as unique impedance arcs and the shape of the curve provides insight into possible mechanism or governing phenomena.

10. Gas Chromatography

A Gas Chromatograph is used to detect the components based on the selective affinity of components towards the adsorbent materials. The sample is introduced in the liquid/gas form with the help of GC syringe into the injection port, it gets vaporized at injection port then passes through column with the help of continuously flowing carrier stream (mobile phase), mainly H_2 (for TCD), and gets separated/detected at the detection port with suitable temperature programming. We visualize this on computer in the form of peaks. Carrier medium can be liquid (e.g. HPLC) or gas (e.g. GC) for the ease of separation/detection, if it is gas then called gas chromatography otherwise called liquid

chromatography. Different chemical constituents of the sample travel through the column at different rates depending upon,

1. Physical properties
2. Chemical properties, and
3. Interaction with a specific column filling (stationary phase).

As the chemicals exit the end of the column, they are detected and identified electronically. The function of the stationary phase in the column is to separate different components, causing each one to exit the column at a different time (retention time). Other parameters that can be used to alter the order or time of retention are the carrier gas flow rate, and the temperature. Physical Components involve inlet port, Adsorption column, detector port, flow controller (to control the flow of carrier gas), etc.

Packed columns are 1.5 - 10 m in length and have an internal diameter of 2 - 4 mm. The tubing is usually made of stainless steel or glass and contains a packing of finely divided, inert, solid support material (eg. diatomaceous earth) that is coated with a liquid or solid stationary phase. The nature of the coating material determines what type of materials will be most strongly adsorbed. Capillary columns have a very small internal diameter, on the order of a few tenths of millimeters, and lengths between 25-60 meters are common. The inner column walls are coated with the active materials (WCOT columns). Some columns are quasi solid filled with many parallel micro pores (PLOT columns). Most capillary columns are made of fused silica with a polyimide outer coating. These columns are flexible, so a very long column can be wound into a small coil.

Temperature dependence of molecular adsorption and of the rate of progression along the column necessitates a careful control of the column temperature to within a few tenths of a degree for precise work. Reducing the temperature produces the greatest level of separation, but can result in very long elution times. The choice of carrier gas (mobile phase) is important, with hydrogen being the most efficient and providing the best separation. However, helium has a larger range of flow rates that are comparable to hydrogen in efficiency, with the added advantage that helium is non-flammable, and works with a greater number of detectors. Therefore, helium is the most common carrier gas used.

Detectors

A number of detectors are used in gas chromatography. The most common are the Flame ionization detector (FID) and the thermal conductivity detector (TCD). While TCDs are essentially universal and can be used to detect any component other than the carrier gas (as long as their thermal conductivities are different than that of the carrier gas, at detector temperature), FIDs are sensitive primarily to hydrocarbons, and are more sensitive to them than TCD. Both detectors are also quite robust. Since TCD is non-destructive, it can be operating in-series before an FID (destructive), thus providing complementary detection of the same eluents.

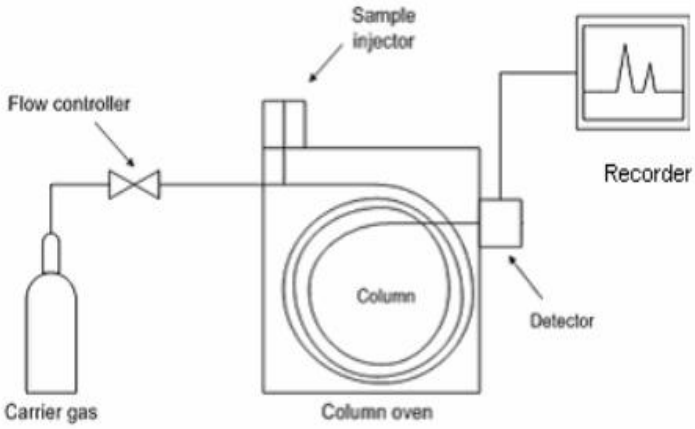

Figure 6. Experimental set up for Gas Chromatograph

Appendix 2

2.1. Details of calculations of the amount of 4ABBN to be used based on the number of ZnO on the surface of the particles.

(a) Number of moles of Zinc acetate dihydrate (ZA) in y ml = **x moles**

Assuming 100% conversion of ZA to ZnONPs, no: of moles of ZnONPs = **t moles in y ml**

(b) Total radius of ZnO = **0.202 nm**

Volume of one ZnO molecule = $4/3\pi r^3$ = **0.034508 nm^3**

(c) Volume of one ZnONP of 'a' radius (from TEM) = $4/3\pi a^3$ = **b nm^3**

(d) Total no: of molecules which can be accommodated

in one particle = b nm^3/0.034508 nm^3 = **c molecules**

(e) Total no: of ZnO molecules = t moles * N = **s molecules**

(f) Total no: of ZnO particles = s/c = **r particles**

(g) Total no: of ZnO particles exposed

on the surface = 4π(a nm^2)/π (0.202 nm^2) = **e particles**

(h) Total no: of ZnO molecules exposed on the surface = e* r = **f molecules**

(i) Total no: of organic linkers required = f molecules/2 = **k molecules**

No: of moles of organic linker = k molecules/N **=** **m moles**

Appendix 3

Computational Details

Chapter 2: ZnO-azonaphthol composites

The calculations were done using the Quantum ESPRESSO software, which is a plane wave based implementation of density functional theory (DFT). The electron-ion interactions were described using ultrasoft pseudopotentials. The exchange-correlation potential had been described by the Purdew, Burke and Ernzenhof (PBE) parametrization within the generalized gradient approximation. We have used cut offs of 35 Ry and 400 Ry for the wavefunction and charge density respectively. To test the accuracy of the pseudopotentials used in the calculations, lattice parameters of bulk ZnO in its wurtzite structure and the bond length of oxygen molecule in gas phase were determined. The wurtzite structure of ZnO has a hexagonal unit cell. For bulk ZnO, the lattice parameter was found to be 3.29 Å and the c/a ratio to be 1.61. This is in excellent agreement with previously reported experimental values and calculations.

Within DFT, the band gap (Eg) of ZnO is severely underestimated (Eg^{DFT}=0.78 eV and Eg^{expt}=3.3 eV). The wrong positions of the Zn 3d orbitals by the pseudopotentials result in spurious interaction with the sp bands of the O which is responsible for this severe underestimation. This can be corrected by many-body techniques, which are almost impossible to use for these large systems due to the enormous computational cost involved in these calculations. Hence we used an alternative technique, which was suggested by Janotti and coworkers and later successfully used by Calzolari et al. We have used an ad hoc Hubbard U potential within the DFT+U scheme to correct for this band gap underestimation and improve the line up for the molecular states. We note that the Hubbard U values included in our calculations are just empirical parameters to correct the gap. We have used Hubbard potentials of U=12.0 eV on the 3d orbitals of Zn and U=6.5 eV on the 2p orbitals of O. These values of U are obtained by fitting the experimental ZnO bulk band structure. We have first optimized the ZnO slab with the dye at the DFT level. Then we applied the U and relaxed again. We note that this is in slight variance with the method used by Calzolari et al. where they have not relaxed the structure.

The ZnO nanoparticles used in the experiment are of diameters 3.5 and 30 nm, which is larger than the Bohr exciton radius of 2.87 nm in ZnO. Hence we expect that quantum confinement effects will not be significant. Therefore we have used the most stable non-polar ZnO ($10\bar{1}0$) surface to model the ZnO-4ABBN composites. The ZnO ($10\bar{1}0$) surface was modelled with an asymmetric slab having six Zn-O bilayers. The slab is oriented such that the surface is normal to the z-axis. The 4ABBN molecule was placed on one side of the slab. To remove the spurious surface effects from the bottom of the slab, it was passivated with pseudo hydrogens. We have used a vacuum of about 20 Å after the molecule is adsorbed on the surface to minimize the interaction between the periodic images perpendicular to the slab. Since we are interested in the interaction of the molecule with the substrate, we had used a (5×2) supercell resulting in a minimum separation of about 8 Å between the periodic images of the molecules in the x-y plane. We have checked that using a (6×3) supercell, where the minimum distance between the periodic images of the molecule is about 15.5 Å, the results remain unchanged. The Brillouin zone integrations had been done using the Gamma point only.

The calculations of the different configurations of 4ABBN in gas phase were done using the Gaussian09 Software[1]. We have used PBE exchange correlation functional and 6-311++G(d,p) basis set. Taking the lowest energy configuration obtained from this scan, we optimized it further with the Quantum ESPRESSO software[2] using the same exchange correlation functional. However, with Quantum ESPRESSO we have used a planewave basis set, the details of which are given in the paper.

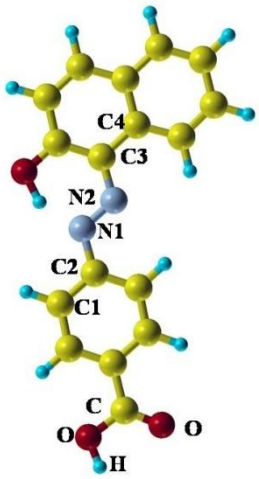

Figure 1. Lowest energy structure of 4ABBN in gas phase

In order to determine the lowest energy structure of the 4ABBN in gas phase we started with the planar structure and optimized its geometry. The optimized configuration is shown in Figure 1. In this structure the H of the -OH group forms an H bond with the N of the azo group, which stabilizes this molecule. However, the molecule can rotate about the dihedral angles C1C2N1N2 and N1N2C3C4, which are marked in the figure. The results of the dihedral scans are shown in Figures 2 and 3 respectively.

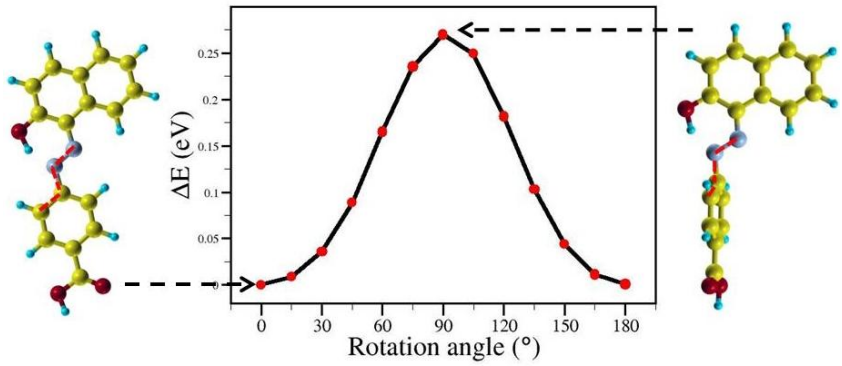

Figure 2. Potential energy profile as a function of the C1C2N1N2 dihedral angle as marked with red lines in the figure.

For all the cases, we find that the planar starting configuration shown in Figure 1 to be the lowest in energy. This gives us confidence that indeed the planar configuration shown in Figure 1 corresponds to the global minima of 4ABBN in gas phase.

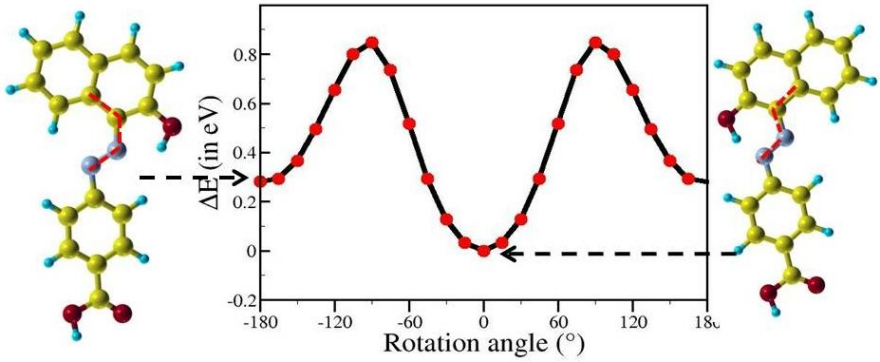

Figure 3. Potential energy profile as a function of the N1N2 C3C4 dihedral angle as marked with red lines in the figure.

Tests for convergence of supercell size

Since we are considering periodic boundary conditions and we are interested primarily in the interaction of the 4ABBN with ZnO, we need to ensure that the size of the

supercell used in our calculation is large enough to minimize the spurious interactions between the periodic images of the molecules. Hence we checked how the alignment of the OP/RP with respect to the positions of the VBM and CBM changes with respect to change in supercell size. Figure 4 shows the same calculated with (5×2) and (6×3) supercells, the minimum separation between the periodic images being 8 and 15 Å respectively. We find that there is no substantial changes in the result. Hence in the main paper, we reported the results for the (5×2) supercell.

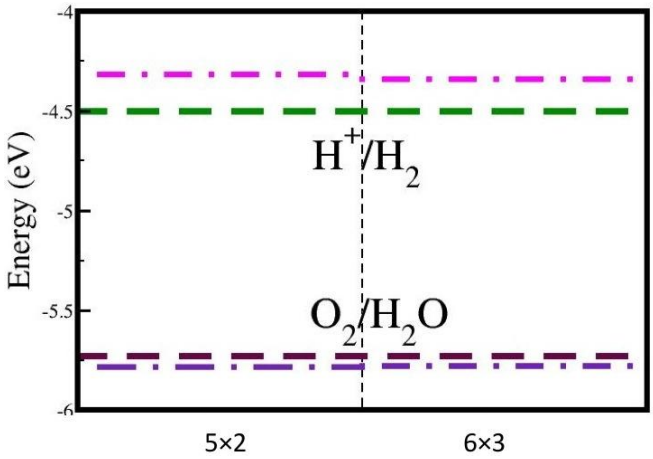

Figure 4. Alignment of the redox potentials with respect to the valence band maximum (VBM) and the conduction band minimum (CBM) for (5×2) and (6×3) super cell of composite system.

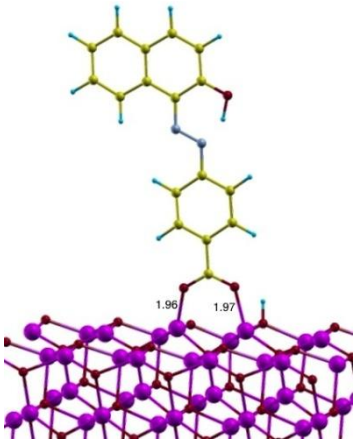

Figure 5. Optimized structure of 4ABBN on ZnO($10\bar{1}0$). The magenta, red, yellow, cyan and grey spheres represent Zn, O, C, H and N atoms respectively. The bond lengths are given in Å.

Chapter 3: ZnO-azoquinoline composites

3ABBN8HQ in gas phase and solvent:

Azoquinoline can exist in two tautomeric forms, namely, the azo and the hydrazone form. To explore the relative stability of the two tautomers (in gas phase and in solvent, methanol in the present case) and their optical properties we have carried out density functional theory (DFT) based calculations using the Cam-B3LYP exchange-correlation functional. The wavefunctions have been expanded in 6-311++G(d,p) basis set. The effect of the solvent has been described using a polarizable continuum model. For certain cases, we have used explicit methanol molecules in the calculations.

To study the optical properties of the molecules we have performed time dependent density functional theory (TDDFT) based calculations. The TDDFT calculations were done using the Davidson algorithm as implemented within Gaussian 09 Revision D.01 software. Since the absorption spectrum is sensitive to the choice of the exchange correlation functional, we have calculated the absorption spectra using Cam-B3LYP, B3LYPand PBE functionals. We find that the results are qualitatively similar (Figure 6 and Figure 7).

Figure 6(a) shows the experimental and the computed absorption spectra of the dye in methanol. The experimental spectrum (black dotted line in Figure 6(a)) has two sharp peaks at around 320 and 405 nm and a broad one at around 475 nm. To understand the nature of the electronic states involved in the transitions that give rise to these peaks, we have plotted the computed spectra of the azo (solid black line in Figure 6(a)) and hydrazone (red dashed line in Figure 6(a)) form of the dye. For both the forms, the computed spectra have a single sharp peak; the peak for the azo form is at 368 nm while that for the hydrazone form is at 394 nm. Both these peaks are due to transitions involving the highest occupied molecular orbital (HOMO) and the lowest unoccupied molecular orbital (LUMO) of the two forms of the dye. The wavefunctions corresponding to the HOMOs and the LUMOs of the two forms of the dye (as shown in Figure 6(b)-(e)) have a π and π^* character. Based on these calculations we assign the experimental peak at 320 nm to originate from the π to π^* transitions within the azo form while the one at 405 nm has been assigned to the π to π^* transitions within the

hydrazone form. However, these cannot explain the origin of the broad shoulder observed at around 475 nm in the experimental spectrum.

It is now well established that it is important to include the solvent molecules explicitly into the calculations of the optical properties of a solvated molecule because the solvent molecules not only influence the structure of the solute molecules (eg. loss of planarity, etc.) but also change the electronic structure of the solute molecules due to strong interactions with the solvent and these effects are not captured typically in the PCM model.[38] Hence to elucidate the origin of the broad absorption peak at 475 nm, we explicitly add one methanol molecule (in addition to the PCM model) in our calculations. For the azo form of the dye, the methanol molecule can form hydrogen bonds with the dye through the –COOH, -N=N- and the –OH functional groups of the dye. Similarly for the hydrazone form, the hydrogen bond with methanol can be formed through the –C=O, -COOH and –N-NH- groups present in the dye. Accordingly we have placed one methanol molecule at each of the above mentioned positions, optimized the structure and computed the absorption spectra. For the azo case we find that the configuration in which the methanol is close to the –COOH group has the lowest energy while the ones having methanol interacting with the –N=N- and –OH groups are higher in energies compared to that for the –COOH configurations by about 0.18 eV and 0.07 eV respectively. We note that these calculations are done at 0 K with only one solvent molecule while the real system is at room temperature in presence of lots of solvent molecules. Hence the dipole-dipole interactions between the solute and the solvent and the finite temperature effects might stabilize these (slightly) high energy configurations. For the –N=N- configuration, we find that the molecule loses its planar structure with the C-N-N-C dihedral angle of 4°. The computed absorption spectrum for this configuration is shown in Figure 6(a) (blue dash-dot line). We find that in addition to the main peak at around 357 nm, there is a low intensity peak at 436 nm. The electronic states involved in these transitions are primarily from HOMO-1 to LUMO and HOMO to LUMO. For the long wavelength peak, the HOMO to LUMO transition has a larger contribution while for the peak at 357 nm the HOMO-1 to LUMO transition is more dominant. The wavefunctions corresponding to the HOMO-1 and HOMO of this configuration is shown in Figure 6(f) and (g) respectively. We find that in this case, (a) the HOMO π character changes to a mixed n/π type, (b) the wavefunction

corresponding to HOMO-1 has a significant weight on the solvent methanol molecule and (c) the LUMO is unchanged (SI-9). For the configurations where the methanol molecule is placed near the –COOH and –OH groups, we find that the planarity of the dye molecule is not lost. Further for these configurations we do not observe any long wavelength peak in the absorption spectrum (Figure 8). Similarly, when methanol is placed near the different functional groups of the hydrazone form we do not observe the long wavelength peak in the absorption spectrum (Figure 9). Based on these results, we envisage that the long wavelength broad peak in the experimental absorption spectrum of the dye originates due to the loss in planarity of the dye molecule that is induced by solvation in methanol and the electronic transition corresponding to that peak is a n/π to π* transition.

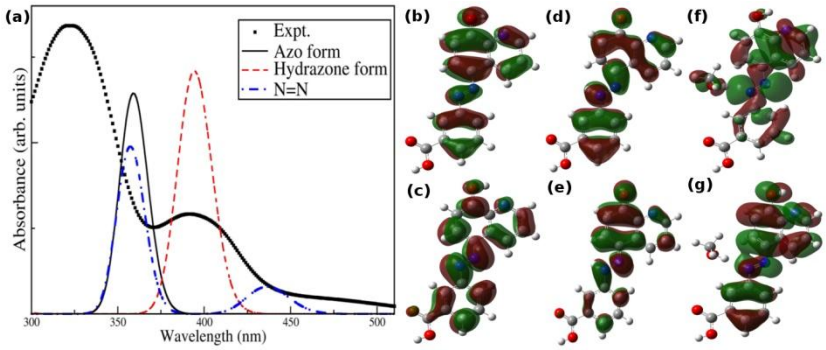

Figure 6. (a) Experimental absorption spectra of the azoquinoline dye (black dotted line), computed absorption spectra of the azo form (solid black line) and the hydrazone form (red dashed line) where the solvent is treated within the PCM model and the azo form with explicit methanol molecule forming hydrogen bond with N=N and the rest of the solvent treated with the PCM model (blue dash-dot line). Isosurfaces corresponding to (b) HOMO and (c) LUMO of the azo form, (d) HOMO and (e) LUMO of the hydrazone form and (f) HOMO-1 and (g) HOMO of the azo form of the dye with a single explicit methanol molecule at N=N.

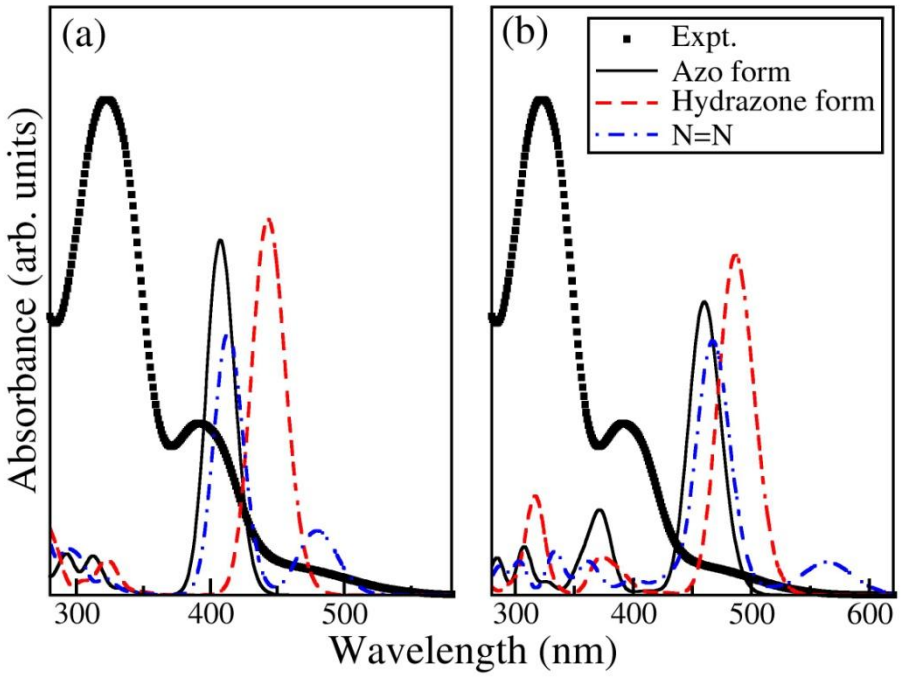

Figure 7. Experimental absorption spectra of the azoquinoline dye (black dotted line), computed absorption spectra of the azo form (solid black line) and the hydrazone form (red dashed line) where the solvent is treated within the PCM model and the azo form with explicit methanol molecule forming hydrogen bond with N=N and the rest of the solvent treated with the PCM model (blue dash-dot line). The computed spectra were calculated by using (a) B3LYP and (b) PBE exchange correlation functional.

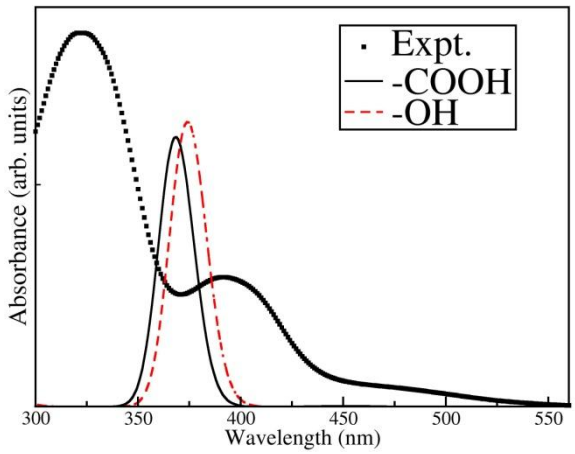

Figure 8. Experimental absorption spectra of the azoquinoline dye (black dotted line), computed absorption spectra of the azo form with explicit methanol molecule forming hydrogen bond with -COOH and -OH (black solid line and red dashed line respectively) and the rest of the solvent treated with the PCM model.

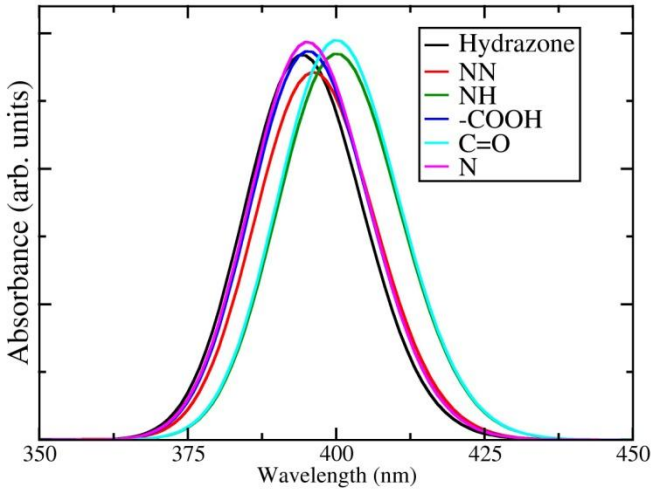

Figure 9. The computed absorption spectra of the hydrazone form (black solid line) where the solvent is treated within the PCM model and the hydrazone form with explicit methanol molecule forming hydrogen bond with different hetero atoms such as nitrogen (N) and oxygen (O) and the rest of the solvent treated with the PCM model.

ZnO-3ABBNHQ composite:

The calculations on the model ZnO-azoquinoline system have been performed using the Quantum ESPRESSO software , which is a plane wave based implementation of density functional theory (DFT). The electron-ion interactions were described using ultrasoft pseudopotentials. The exchange-correlation potential had been described by the Purdew, Burke and Ernzenhof (PBE) parametrization within the generalized gradient approximation. Moreover, the band gap of ZnO is severely underestimated because of the wrong position of the Zn *3d* orbitals. To correct for this we use *fictitious* Hubbard potentials of U=12.0 eV on the *3d* orbitals of Zn and U=6.5 eV on the *2p* orbitals of O. The details regarding the choice of the value of U and other computational details can be found in our previous work. The Brillouin zne integrations had been done using the Gamma point only.

The ZnO-azoquinoline composites have been modeled using a ZnO($10\bar{1}0$) surface to which the dye molecule is attached. An asymmetric slab using six ZnO bilayers represents the surface. The bottom of the slab is passivated with pseudo-hydrogen atoms to remove the spurious electronic states in the band gap originating from the dangling bonds. The dye is placed on the other side of the slab. Since we are interested

in the interaction between the dye molecule and ZnO, we have used a (5×2) surface supercell resulting in a minimum separation of about 8 Å between the periodic images of the molecules in the x-y plane. Further the periodic images along the z-direction are separated by using a vacuum of 20 Å. Additionally, to cancel the effects of the spurious dipole moment generated by the presence of the molecule on one side of the slab and pseudo-hydrogen atoms on the other side, we have also applied an external electric field in the direction opposite to that of the dipole moment.

For further understanding the electron transfer possibilities in the composite, we studied the interactions of the azo dye with ZnO($10\bar{1}0$). For the azo form we considered two configurations where the dye binds to the ZnO surface through the –COOH group (Figure 10(a)) and through the hydroxyl imine group (Figure 10(b)). Our calculations show that for both the configurations the molecule binds vertically to the slab retaining their planar structure. Moreover, the dye molecule spontaneously deprotonates during the geometry relaxation. The proton released from the anchoring groups binds to the nearest electron rich surface O atoms of ZnO. The configuration in which the molecule is anchored through the –COOH group is about 0.67 eV lower in energy than the one in which it is anchored through the hydroxyl imine group. The relaxed structure for the –COOH chelating group is shown in Figure 10(a). The newly formed Zn-O bond lengths are about 2.03 Å and 1.94 Å for -COOH chelating group. To study the effect of the solvent on the planarity of the dye molecule when the composite is formed, we have placed a methanol molecule near the –N=N- bond. The relaxed geometry is shown in Figure 10(c). Similar to what we observed for the dye molecule in the solvent, here also the molecule loses its planarity. The C-N-N-C angle deviates slightly from zero to about 1°. We note that this deviation is much smaller than what is observed for the molecule in solvent (the C-N-N-C dihedral angle to be about 4°).

Figures 11 shows the density of states (DOS) and the wavefunctions of the frontier orbitals of the model composite in the absence and presence of methanol respectively. The electronic states plotted in the DOS are aligned with respect to the energy of vacuum that has been set to zero.

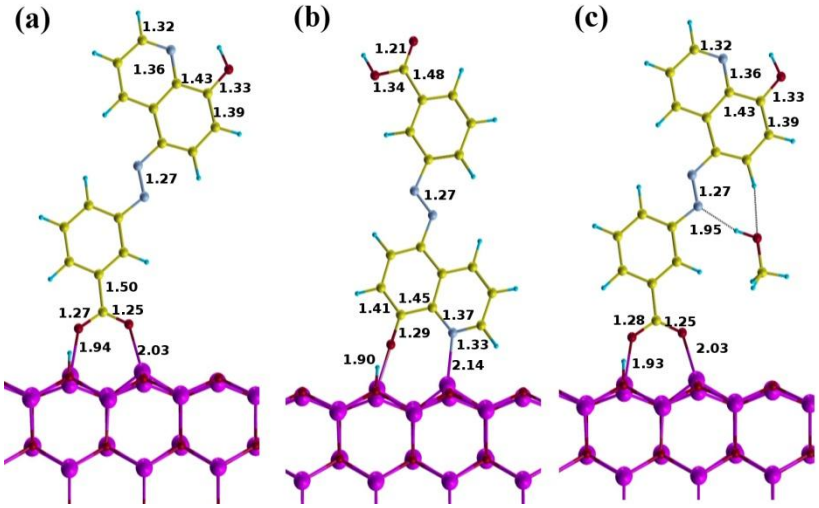

Figure 10. Optimized structure of the azoquinoline carboxylic acid dye anchored to ZnO through (a) -COOH (benzoic acid moiety) and (b) N, -OH (hydroxyl imine moiety). (c) Also shown is the relaxed structure of the molecule (anchored through –COOH group) in presence of methanol. The magenta, red, yellow, cyan and grey spheres represent Zn, O, C, H and N atoms respectively. The bond lengths are given in Å.

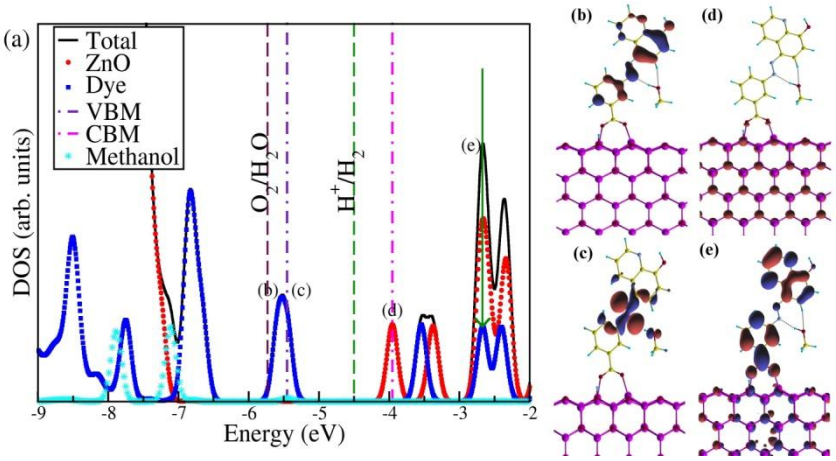

Figure 11. (a) Total and projected DOS for the -COOH anchoring configuration of the dye on ZnO in presence of an explicit methanol molecule. Dot-dashed violet and magenta vertical dashed lines denote the valence band maxima (VBM) and the conduction band minima (CBM) respectively of the composite. The dashed brown and green lines mark the water oxidation and reduction potentials respectively. The isosurfaces corresponding to VBM-1, VBM, CBM and CBM+2 are shown in (b), (c), (d) and (e) respectively. The green arrow highlights the coupling of the dye empty state with ZnO.

4ABBN8HQ molecule in gas phase and solvent:

We have performed density functional theory (DFT) based calculations using Gaussian 09 Revision D.01 software and used Cam-B3LYP exchange-correlation functional and 6-311++G(d,p) localized basis set. The polarisable comtinuum model has been used for describing the solvent effect. Inorder to compare with the experimental details, for certain cases, we have used explicit methanol molecules as solvent in the calculations. The explicit methanol molecules were placed at various hydrogen bonding positions such as carbonyl (C=O), carboxylic (-COOH), hydroxylic (-OH) and azide (-N=N-) group of both tautomers of the dye molecule.

To study the absorption spectra properties of the molecules we have performed time dependent density functional theory (TDDFT) based calculations using the Davidson algorithm. Since these calculations are sensitive to the choice of the exchange correlation functional, we have calculated the absorption spectra using Cam-B3LYP, B3LYP and PBE functionals. We performed several dihedral scans to explore structural isomers of the dye molecule.

Lowest energy structure of dye in gas phase

The calculations of the different configurations of dye in gas phase were done using the Gaussian 09 Revision D.01 software [Ref G09]. We have used the B3LYP hybrid [ref] exchange-correlation (XC) functional and the 6-311++G(d,p) basis set. We found that overall red (blue) shift with PBE (cam-B3LYP hybrid) XC functional. We found the planar configuration of dye is corresponds to the global minima in gas phase with PCM solvent model. Then we incorporated explicit methanol molecules at various hydrogenbonding sites inorder to understand the effect of solvent molecules.

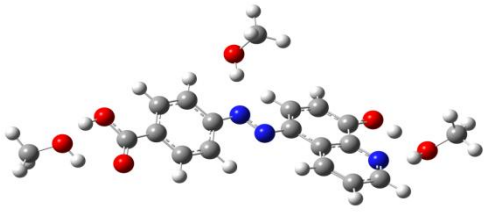

Figure 12. The structure of dye gas phase molecule with 3 explicit methanol molecules at 3 different hydrogen bonding positions such as a) at -COOH group b) at -OH and quinoline nitrogen group c) at N=N azide group.

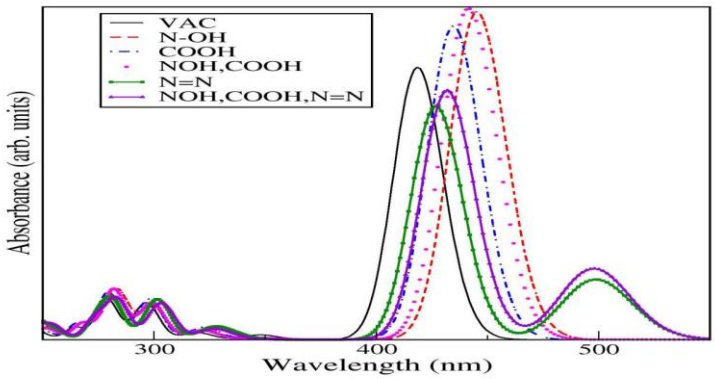

Figure 13. The absorption spectra of dye gas phase molecule as a function of explicit methanol molecules. These absorption spectra calculations were done with B3LYP XC and 6-311++g(d,p) basis set. Similarly we have used PCM solvent model for all the systems.

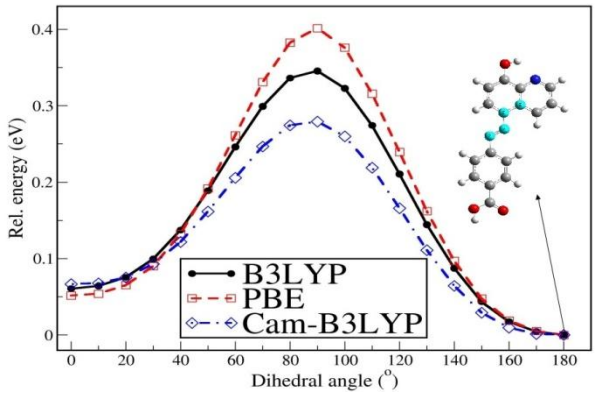

Figure 14. Potential energy profile as a function of the NNCC dihedral angle as marked with cyan color. These absorption spectra calculations were done with B3LYP (PBE and Cam-B3LYP) XC and 6-311++g(d,p) basis set. Similarly we have used PCM solvent model for all the systems.

We computed absorption spectra of stable (planar) dye molecule of both tautomeric forms, found single sharp peaks at 378 nm from azo form (solid black line in Figure 15(a)) and 396 nm for hydrazone form (red dashed line in Figure 15(a)). The nature of these transitions are HOMO to LUMO which are coming from π to π* of the molecule (Figure 15(b) to Figure 15(e)). So these two tautomeric forms are able to explain the two sharp peaks (320 nm and 420 nm) of experimental absorption spectra (Figure

15(a) black filled circles). But we found that there exists a transition n to π* of the molecule which has negligible oscillatory strength hence it is forbidden transitions. This n to π* transition can be enhanced by symmetry breaking of the dye molecule so we placed explicit methanol molecules at three functional groups such as azide (N=N), carboxylic (-COOH) and hydroxyl (-OH). Interestingly, we found that the explicit methanol placed at N=N causes loss of planarity of the molecule then which leads to enhancement of the peak position around 448 nm. For the –N=N- configuration we find that the molecule loses its planar structure with the C-N-N-C dihedral angle of 3°. The computed absorption spectra for this configuration are shown in Figure 15 (a) (blue dash-dot line). We find that in addition to the main peak at around 371 nm, there is a low intensity peak at 448 nm. The electronic states involved in these transitions are primarily from HOMO-1 to LUMO and HOMO to LUMO. For the long wavelength peak, the HOMO to LUMO transition has a larger contribution while for the peak at 371 nm the HOMO-1 to LUMO transition is more dominant. The wavefunctions corresponding to the the HOMO-1 and HOMO of this configuration is shown in Figure 15(f) and (g) respectively. We find that in this case, (a) the HOMO π character changes to a mixed n/π type, (b) the wavefunction corresponding to HOMO-1 has a significant weight on the solvent methanol molecule and (c) the LUMO is unchanged. Similarly when methanol is placed near the different functional groups of the hydrazone form we do not observe the long wavelength peak in the absorption spectrum. Based on these results, we predict that the long wavelength broad peak in the experimental absorption spectrum of the dye originates because of the loss in planarity of the dye molecule that is induced by solvation in methanol and the electronic transition corresponding to that peak is a n/π to π* transition.

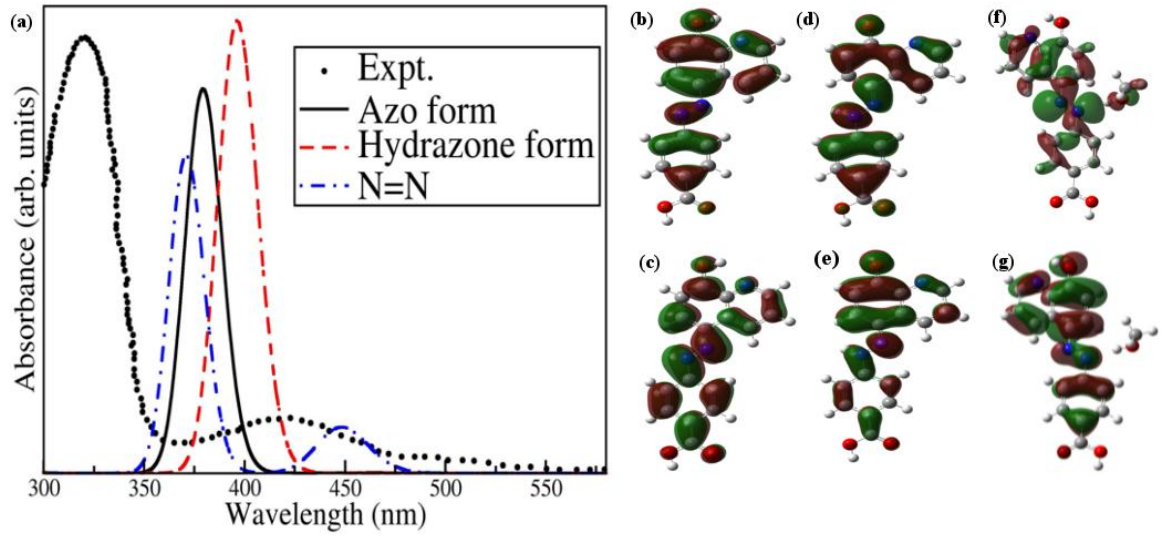

Figure 15. (a) Experimental absorption spectra of the azoquinoline dye (black dotted line), computed absorption spectra of the azo form (solid black line) and the hydrazone form (red dashed line) where the solvent is treated within the PCM model and the azo form with explicit methanol molecule forming hydrogen bond with N=N and the rest of the solvent treated with the PCM model (blue dash-dot line). Isosurfaces corresponding to (b) HOMO and (c) LUMO of the azo form, (d) HOMO and (e) LUMO of the hydrazone form and (f) HOMO-1 and (g) HOMO of the azo form of the dye with a single explicit methanol molecule at N=N.

ZnO-4ABBNHQ composite:

Our calculations are based on first-principles density functional theory (DFT) and plane-wave pseudopotential method as implemented in Quantum ESPRESSO (QE). The ionic core–valence electron interactions are represented with ultrasoft pseudopotentials and electronic exchange correlation energy is approximated with a generalized gradient approximation (GGA) as parametrized by Perdew–Burke–Ernzerhof for Zn, O, C, H, and N atoms. Kohn–Sham wave functions are expanded in a plane wave basis set truncated with energy cutoff of 35 Ry (and a corresponding cutoff of 400 Ry for charge density). The band gap of ZnO is severely underestimated because of the wrong position of the Zn 3d orbitals. To correct for this we use fictitious Hubbard potentials of U=12.0 eV on the 3d orbitals of Zn and U=6.5 eV on the 2p orbitals of O. The Brillouin zone integration has been performed using the Gamma point only. We modeled 5×2 super cell of ZnO($10\bar{1}0$) surface with six ZnO

bilayers. Further the composite have been modeled by using ZnO asymmetric slab to which dye molecule is attached. The two functional (chelating) groups are attached with surface of the ZnO. Additionally we investigated electronic structure of the single anchoring, for that the bottom of the ZnO($10\bar{1}0$) slab is passivated with pseudo-hydrogen atoms to remove the spurious electronic states in the band gap originating from the dangling bonds. The dye is placed on the other side of the slab.

For further understanding the electron transfer possibilities in the composite, we studied the interactions of the azo dye with ZnO(101 0). The clean ZnO (1010) surface contains ordered rows of buckled Zn-O dimers along the polar [0001] direction with a net electron accumulation on the O atoms. Our calculations shows that -COOH of dye binds on two Zn atoms and quinolinic N and -OH moieties with opposite side of Zn atoms as shown in (Figure 16). During the relaxation process, dye molecule spontaneously gets deprotonated from -COOH and -OH group, releasing an H^+ ion, which gets attached to the neighbouring electron rich O of the ZnO surface. The newly formed Zn-O bond lengths are about 1.92 Å and 1.96 Å for -COOH chelating group and the newly formed Zn-O and Zn-N bond lengths are 1.92 and 2.23 Å with hydroxylamine functional group. Further the molecule lost the planarity and its dihedral (CNNC) is 22^o. We do not observe any modification in middle layers out of six bilayers. However surface layers are expanded (compressed) by 0.12 Å (0.39 Å) of AA (AB) planes. Further we do not observe any distortion of the surface except at the adsorption site where the buckling of the Zn-O dimers are modified at chelating site.

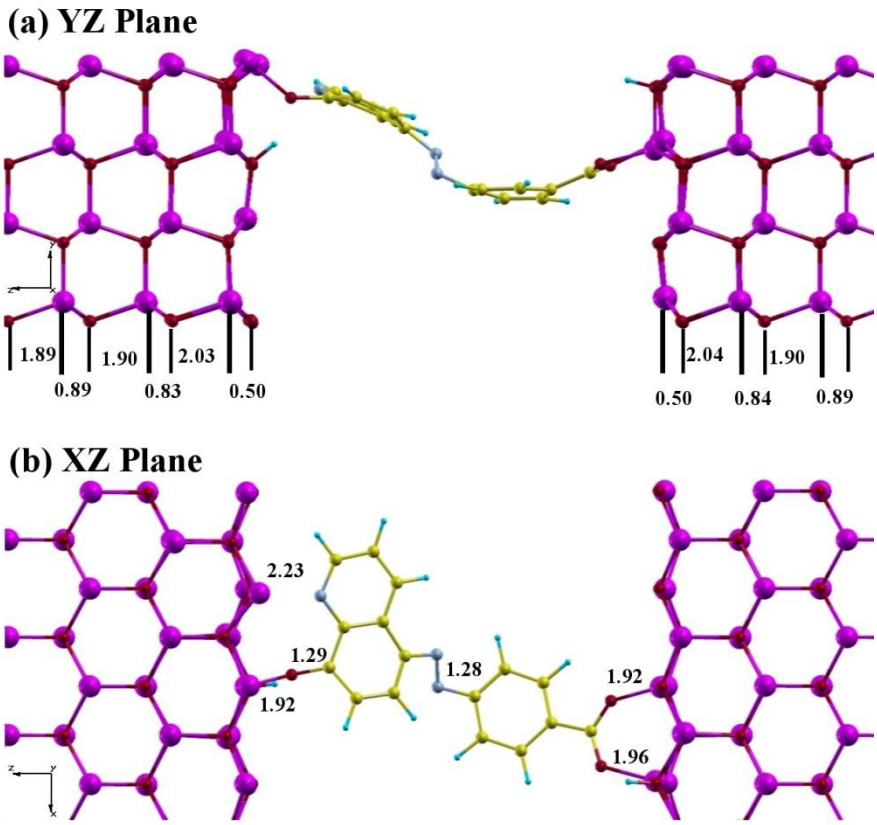

Figure 16. Optimized structure of dye between ZnO (1010) surface with a) YZ plane and b) XZ plane orientations. The magenta, red, yellow, cyan and grey spheres represent Zn, O, C, H and N atoms respectively. The bond lengths are given in Å.

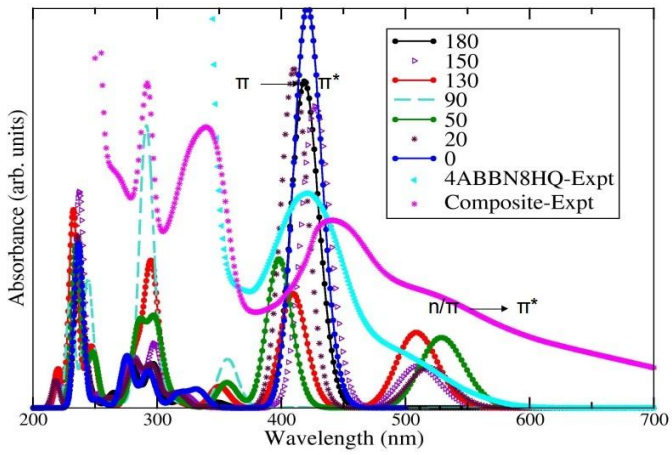

Figure 17. The absorption spectra of dye gas phase molecule as a function of NNCC dihedral angle compared with experimental absorption spectra. These absorption spectra calculations were done with B3LYP exchange correlational functional and 6-311++g(d,p) basis set. Similarly we have used PCM solvent model for all the systems.

Absorption struture of relaxed dye molecule from the 4ABBN8HQ-ZnO composite:

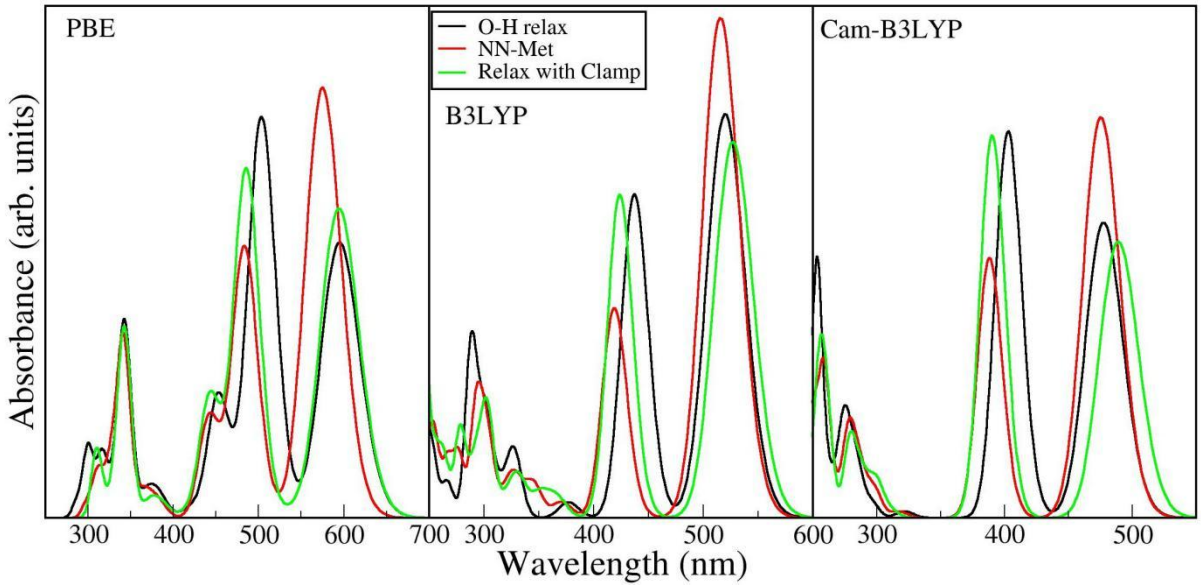

Figure 18. Absorption spectra of dye gas phase molecule considered from relaxed structure of ZnO- dye composites. Here we performed 3 different absorption spectra calculations. a) keeping constant of all coordinates and relaxing -OH groups (black line) b) incorporation of 1 explicit methanol at N=N group to a) (red line) and c) fixing of anchoring atoms (such as oxygen atoms of -COOH, -OH and nitrogen atoms of quinoline) and relaxing all atoms (green line).

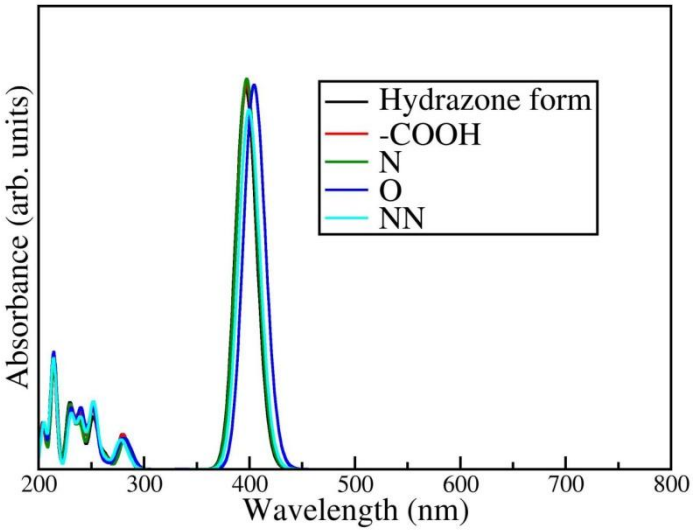

Figure 19. The computed absorption spectra of the hydrazone form (black solid line) where the solvent is treated within the PCM model and the hydrazone form with explicit methanol molecule forming hydrogen bond with different hetero atoms such as nitrogen (N) and oxygen (O) and the rest of the solvent treated with the PCM model.

APPENDIX-4

CHAPTER 2

^{1}H

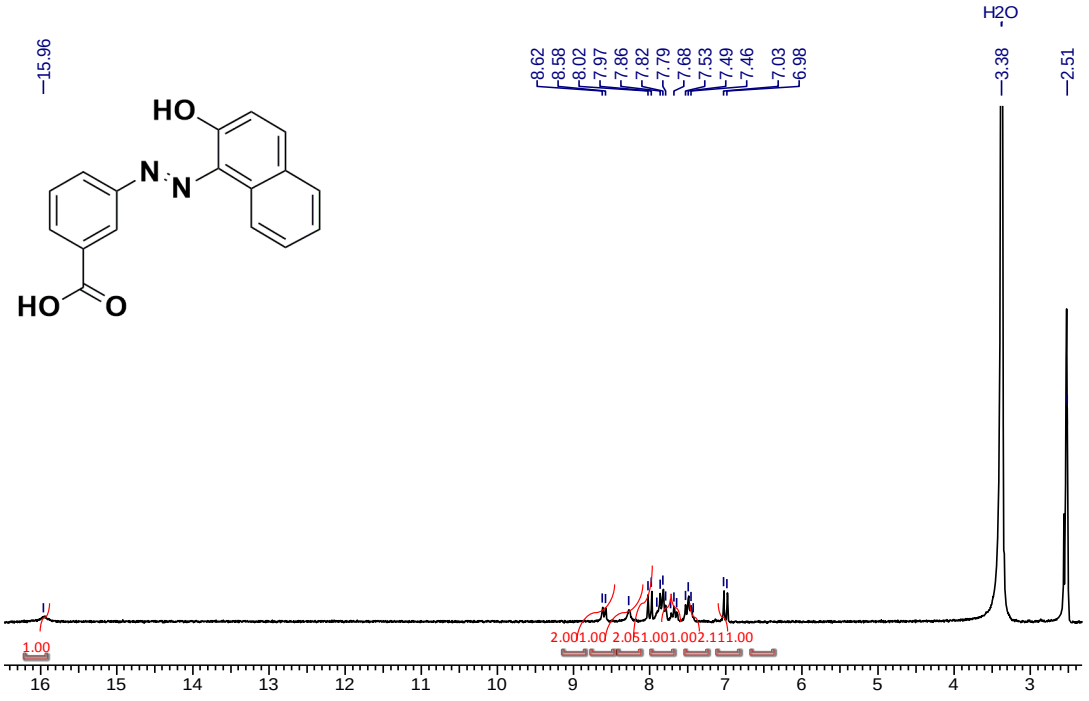

^{13}C

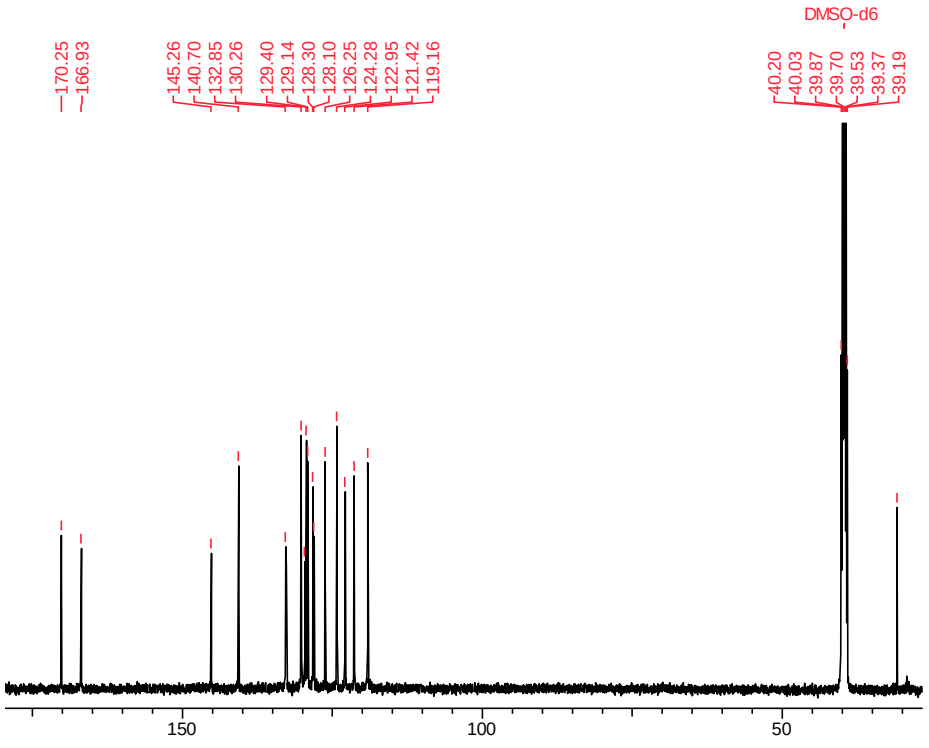

DEPT

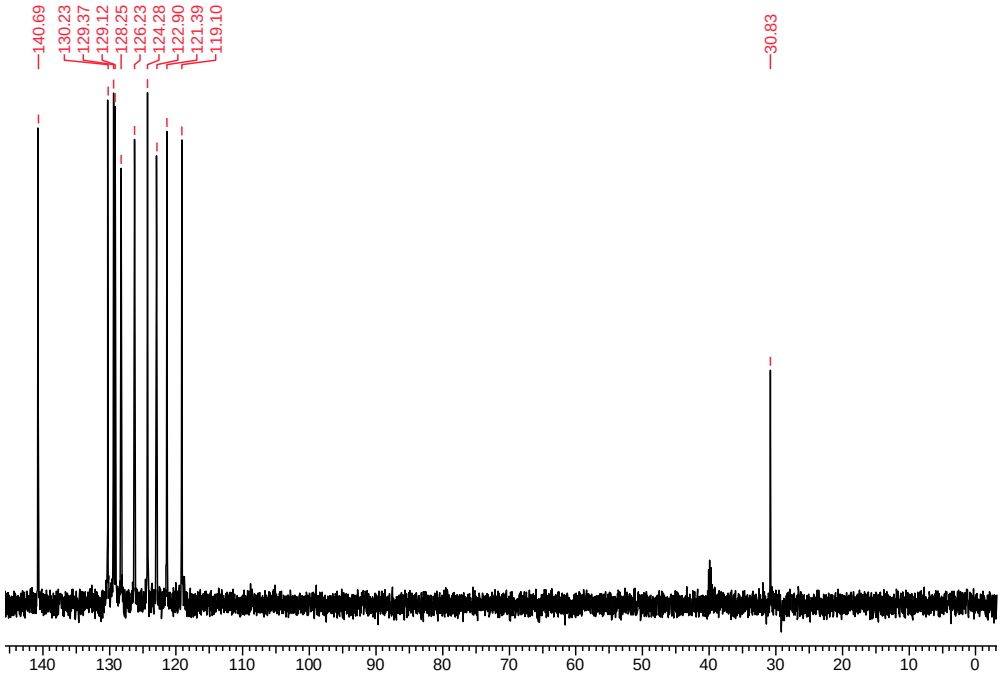

Figure 1. ^{1}H, ^{13}C and DEPT of 3ABBN.

^{1}H

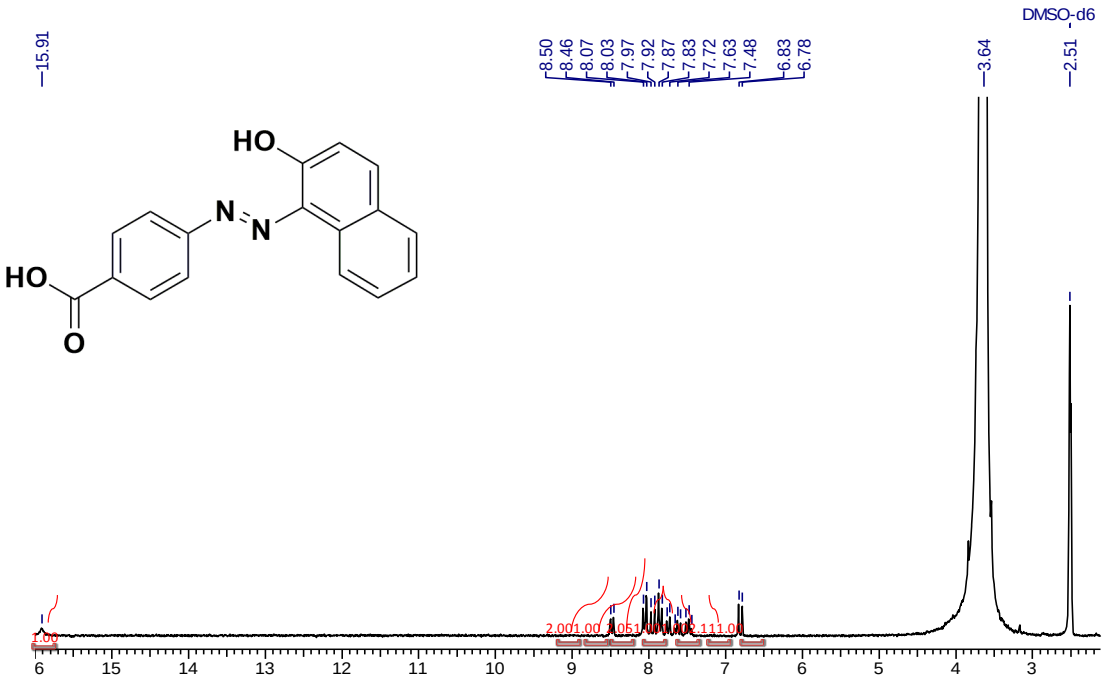

^{13}C

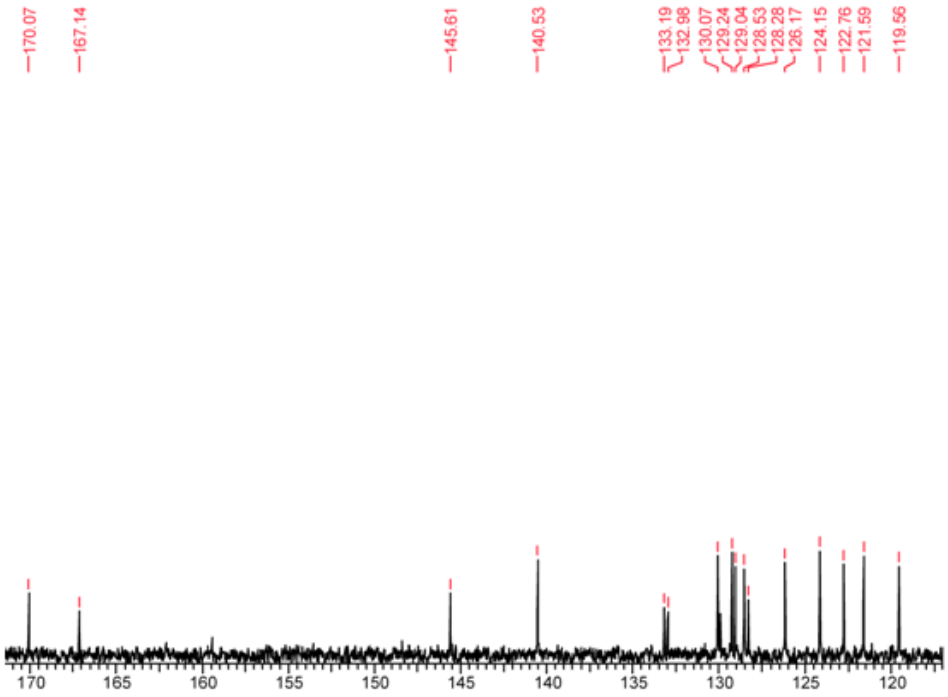

DEPT

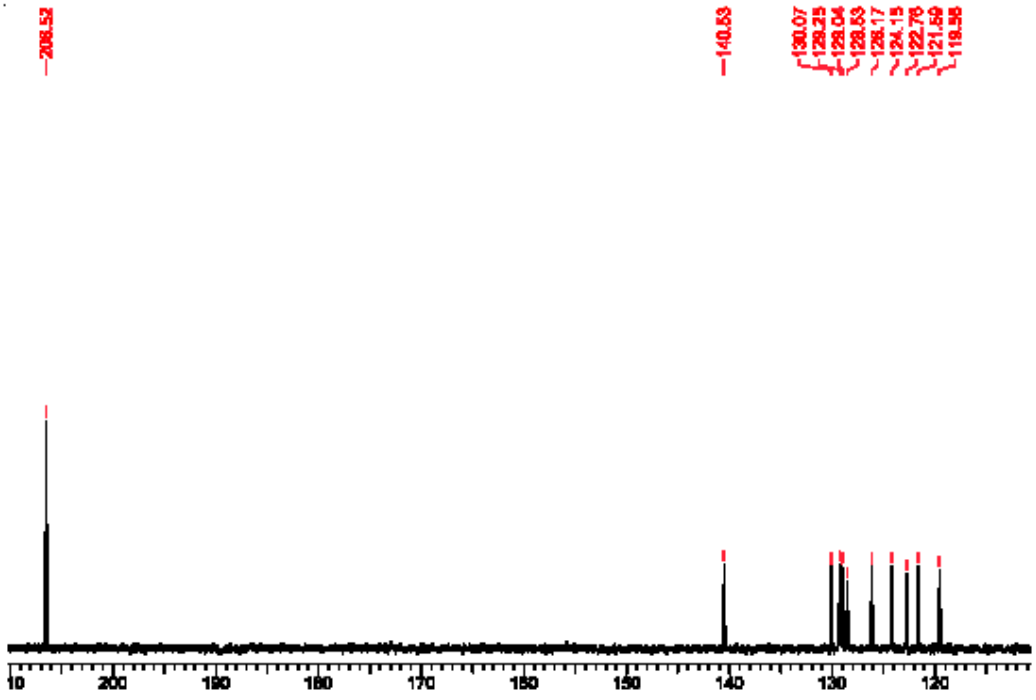

Figure 2. ^{1}H, ^{13}C and DEPT of 4ABBN.

CHAPTER 3

^{1}H NMR

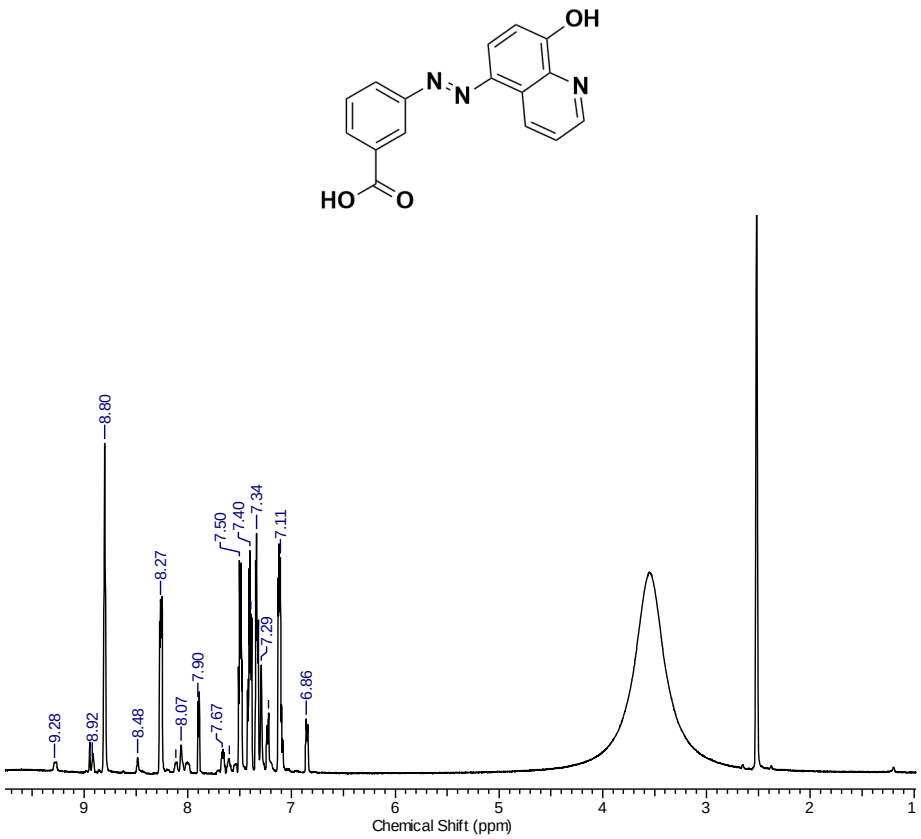

^{13}C

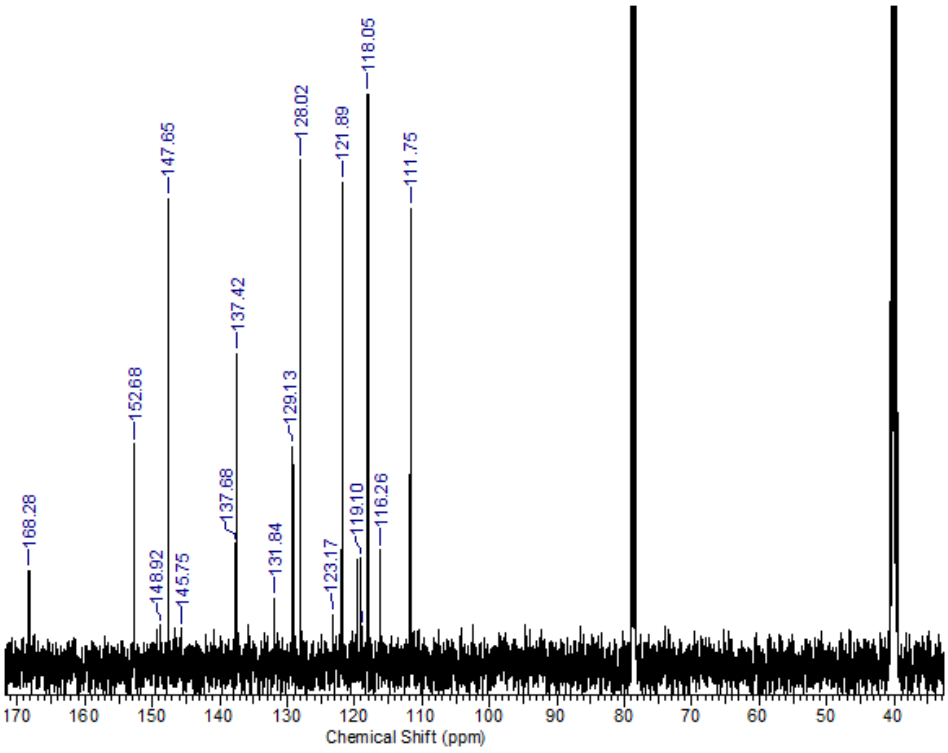

DEPT

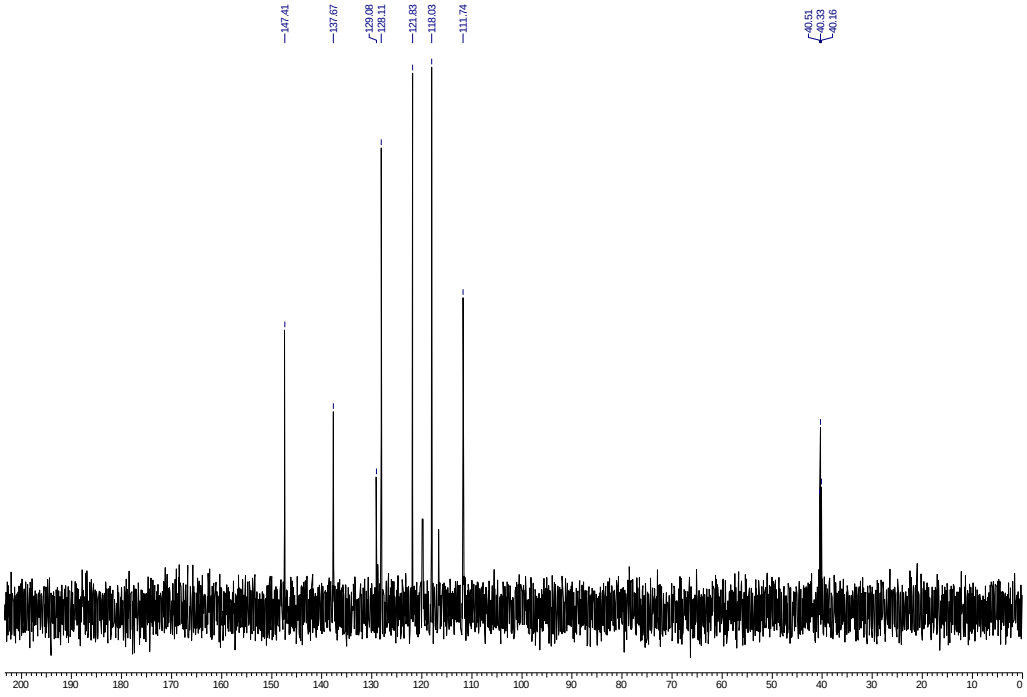

Figure 3. ^{1}H, ^{13}C and DEPT of 3ABBNHQ

^{1}H NMR

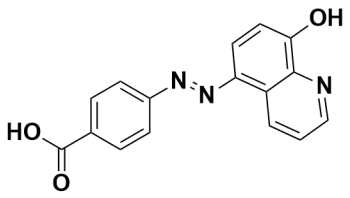

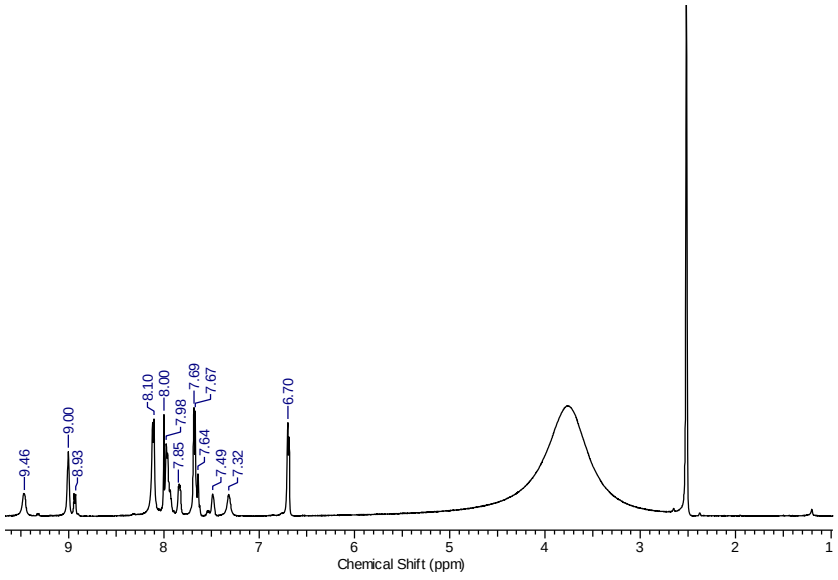

^{13}C NMR

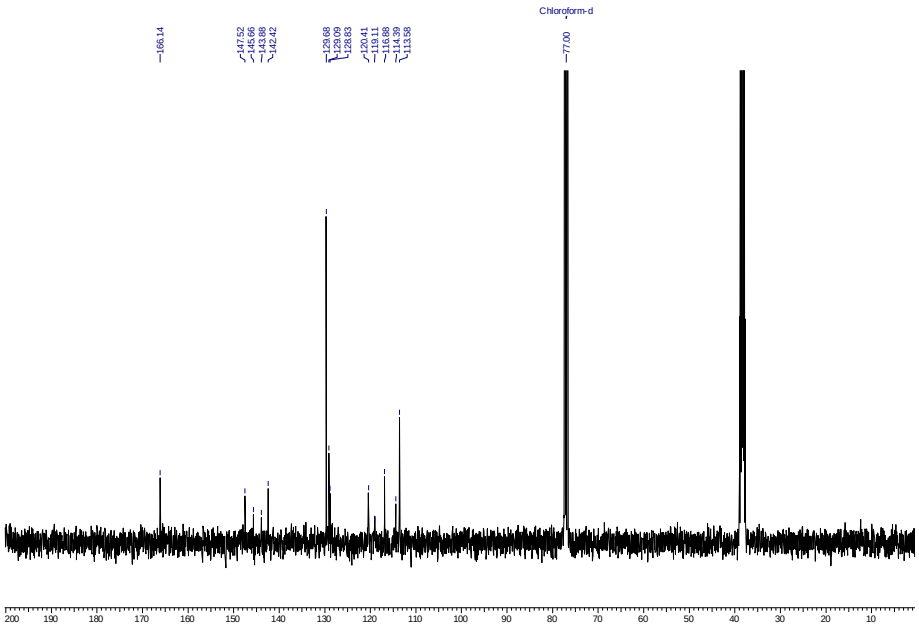

DEPT

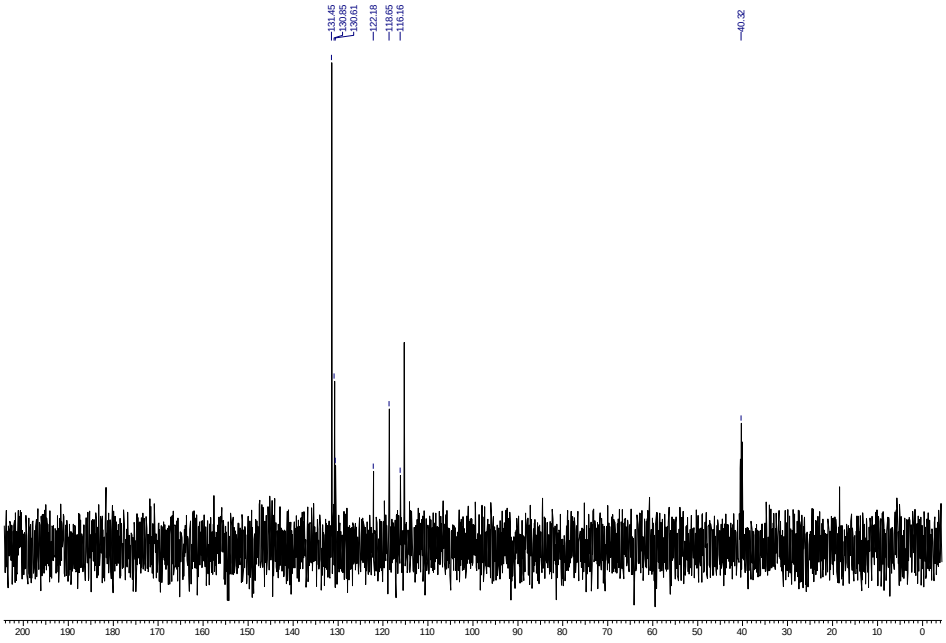

Figure 2. ^{1}H, ^{13}C and DEPT of 4ABBNHQ

CHAPTER 4

^{1}H NMR

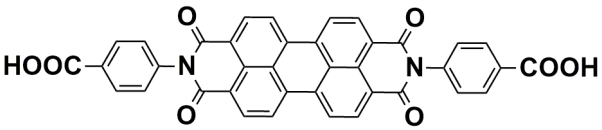

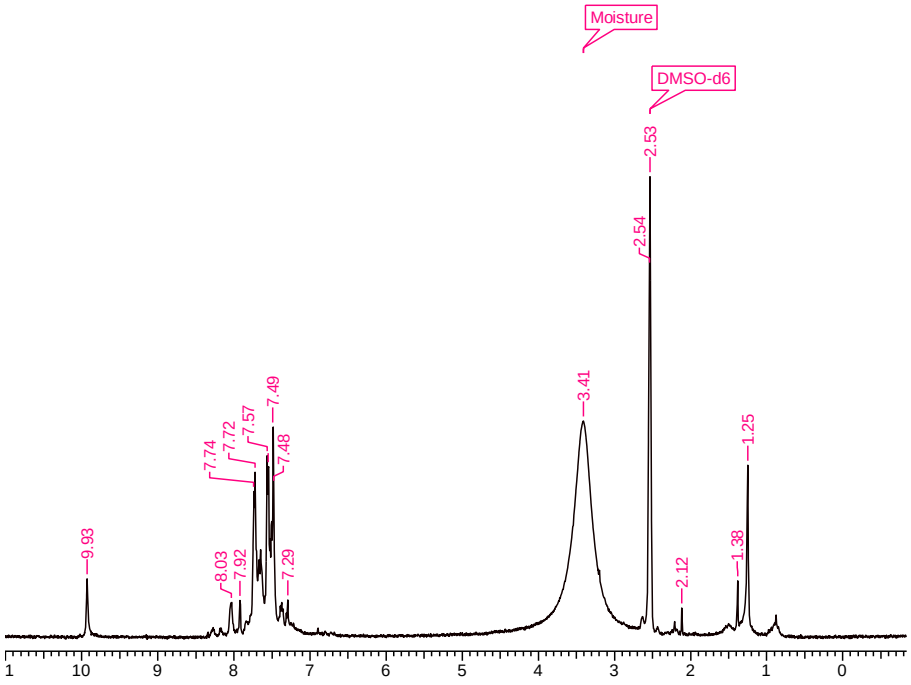

^{13}C NMR

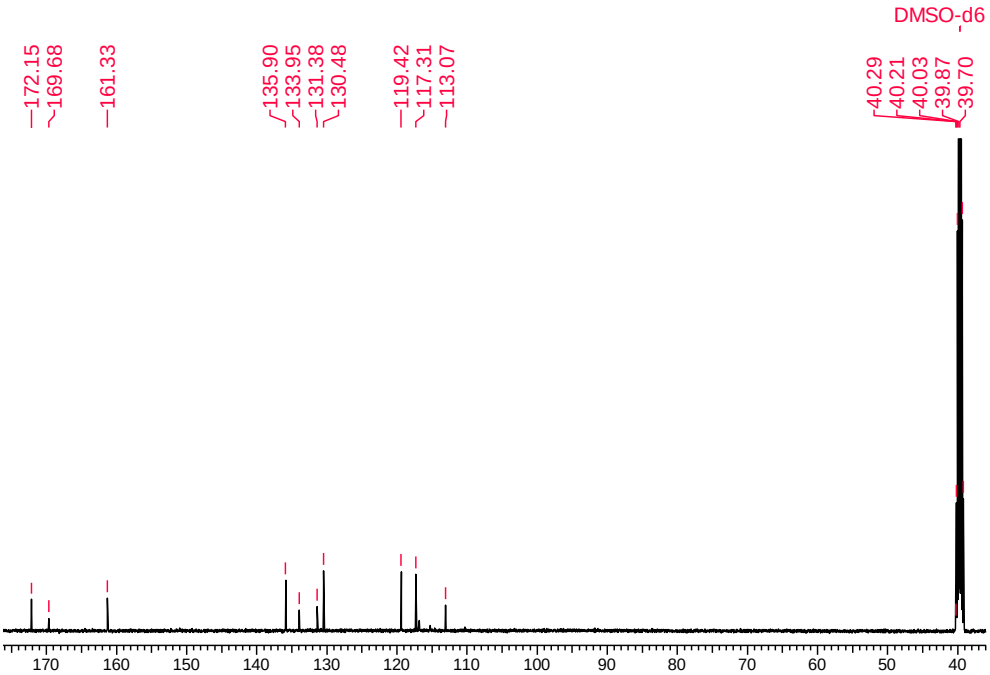

DEPT

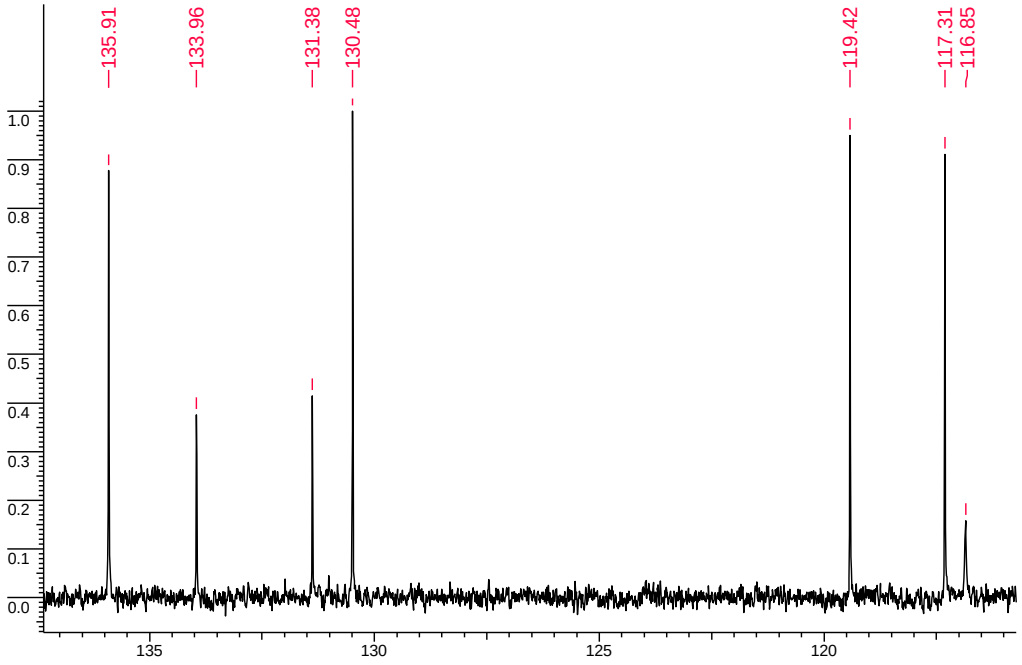

Figure 5. ^{1}H, ^{13}C and DEPT of PTCDACOOH2

CHAPTER 5

^{1}H NMR

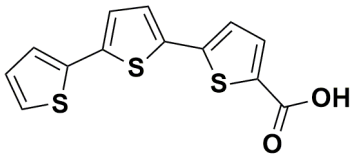

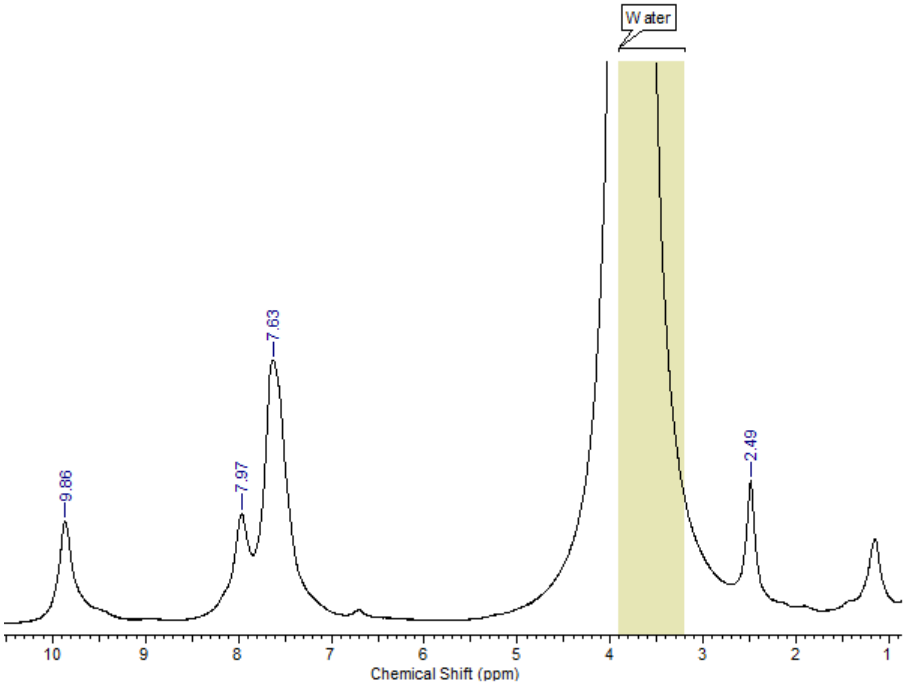

^{13}C NMR

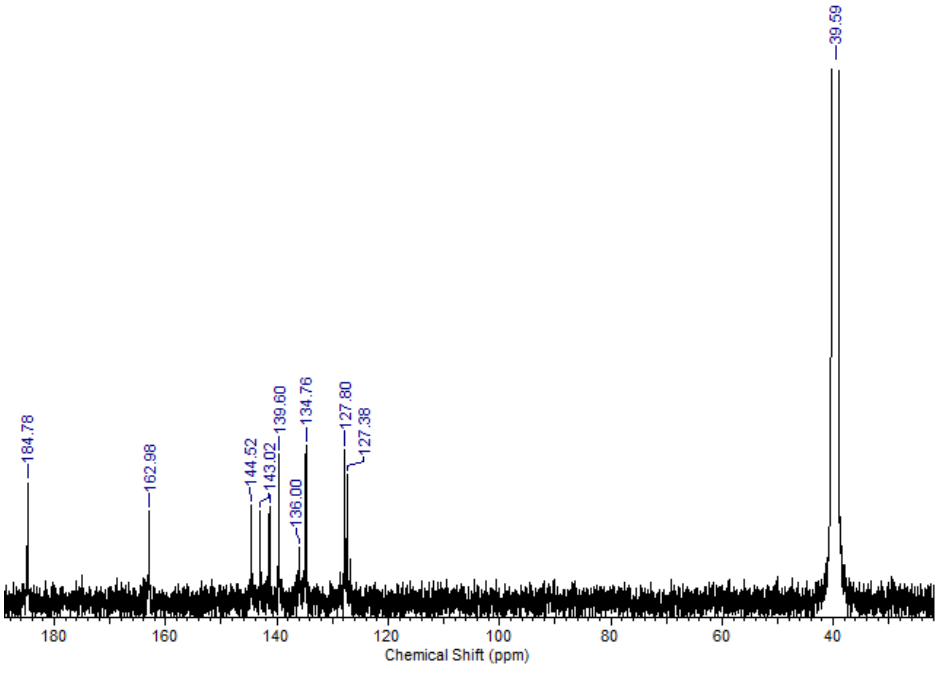

DEPT

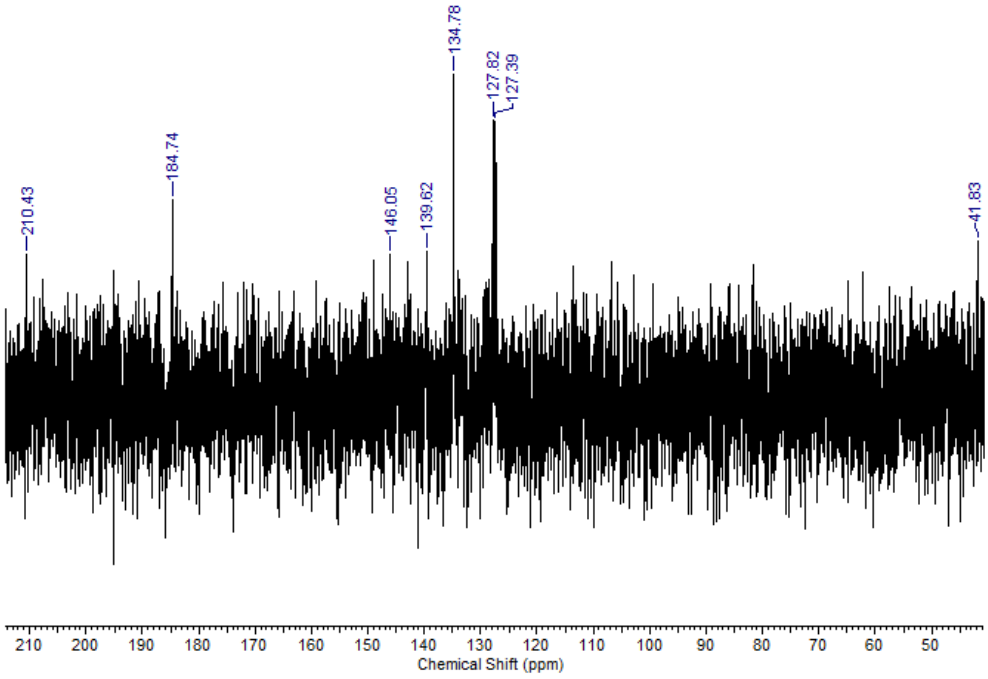

Figure 6. ^{1}H, ^{13}C and DEPT of TTTCOOH

^{1}H NMR

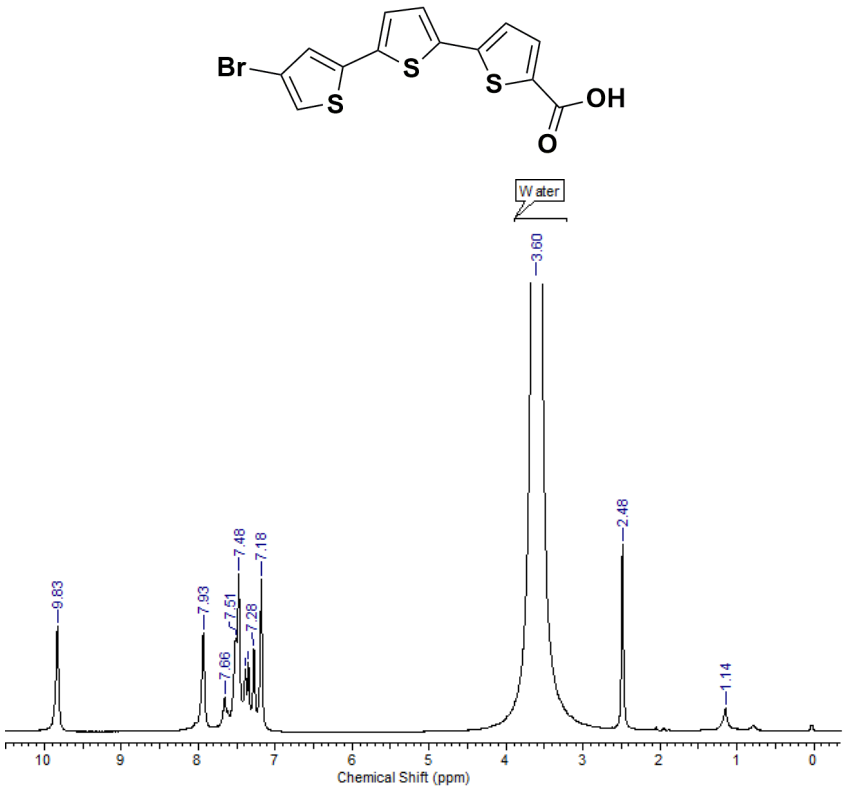

^{13}C

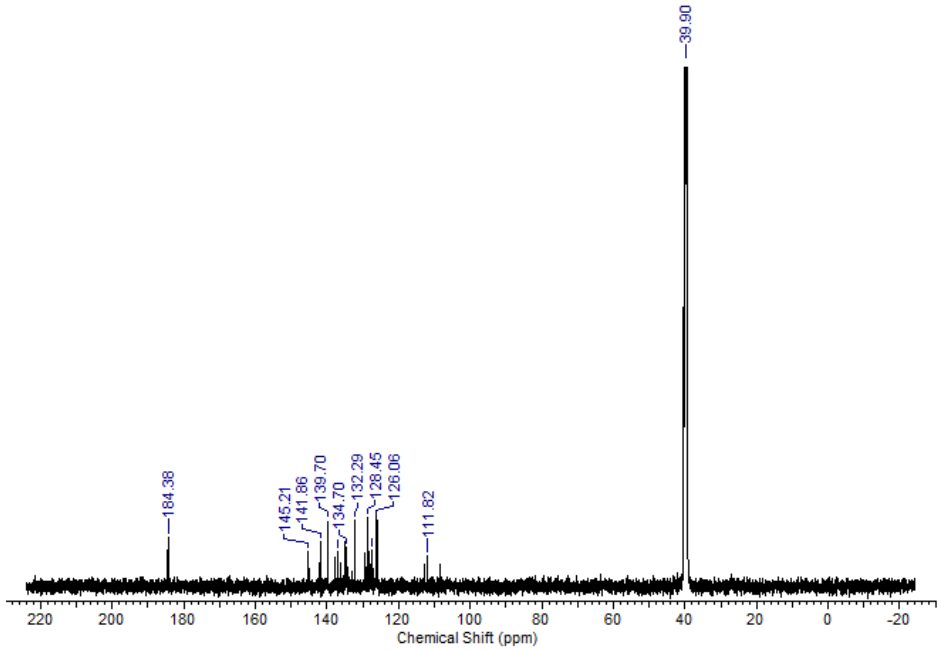

DEPT

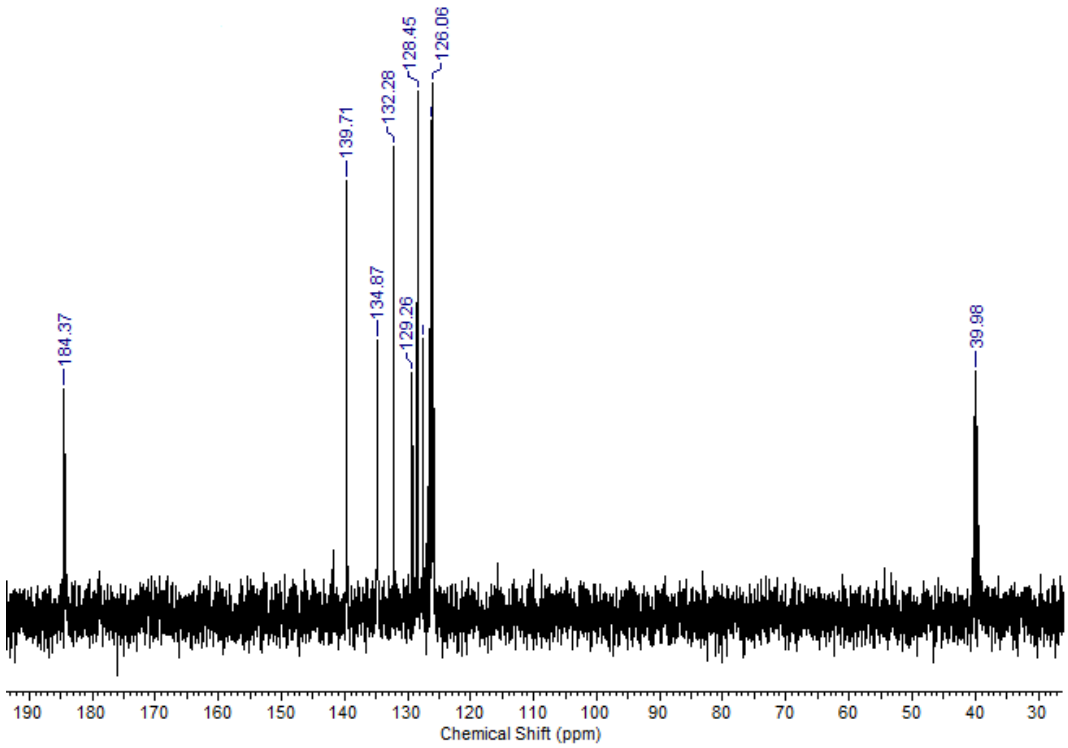

Figure 7. ^{1}H, ^{13}C and DEPT of BrTTTCOOH